

AD-A097 946

ENVIRONMENTAL RESEARCH INST OF MICHIGAN ANN ARBOR RA--ETC F/6 17/9  
IMAGING OCEAN WAVES WITH SAR; A SAR OCEAN WAVE ALGORITHM DEVELO--ETC(U)  
DEC 79 R A SHUCHMAN; K H KNORR; J C DWYER N00014-76-C-1048

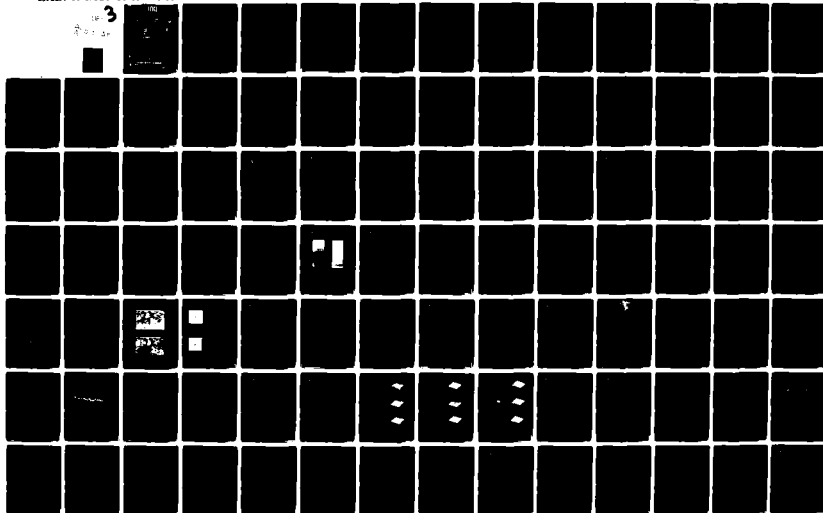
UNCLASSIFIED

FRIM124300-5-T

NL

3

10-1-80



LEVEL III

AD 58617

12

124300-5-T

AD A 097946

DTIC FILE COPY

9

Interim Technical Report

6

# IMAGING OCEAN WAVES WITH SAR,

A SAR Ocean Wave Algorithm

Development Program.

10

Robert SHUCHMAN  
Ken R.H. KNORR  
J. Craig DWYER  
Philip D.L. JACKSON  
Alex KLOOSTER  
A.L. MAFFETT

DTIC  
ELECTRONIC  
APR 20 1981

12 193

11

DEC 1979

(Revised December 1980)

APPROVED FOR PUBLIC RELEASE  
DISTRIBUTION UNLIMITED.

14

ERIM 124300-5-T

NT

A058617

Geography Branch  
Office of Naval Research  
Arlington, Virginia 22217

15

Contract No. N00014-76-C-1048  
Technical Monitor: Mr. Hans Dolenzek

ENVIRONMENTAL  
RESEARCH INSTITUTE OF MICHIGAN

BOX 8618 • ANN ARBOR • MICHIGAN 48107

408392  
81 4 20 062

TECHNICAL REPORT STANDARD TITLE PAGE

1. Report No. 124300-5-T		2. Government Accession No. AD-A 097 946		3. Recipient's Catalog No.	
4. Title and Subtitle Imaging Ocean Waves With SAR--A SAR Ocean Wave Algorithm Development Program				5. Report Date December 1979	
				6. Performing Organization Code	
7. Author(s) R.A. Shuchman, K.H. Knorr, J.C. Dwyer, P. L. Jackson, A. Klooster and A.L. Maffett				8. Performing Organization Report No. 124300-5-T	
9. Performing Organization Name and Address Environmental Research Institute of Michigan Radar and Optics Division P. O. Box 8618 Ann Arbor, MI 48197				10. Work Unit No.	
				11. Contract or Grant No. N00014-76-C-1048	
12. Sponsoring Agency Name and Address Geography Branch Office of Naval Research Arlington, VA 22217				13. Type of Report and Period Covered Interim Technical Rept.	
				14. Sponsoring Agency Code	
15. Supplementary Notes The technical monitor for this program is Mr. Hans Dolezalek					
16. Abstract <p>&gt; Four principal activities are discussed in this report. They include: (1) SAR geometric distortion and an optical technique to correct these distortions, (2) a digital spectral estimation package designed specifically for SAR ocean wave data, (3) determination of wave height from SAR data, and (4) examination of the mechanism involved in SAR imaging of ocean waves.</p> <p>In the first activity, the slant range distortion of SAR imagery was theoretically considered. This was followed by the consideration of an optical configuration required to correct the data. The optical configuration was then set up and actual SAR data was range distortion corrected. The ERIM optical setup was tested on both computer-generated and actual SAR slant-range data; analysis of the resulting ground-range-corrected data indicated that less than 0.5% error resulted. SAR range distortions for a curved Earth's surface were also studied and actual satellite SAR data from SEASAT was optically corrected and used in SEASAT validation activities.</p> <p>The second activity involved the design and implementation of a computer software system that obtains spectral estimates of wavelength and direction information for surface gravity waves. The software system utilizes either standard fast Fourier transform techniques or maximum entropy spectral analysis (MESA), both sometimes referred to as semicausal methods. Output products of the ERIM-developed SAR two-dimensional aperture-estimation package include: (1) contour and perspective (3-D) plots of spectrum estimates, (2) a</p>					
17. Key Words Ocean waves      S ISAT Remote sensing      Digital processing Data processing      Spectral analysis SAR imagery      Semi-causal Multi-frequency synthetic aperture radar			18. Distribution Statement Distribution of this document is unlimited.		
19. Security Classif. (of this report) Unclassified		20. Security Classif. (of this page) N/A		21. No. of Pages	
				22. Price	

## 16. Abstract

one-dimensional wave-number spectrum, (3) the maximum direction, (4) the average directional spectrum, (5) the directional spread for a given wave number, and (6) the cosine spread function of the one-dimensional spectrum.

In the third activity, the question of wave height determination using SAR was explored. The effort looked extensively at a technique reported by Jain (1977) that obtains wave height information by using the radar chirp bandwidth information. The experiments performed did not confirm the validity of Jain's technique to infer wave height, but rather it demonstrated some rather serious shortcomings of the technique.

The fourth activity discussed in this report was the SAR modeling of ocean surface conditions. A number of existing models which attempt to explain wave imagery obtained with a synthetic aperture radar were examined. These models are of two types: (1) static models that depend on instantaneous surface features and (2) dynamic models that employ surface velocities. This study attempts to draw together analytical and experimental results based on a combination of these two types in order to approach a more satisfactory model for SAR ocean wave imaging.

Accession For	
NTIS GRA&I	<input checked="checked" type="checkbox"/>
DTIC TAB	<input type="checkbox"/>
Unannounced	<input type="checkbox"/>
Justification	
By _____	
Distribution/	
Availability Codes	
Dist	Avail and/or Special
A	

## PREFACE

The work described in this interim report was conducted by the Radar and Optics Division of the Environmental Research Institute of Michigan. This work was supported by the Office of Naval Research, Geography branch under Contract No. N00014-76-C-1048. The Technical Monitor was Hans Dolezalek.

The Principal Investigator for this project is Robert A. Shuchman. Section 5, which deals with synthetic aperture radar (SAR) geometry and the optical slant-to-ground-range conversion, was written by Philip Jackson, Juris Upatnieks, Alex Klooster, and Carl Leonard. Ken Knorr was responsible for the digital spectral analysis package discussed in this report; he was assisted by William McLeish of the National Oceanic and Atmospheric Administration/Sea-Air-Interaction Laboratory (NOAA/SAIL).

Section 7, which discusses wave height determination using SAR, was contributed by Craig Dwyer; he was assisted by Ivan Cindrich, James Marks, Alex Klooster, and Jack Losee. Section 8, which deals with SAR imaging of ocean waves was prepared by Robert Shuchman, Andrew Maffett and Alex Klooster.

Thanks are given to Jack Walker, Richard Larson, and Eric Kasischke for reviewing this report.

## TABLE OF CONTENTS

PREFACE . . . . .	iii
LIST OF FIGURES . . . . .	vii
LIST OF TABLES . . . . .	ix
1. INTRODUCTION . . . . .	1
2. SUMMARY . . . . .	3
3. SAR SENSING OF SURFACE OCEAN CONDITIONS: A Review of the Present State of the Art and Recommendations for Further Study . . . . .	9
3.1 Dominant Wavelength and Direction . . . . .	9
3.2 Wave Height Determination . . . . .	10
3.3 Surface Currents . . . . .	11
3.4 Internal Waves and Ocean Frontal Boundaries . . . . .	13
3.5 Detection of Bottom Topographic Features with SAR . . . . .	14
3.6 SAR as an Indicator of Wind and Air/Sea Temperature . . . . .	16
4. RESULTS FROM ONR-SPONSORED ACTIVITIES: Applications of this Presently Funded ONR Research Activity . . . . .	19
5. SAR GEOMETRIC DISTORTIONS AND AN OPTICAL CORRECTION ALGORITHM . . . . .	21
5.1 Introduction . . . . .	21
5.2 Derivation of the Slant vs. Ground Range Equation . . . . .	25
5.3 Derivation of Optical System Equation . . . . .	30
5.4 Optical System Parameter Selection . . . . .	34
5.5 Summary and Conclusions of Theoretical Considerations . . . . .	39
5.6 Experimental Verification of the Optical Correction for the Range Dimension Distortion . . . . .	39
5.7 Range Distortion Correction for a Curved Earth Surface . . . . .	43
5.8 Correction of Range Distortion for Actual Radar Data . . . . .	46
5.9 Slant-to-Ground-Range Conversion of SEASAT Imagery . . . . .	51
6. SAR DIGITAL SPECTRAL ESTIMATION ALGORITHM . . . . .	59
6.1 Introduction . . . . .	59
6.2 Software Description . . . . .	63
6.3 Digital Spectral Estimations . . . . .	70
7. WAVE HEIGHT DETERMINATION FROM SYNTHETIC APERTURE RADAR . . . . .	87
7.1 Review of Jain's Algorithm . . . . .	87
7.2 Evaluation of Jain's Theory . . . . .	89
7.2.1 Speckle Correlation Techniques for Measurement of Surface Roughness . . . . .	89
7.2.2 Jain's Theory . . . . .	93
7.2.3 An Alternate Theory . . . . .	97

TABLE OF CONTENTS  
(concluded)

7.3	Experimental Results	104
7.3.1	Experimental Procedures	104
7.3.2	First Set of Experimental Data	112
7.3.3	Second Set of Experimental Data	113
7.3.4	Third Set of Data	117
7.3.5	Summary Discussion	120
8.	SYNTHETIC APERTURE RADAR MODELLING OF SURFACE OCEAN WAVES . . . .	123
	REFERENCES . . . . .	127
APPENDIX A:	RADAR IMAGE DISTORTION OF OCEAN WAVES DUE TO MOTION EFFECTS . . . . .	A-1
APPENDIX B:	"DETERMINATION OF OCEAN WAVE HEIGHTS FROM SYNTHETIC APERTURE RADAR IMAGERY" . . . . .	B-1
APPENDIX C:	TWO PAPERS ON SAR MODELLING OF OCEAN WAVES . . . . .	C-1

## LIST OF FIGURES

1. Side-Looking SAR Geometry . . . . .	22
2. Diagram Showing Slant Range Distortion of Linear Waves Oblique to Flight Path . . . . .	23
3. Conventional Radar Configuration . . . . .	26
4. Plot of the Ratios of $R_g/R_s$ and $\Delta R_g/\Delta R_s$ versus the Depression Angle $\theta_d$ . . . . .	27
5. Geometry Used to Derive the Slant Range Expression . . . . .	29
6. Proposed Optical Imaging System . . . . .	32
7. The Input Optical Data with Range Dimension Distortion, Compressed at Top near Nadir . . . . .	41
8. Demonstration of the Optical Correction of Range Distortion of Data in Figure 7 . . . . .	41
9. Optical System for Correction of Range Dimension Distortion . . .	42
10. The Schematic Diagram for the Optical System that Corrected the Range Distortion . . . . .	50
11. Optical Correction of Range Distorted Imagery . . . . .	52
12. Optical Fourier Transform (OFT) and Digital Fast Fourier Transform (FFT) of Uncorrected and Slant Range-Corrected SAR Wave Data . . . . .	53
13. Optical Configuration for SEASAT Correction System . . . . .	55
14. Composite of Truncated 2-Dimensional Reference Function . . . . .	61
15. Composite of 2-Dimensional Reference Function . . . . .	62
16. Flow Chart of SAR Two-Dimensional Spectral Estimation Package . . . . .	64
17. An Average Scan Line of SAR Wave Data . . . . .	66
18. GOASEX SAR Data (128 x 128 Samples) Showing Resulting FFT and S-C Spectral Estimates . . . . .	71
19. GOASEX SAR Data (17 x 17 Samples) Showing Resulting FFT and S-C Spectral Estimates . . . . .	72
20. GOASEX SAR Data (11 x 11 Samples) Showing Resulting FFT and S-C Spectral Estimates . . . . .	73
21. GOASEX X-Band SAR Data . . . . .	77
22. GOASEX L-Band SAR Data . . . . .	78



LIST OF FIGURES  
(concluded)

23. Summary of Viewing Geometry for Figures 21 and 22 . . . . .	79
24. One-Dimensional Spectral Estimation of X-Band SAR Data . . . . .	80
25. One-Dimensional Spectral Estimation of L-Band SAR Data . . . . .	81
26. Numerical Listing of the One-Dimensional Spectral Estimation of the X-Band SAR Data (Figure 24) . . . . .	83
27. Numerical Listing of the One-Dimensional Spectra Estimation of the L-Band SAR Data (Figure 25) . . . . .	84
28. Plots of Energy Spread and Function $G(k)$ . . . . .	85
29. Cosine Spreading Function, Average Direction, Maximum Angle, and One-Dimensional Plots . . . . .	86
30. SAR Optical Processor . . . . .	88
31. Normal Geometry for Speckle Correlation . . . . .	90
32. Illustration of an Inconsistency in Jain's Result . . . . .	96
33. Radar Geometry . . . . .	98
34. Radar Image Approximation for Resolved Scatterers . . . . .	99
35. Radar Image Approximation for Unresolved Scatterers . . . . .	99
36. Illustration of How a High Sea State Produces a Smaller rms $\Delta\phi$ . . . . .	102
37. Method for Obtaining the Cross Correlation of a Pair of Frames . . . . .	109
38. Photographs of Composite Frame Correlation Function . . . . .	111
39. Speckle Pattern Decorrelation vs. Change in Processed Center Frequency for a Processed Bandwidth of 2 MHz . . . . .	114
40. Speckle Correlation vs. Wave Height for $W = 2$ MHz, $\Delta f = 1/2$ MHz . . . . .	115
41. Speckle Correlation vs. Wave Height for $W = 10$ MHz, $\Delta f = 5$ MHz . . . . .	116
42. Speckle Correlation vs. Wave Height for $W = 13$ MHz, $\Delta f = 6$ MHz . . . . .	119

## LIST OF TABLES

1. Ground Range Calculations . . . . .	31
2. Radar and Optical System Coefficients . . . . .	35
3. Summary of Optical System Coefficients . . . . .	37
4. Calculated Values for Optical Correction System . . . . .	44
5. Optical Correction System Parameters . . . . .	45
6. Discrepancy of Optical System in Correction . . . . .	47
7. Calculated Values for Optical Correction of an Example Range Distortion . . . . .	49
8. Summary of Experimental Conditions . . . . .	105

## IMAGING OCEAN WAVES WITH SAR

A SAR Ocean Wave Algorithm Development Program

## 1

## INTRODUCTION

The purpose of this Office of Naval Research (ONR) study is to demonstrate the utility of synthetic aperture radar (SAR) for the determination of ocean surface conditions with special consideration of shallow-water and near-shore areas. ERIM has been working the last three years for ONR developing algorithms that reduce raw SAR data into oceanographically meaningful information.

This interim report on Contract N00014-76-C-1048 summarizes work on four tasks comprising two years of effort exploring problems of imaging ocean waves with SAR. The performance period for the work reported herein was August 1977 - August 1979.

The four tasks to be discussed in this report include:

- (1) SAR geometric distortions and an optical technique to correct these distortions,
- (2) a digital technique for the estimation of ocean wave spectra from SAR data,
- (3) determination of wave height from SAR data, and
- (4) examination of the mechanism involved in SAR imaging of ocean waves.

Each of the above mentioned tasks is reported in an individual section. Some sections (notably the one dealing with imaging mechanisms) have been reported in symposium proceedings, and, hence employ a journalistic format.

2  
SUMMARY

This report considers four principal activities:

- (1) SAR geometric distortions and an optical technique to correct these distortions,
- (2) a digital technique for the estimation of ocean wave spectra from SAR data,
- (3) determination of wave height from SAR data, and
- ✓ (4) examination of the mechanism involved in SAR imaging of ocean waves.

In the first activity, the slant range distortion of SAR imagery was theoretically considered. This was followed by the consideration of an optical configuration required to correct the data. The optical configuration was then set up and actual SAR data was range-distortion corrected.

The nonlinear mapping between slant and ground range is related to the viewing angle of the radar. The ground-range distortion becomes more acute as the depression angle (angle from horizontal) increases. SEASAT, with its 70° depression angle, has a 30% distortion in ground range due to slant-range distortion. Such a difference will also cause smearing and consequent impairment in defining or processing the true ocean-wave frequency. A cubic expression for the slant-to-ground distortion was derived. This expression was then used to devise an optical setup to correct the distortion.

The method used to correct this nonlinear mapping is to use tilted plane imaging system in which both the input and output planes are tilted. This arrangement results in good correction over a typical SAR image. A side effect of using tilted planes is that the image scale in the cross-range direction is distorted. This

distortion can be compensated for by imaging with a non-tracking optical system in which both the object and image recording films are moved in synchronism, with a narrow slit placed over the recording film in the range direction.

The ERIM optical setup was tested on both computer-generated and actual SAR slant-range data; analysis of the resulting ground-range-corrected data indicated that less than 0.5% error resulted. SAR range distortions for a curved Earth's surface were also studied and actual satellite SAR data from SEASAT was optically corrected and used in SEASAT validation activities. This technique was developed at ERIM for processing SAR data, and is now used at the Jet Propulsion Laboratory.

The second activity involved the design and implementation of a computer software system that obtains spectral estimates of wavelength and direction information for surface gravity waves. Prior to the development of these spectral estimation programs, ERIM had developed computer software which corrected for slant-to-ground range and radiometric distortions of SAR imagery (Shuchman, et al., 1977). The software system utilizes either standard fast Fourier transform techniques or maximum entropy spectral analysis (MESA), both of which are sometimes referred to as semicausal methods. Output products of the ERIM-developed SAR two-dimensional aperture-estimation package include: (1) contour and perspective (3-D) plots of spectrum estimates, (2) a one-dimensional wave-number spectrum, (3) the maximum direction, (4) the average directional spectrum, (5) the directional spread for a given wave number, (6) and the cosine spread function of the one-dimensional spectrum.

In the third activity, the question of wave height determination using SAR was explored. The effort looked extensively at a technique reported by Jain (1977) that obtains wave height information by using the radar chirp bandwidth information. ERIM's work in this area has

included attempts to experimentally verify Jain's results as well as to consider further the underlying theory developed by Jain. ERIM's experimental data did not confirm the validity of Jain's technique to infer wave height, but rather it demonstrated some rather serious shortcomings of the technique.

For Jain's technique to be of operational value, substantial differences in correlation strength are required. The use of analog techniques to obtain the correlation function is adequate to confirm the existence of differences in correlation strength, but the absolute level of correlation (which is required for utility of this algorithm) is significantly altered by the nonlinearities involved.

Noise is another fundamental problem associated with this technique. The radar itself is an analog device subject to variability. Although processor noise could be alleviated by the use of a tracking processor, receiver, recorder, and film-grain noise would still be present. The average signal-to-noise ratio (SNR) of sea imagery is typically low (3-6 dB) due to the low radar cross section (RCS) of the sea. The sea's RCS is subject to large variability with sea state and so we can expect the average SNR to vary with sea state also. This will influence the results. The effects of this noise in either increasing or decreasing the correlation strength are likely to depend on whether positives or negatives are used in the analog correlation process.

ERIM has tried to repeat Jain's experiments. Experimental problems were encountered, however, which prohibited obtaining a fully conclusive answer to the question as to whether Jain's experiments lead to the suggested technique for wave height estimation. Nevertheless, the sensitivity and consistency of those results which were obtained at ERIM appear good enough to rule out the practicality of Jain's method, at least for the bandwidths and frequency changes tried. On the positive side, the experimental problems serve to emphasize the non-triviality of measuring the correlation function with

the degree of accuracy claimed by Jain, and they demonstrate how easily the results can be influenced by extraneous factors.

The final activity discussed in this report was examination of the mechanisms involved in SAR imaging of ocean surface conditions. A number of existing models which attempt to explain wave imagery obtained with a synthetic aperture radar (SAR) were examined. These models are of two types: (1) static models that depend on instantaneous surface features and (2) dynamic models that employ surface velocities. In the literature, SAR imagery has been discussed using both types of models. Such discussions can be fruitless because no widely accepted understanding of the imaging mechanism exists as yet. This study attempts to draw together analytical and experimental results based on a combination of these two types in order to approach a more satisfactory model for SAR ocean wave imaging.

Radar backscatter values ( $\sigma_0$ ) were calculated from 1.3 and 9.4 GHz SAR data collected off Marineland, Florida. These data (averaged over many wave trains) can best be modeled by the Bragg-Rice-Phillips model which is based on the roughness variation and the complex dielectric constant of oceans. This result suggests that capillaries on the surface of oceanic waves are the primary cause for the surface return observed by a synthetic aperture radar.

The authors' observation of moving ocean, as imaged by SAR and studied in the SAR optical correlator, supports a theory that the ocean surface appears relatively stationary in the absence of currents. The reflecting surface is most likely moving slowly (with, e.g., capillary-wave phase velocity and gravity-wave orbital wave velocity) relative to the phase velocity of the large gravity waves. The stationary theory still applies, since the phase velocity of the capillaries and orbital velocity of the gravity waves are nearly stationary when compared to the phase velocity of the gravity waves.

An examination of the effect of salinity and sea temperature upon sea surface reflection coefficients at small and medium incidence angles indicated that these effects seem to be insignificant for either of the linear polarizations. At large incidence angles, i.e., near-grazing, there is a more pronounced change in the behavior of the vertical polarization reflection coefficient.



## SAR SENSING OF SURFACE OCEAN CONDITIONS

### A Review of the Present State of the Art and Recommendations for Further Study

This section summarizes the present state of the art in imaging ocean surface conditions with synthetic aperture radar (SAR). This section serves both the purpose of familiarizing the reader with the present degree of interpretability of SAR ocean data, as well as pointing out areas of needed future research. Thus, this section can be considered a recommendations section for further SAR ocean sensing studies.

#### 3.1 DOMINANT WAVELENGTH AND DIRECTION

Radar oceanographers are in general agreement that SARs successfully image gravity waves that are traveling within  $\pm 75^\circ$  of the range direction. Principally, only SAR images of ocean swells have compared favorably to sea truth such as a pitch and roll buoy data (Shemdin, et al., 1978 and Gonzalez, et al., 1979). However, Shuchman and Meadows (1980) and Schwab, et al. (1980) have reported that a SAR (X-band, horizontal parallel polarization) has successfully imaged wind waves on Lake Michigan. It should be noted that the Lake Michigan SAR wave data had fine resolution (2.5 x 2.5 meters) and the waves were propagating nearly in the range direction. The question of the minimum resolution size required to image a given ocean wave has not been determined absolutely and should be studied. Preliminary considerations relating to this question were reported by Shuchman, et al. (1978). In that analysis of Marineland SAR data, it was determined that a minimum of 4-6 resolution cells per ocean wavelength in both range and azimuth are necessary to successfully discern waves in the SAR imagery.

The question of determining the dominant wavelength and direction with regard to radar look direction has not been fully studied. For

example, are dominant wavelength and direction of the gravity wave field only obtainable when waves travel nearly in the range dimension? Data presented in Section 6.3 of this report show spectral estimates agreeing with sea truth for the same wave imaged up-wave, down-wave and cross-wave. However, this is only one data set and appears to be contrary to observations reported by Shemdin, et al. (1978). Thus, the question of radar look direction (viewing angle) versus ocean wave detectability needs further study. The spectral estimation procedure for calculating dominant wavelength and direction is undergoing a rapid change. Whether a fast Fourier transform or another semi-causal estimation is used, a better understanding of the content and significance of ocean spectra as derived from SAR data is necessary. For example, only the dominant peak and direction are obtained from the spectral estimation. Motion-induced artifacts or perhaps 2nd-and 3rd-order harmonics are sometimes visible in SAR spectra. These effects need to be quantified. Information on wind or local sea is inherent in the spectral estimate, but to date this information is not extractable, because the shape of a SAR spectrum is not understood.

### 3.2 WAVE HEIGHT DETERMINATION

As will be discussed in detail in Section 7 of this report, wave height determination from SAR appears to be potentially feasible; however, to date, an operational algorithm for calculating wave height is not available. Wave height information would enable oceanographers to use SAR data not only to calculate dominant wavelength and directional information, but also to obtain power density spectra. Presently, a technique reported by Jain (1977) has utilized the chirp bandwidth signal of the SAR to extract wave height. This technique has utilized analog SAR signal histories. Other techniques, such as the utilization of Doppler perturbations or the analysis of different radar squints should be considered. To summarize,

the SAR imaging mechanism must be solved before a viable wave height algorithm can be constructed.

### 3.3 SURFACE CURRENTS

Synthetic aperture radar (SAR) has potential for mapping ocean surface currents. This instrument responds primarily to backscatter from capillary waves, which, in conventional SAR processing, are assumed stationary. However, these scatterers are not stationary; they move with a velocity which is the resultant of their own phase velocity plus velocities due to the presence of currents and longer gravity waves. The radial (line of sight) component of this resultant velocity produces a Doppler shift in the temporal frequency of the return signal, which translates to a spatial frequency shift recorded on SAR signal film. The relative contributions to this shift by currents, gravity wave orbital motions, and capillary phase velocities are being studied by means of a theoretical model now under development.

Shuchman, et al. (1979), using X- and L-band SAR data of near shore and Gulf Stream ocean surfaces, measured the Doppler shift of moving ocean scatterers relative to stationary scatterers. Currents deduced from these Doppler shift calculations (averaged over a  $500 \times 500 \text{ m}^2$  area) were found to be consistent with available sea truth gathered during the Marineland Experiment. Additionally, SEASAT-SAR satellite data of the Columbia River, Oregon, is being evaluated to assess the potential of using SAR to map ocean surface currents.

The above described technique utilizes the measurement of Doppler shifts in the SAR signal history induced by radial velocities. Thus, to be measured, oceanic surface currents must be travelling perpendicular to the SAR flight track. Additionally, because a radial velocity is sensed (line-of-sight), the measurement must be corrected to the horizontal datum plane. This is done on the basis of the SAR geometry.

Azimuth traveling currents can theoretically be measured by observing defocusing effects in the SAR signal processor (Shuchman and Zelenka, 1978). However, the authors believe the defocusing effects are too subtle to be accurately measured.

Surface currents are inherently harder to measure using satellite data as opposed to aircraft data. This is due to the increased Doppler bandwidth of the satellite with respect to aircraft. For example, the aircraft Doppler bandwidth at Marineland is approximately 100 Hz, while SEASAT's is approximately 1000 Hz. A 1.5 m/sec radial velocity produces a Doppler shift of approximately 10 Hz, thus a shift measurement for the aircraft is a 10% change while for the satellite, the change is 1%. It should be noted, however, that the satellite platform is more stable than an aircraft's and a 1% shift may indeed be measurable.

The effect of a gravity-wave field on a current area to be measured has not been studied in detail to date. Initial observations indicate that the wave motion causes a symmetrical broadening of the Doppler history and therefore does not alter the shift induced by the current.

In conclusion, the current measurements presented in the literature appear consistent, in the sense that Doppler shifts were detected and the shifts appear in the proper direction. However, the limited sea truth available for Marineland prevents a definitive statement as to the ultimate feasibility of using SAR to sense current motion. Additionally, high-velocity-current data has been collected off Vancouver Island, which is a physical situation very different from the large area, low velocity situation off Marineland. This data will be analyzed in the near future. The SEASAT measurements need further theoretical consideration to explain the overly large Doppler shift in the Columbia River, for example.

Surface currents can be measured inherently also by observation of the refraction of gravity waves as they cross a current boundary. This refraction, as observed by a SAR, needs to be documented.

### 3.4 INTERNAL WAVES AND OCEAN FRONTAL BOUNDARIES

Prior to the launch of the SEASAT SAR, the utility of SAR as a mapper of internal waves and ocean frontal boundaries was limited. Weissman, et al. (1980) reported on aircraft SAR sensing of the Gulf Stream boundary, but internal wave pockets were not clearly identified. This was because aircraft SARs have limited swath widths (typically 10 kilometers)\* and internal waves are large-scale structures. SEASAT, with its synoptic 100 km swath and lengths up to 4000 kilometers, has given oceanographers the opportunity to observe mesoscale features on the surface of the ocean. Shuchman and Kasischke (1979) and Gower and Hughes (1979) have reported observing both internal wave features and ocean frontal boundaries on SEASAT SAR data.

The SEASAT imagery examined to date has shown many interesting surface anomalies that appear to be a result of internal wave interaction with the ocean's bottom. Two kinds of surface manifestations have been examined. One type appears to be a true internal wave, while other examples, such as those which occurred over the Wyville Thomson Ridge, show surface manifestations which are not truly internal-wavelike in structure. This second type of feature had not been observed in remote, mid-ocean regions prior to examination of SEASAT data.

In all cases, the observed anomalies appeared in the imagery over topographic uplifts of the oceanic bottom. The water depth for the examples presented, varied from 80 to 450 meters.

---

\*The ERIM X-L radar now has a 22 km swath capability.

To date, the imaging mechanism for these mesascale features is not totally understood. Two theories try to explain the occurrence of the features in SAR imagery. One theory is dependent upon surface slick formation, while the other theory explains the internal wave detection as a result of long- and short-wave interaction. The bounds and limits of detection of these features have also not been determined as yet. For example, are these surface anomalies always present on the surface of the ocean? Or, how do the tides and currents of an area affect these surface anomalies? Additionally, the question of minimum and maximum depth of water and bottom feature height necessary to cause these surface anomalies must be determined.

To summarize, SAR does appear to image frontal features, current boundaries, and internal wave features. Work remains to be done which correlates the radar signals to the observed ocean features. A deep-water SAR test program aimed at better understanding the imaging of frontal features and internal waves needs to be conducted.

### 3.5 DETECTION OF BOTTOM TOPOGRAPHIC FEATURES WITH SAR

Recent studies at ERIM (Kasischke, et al., 1980; Shuchman and Kasischke, 1979; Shuchman, et al., 1979a) have demonstrated the potential of using synthetic aperture radar data in providing bathymetric information. The primary goals of these studies were to evaluate the potential of SARs to provide data for improving the Defense Mapping Agency's nautical chart products, primarily through the detection and placement of submerged features hazardous to navigation.

Five different physical oceanographic phenomena have been observed on SAR imagery that permit detection of underwater hazards. These include:

1. The change in direction and wavelength of ocean swell as they enter coastal regions which can be observed on SAR imagery;

2. A distinct change in radar backscatter which is associated with an ocean swell propagating over a distinct depth discontinuity;
3. A distinct change in radar backscatter which is associated with a current flowing over a bottom feature;
4. Observation of classic internal wave patterns over continental shelf regions; and
5. Anomalous SAR backscatter signatures found in deep ocean regions over topographic "bumps" on the ocean bottom.

Models which incorporate the way an ocean waves changes as it enters shallow waters can be used to gain an estimate of water depths in coastal regions. When a gravity wave enters a shallow-water region from deep water, its wavelength and direction change in direct proportion to the water depth. By measuring the change in wavelength or direction, an estimate of the water depth can be obtained. Since a SAR can measure both ocean wavelength and direction, this information can be used in a wave refraction model. This was done in studies by Shuchman, et al. (1979a).

Basic SAR/Oceanographic theory holds that the microwave energy from the radar is being reflected from the ocean's surface by the small capillary and ultra-gravity waves present at the ocean's surface. Capillary and ultra-gravity waves have wavelengths between one and fifty centimeters and are generated by winds. Any change in this small wave structure will alter the radar backscatter being received by the SAR. When a gravity wave field crosses a sharp depth discontinuity, such as a coral reef or seamount surrounding an island the structure of the gravity wave is changed. The interaction between the changing gravity wave field and the small wave field is sufficient to alter the small wave structure, and hence change the radar backscatter. Such a phenomenon was noted on SAR imagery of an island area studied by Kasischke, et al., (1980).

Tidal currents flowing over bottom features are also visible on SAR imagery, as the upward flow of energy of the current influences the surface small wave structure. This hydrodynamic interaction is another manner in which bottom hypsographic information can be obtained from SAR data. In a study of SEASAT data collected over the English Channel, Kasischke, et al. (1980) found over a 90% correlation between signatures on the SAR data and sand ridges and banks. In a study of SEASAT data collected over Nantucket Island, a 77% correlation was found between distinct surface patterns noted on the SAR imagery and distinct bottom topographic features. In both these examples, a strong tidal current was present at the time of the SEASAT overpass.

As was discussed in the previous section, internal wave packets propagating shorewards over a continental shelf region also act as a mechanism permitting SAR detection of changes in bottom form. The internal wave energy field alters the small capillary and ultra-gravity waves sufficiently so that the internal waves are visible on SAR imagery (Shuchman and Kasischke, 1979).

Finally, surface anomalies, similar to internal waves, but not as well structured (into wave packets), have been noticed on SAR images in deep-water areas between major continental shelf boundaries (Shuchman and Kasischke, 1979). The interesting fact about these surface anomalies is that in large part, they occurred over a major underwater ridge or seamount.

### 3.6 SAR AS AN INDICATOR OF WIND AND AIR/SEA TEMPERATURE

Potentially, a calibrated SAR can obtain radar backscatter ( $\sigma_0$ ) measurements over small- and large-scale areas on the ocean. The backscatter values can be related to wind and, perhaps, surface temperature in a fashion similar to that now done with scatterometer data collected by SEASAT. Beal (1979), Weissman, et al. (1980) and



Thompson, et al. (1979) have successfully correlated wind data to received backscatter from the SAR. The major problem to date in this area has been that the optical processing of SAR data does not lend itself readily to the calibration of  $\sigma_0$ . The advent of digital processing and a calibrated SAR, such as the ERIM X-L system, should provide a breakthrough in this area. ERIM has developed this digital processing capability through a contract effort sponsored by MIT/Lincoln Labs. Again, a definitive test of SAR utility in mapping surface wind speeds needs to be conducted.

The use of SAR as a sea surface temperature indicator is less clear. To date, an accepted theory that relates to electromagnetic (EM) return to temperature does not exist. Once again, the EM interaction of SAR with the ocean surface is not understood well enough at present to yield insight in the determination of temperature.

## RESULTS FROM ONR-SPONSORED ACTIVITIES

Applications of This Presently Funded  
ONR Research Activity

Although the present examination of problems of imaging ocean waves with synthetic aperture radar is making important contributions to basic remote sensing, we wish to note that the developments which we are making are also of potential use for proposed 6.2 programs of the U.S. Navy and in programs of other government agencies. Some of the anticipated or potential applications of these techniques are discussed below.

1. The presently developed ONR algorithms have been used in the processing and analysis of SEASAT data. Specifically, NOAA Contract No. MO-A01-78-00-4339 exploring SEASAT SAR coastal ocean wave imaging capability utilized both optical and digital spectral-estimation algorithms developed under ONR sponsorship. Additionally, SEASAT SAR data collected during JASIN will be analyzed for ONR-Code 480 using the above-mentioned algorithms.
2. In addition to the processing of NASA SEASAT-A data, the developed algorithms are being used in a joint ERIM-NOAA program to further study the ERIM-GOASEX and Lake Michigan data collected by the ERIM X-L SAR system.
3. Knowledge obtained from the ONR effort is available to design future SAR satellite sensors, such as NOSS, and oceanographic SAR shuttle missions that image ocean waves.
4. Upon development of a SAR wave-height estimator algorithm, power density spectra can be obtained from the SAR ocean wave data, hopefully in near real-time. This data could greatly aid U.S. Navy oceanographers working on sea state prediction

PRECEDING PAGE BLANK-NOT FILLED

5  
SAR GEOMETRIC DISTORTIONS AND AN OPTICAL  
CORRECTION ALGORITHM

This section of the report discusses the optical correction of slant-range distortion in SAR images. First, a theoretical presentation of the problem is given; this is followed by consideration of an optical configuration required to correct the data. Finally, actual SAR data is corrected and evaluated.

### 5.1 INTRODUCTION

A side-looking geometry is used to obtain synthetic aperture radar (SAR) images, as shown in Figure 1. A SAR image is based upon the distance (ranges) from a SAR vehicle to the reflecting objects on the ground. The distances between reflecting objects in such an image termed "slant-range," are not identical to the actual distances between the objects along the ground, termed "ground-range". The slant-range SAR image is a distortion of the true ground-range image.

This slant-range distortion is particularly troublesome when linears are imaged. When straight-line features such as ocean waves or roads are imaged in slant range, they appear curved unless they are precisely parallel to either the range or the along-track direction. As shown in Figure 2, the curvature increases toward the near range (the closest portion of the image to the groundtrack of the SAR vehicle).

For visual inspection, such curvature produces few problems; not only can personal viewing adjustments be made, but no quantitative measurements are required. For these reasons, little effort hitherto has been expended for correction of this distortion. However, we now require machine processing of SAR images for directionality of such features as ocean waves or geologic linears;

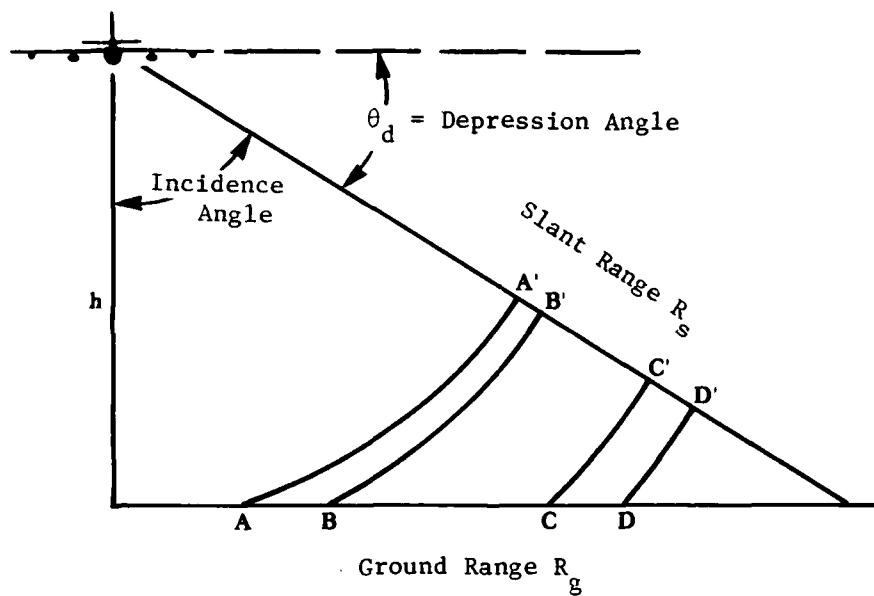
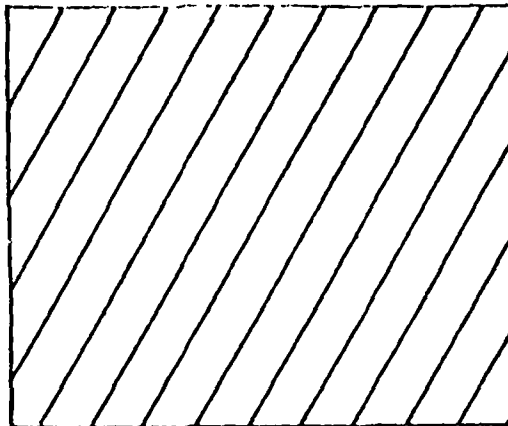


FIGURE 1. SIDE-LOOKING SAR GEOMETRY.

Ground Track  
(NADIR)

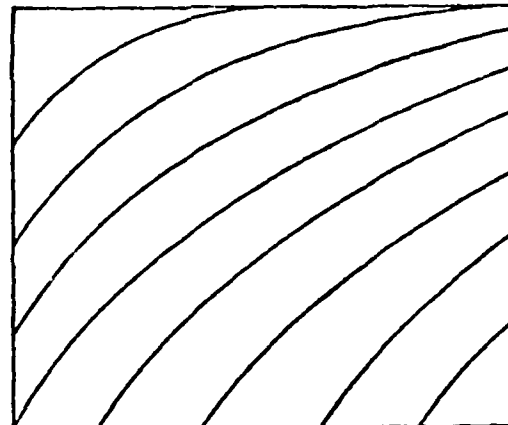
Far Range



(a) Ground Range Representation  
of Waves

Ground Track  
(NADIR)

Far Range



(b) Slant Range Representation  
of Waves in SAR Image

**FIGURE 2.** Diagram Showing Slant Range Distortion of Linear Waves Oblique to Flight Path. (Each wave asymptotically approaches ground track. (b) appears as if (a) is wrapped around a cylinder. Note that the curvature in (b) will cause radial diffusion of energy in the two-dimensional transform plane, leading to confusion in determining wave direction.)

the slant-range distortion of the true ground-range image impairs such processing.

This impairment occurs because both the optical and digital two-dimensional Fourier transform are used in processing for directionality. A straight line on the image will cause energy in the two-dimensional Fourier transform to be concentrated in a direction perpendicular to this line. If the line is curved, this energy will be dispersed perpendicularly to each section of the curved line. This dispersion will cause a diffusion or "smearing" of the energy in the Fourier transform as opposed to the concentrated energy produced by a straight line.

Also, if the linears (wavefronts) lie along the azimuth direction, the spacing between them will be distorted by slant range. For example, the spatial frequency of ocean waves whose crests are parallel to the azimuth direction will be larger at far range than at near range. With the near range at  $17^\circ$  incidence angle and the far range at  $23^\circ$  (SEASAT geometry), the difference in apparent frequency across a uniform ocean wave field is ~30%. Such a difference will also cause smearing and consequent impairment in defining or processing the true ocean wave frequency.

Whether the desired output is (1) the Fourier transform itself or (2) a filtered image formed by using the transform as a filter, the slant-range distortion degrades the result. Therefore, a means of correcting the image to ground range will aid in machine processing for directionality.

An optical method of correcting this distortion has been developed and confirmed on actual data. The correction is achieved by constructing an optical setup which images the distorted data in such a way that the distortion is compensated for. In the following discussion, a cubic expression for the slant-to-ground range distortion is derived. An optical setup is then devised in which the cubic

expression for the distortion closely approximates the expression for the radar case.

## 5.2 DERIVATION OF THE SLANT VS. GROUND RANGE EQUATION

A radar configuration is shown in Figure 3. Slant range is the distance from the SAR vehicle to a reflecting object on the ground. The arcs labeled a, b, c, d, ., i, with center of curvature at the vehicle are uniformly separated slant range contours. Note that the intersections of these contours with the ground, labeled (a', b', c', . . ., i'), are not uniformly spaced. Thus, the distortion arises. As an example, the large distance a'-b' on the ground is imaged in slant range with precisely the same spacing as the small distance h'-i'. In deriving the cubic expression for the distortion, the depression angle  $\theta_d$  is employed. The angle  $\theta_d$  is the complement of the incidence angle  $\psi$ , and is commonly used in SAR analysis. The rate of change between slant and ground range is

$$\frac{\Delta R_g}{\Delta R_s} = \frac{1}{\cos \theta_d} \quad (1)$$

As  $\theta_d \rightarrow 90^\circ$ ,  $\Delta R_g/\Delta R_s \rightarrow \infty$ , and as  $\theta_d \rightarrow 0^\circ$ ,  $dR_g/dR_s \rightarrow 1$ . Thus, the distortion becomes more significant as the depression angle  $\theta_d$  increases, or as the slant range  $R_s$  approaches the aircraft altitude  $h$  in magnitude. Figure 4 shows a plot of the ratios  $R_g/R_s$  and  $\Delta R_g/\Delta R_s$  vs. the depression angle  $\theta_d$ . As the depression angle increases, the ratio  $R_g/R_s$  decreases, while  $\Delta R_g/\Delta R_s$  increases, both in a non-linear manner.

The method we have used to correct this nonlinear mapping is to use tilted plane imaging systems in which both the input and output planes are tilted. This arrangement results in good correction over a typical SAR image. A side effect of using tilted planes is that the image scale in the cross-range direction is distorted. This

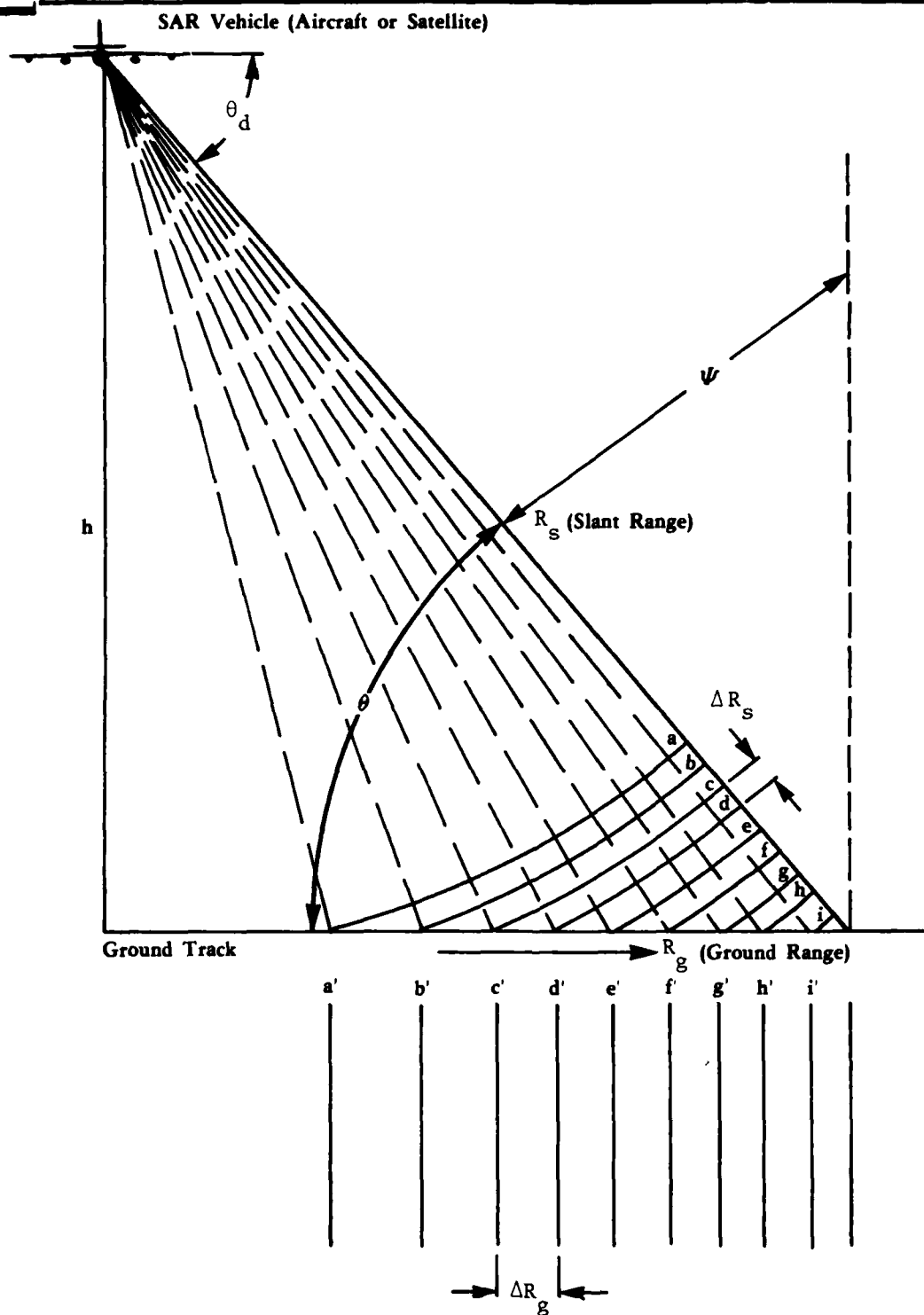


FIGURE 3. CONVENTIONAL RADAR CONFIGURATION.



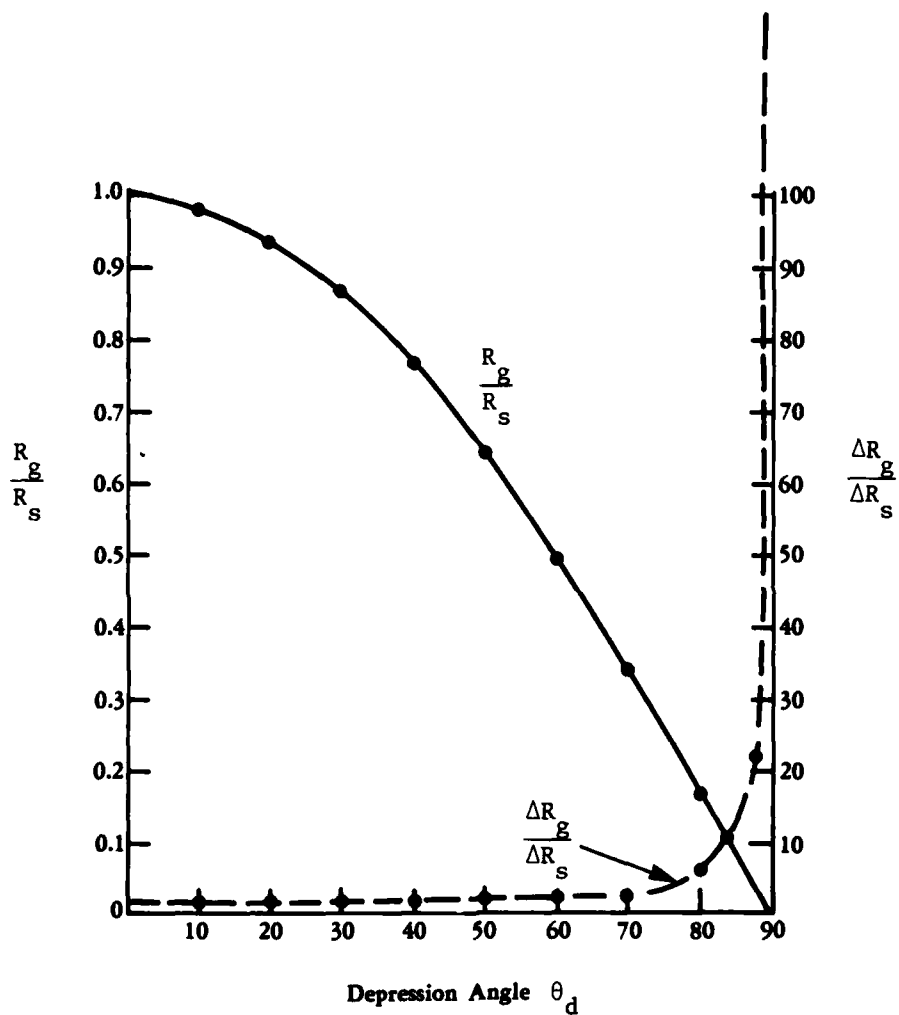


FIGURE 4. PLOT OF THE RATIOS OF  $R_g/R_s$  AND  $\Delta R_g/\Delta R_s$  VERSUS THE DEPRESSION ANGLE  $\theta_d$ .

distortion can be compensated for by imaging with a non-tracking optical system, in which both the object and image recording film are moved in synchronism, with a narrow slit placed over the recording film in the range direction.

The geometry used to derive the expression of slant vs. ground range is shown in Figure 5. In this figure,  $R_{so}$  is the average slant range and  $y_0$  is the average ground range. From this figure, the following identities can be written:

$$R_{so}^2 = h^2 + y_0^2 \quad (2)$$

$$R_s = R_{so} - r \quad (3)$$

$$y_0 - y = \sqrt{(r_{so} - r)^2 - h^2} \quad (4)$$

$$y_0 - y = y_0 \sqrt{1 - \frac{2R_{so}r - r^2}{y_0^2}} \quad (5)$$

after squaring terms in Eq. (4) and substituting  $y_0^2$  for  $R_{so}^2 - h^2$ . Equation 5 can be rewritten using the first three terms of the binomial expansion. Thus,

$$y = \frac{R_{so}}{y_0} r + \frac{1}{2y_0} \left( \frac{R_{so}^2}{y_0^2} - 1 \right) r^2 + \frac{R_{so}}{2y_0^3} \left( \frac{R_{so}^2}{y_0^2} - 1 \right) r^3 + \dots \quad (6)$$

Using the identities

$$\frac{R_{so}}{y_0} = \frac{1}{\cos \theta_d} \quad \text{and} \quad (7)$$

$$\frac{R_{so}^2}{y_0^2} - 1 = \tan^2 \theta_0, \quad (8)$$

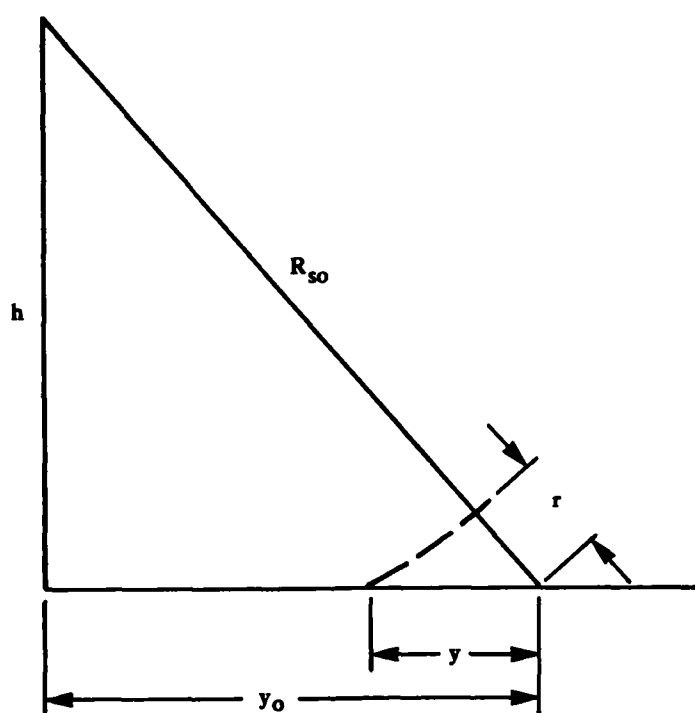


FIGURE 5. GEOMETRY USED TO DERIVE THE SLANT RANGE EXPRESSION.

Eq. (6) becomes

$$y = \frac{1}{\cos \theta_d} \left[ r + \frac{1}{2y_0} (\tan \theta_d \sin \theta_d) r^2 + \frac{1}{2y_0^2} (\tan^2 \theta_d) r^3 \right] . \quad (9)$$

As an example, consider the case where  $y_0 = 300$  km and  $h = 794$  km, then  $\theta_d = 69.302^\circ$  and  $R_{s0} = 848.79$  km, and Eq. (9) becomes

$$y = 2.829 [r + 4.126 \times 10^{-3} r^2 + 3.892 \times 10^{-5} r^3] \quad (10)$$

This equation can be used to calculate ground range from slant range data. Table 1 shows the exact ground range and the ground ranges computed using (1) a linear approximation from the first term of Eq. (10) and (2) all the terms of Eq. (10). This table indicates that a linear approximation results in errors of +7.5% and -9.3% and that, by use of all the terms of Eq. (10), these errors are reduced to +0.28% and -0.45%.

### 5.3 DERIVATION OF OPTICAL SYSTEM EQUATION

In this section, an expression relating the one-dimensional coordinates of the object and image planes, both tilted, will be derived. The objective is to obtain an expression similar to that relating radar ground range and slant range. If such an equation can be obtained, then a correction can be effected.

The proposed optical imaging system is shown in Figure 6. The tilted object plane is labeled "P" and the corresponding image plane is "Q". All distances along the optical axis are measured from the focal points of the lens. From a ray through the center of the lens, the relationship

$$\frac{x_1}{p + F} = \frac{x_2}{q + F} \quad (11)$$

can be written, where  $F$  is the focal length of the lens, and  $x_1$ ,  $x_2$ ,  $p$ , and  $q$  are denoted on Figure 6. Using the basic optical relationship  $q = F^2/p$ , Eq. (11) becomes

TABLE 1  
GROUND RANGE CALCULATIONS

<u>r</u>	<u>y exact</u>	From 1st term of Eq. 10 <u>y</u>	<u>error</u>	From Eq. 10 <u>y</u>	<u>error</u>
-20 km	-52.64 km	-56.59 km	+7.5%	-52.79 km	+0.28%
0 km	0	0	0%	0	0%
+20 km	62.41 km	56.59 km	-9.3%	62.13 km	-0.45%

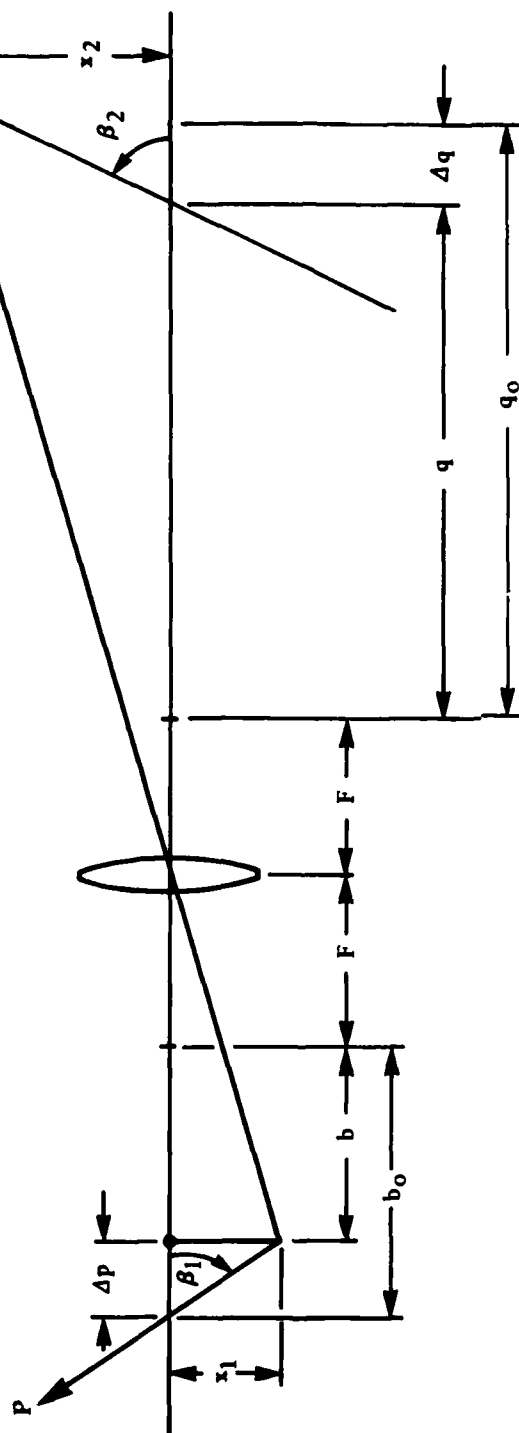


FIGURE 6. PROPOSED OPTICAL IMAGING SYSTEM

$$x_1 = x_2 \frac{p}{F} \quad (12)$$

Next, we let  $p = p_0 - \Delta p$  and  $q = q_0 + \Delta q$  in  $q = F/p$ :

$$q_0 + \Delta q = \frac{F^2}{p_0 - \Delta p} \quad (13)$$

$$q_0 + \Delta q = F^2 \left[ \frac{1}{p_0} + \frac{1}{p_0} \frac{\Delta p}{p_0 + \Delta p} \right] \quad (14)$$

$$q_0 = \frac{F^2}{p_0} \quad (15)$$

By substitution and collection of terms, we get

$$\Delta q = + \frac{F^2}{p_0} \left( \frac{\Delta p}{p_0 + \Delta p} \right) \quad (16)$$

From Figure 6, we see that

$$x_1 = \Delta p \tan \beta_1 \quad (17)$$

Solving for  $x_2$ ,  $x_1$ , and  $p = p_0 - \Delta p$ , we get

$$x_2 = f \tan \beta_1 \left( \frac{\Delta p}{p_0 - \Delta p} \right) \quad (18)$$

Equations (16) and (18) are combined to find  $y$ :

$$y = (\Delta q^2 + x_2^2)^{1/2} = \frac{F^2}{p_0} \left[ 1 + \left( \frac{p_0 \tan \beta_2}{1} \right)^2 \right]^{1/2} \left( \frac{\Delta p}{p_0} \right) \left( \frac{1}{1 - \frac{\Delta p}{p_0}} \right) \quad (19)$$

$$y = \left[ \left( \frac{F \Delta}{p_0} \right)^2 + \left( \frac{p_0 \tan \beta_1}{F} \right)^2 \right]^{1/2} \Delta p \left[ 1 + \frac{\Delta p}{p_0} + \left( \frac{\Delta p}{p_0} \right)^2 + \left( \frac{\Delta p}{p_0} \right)^3 + \dots \right] \quad (20)$$

By substituting  $p = r \cos \beta_1$  and rearranging terms, we get

$$y = \left(\frac{F}{p_0}\right)^2 \left[ 1 + \left(\frac{p_0 \tan \beta_1}{F}\right)^2 \right]^{1/2} \cos \beta_1 \left[ r + \left(\frac{\cos \beta_1}{p_0}\right) r^2 \right] + \left(\frac{\cos \beta_1}{p_0}\right)^2 r^3 + \dots \quad (21)$$

which is similar to the corresponding radar slant-to-ground range Eq. (9). The coefficient in front of the binominal expansion is the magnification between  $r$  and  $y$  parameters in Eq. (21) or between slant and ground range in Eq. (9). By proper choices of  $F$ ,  $p_0$ , and  $\beta$ , any magnification or scale change can be selected.

#### 5.4 OPTICAL SYSTEM PARAMETER SELECTION

Table 2 lists the coefficients of the radar system and the optical processor. The first term in the radar equation represents the average range-to-azimuth scale distortion. This term approaches zero for small angles of incidence and becomes large for large angles of incidence. This distortion is not important, since it is removed in the coherent optical data processor.

The corresponding coefficient of the optical system is the magnification between the input image and output image planes. If the angle  $\beta_1$  is the  $90^\circ$ , this coefficient reduces to  $F/p_0$ , which is the lateral magnification of the system; if  $\beta_1 = 0^\circ$ , this coefficient reduces to  $(F/p_0)^2$ , which is the axial magnification.

The second coefficient of the radar equation is the most significant term causing range distortion. The corresponding coefficient in the optical system equation corrects for the range distortion and the two terms should be made equal. In practice, angle  $\beta_1$  can be chosen to be some reasonable value such as  $60^\circ \leq \beta_1 \leq 80^\circ$ , and the required  $p_0$  can then be selected:



TABLE 2  
RADAR AND OPTICAL SYSTEM COEFFICIENTS

Coefficient	Description	Radar	Optical System
Common	Radar: average range to azimuth scale distortion	$\frac{1}{\cos \theta_d}$	$\left(\frac{F}{p_o}\right)^2 \left[ 1 + \left( \frac{p_o \tan \beta_1}{F} \right)^2 \right]^{1/2} \cos \beta_1$
	Optical: average magnification, coefficient of linear term		
2nd	Coefficient of quadratic term	$\frac{\tan \theta_d \sin \theta_d}{2y_o}$	$\frac{\cos \beta_1}{p_o}$
3rd	Coefficient of cubic term	$\frac{\tan^2 \theta_d}{2y_o}$	$\left( \frac{\cos \beta_1}{p_o} \right)^2$

$$p_0 = (\cos \beta_1) \frac{2y_0}{\tan \theta_d \sin \theta_d} \quad (22)$$

This choice of  $p_0$  and  $\beta_1$  does not involve the lens focal length  $F$ . Any lens positioned at distance  $(F + p_0)$  from the object plane will form an image with the quadratic error term removed. The choice of  $\beta_1$  and  $p_0$  might be limited by other considerations, such as required angular field of the lens, magnification of the image, and angle  $\beta_2$ . The equation for calculating all the parameters of interest for the optical system are listed in Table 3.

The coefficient of the cubic term in the optical system equation is simply the square of the quadratic term coefficient. Thus, it cannot be made exactly equal to the coefficient of the cubic term in the radar equation. The radar and optical coefficients differ by the factor  $(\sin^2 \theta_d / 2y_0)$ . The third term is not very large and the error due to this factor is not significant in many cases of interest. For the example used to obtain Eq. (10), the maximum error at  $r = 20$  km is 0.9%.

Examples for calculating the optical system parameters are as follows:

Example 1:

Find the parameters of the optical system to match the radar equation as given by Eq. (10). We select  $\beta_1$  and  $F_1$  and then calculate the other parameters:

- (a) Let  $\beta_1 = 75.2^\circ$  and  $F = 152$  mm, and the scale be 1 mm = 1 km, then

$$p_0 = 62 \text{ mm},$$

$$q_0 = 372 \text{ mm},$$

$$\beta_2 = 57.07^\circ, \text{ and}$$

$$M = 2.82.$$

TABLE 3  
SUMMARY OF OPTICAL SYSTEM PARAMETERS

Object Plane		Image Plane	
1. $p_o$	$p_o = (\cos \beta_1) \left( \frac{2y_o K}{\tan \theta_d \sin \theta_d} \right)^*$	4. $q_o = \frac{F^2}{p_o}$	
2. $\beta_1$		5. $\beta_2 = \tan^{-1} \left( \frac{p_o}{F} \tan \beta_1 \right)$	

Common Terms

3.  $F$  (arbitrary, desirable to have  $F \approx p_o$ )

6. Magnification:  $M = \left( \frac{F}{p_o} \right)^2 \left[ 1 + \left( \frac{p_o \tan \beta_1}{F} \right)^2 \right]^{1/2} \cos \beta_1$

\*  $K$  is scale factor,  $y_o$  in kilometers.

(b) Let  $\beta_1 = 65^\circ$  and  $F = 100$  mm, then

$$\begin{aligned} p_0 &= 102.4 \text{ mm,} \\ q_0 &= 97.63 \text{ mm,} \\ \beta_2 &= 65.5^\circ, \text{ and} \\ M &= 0.972 \end{aligned}$$

Example 2:

Find the parameters of the optical system so that the coefficients of the optical equation match those of the radar equation for the case where  $R_{SO} = (43 \text{ km})^{1/2}$ ,  $\theta_d = 31.383^\circ$  and  $y_0 = 5.196$  km. These parameters correspond to an airplane-based SAR system.

(a) Let  $\beta_1 = 70^\circ$ ,  $F = 100$  mm, and the scale be 1 mm = 0.1 km, then

$$\begin{aligned} p_0 &= 111.9 \text{ mm,} \\ q_0 &= 89.37 \text{ mm,} \\ \beta_2 &= 71.98^\circ, \text{ and} \\ M &= 0.840 \end{aligned}$$

(b) Let  $\beta_1 = 70^\circ$ ,  $F = 100$  mm, and the scale be 1 mm = 1 km, then

$$\begin{aligned} p_0 &= 11.2 \text{ mm,} \\ q_0 &= 892 \text{ mm,} \\ \beta_2 &= 17.1, \text{ and} \\ M &= 28.6 \end{aligned}$$

In this example,  $\beta_2$  is unreasonably small and this choice of  $\beta_1$  and  $F$  are impractical.

(c) Let  $\beta_1 = 70^\circ$ ,  $F = 15$  mm, and the scale be 1 mm = 1 km, then

$$\begin{aligned} p_0 &= 11.2 \text{ mm,} \\ q_0 &= 20.0 \text{ mm,} \\ \beta_2 &= 64.0, \text{ and} \\ M &= 1.403. \end{aligned}$$

## 5.5 SUMMARY AND CONCLUSIONS OF THEORETICAL CONSIDERATIONS

Examination of the slant and ground range relationship for a SAR system shows that considerable error is introduced at large angles of incidence. The error for a satellite-based SAR is about 10% in distance from the midpoint, or 23% -13% in scale over a 20 km change in slant range. These errors impair machine processing for directionality and frequency of such features as ocean waves.

An equation for ground range in terms of slant range was derived by using the first three terms of the binomial expansion. When the equation was used for a typical example of a satellite SAR system, less than 1/2% error resulted.

An optical imaging system with tilted input and output planes was analyzed and an equation was derived. It was found that an exact match of the first two terms of the binomial expansion in both the radar and optical system equations is possible, and that an approximate match is achieved for the third term. Thus, ground range error can be corrected with a tilted-plane imaging system. As a side effect, a distortion is introduced in the azimuth range, but this can be reduced to an insignificant level by the use of a slit in the image plane.

Since a tilted input plane is needed, it might be possible to couple the tilted-plane imaging system directly to the output of an optical SAR processor. This aspect was not explored at this time but appears to be a possibility. The optical imaging system proposed here does not require coherence or monochromaticity.

## 5.6 EXPERIMENTAL VERIFICATION OF THE OPTICAL CORRECTION FOR THE RANGE DIMENSION DISTORTION

As shown in the preceding discussion, images produced by SAR have a distortion in the range direction which is generated due to the slant of the observed field relative to the viewing axis. An optical

correction technique was described previously and the work described here is based on those results. A simulated SAR image is shown in Figure 7 which has a set of image lines with a spacing which suffers from range dimension distortion. This example demonstrates a situation in which the center line of the field is at  $69.3^\circ$  depression angle. As can be seen in Figure 7, the range lines are closer together, above, corresponding to the narrowing of range increments toward the nadir. With an optical distortion correction system, the range interval marks are placed at equal intervals, as shown in Figure 8. As will be described later, the error in placement of these marks is 0.5 percent or less.

A schematic diagram of the arrangement for generating the results shown in Figure 8 is given in Figure 9. A diffuse white light source was used to illuminate the input transparency from the left. The transparency was attached to a flat glass plate at a prescribed angle,  $\theta_1$ . A small aperture was required with the imaging lens to produce a large depth of focus for the output recording plane. This small aperture requirement is a result of field curvature in the input image at the output recording.

An error analysis of the data was undertaken. Of major concern was a barrel distortion (see Figure 8) in which the edges are foreshortened relative to the center. A measure "a" of this distortion was determined by dividing the distance from the -40 mark to the +40 mark by the distance from the -10 mark to the +10 mark. However, another measure is required because the grossly-distorted input transparency appears theoretically to be fairly good by this first measure (3.996 vs. 4.0, ideal). Hence, a second measure "b" was also used: the distance from -40 to -30 divided by the distance from 30 to 40. The measure b is calculated for the input parameters to be 1.228 and, of course, 1.0 for the output parameters. The percentage error, J, is the average of the two errors in the a and b measures:

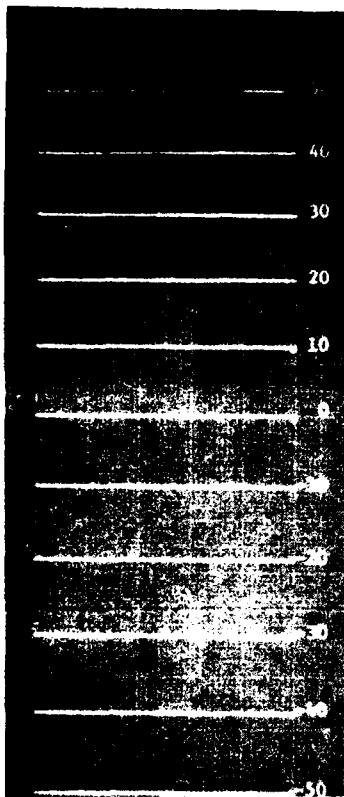


Figure 7. The input optical data with range dimension distortion, compressed at top near nadir.

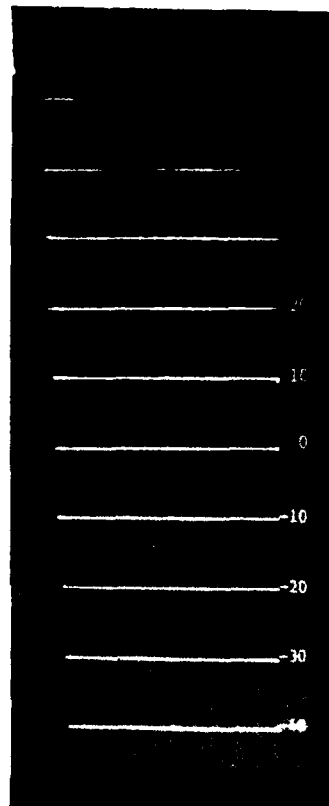


Figure 8. Demonstration of the optical correction of range distortion of data in Figure 7.

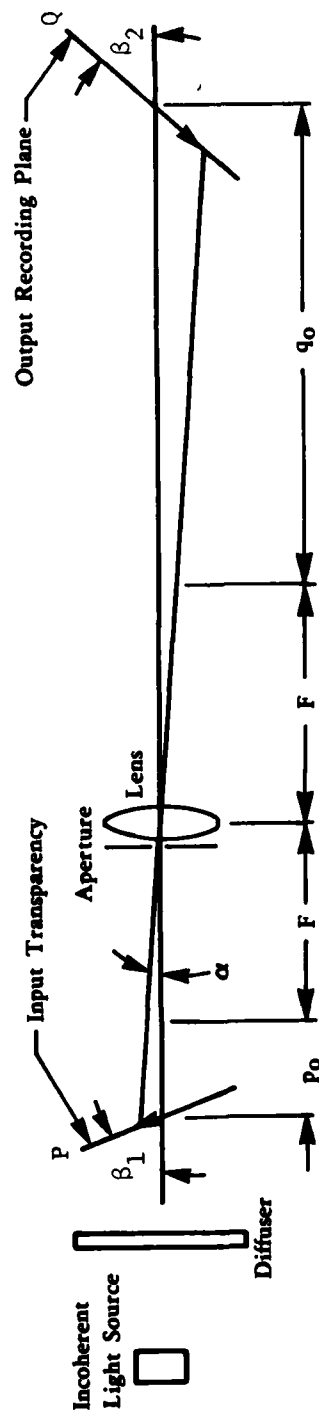


FIGURE 9. OPTICAL SYSTEM FOR CORRECTION OF RANGE DIMENSION DISTORTION.



$$J = \frac{100}{2} \left[ 1 - \frac{a_m}{a_0} + 1 - \frac{b_m}{b_0} \right], \quad (23)$$

where the subscript zero refers to the calculated or ideal value and m refers to the measured value. The experimental setup produced the following results:

<u>Measure</u>	<u>a</u>	<u>b</u>	<u>J(%)</u>
Calculated	1.228	3.996	0.0 (definition)
Experimentally Obtained*	1.222	3.983	0.4

The above result indicates less than a 0.5% error using the optical configuration shown in Figure 9.

#### 5.7 RANGE DISTORTION CORRECTION FOR A CURVED EARTH SURFACE

The previous discussion (Sections 5.1-5.6) has related how optical techniques could be used to correct for the range distortion with the earth modelled by a flat surface; the results found were satisfactory. The equations generated in the curved-surface analysis did not lend themselves readily to a power series expansion, in that the coefficient of each term was a slowly converging infinite series. To analyze the ability of an optical correction system to operate on a curved earth surface, the exact range marks were calculated and the exact optical solution was fitted to these range marks. The results of this analysis show that there is essentially no difference in the accuracy of the results between a flat and curved surface for the given parameters. The results of these calculations are given in Table 4. The parameters required for the optical correction systems are given in Table 5.

A system for evaluating the accuracy of a fit was described in Section 5.6, in which the accuracy was determined by the factor J,

\*Results from 10 experiments were averaged.

TABLE 4  
CALCULATED VALUES FOR OPTICAL CORRECTION SYSTEM

Actual Ground Range (Center = 300 km)	Flat Surface		Curved Earth	
	Radar Range (km)	Optical Correction System's Range (mm)	Radar Range (km)	Optical Correction System's Range (mm)
-50	-16.3572	-49.8671	-18.2681	-49.8664
-40	-13.2995	-40.0009	-14.8500	-40.0000
-30	-10.1337	-30.0612	-11.3127	-30.0607
-20	- 6.8600	-20.0654	- 7.6576	-20.0682
-10	- 3.4827	-10.0420	- 3.8861	-10.0418
0	0	0	0	0
10	3.5858	10.0405	3.9993	10.0405
20	7.2734	20.0636	8.1102	20.0638
30	11.0615	30.0545	12.3310	30.0549
40	14.9487	39.9994	16.6602	40.0006
50	18.9338	49.8860	21.0962	49.8882

TABLE 5

## OPTICAL CORRECTION SYSTEM PARAMETERS

	<u>For Power Series Expansion, Flat Surface</u>	<u>For Fit at 0 and <math>\pm 40</math> Flat Surface</u>	<u>For Fit at 0 and <math>\pm 40</math> Curved Surface</u>
s	0.004126	0.004149	0.003658
$\beta_1$	75.1983 $^\circ$	75.159 $^\circ$	75.877 $^\circ$

an average of the barrel distortion and the end-to-end stretch in the field. This was figured from -40 to +40 mm in the data given. The total field of interest is -50 to +50 mm. (The reason the 80 mm base was used previously was for comparison purposes of the given data inputs, in that the marks at the edges were frequently obstructed by the edge of the film holder.) The results of this evaluation are given in Table 6.

Several conclusions can be drawn from Table 6. The average error,  $J$ , as listed in the last column, is under 0.5% in all cases. By comparing the first two lines with the last two lines, we see that the results for the curved surface are essentially the same as the results for the flat surface, for the given observation parameters. By comparing the first and second lines or the third and fourth lines, it is seen that the average distortion varies as the cube of the base. This result is also suggested by the values of Table 4 in that at one end, the deviation is on the plus side, but on the other end, the deviation is on the minus side.

The results obtained here with the flat-surface model were quite similar to those obtained experimentally. We saw that the curved-surface model behaves very similarly to the flat model, except for different system parameters; hence, the expected results are also within 0.5% accuracy for the curved surface input.

## 5.8 CORRECTION OF RANGE DISTORTION FOR ACTUAL RADAR DATA

Radar images that exhibited range distortion were corrected by optical techniques, as had been suggested by the previous discussion. The corrections were made first on land imagery which included recognizable and measurable ground landmarks, and then the system was extended to lake imagery produced on the same flight. This section discusses the technical details of the corrections which were encountered here, relating them to further applications of the correction system. First, we will cover correction calculations for an

TABLE 6  
DISCREPANCY OF OPTICAL SYSTEM IN CORRECTION

<u>Modelled Surface</u>	<u>Base Length (mm)</u>	<u>Barrel Distortion (%)</u>	<u>Stretch Distortion (%)</u>	<u>Average Distortion J (%)</u>
Curved	100	0.658	0.215	0.437
Curved	80	0.410	0.064	0.237
Flat	100	0.661	0.207	0.434
Flat	80	0.412	0.052	0.232

example case, followed by a discussion of the correlation of predicted and measured results.

In the example case, an X-band SAR image collected on 6 October 1977 is given; the aircraft altitude was ~2745 m with the radar range extending from 3900 m to 2440 m and the recorded image was 42 mm wide. The best correction of the range distortion is desired while maintaining the same image size.

To correct for the range distortion, simulated range marks are calculated as if on the original, and then a fit is made according to the equations governing the optical system. The near-, center-, and far-range distances of 3900 m, 5120 m, and 6340 m correspond to ground distances of 2775 m, 4325 m, and 5715 m, respectively. This is about a 3050 m spread, so nominal range marks were set according to the first column of Table 7, extending from -1525 m to 1525 m. For these ground range marks, the corresponding slant range distances can be calculated, and are given in the second column. For the calculations, 4325 m were added to first column and 5120 m subtracted from the second. Because 42 mm on the film correspond to 2440 m, the range marks on the film can be calculated and are given in the third column. This represents the actual data. From this, we want to generate what the ideal correction would give. At the 1220 m ground range, the average slant range distance is 1020 m, and the average film distance is 17.5875 mm. From this last number, the fourth column is generated on a linear basis. A fit was made to the 0 and 17.5875 marks and is given in the last column. The J for the original data range distance (column 3) over the full 3050 m base is 12.2%, and for the corrected version (column 5) is 1.5%. Hence, almost an order of magnitude improvement is predicted.

The system that was implemented to make the geometric correction is shown in Figure 10. There were some simplifying results with

TABLE 7

CALCULATED VALUES FOR OPTICAL CORRECTION OF AN EXAMPLE RANGE DISTORTION  
(First two columns in meters, last three columns in mm.)

<u>Nominal Ground Distance</u>	<u>Slant Range Distance</u>	<u>Data Range Distance</u>	<u>Ideal Range Distance</u>	<u>Corrected Range Distance</u>
-1525	-1201	-20.685	-21.984	-21.789
-1220	- 978	-16.840	-17.5875	-17.564
- 915	- 745	-12.826	-13.191	-13.242
- 610	- 503	-8.667	-8.794	-8.855
- 305	- 255	-4.386	-4.397	-4.434
0	0	0	0	0
305	260	4.476	4.397	4.427
610	524	9.029	8.794	8.834
915	792	13.649	13.191	13.207
1220	106	18.328	17.5875	17.540
1525	1339	23.058	21.984	21.825

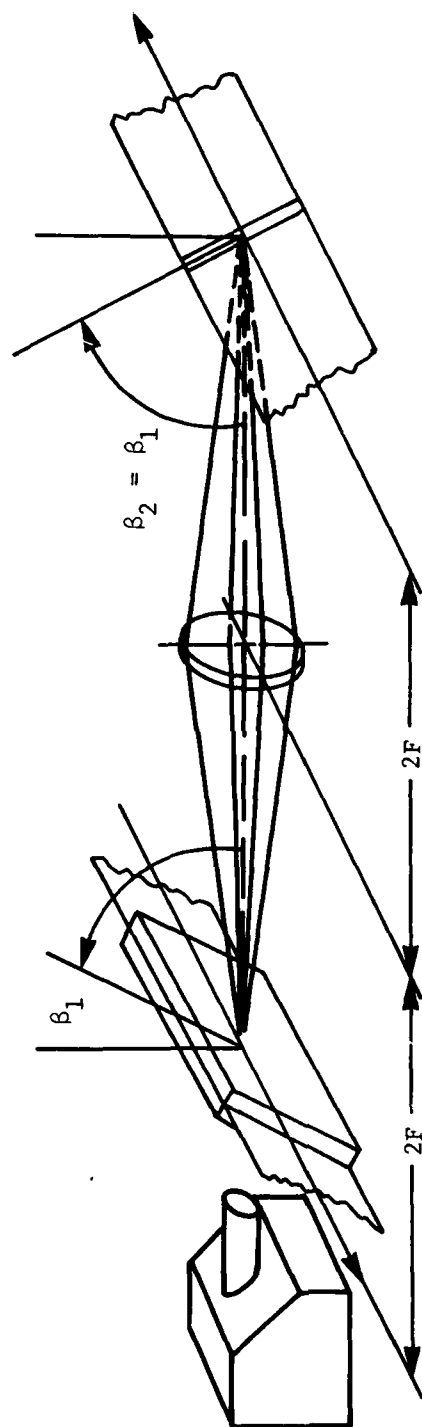


FIGURE 10. THE SCHEMATIC DIAGRAM FOR THE OPTICAL SYSTEM THAT CORRECTED THE RANGE DISTORTION. The uncorrected film is placed in the optical gate, left, and translated to the left. The corrected image is produced at the right as the film translates past the slit to the right. For the particular radar image,  $F = 147$  mm and  $\beta_1 = 59.5^\circ$ .



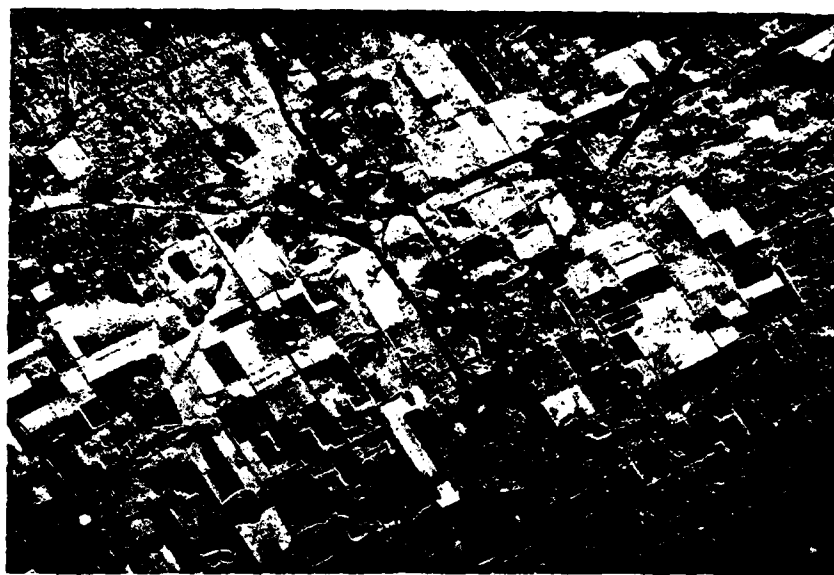
this particular case. A one-to-one image is desired so  $M = 1$  and Eq. (2) in Table 3 reduces to  $\beta_1 = \cos^{-1} x$ . Then (also in Table 3), Eq. (3) becomes  $p_0 = F$ , Eq. (4) becomes  $q_0 = F$ , and Eq. (5) becomes  $\beta_2 = \beta_1$ . Hence, the system is symmetrical about the imaging lens with input and output at  $2F$  distance and sloped at angle  $\beta_1$ . Figure 10 illustrates this system. The correction shown in Table 7 required  $x = 0.00245$  with  $x = F_s$  the maximum desirable focal length of 408 mm. A much smaller focal length is desired to increase the angle  $\beta_1$  from zero to some reasonable value. A lens with a focal length of 210 mm was used, so that  $\beta_1$  is  $59.0^\circ$ .

The system was set up with these parameters and the results obtained were short of completely correcting for the curvature. Since decreasing  $\beta_1$  further would cause vignetting in the system, a 147 mm focal length lens was used. Trial and error with this lens gave a  $\beta_1$  of  $59.5^\circ$ . Hence, the actual  $s$  is 0.00345. The results for this system are shown in Figure 11. In Figure 11a is the uncorrected image, and in Figure 11b the corrected image. The straightening here is demonstrated by the narrower of the two main roads running up toward the left. Image quality was noticeably improved when an air gap slit was used in the output.

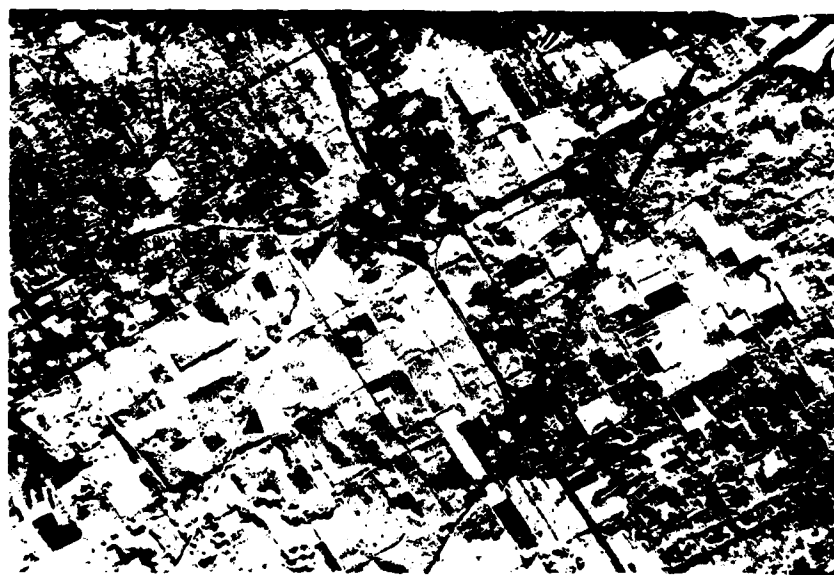
The optical correction algorithm was also applied to SAR data collected over Lake Michigan. Figure 12 shows an optical Fourier transform (OFT) performed on both geometrically corrected and uncorrected data. A digital fast Fourier transform (FFT) of the same Lake Michigan area is also presented in the figure. The digital slant-to-ground-range conversion was performed using previously reported ONR-developed algorithms (Shuchman, et al., 1977).

## 5.9 SLANT-TO-GROUND-RANGE CONVERSION OF SEASAT IMAGERY

Also considered as part of this effort was the optical slant-to-ground-range conversion of SEASAT imagery. Two strips of SEASAT

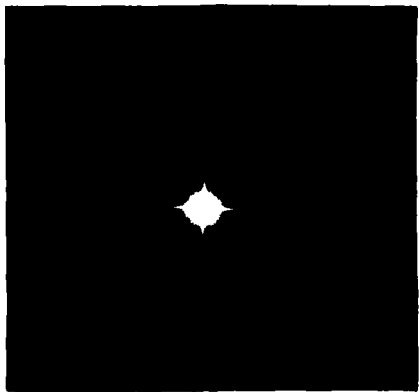


Uncorrected

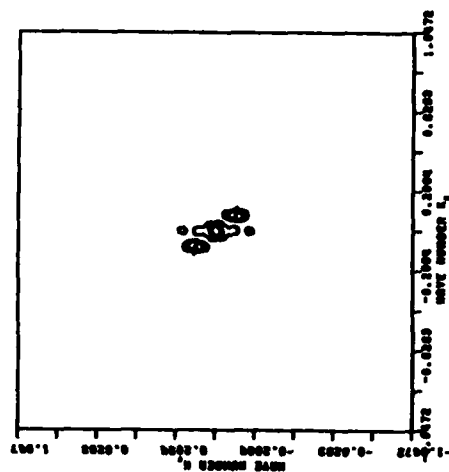


Corrected

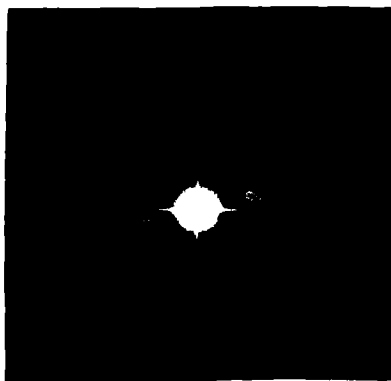
FIGURE 11. OPTICAL CORRECTION OF RANGE DISTORTED IMAGERY.



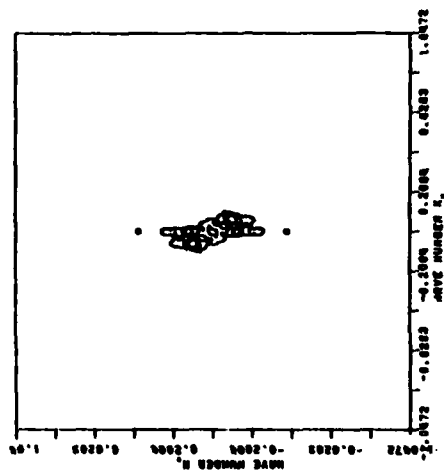
OFT of Optically-Corrected  
Lake Michigan Wave Data



FFT of Digitally-Corrected  
Lake Michigan Wave Data



OFT of Uncorrected Range-Distorted  
Lake Michigan Wave Data



FFT of Range-Distorted  
Lake Michigan Wave Data

FIGURE 12. Optical Fourier Transform (OFT) and Digital  
Fast Fourier Transform (FFT) of Uncorrected and Slant  
Range-Corrected SAR Wave Data

radar imagery from orbit 762 have been optically corrected to a ground range coordinate system using the technique presented in Sections 4.1-4.6. From this imagery, it was determined that the SAR slant-to-ground-range error for the SEASAT radar geometry may be reduced to less than 1/2% by use of a simple tilted plane imaging system. As previously shown, the parameters for the optical correction system may be determined from the radar data collection geometry. Alternatively, one may measure the magnification characteristics of the correction system and use an iterative technique to achieve the desired corrections. This second technique was used for the data correction to be described, since it does not require knowledge of principal plane or focal plane locations for the imaging lens.

The two strips of SEASAT radar imagery to be corrected were made from signal films recorded by ERIM at the Shoe Cove tracking station. Approximately 1000 km of data over the North Atlantic between northern Scotland and Iceland is represented at near edge swaths 1 and 2. The along-track scale factor for both images was approximately 690,000. The range scale for the 0 and 55  $\mu$ sec images is given by:

$$\text{SCALE}_0 = 791,200 - 1694 D, \text{ for } 0 \text{ delay and}$$

$$\text{SCALE}_{55} = 738,200 - 1366 D, \text{ for } 55 \mu\text{sec delay,}$$

where D is the distance from the near range edge of the image film measured in millimeters. The optical configuration for the correction system is shown in Figure 13.

The magnification of the optical system as a function of input and output tilt angles was measured by means of a pair of matched precision diffraction gratings. One grating was positioned at the input plane and the second was mounted on a stand at the recording camera position. With the first grating imaged on the second, Moire fringes were observed indicating the system magnification as a function of range coordinates and tilt angle.

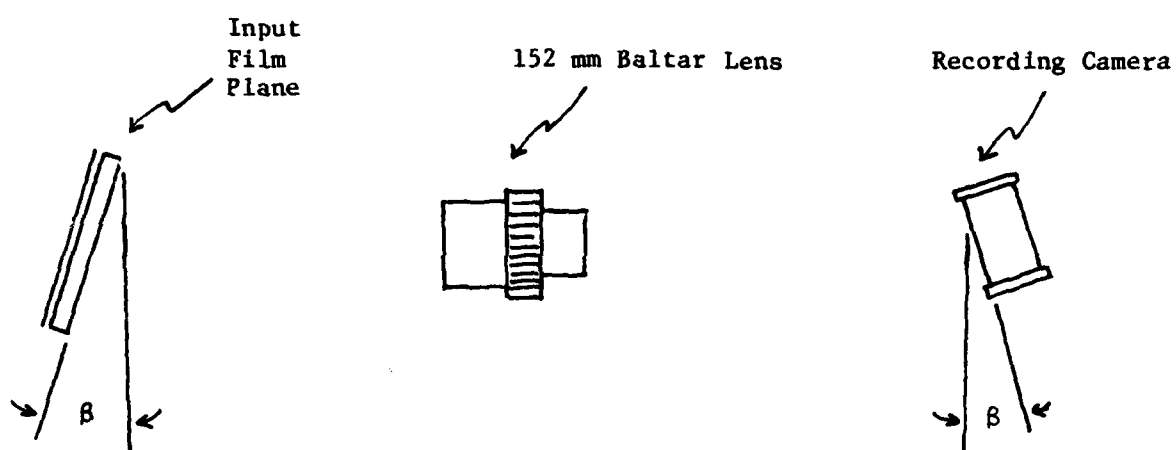


FIGURE 13. OPTICAL CONFIGURATION FOR SEASAT CORRECTION SYSTEM.

For the 0 delay imagery, the azimuth and range scales were equal at the distance D given by

$$791,200 - 1694D = 690,000$$

or

$$D = 59.74 \text{ mm.}$$

A zero beat was obtained for this range location. At a distance of 10.26 mm from the near-range edge of the image film, the scale was

$$791,200 - 1,694(10.26) = 773,820.$$

The required magnification for this position was then

$$\frac{773,820}{690,000} = 1.1214.$$

The image of the 18 lp/mm grating for this position (properly corrected) would thus be

$$\frac{18}{1.1214} = 16.05 \text{ lp/mm}$$

and the observed Moire fringe pattern would have a spatial frequency of

$$18 - 16.05 = 1.95 \text{ lp/mm.}$$

The camera position, lens position, and system tilt angle were adjusted by trial and error to achieve the required sharply-focussed Moire fringe patterns. A tilt angle of  $12^\circ$  was obtained for these conditions.

For the 55  $\mu$ sec delay image, the scales were equal at

$$738,200 - 1366D = 690,000$$

or

$$D = 35.3 \text{ mm.}$$

The required tilt angle was assumed proportional to the variable scale factor as shown below.

$$\beta = 12^{\circ} \times 1366/1694 = 9.7^{\circ}.$$

The tilt angle for the compensation system was therefore preset to  $9.7^{\circ}$  and the lens and camera positions were adjusted to produce a sharply-focussed zero beat fringe pattern at the image of the 35.3 mm range position.

Then, a spinning ground-glass diffuser illuminated by the green light from an argon laser was used as the light source. The output images were recorded on 70 mm 3414 film using the camera from the MA Optical Processor. The signal film drive was used to translate the input data. The signal film drive frequency was 12.205 kHz and the camera drive frequency was 119.7 Hz for both recordings. A 150  $\mu\text{m}$  air slit was used on the camera.

## SAR DIGITAL SPECTRAL ESTIMATION ALGORITHM

This section describes in detail a computer software system designed specifically to obtain spectral estimates of wavelength and directional information about surface gravity waves imaged by SAR. First, the computer system is described, and then examples of output and a demonstration of its utility are presented.

## 6.1 INTRODUCTION

Presently, the bulk processing of SEASAT SAR imagery is primarily an optical and photographic operation. This is true not only for the image generation process, but also for spectral estimates. Most spectral estimates generated from SAR data have utilized optical Fourier transforms (OFTs) as reported (for example) by Gonzelez, et al. (1979). OFTs however, have certain limitations such that they are useful only for predicting dominant wavelength and direction (Shuchman, et al., 1977). Thus, sophisticated analysis is not possible with OFTs.

Digital techniques (as developed for this ONR program) are more versatile, repeatable, and noise-free when compared to optical techniques; however, it should be noted that, for at least the near future, they lack the capability of processing large amounts of SAR data in near real time. Additionally, digital techniques are limited in the size of the transform aperture. For example, 512 pixels (resolution elements) are typically the area that is digitally transformed. In spite of these shortcomings, digital techniques offer the most promise in terms of extracting useful and detailed information about the ocean surface from SAR.

Two digital spectral estimation techniques are employed in the software package to be described. One technique, the fast Fourier transform (FFT), is well known and documented (Brigham, 1974). The

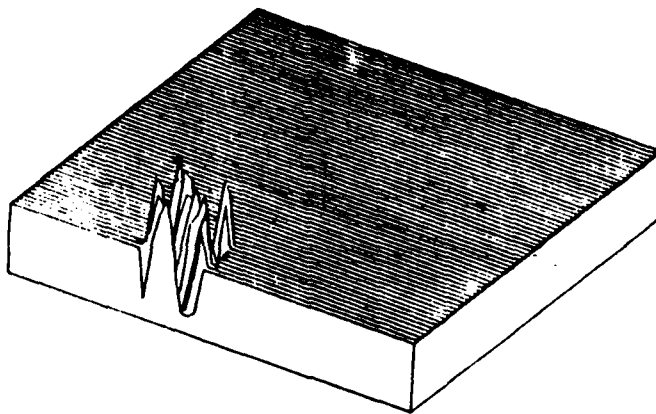


second technique or algorithm is relatively new and is termed "semicausal model"; this was developed by Jain and Ranganath (1978) and has been programmed with preliminary testing at ERIM by Jackson (1978).

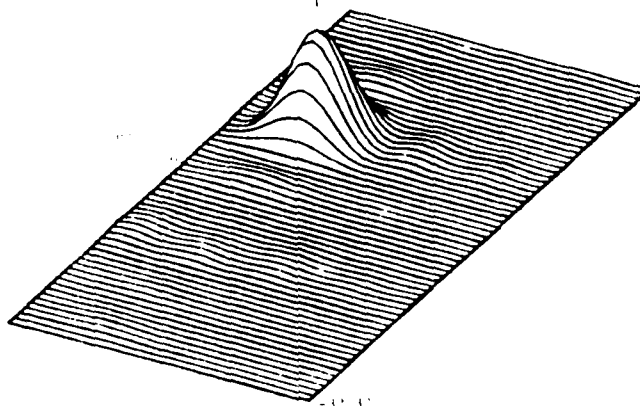
This new two-dimensional frequency analysis algorithm shows promise for small ocean-area spectral analysis, for example ocean areas where extensive wave refraction is occurring. The semicausal model is based on autoregressive techniques and, compared with the Fourier transform, it produces fine frequency resolution for short truncations of data. Preliminary testing of this new algorithm has demonstrated this promise. While related to the well-known maximum entropy spectral analysis (MESA) as described by Burg (1967) and Ulrich (1972), it is substantially different in concept. In our experiments with this two-dimensional algorithm, no identifiable negative results were found. Compared with the FFT, finer resolution and elimination of sidelobes were obtained; also, interference by large pseudo or zero-frequency ("d.c.") spectral components was reduced or eliminated.

The capability of obtaining precise direction and wavelength information over an aperture smaller than one wavelength makes this algorithm more suitable than the Fourier transform for small-region analysis. Figures 14 and 15 illustrate the comparative resolution between the semicausal model and the FFT.

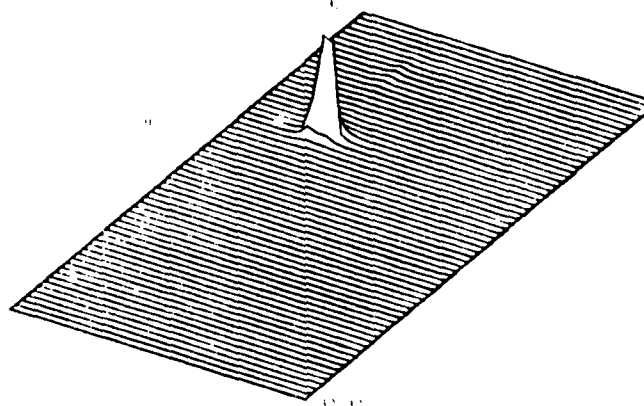
Figure 14(a) shows the function, a simulation of an ocean wave by a sinusoid with 30% random noise, which is truncated at approximately 2 wavelengths. Figure 14(b) shows the square of the two-dimensional FFT of the function shown, in which a wide main lobe and sidelobes are evident. Figure 14(c) shows the semicausal model frequency analysis of the function shown in Figure 14(a). A narrow main lobe with essentially no sidelobes is achieved by using the semicausal model. A finer frequency resolution of restricted regions is thus shown to be produced by this new method than is



(a) Plot of  $\sin\left(\frac{2\pi}{8}i + \frac{2\pi}{6}j\right) + 30\%$  additional noise,  $i = 22-30$ ,  $j = 1.9$ .

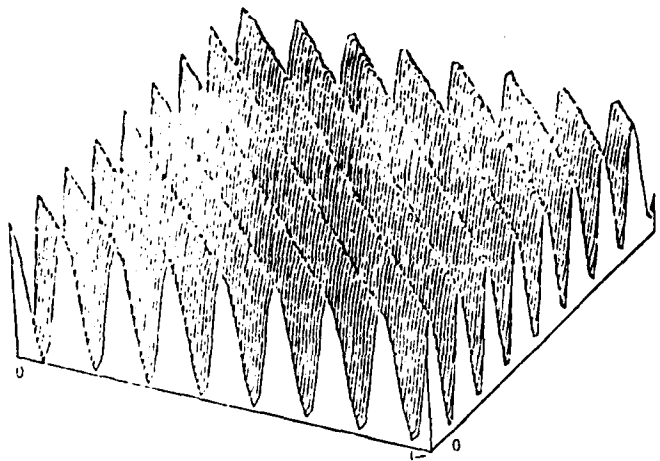


(b) FFT Spectrum of Function (a).

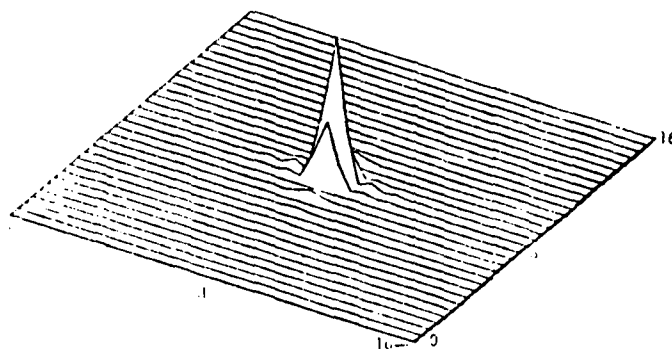


(c) Semicausal Spectrum of Function (a).

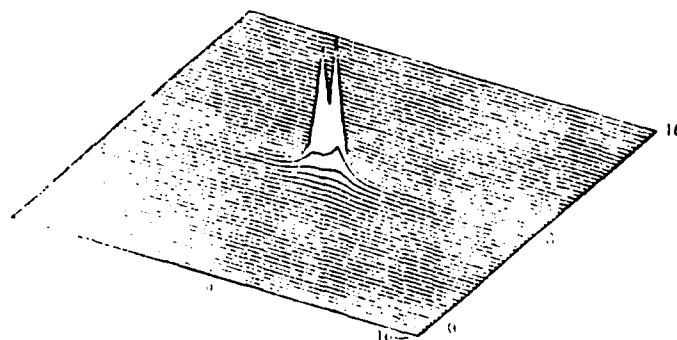
FIGURE 14. COMPOSITE OF TRUNCATED 2-DIMENSIONAL REFERENCE FUNCTION (a) WITH RESULTING FFT (b) AND SEMICAUSAL SPECTRUM (c).



(a) Plot of  $\sin \frac{2\pi}{8}(i + j) + \sin \frac{2\pi}{8.05}(i + j) + 7\%$  Additive White Noise.



(b) FFT Spectrum of Function (a).



(c) Semicausal Spectrum of Function (a).

FIGURE 15. COMPOSITE OF 2-DIMENSIONAL REFERENCE FUNCTION (a) WITH RESULTING FFT (b) AND SEMICAUSAL SPECTRUM (c).

achieved by the FFT. This fine resolution would be useful in refractive wave regions where the direction and wavelength are undergoing change.

Figure 15 illustrates the frequency resolving capabilities of the semicausal model as compared to the FFT. The two components of the reference function shown in Figure 14(a) are not discernible by eye, and are below the Fourier transform resolving capability. In this function,  $\Delta f \Delta t = 0.4$ , where  $\Delta f$  is the difference in frequency and  $\Delta t$  is the length of the data segment;  $\Delta f \Delta t \approx 1$  is the resolution limit of the Fourier transform. The FFT of this function is shown in Figure 15(b), where only a single lobe is evident. In Figure 15(c), the semicausal model shows frequency resolution of the two close components. This capability of modern spectral analysis techniques is clearly shown in Lacoss (1971) for one-dimensional frequency discrimination.

Two aspects of frequency resolution are shown in Figures 14 and 15: (1) overcoming the aperture effects on short truncations of data and (2) discriminating between closely-related frequency components on extensive regions of data.

## 6.2 SOFTWARE DESCRIPTION

The flow chart of the SAR spectral estimation algorithm is given in Figure 16. The process is started with a computer-compatible tape (CCT). This data is typically generated on the ERIM hybrid optical-digital processor described by Ausherman, et al. (1975). This device enables full dynamic range (approx. 40 dB) SAR output data to be created on a CCT, instead of film as is typically done.

The tape data is first reformatted to be compatible with the University of Michigan Amdahl Computer (the current computer system used to run the spectral estimations). After reformatting, the SAR

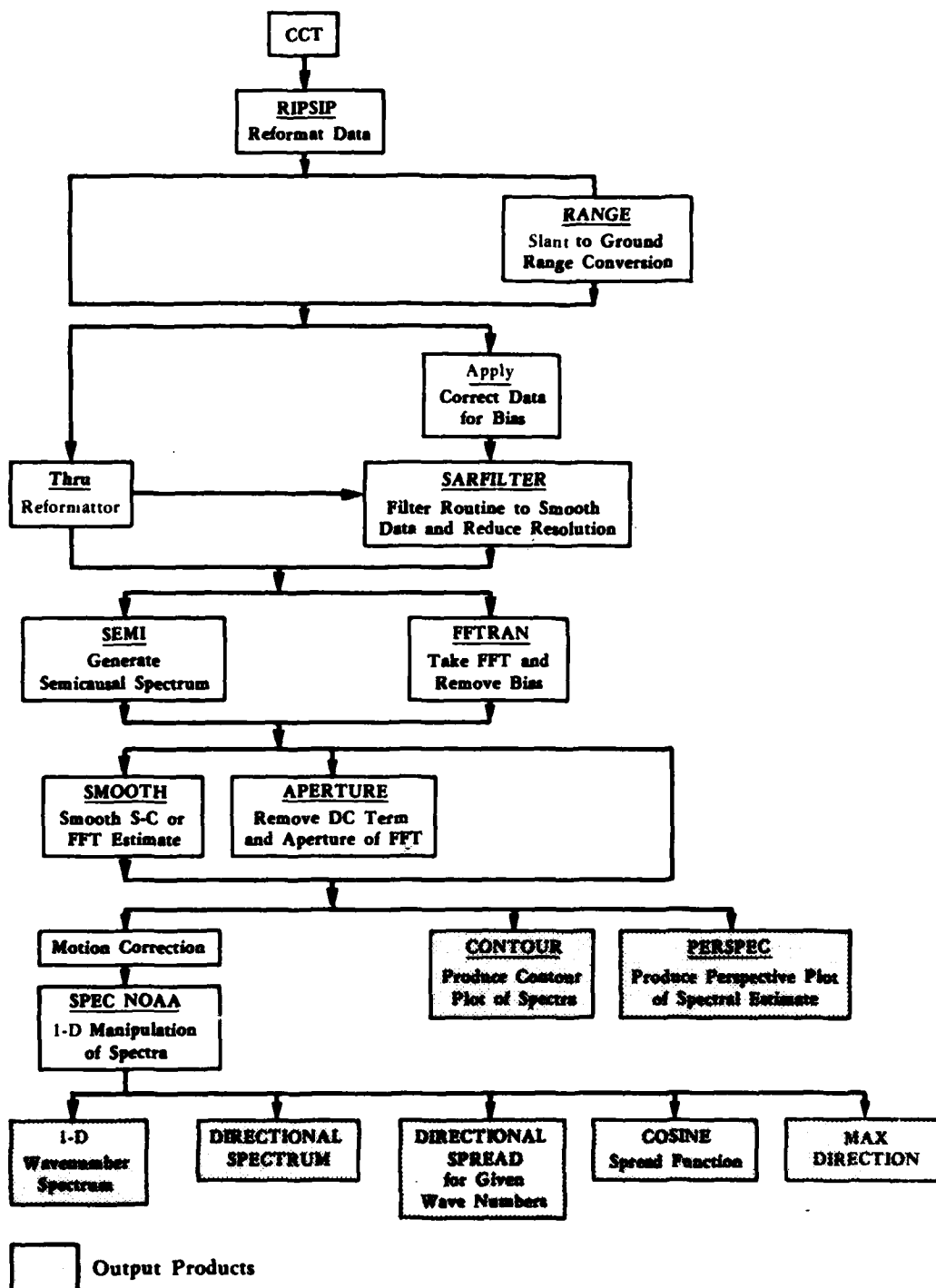


FIGURE 16. FLOW CHART OF SAR TWO-DIMENSIONAL SPECTRAL ESTIMATION PACKAGE

data is digitally corrected for geometric distortions. The digital geometric-correction algorithm has been described in detail by Feldkamp (1977) as well as Shuchman, et al. (1977).

After geometric rectification, the average range scan line is computed. An average scan line of SAR wave data is shown in Figure 17. Note the taper and bias in Figure 17. This tapering is a result of radiometric (antenna, power loss, etc.) effects of the radar. The variations, if uncorrected, typically cause a large D.C. term to result in the FFT; thus, it is advantageous to remove this bias prior to generating the FFT. This is accomplished by taking the average scan line, smoothing it, and then applying the smooth curve correction to the entire data set.

After correcting for radiometric effects, the data is smoothed by using a  $(\sin x) / x$  weighting function on a 4-pixel by 4-line section of the data. The output from this routine has 1/2 the resolution which the original contained. This is done to smooth the data (reduce speckle effects) as well as to allow a larger SAR-imaged ocean area to be within the FFT or S-C aperture. Alternatively, the SAR digital data does not have to go through the Apply or SAR filter routine; the data can go through a reformatter (Thru) and straight into the fast Fourier transform (FFT) or semicausal (S-C) programs. Either of these programs is designed to generate the actual spectral estimate of the SAR scene.

After the FFT or S-C transform generation, the data can either go directly into a contour or perspective-plot generation program or the data can be motion corrected and one-dimensional manipulation of the data can take place. The SAR process distorts the apparent wavelength of waves moving in the azimuth direction and distorts the apparent direction of waves with a velocity component in the range direction. A detailed description of these effects and appropriate corrections can be found in Raney and Lowry (1977). Additionally, Appendix A of this report discusses these distortions in detail.

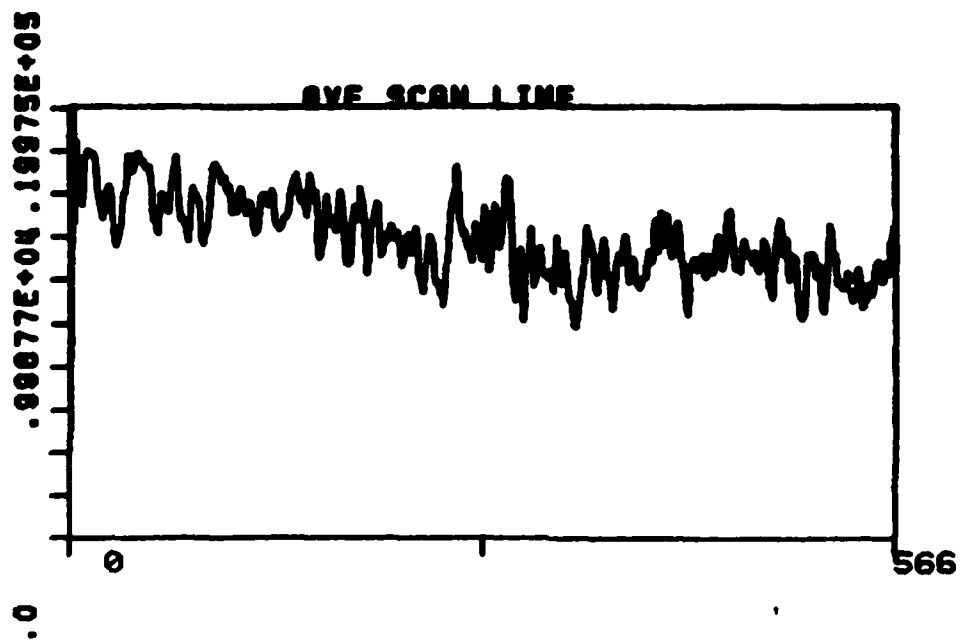


FIGURE 17. AN AVERAGE SCAN LINE OF SAR WAVE DATA.

Spectral estimates generated, using either the FFT or S-C data can also be smoothed (this increases the degrees of freedom) or have an aperture removal performed on the data. After either of these steps, the data (as before) can be displayed either as a contour plot or a perspective plot, or can be fed into the one-dimensional manipulation program.

In order to compute the 1-D SAR spectrum from SAR imagery, a two-dimensional FFT or S-C estimate of the image is taken. This results in a two-dimensional SAR spectrum  $S(k_x, k_y)$ , where  $k_x$  and  $k_y$  are the orthogonal components of wave number. The location of the maxima of the two-dimensional spectrum gives us the peak wave number and the peak directions. The peak wave number may be found by using the dispersion equation.

From  $S(k_x, k_y)$ , we can find  $S(k, \theta)$  which gives us the directional distributions, where  $k^2 = k_x^2 + k_y^2$  and  $\theta = \arctan(k_y/k_x)$ . Then the one-dimensional spectrum  $S(k)$  can be calculated as follows:

$$S(k) = \int_0^{2\pi} S(k, \theta) k d\theta \quad (24)$$

This equation can be directly translated into a summation on  $\theta$  which is used in our computer program,

$$S(k_i) = \frac{2\pi}{N} \sum_{n=0}^{N=180} S(k_i, \theta_n) \Delta\theta, \quad (25)$$

where  $k_i$  is the wave number ranging in value from zero to  $k_{\max} = 2\pi/(\text{pixel size (m)} \times 2)$ . Theta ranges from  $0^\circ$  to  $180^\circ$  with about 90 divisions.



The wave direction and wavelength on the SAR image must be corrected due to the aircraft motion. The wave phase spread must also be corrected due to water depth. Equation (26) yields the wave phase speed in terms of the wave number and the water depth

$$C = \sqrt{g/k \tanh(kz)}, \quad (26)$$

where  $g$  = gravitational constant and

$z$  = water depth.

Due to aircraft motion, the wavelength is going to be modified. (see Appendix A). It can be shown that  $\gamma$  (which is the angular shift between the true and apparent positions of the peak) may be found by using

$$\gamma = \arcsin(C/V \cos(\theta)) \quad (27)$$

where  $\theta$  is the observed angle,

$C$  is the wave phase spread, and

$V$  is the aircraft speed.

One then finds the actual angle with Eq. (28).

$$\theta_A = \theta + \gamma \quad (28)$$

The true wavelength is then defined to be

$$L = L_{\text{obs}} \cos \theta_A / \cos \theta, \quad (29)$$

where  $L_{\text{obs}}$  is the observed wavelength. If  $\theta$  is either  $90^\circ$  or  $270^\circ$ , then one must use

$$L = L_{\text{obs}} (V \pm C) / V, \quad (30)$$

where the choice of sign depends on the observed wave motion (i.e., if the wave travels in the same direction as the aircraft, then the sign is positive, if not, it is minus).

Therefore, in order to compute the one-dimensional spectrum, the wave numbers  $k_{\text{max}}$  to  $\gamma$  are broken up into 32 intervals. For each  $k$  interval, the wave phase speed is calculated.

The summation from  $0^\circ$  to  $180^\circ$  is then performed, where at each  $\theta$  interval, the rate of  $L/L_{\text{obs}}$  is calculated. Since we have chosen a  $k$  to scan, we form a  $k_{\text{mod}} = k L/L_{\text{obs}}$  which yields the shifted  $k$  due to aircraft motion. Using  $k_{\text{mod}}$  and the angle, one then finds the  $k_x$  and  $k_y$  indexes on the two-dimensional FFT spectra which correspond to the  $k_{\text{mod}}$  and angle.

Using these  $k_x$  and  $k_y$  index values as the center of a triangle, a weighted average of the energy value on the vertex points is taken. One finds that the energy values must also be corrected due to motion effects using

$$E = E_{\text{point}}(1 \pm 1/2 C/V \times \cos \psi). \quad (31)$$

Summing up all the energy values for this wave number interval, multiplying by  $2\pi$ , and dividing by the number of points taken, yields the one-dimensional average of energy for the  $k_i$ .

This routine is performed from  $\gamma$  to  $k_{\text{max}}$  and the resulting  $S(k)$  is plotted as a function of wave number. As the program scans each  $k_i$ , the angle at which the energy is maximum is also retained and plotted. Additionally, for any given wave number  $k_i$ , the direction spread (i.e., the 180 angles) can be retained and plotted.

Directional properties of the waves recorded by the radar are also examined in the software package following the approach given by Longuet-Higgins, et al. (1963). For each value of  $k$  evaluated, the first two Fourier harmonics of  $S(k, \theta)$  were calculated by direct transformation with

$$a_1 + ib_1 \frac{1}{S_T} \sum_{n=0}^{180} S(k, \theta_n) \cos \theta_n + \frac{i}{S_T} \sum_{n=0}^{180} S(k, \theta_n) \sin \theta_n \quad (32)$$

and

$$a_2 + ib_2 \frac{1}{S_T} \sum_{n=0}^{180} S(k, \theta_n) \cos 2\theta_n + \frac{i}{S_T} \sum_{n=0}^{180} S(k, \theta_n) \sin 2\theta_n, \quad (33)$$

where  $S_T = \sum_{n=0}^{180} S(k, \theta_n)$ . A smoothed directional distribution function was calculated with

$$G(\theta) = \frac{1}{2} + \frac{2}{3} (a_1 \cos \theta + b_1 \sin \theta) + \frac{1}{6} (a_2 \cos 2\theta + b_2 \sin 2\theta) \quad (34)$$

and the mean direction was obtained with

$$\bar{\theta} = \tan^{-1} \left( \frac{b_1}{a_1} \right) \quad (35)$$

The exponent factor of a cosine fit to the directional distribution of the form

$$\cos^{2H(k)} (\theta - \bar{\theta})/2 \quad (36)$$

was approximated following Mitsuyasu et al. (1975) with

$$H(k) = 1 / \left[ 1 - a_1^2 + b_1^2 \right]^{1/2} - 1 \quad (37)$$

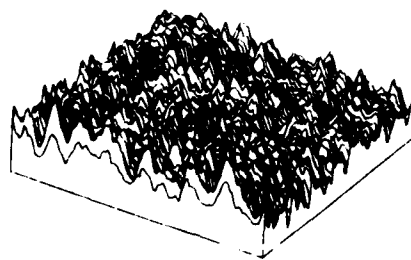
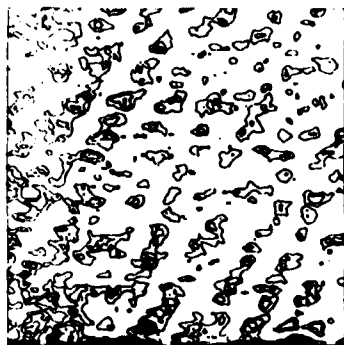
This value, referred to as the cosine spreading function, is again plotted as a function of wave number  $k$ .

### 6.3 DIGITAL SPECTRAL ESTIMATIONS

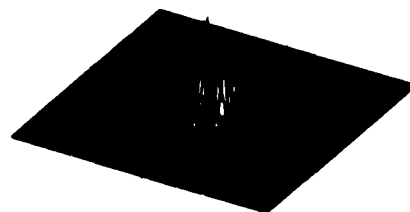
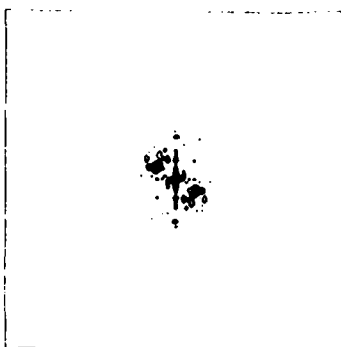
As indicated in Figure 16, the digital spectral estimation software package allows one to display spectrally-analyzed data in a number of ways. The semicausal model was compared to standard FFT analysis for aircraft SAR data. The aircraft SAR data, shown in Figures 18-20, are at X-band (3 cm) wavelength, collected on 23 September 1978 during the GOASEX experiment. Sea truth indicates a 130 meter, 2.5-significant-wave-height swell in the area. The resolution (pixel size) of the aircraft data is 10 meters. Both data sets were digitized from output imagery using ERIM hybrid optical facilities

Contour Plots

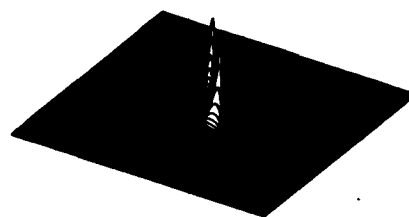
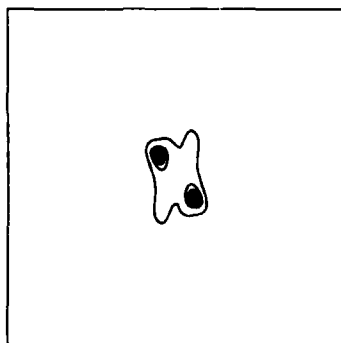
Perspective Plots



GOASEX Wave Data, 128 x 128 Samples (10 Meters/Sample)



FFT Spectrum of Above Data

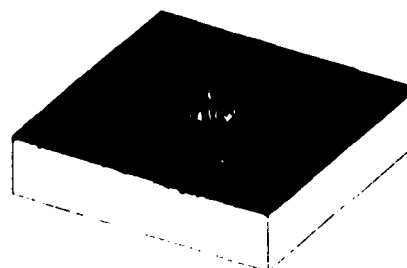
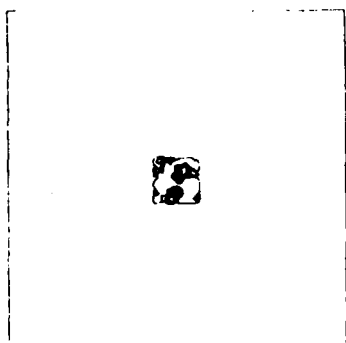


S-C Spectrum of Above Data

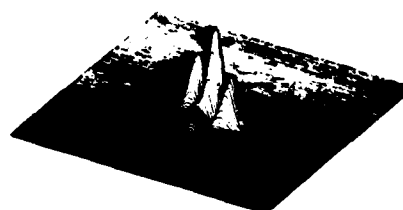
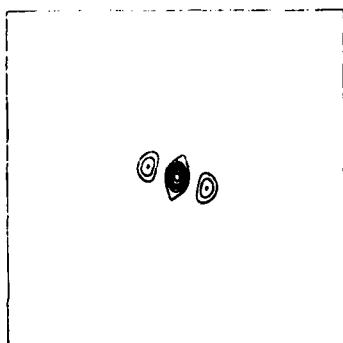
FIGURE 18. GOASEX SAR DATA (128 x 128 Samples) SHOWING RESULTING FFT AND S-C SPECTRAL ESTIMATES. (Four quadrants of spectra shown,  $k = 0$  at center,  $k = 0.31 \text{ m}^{-1}$  at edge of square.)

Contour Plots

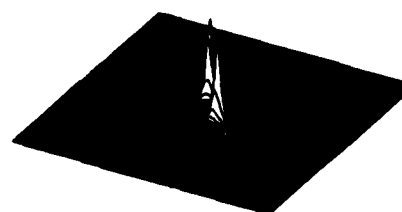
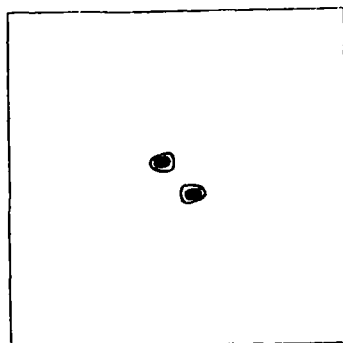
Perspective Plots



GOASEX Wave Data, 17 x 17 Samples (10 Meters/Sample)



FFT Spectrum of Above Data

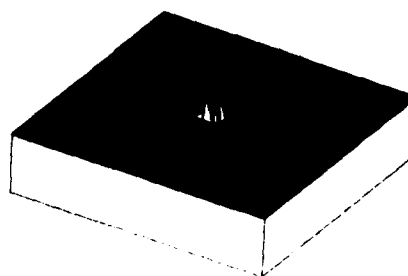
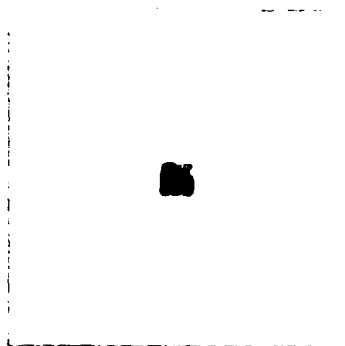


S-C Spectrum of Above Data

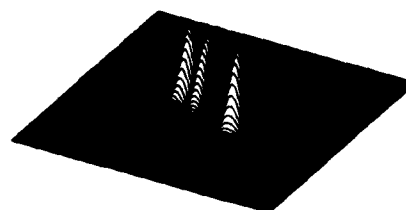
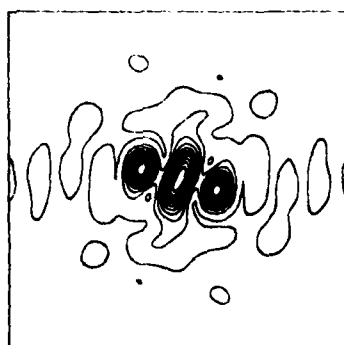
FIGURE 19. GOASEX SAR DATA (17 x 17 samples) SHOWING RESULTING FFT AND S-C SPECTRAL ESTIMATES. (Four quadrants of spectra shown,  $k = 0$  at center,  $k = 0.31 \text{ m}^{-1}$  at edge of square.)

Contour Plots

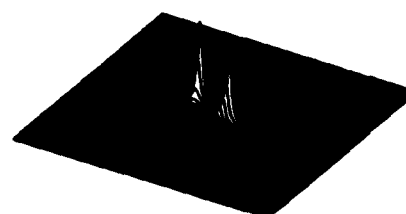
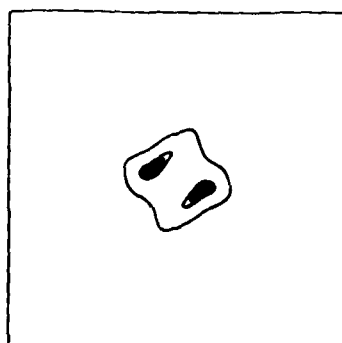
Perspective Plots



GOASEX Wave Data, 11 x 11 Samples (10 Meters/Sample)



FFT Spectrum of Above Data



S-C Spectrum of Above Data

FIGURE 20. GOASEX SAR DATA (11 x 11 Samples) SHOWING RESULTING FFT AND S-C SPECTRAL ESTIMATES. (Four quadrants of spectra shown,  $k = 0$  at center,  $k = 0.31 \text{ m}^{-1}$  at edge of square.)

previously described. In Figures 18-20, the wave data, FFT, and semicausal (S-C) spectra are shown in both perspective and contour forms.

Three restricted regions of GOASEX data and their spectra are shown in Figures 18-20. In Figure 18, wave data and spectra are shown for a region of  $(1.28 \times 1.28) \text{ km}^2$  sampled at 10 m spacing. With 130 m wavelengths, the data region (aperture) is therefore approximately 10 wavelengths. The wave crests can be counted on the contour plot in Figure 18(a). Bias (d.c.) has been removed from this data. The spectra are represented in four quadrants,  $k = 0$  being at the center of the spectral plane, and  $k = 0.31$  at the edge of the square. The wave number is  $0.05 \text{ m}^{-1}$  ( $2/130 \text{ m}$ ) as indicated both with the FFT and the S-C spectra. The direction of the spectral peaks from the center of the spectral plane indicates the direction of the perpendicular of the imaged ocean wavefronts — in this case, approximately  $320^\circ$  or  $140^\circ$  azimuth. Note that the FFT (Figure 18(b)) has many sharp peaks due, no doubt, to interference effects, in addition to showing a substantial "d.c." contribution. The S-C spectrum (Figure 18(c)) has only two high peaks showing the correct wave number component, and the d.c. contribution is negligible. In this case, the S-C spectrum clearly shows the correct wave number and direction in both the perspective plot and the contour plot. With careful contouring, the correct wave number and direction can be brought out with the FFT.

A reduced aperture over the same wave data is used to obtain the spectra shown in Figure 19. Here, 17 sample points represent a region  $170 \times 170 \text{ m}^2$ , or an aperture of 1.31 wavelengths of 130 m each. The aperture effect is clearly beginning to show with the FFT. In Figure 19(b), the frequency components are approximately 3 dB below the d.c. component and are relatively broad, reflecting the restricted size of the aperture, as is always expected with the Fourier transform. The S-C spectrum still indicates no d.c. and still shows

a relatively narrow frequency component. The directions and wave numbers begin to differ between the FFT and the S-C. The wave numbers measure 0.06 for the FFT, 0.04 for the S-C, while the directions are  $300^\circ$  for the FFT and  $315^\circ$  for the S-C. Clearly, the two spectral methods differ at this aperture. Further work is required to determine which method is correct. Possibly, the aperture effect and the influence of the d.c. component is distorting the FFT, or possibly there is shifting in the S-C.

A still smaller aperture was used for the spectra generated in Figure 20. Here, 11 samples ( $110 \times 110 \text{ m}^2$ ) correspond to an aperture of 0.85 wavelengths. The FFT still indicates the frequency components, with a substantial d.c. contribution, and relatively wide lobe structure. The S-C still shows no d.c. component, and shows relatively sharp peaks. The FFT indicates  $k = 0.07$  while the S-C indicates  $k = 0.05$  (the same  $k$  as found in Figure 18 using  $128 \times 128$  data points). The FFT and S-C agree on the direction of the waves:  $295^\circ$  azimuth. Possibly, the large d.c. component is distorting the distance of the frequency components in the FFT, as this distance grows larger with reduced aperture, while this distance remains near or identical to the large aperture value in the S-C. This question requires studies with reference functions and induced noise.

To summarize, the new spectral analysis methods such as maximum entropy (MESA) and the essentially-equivalent autoregressive technique, have been extensively investigated for one-dimensional problems. While these methods have been shown to be extremely useful for short truncations of discrete data, great care is required in their application. Unlike the Fourier transform (which has had a century and a third of theoretical investigation and testing, and which has become a standard in itself) the new spectral analysis methods should be viewed as potential, rather than proven. Such problems as frequency shifts, spectral splitting, and vulnerability to noise prevent this new technique from being indiscriminately applied to spectral analysis problems.



The semicausal model of Jain and Ranganath (1978), which is the only demonstrated two-dimensional high-resolution spectral analysis method of which we are aware, is related to the one-dimensional MESA and autoregression techniques; however, because of its different nature and boundary constraints, and the fact that many investigators have not tested it for different applications, its investigation for ocean-wave analysis should proceed with great care. Our preliminary work has shown promise for this application, but much work is required before we can be confident of presenting this method as an alternative or operational auxiliary to the Fourier transform.

Because the frequencies and noise of SAR-sensed ocean waves are basically unknown, the SAR data may contain a spread of frequencies, be non-uniform over the analyzed region, and have noise of different kinds. An investigation should always relate the spectral results to a reference model. For example, the spectral analysis, either by means of the semicausal model or the FFT, should be tested by generating synthetic data which is indicated by each spectral result.

Contour plots are also useful when examining SAR data collected over a variety of radar look angles. Figures 21 and 22 show SAR data collected at X and L-band wavelengths, respectively, as a function of radar look direction. The FFT contour plots presented in these figures are from the same GOASEX data presented earlier. Figure 23 summarizes the viewing geometry for Figures 21 and 22 (see the number in the lower right-hand corner of each contour plot). It is not known, at the present time, what causes the asymmetrical shapes on the contours. The alignment of the contours may be an effect of surface wind. This is an area of active study.

Figures 24 and 25 present the one-dimensional plots of relative magnitude as a function of wave number for pass 3 at X-band and L-band, respectively (see Figure 23 for the orientation of pass 3).

**ERIM CV-580** X-BAND SAR

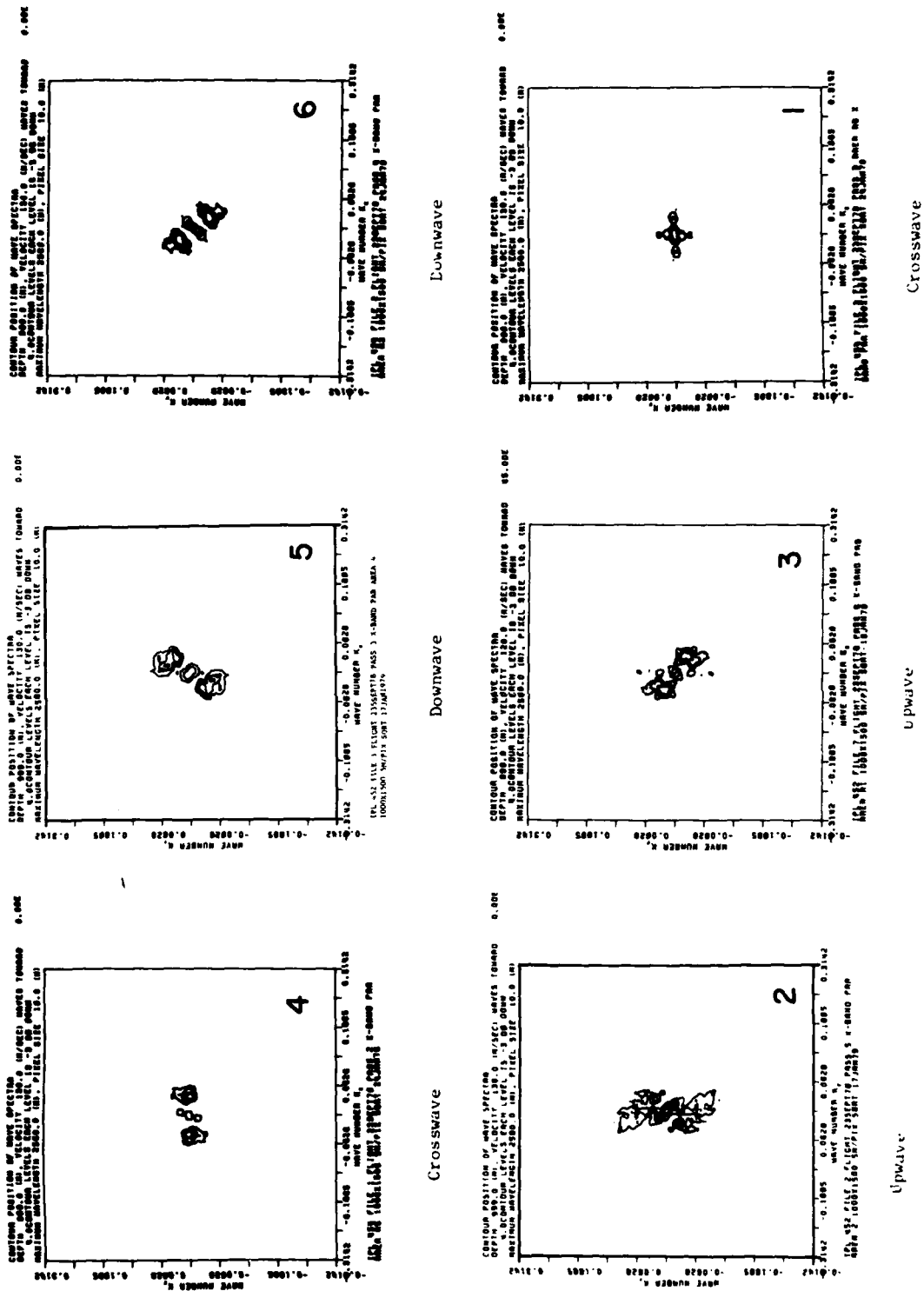


FIGURE 21. GOASEX X-BAND SAR DATA.

# GOASEX REV 1269A 23 SEPTEMBER 1978

## ERIM CV-580 L-BAND SAR

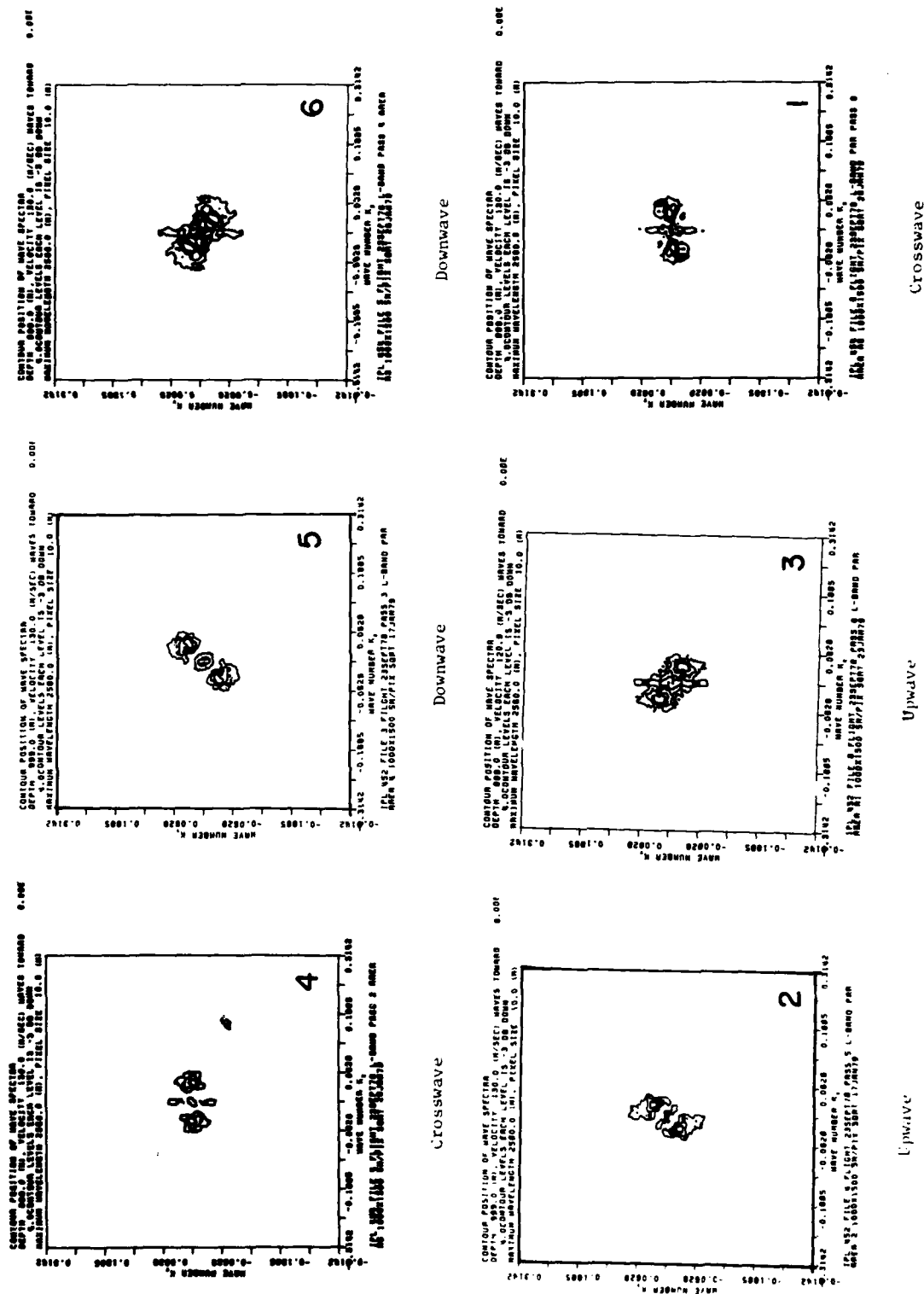
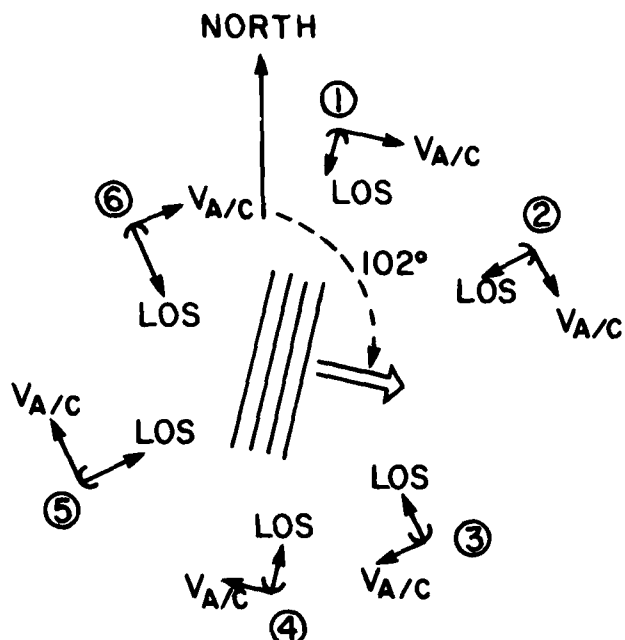


FIGURE 22. GOASEX L-BAND SAR DATA.

# WAVE DETECTION VERSUS SAR LOOK DIRECTION GOASEX REV 1269A - 23 SEPTEMBER 1978



SAR SYSTEM  PLATFORM HEADING (DEGREES TRUE)	*SEASAT			*ERIM CV-580			**ERIM CV-580			RELATIVE WAVE HEADING
	(L-BAND)			(L-BAND)			(X-BAND)			
	$\lambda$ (m)	$\theta_t$ Deg	$\theta_A$ Deg	$\lambda$ (m)	$\theta_t$ Deg	$\theta_A$ Deg	$\lambda$ (m)	$\theta_t$ Deg	$\theta_A$ Deg	
102				160	98	356	160	101	359	CROSSWAVE (1)
152				160	104	312	160	68	275	UPWAVE (2)
242				160	98	216	160	98	216	UPWAVE (3)
293				160	113	190	160	110	187	CROSSWAVE (4)
333	165	94	121	160	109	136	160	107	134	DOWNWAVE (5)
62				160	101	39	160	115	53	DOWNWAVE (6)

From P/R Buoy:  $\lambda = 130$  m  
 $\theta_t = 102$  deg.

\* Optical Fourier Transform Data  
\*\* Digital Fourier Transform Data

FIGURE 23. SUMMARY OF VIEWING GEOMETRY FOR FIGURES 21 AND 22.

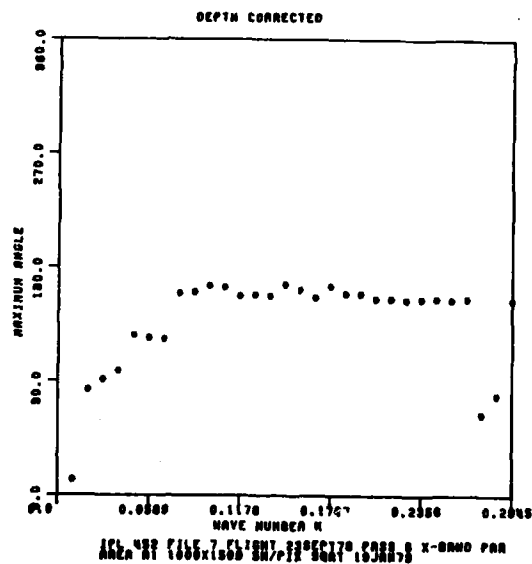
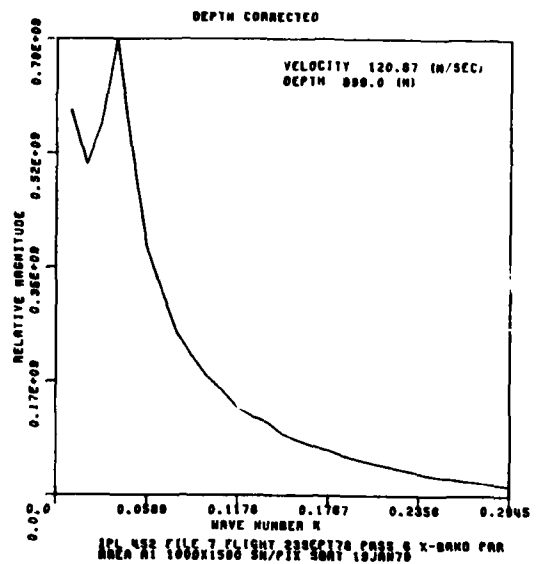


FIGURE 24. ONE-DIMENSIONAL SPECTRAL ESTIMATION OF X-BAND SAR DATA.

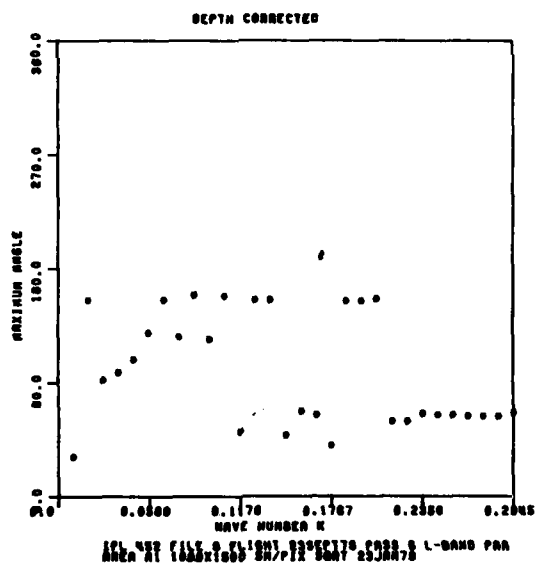
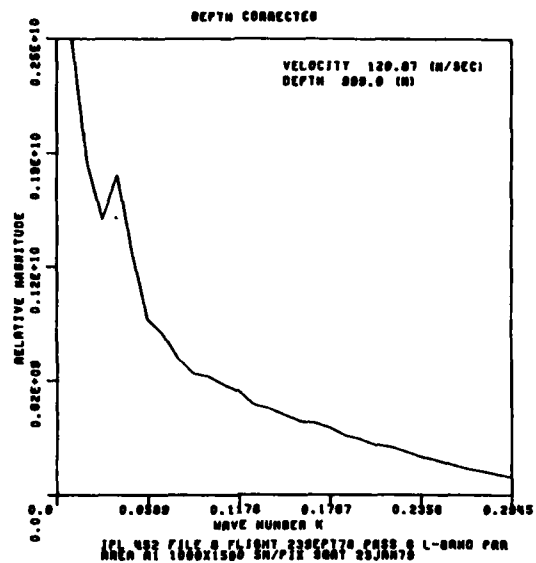


FIGURE 25. ONE-DIMENSIONAL SPECTRAL ESTIMATION OF THE L-BAND SAR DATA.

Also given with the one-dimensional plot is the maximum direction. These data were again generated using the FFT routine as opposed to the semi-causal method: in addition to the graphical output shown, a numerical listing of the plotted values is also obtained. Figures 26 and 27 present the computer listings for the X-band (Figure 24) and L-band (Figure 25) one dimension calculations, respectively.

Figures 28 and 29 represent the additional products that are output of the software package. Figure 28 is the spread in energy about  $0.039 k$ , the peak wavenumber interval along with the function  $G(K)$ . Figure 29 is the cosine spreading function  $H(K)$  and the average direction  $\theta$  previously discussed. For completeness, the maximum angle and the one-dimensional plot are also shown. The data presented in Figures 28 and 29 is the same X-band data presented previously.



IPL 452 FILE 7 FLIGHT 23 SEPT 78 PASS 3  
X-BAND PAR AREA A1 1000x1500 5M/PIX SQRT 19 JAN 79

DEPTH OF WATER 999.0 METERS  
MAX FREQUENCY DISPLAYABLE 0.2793 HZ  
MAX K VALUE DISPLAYABLE 0.3141  
GROUND TRACK ANGLE 242.4000 DEGREES  
WAVE DIRECTION ANGLE 102.0000 DEGREES  
PLANE VELOCITY 120.8700 METERS/SEC  
DELTA K IS 0.00245385

K	WAVLEN	F(K)	F	DIRMAX	TH1	TH12	TH2	SP1	SP2
0.010	640.	.588E+09	0.310	12.	158.	200.	49.	1.763	1.374
0.020	320.	.506E+09	0.439	83.	145.	82.	51.	1.564	1.585
0.029	213.	.569E+09	0.537	91.	132.	103.	46.	2.092	2.335
0.039	160.	.698E+09	0.620	98.	128.	107.	43.	2.542	3.377
0.049	128.	.526E+09	0.694	126.	134.	111.	45.	2.298	2.844
0.059	107.	.380E+09	0.760	124.	141.	126.	43.	2.495	2.438
0.069	91.	.311E+09	0.821	123.	147.	140.	42.	2.810	2.586
0.079	80.	.248E+09	0.877	159.	151.	149.	39.	3.274	3.169
0.088	71.	.212E+09	0.930	160.	154.	155.	39.	3.259	3.133
0.098	64.	.181E+09	0.981	165.	156.	160.	39.	3.285	3.234
0.108	58.	.161E+09	1.029	164.	156.	158.	40.	3.169	3.156
0.118	53.	.135E+09	1.074	157.	157.	160.	41.	2.998	2.935
0.128	49.	.120E+09	1.118	158.	155.	157.	42.	2.809	2.677
0.137	46.	.111E+09	1.160	157.	156.	158.	41.	2.939	2.878
0.147	43.	.930E+08	1.201	166.	156.	159.	42.	2.801	2.751
0.157	40.	.833E+08	1.241	162.	155.	158.	43.	2.499	2.273
0.167	38.	.752E+08	1.279	156.	157.	162.	44.	2.329	2.072
0.177	36.	.694E+08	1.316	165.	154.	160.	45.	2.245	1.964
0.186	34.	.606E+08	1.352	159.	155.	164.	46.	2.126	1.780
0.196	32.	.541E+08	1.387	159.	156.	164.	46.	2.159	1.800
0.206	30.	.491E+08	1.421	155.	154.	164.	47.	2.005	1.542
0.216	29.	.438E+08	1.455	155.	154.	162.	47.	1.927	1.395
0.226	28.	.387E+08	1.487	154.	155.	167.	48.	1.845	1.283
0.236	27.	.339E+08	1.519	155.	154.	175.	48.	1.803	1.215
0.245	26.	.292E+08	1.551	155.	154.	195.	49.	1.731	1.142
0.255	25.	.265E+08	1.581	154.	153.	198.	49.	1.732	1.107
0.265	24.	.233E+08	1.612	155.	155.	223.	50.	1.646	1.235
0.275	23.	.204E+08	1.641	64.	155.	228.	51.	1.526	1.505
0.285	22.	.175E+08	1.670	79.	150.	65.	50.	1.575	1.401
0.294	21.	.146E+08	1.699	154.	146.	73.	48.	1.795	1.104

FIGURE 26. NUMERICAL LISTING OF THE ONE-DIMENSIONAL SPECTRAL ESTIMATION OF THE X-BAND DATA (FIGURE 24).



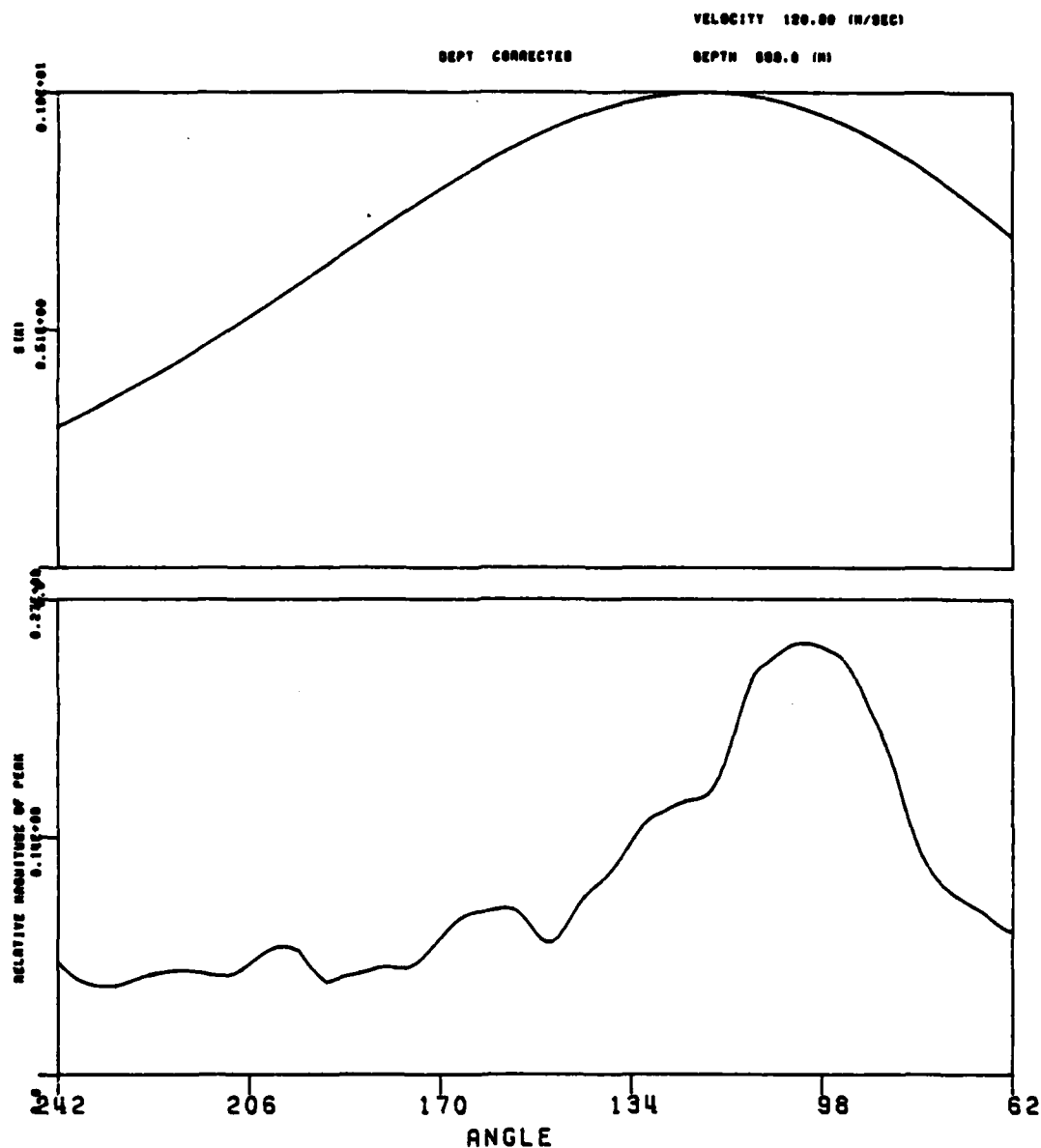


IPL 452 FILE 8 FLIGHT 23 SEPT 78 PASS 3  
L-BAND PAR AREA A1 1000x1500 5M/PIX SQRT 23 JAN 79

DEPTH OF WATER 999.0 METERS  
MAX FREQUENCY DISPLAYABLE 0.2703 HZ  
MAX K VALUE DISPLAYABLE 0.3141  
GROUND TRACK ANGLE 242.4000 DEGREES  
WAVE DIRECTION ANGLE 102.0000 DEGREES  
PLANE VELOCITY 120.8700 METERS/SEC  
DELTA K IS 0.00245385

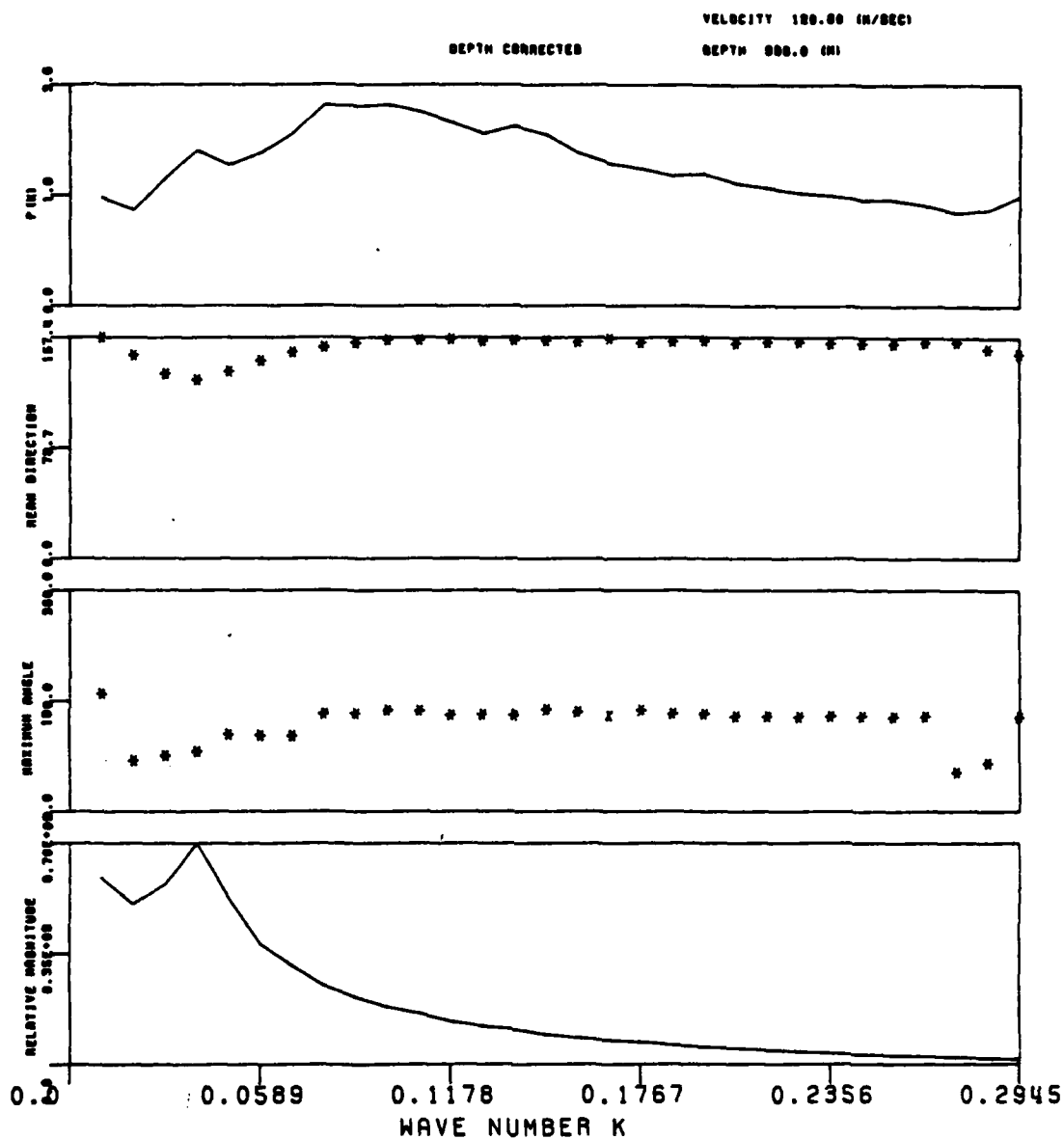
K	WAVLEN	F(K)	F	DIRMAX	TH1	TH12	TH2	SP1	SP2
0.010	640.	.249E+10	0.310	31.	154.	210.	49.	1.736	1.102
0.020	320.	.182E+10	0.439	155.	156.	168.	47.	1.996	1.514
0.029	213.	.151E+10	0.537	92.	142.	109.	48.	1.894	1.664
0.039	160.	.175E+10	0.620	98.	135.	110.	46.	2.146	2.449
0.049	128.	.132E+10	0.694	108.	140.	108.	47.	1.932	2.153
0.059	107.	.959E+09	0.760	129.	145.	120.	47.	2.013	1.749
0.069	91.	.882E+09	0.821	155.	150.	137.	46.	2.153	1.732
0.079	80.	.746E+09	0.877	126.	153.	143.	46.	2.054	1.565
0.088	71.	.662E+09	0.930	159.	150.	144.	47.	1.951	1.397
0.098	64.	.646E+09	0.981	124.	154.	156.	48.	1.905	1.327
0.108	58.	.601E+09	1.029	158.	153.	154.	48.	1.866	1.242
0.118	53.	.565E+09	1.074	51.	155.	183.	49.	1.766	1.188
0.128	49.	.491E+09	1.118	155.	154.	186.	49.	1.724	1.113
0.137	46.	.471E+09	1.160	155.	151.	147.	48.	1.793	1.123
0.147	43.	.435E+09	1.201	48.	153.	223.	50.	1.665	1.142
0.157	40.	.402E+09	1.241	67.	153.	228.	50.	1.610	1.218
0.167	38.	.391E+09	1.279	64.	154.	212.	50.	1.652	1.215
0.177	36.	.364E+09	1.316	40.	157.	199.	49.	1.741	1.234
0.186	34.	.323E+09	1.352	154.	154.	209.	49.	1.708	1.169
0.196	32.	.303E+09	1.387	154.	155.	213.	49.	1.692	1.208
0.206	30.	.274E+09	1.421	156.	154.	205.	49.	1.723	1.132
0.216	29.	.262E+09	1.455	59.	153.	68.	50.	1.622	1.216
0.226	28.	.237E+09	1.487	59.	153.	64.	51.	1.567	1.319
0.236	27.	.208E+09	1.519	65.	153.	238.	51.	1.571	1.342
0.245	26.	.191E+09	1.551	64.	153.	230.	50.	1.633	1.253
0.255	25.	.167E+09	1.581	64.	153.	235.	50.	1.594	1.322
0.265	24.	.145E+09	1.612	63.	153.	235.	51.	1.543	1.407
0.275	23.	.130E+09	1.641	63.	154.	231.	50.	1.590	1.327
0.285	22.	.113E+09	1.670	63.	152.	217.	49.	1.696	1.172
0.294	21.	.976E+08	1.699	66.	145.	121.	48.	1.865	1.095

FIGURE 27. NUMERICAL LISTING OF THE ONE-DIMENSIONAL SPECTRAL ESTIMATION OF THE L-BAND DATA (FIGURE 25).



IPL 452 FILE 7 FLIGHT 23SEPT78 PASS 6 X-BAND PAR  
AREA A1 1000X1500 SM/PIX SQRT 19JAN79  
SPREAD FUNCTION AT K = 0.039

FIGURE 28. PLOTS OF ENERGY SPREAD AND FUNCTION  $G(k)$ .



IPL 452 FILE 7 FLIGHT 23SEPT78 PASS 6 X-BAND PAR  
AREA A1 1000X1500 5M/PIX SQRT 19JAN79

FIGURE 29. COSINE SPREADING FUNCTION, AVERAGE DIRECTION,  
MAXIMUM ANGLE, AND ONE-DIMENSIONAL PLOTS.

## WAVE HEIGHT DETERMINATION FROM SYNTHETIC APERTURE RADAR

This section explores the question of wave height determination using SAR. The past year's effort has looked extensively at a technique reported by Jain (1977) that obtains wave height information from SAR data (see Appendix B). ERIM's work in this research area has included attempts to experimentally verify Jain's results as well as present some further consideration of the underlying theory developed in Jain's paper.

In the following discussion, a review of the basic experimental technique outlined by Jain is given and terminology is defined. This is followed by a discussion of the theoretical development of Jain's techniques. In particular, ERIM examines some of the problems with Jain's theory and the errors and inconsistencies which are apparent in Jain (1977). An alternate theory is then presented which implies results which are the opposite of Jain's. Finally, a description of our own experimental results, including some of the problems ERIM encountered, is presented.

## 7.1 REVIEW OF JAIN'S ALGORITHM

The experimental procedure begins by optically processing a patch of sea imagery. As indicated in Figure 30, the frequency plane aperture of the optical processor is adjusted to pass a bandwidth  $W$  from the radar chirp spectrum. The next step is to reprocess the same patch of imagery using the same bandwidth  $W$  but with the aperture moved a distance,  $\Delta f$ , which is a fractional part of  $W$ , i.e., the center frequency is changed by  $\Delta f$ . This pair of images is then cross correlated.

Jain's theory gives a detailed description of the optical correlation strength as a function of the quantities  $\Delta f$ ,  $W$  and a third parameter,  $\sigma_H$ , which describes the sea state.  $\sigma_H$  is the

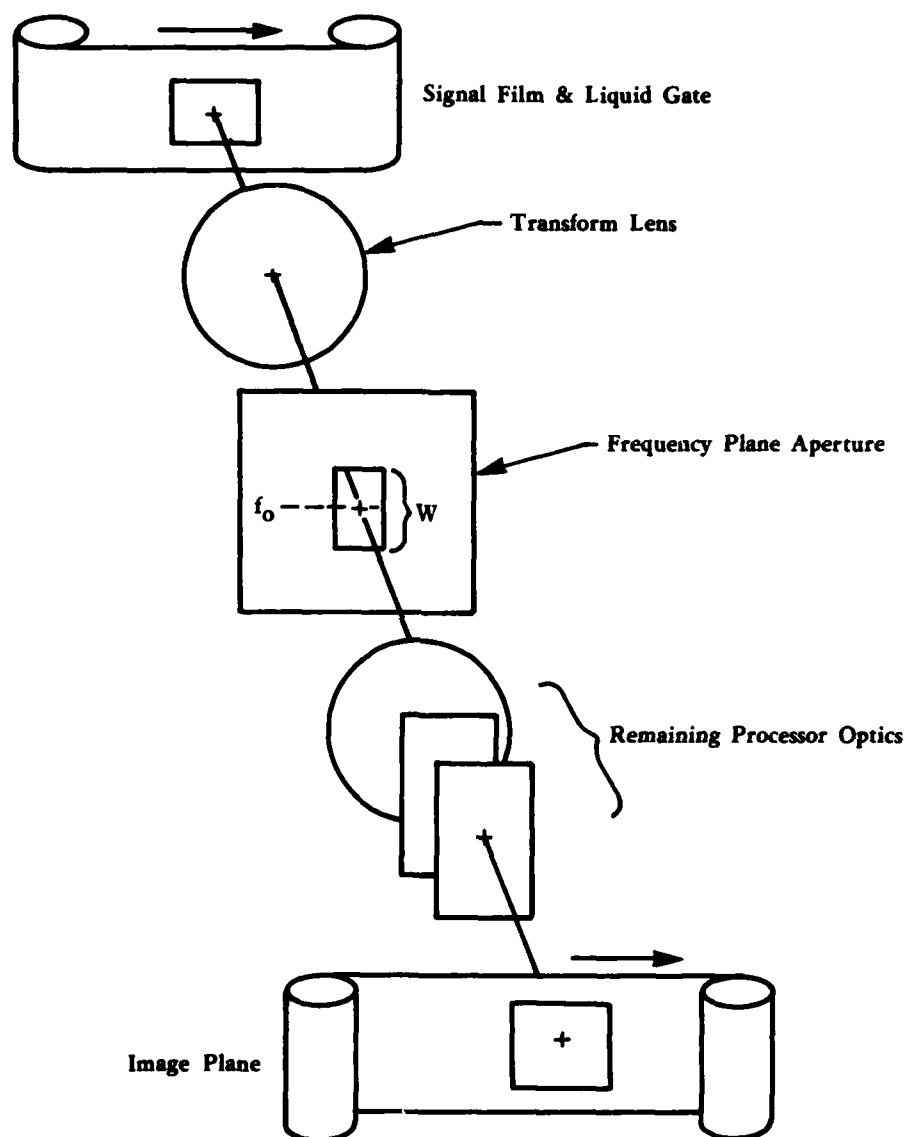


FIGURE 30. SAR OPTICAL PROCESSOR.

standard deviation of the distribution of wave heights, i.e., the rms wave height. The details of this theory are discussed in Section 7.2. It is sufficient here to say that the correlation strength between the two elements of the image pair is a decreasing function of both  $\Delta f$  and  $\sigma_H$ .

Suppose we have SAR data collected over two different sea states, and we process a pair of images for each sea state, identically as described above. In particular, the same  $\Delta f$  and bandwidth are used for each of the two pairs. Any difference in correlation strength between these two pairs will then be due to the difference in wave height. In particular, the image pair with the larger  $\sigma_H$  would produce less correlation. An observable difference in the correlation strength can be used as a simple test of Jain's theory and its practicality. Actually, as a technique for the measurement of  $\sigma_H$ , we would require more than just an observable difference, namely, the measurement of the absolute correlation strength and the detailed knowledge of its functional form provided by the theory. The methods for measuring the correlation of a pair of images will be discussed in Section 7.3.

## 7.2 EVALUATION OF JAIN'S THEORY

Jain's theory and algorithm for obtaining wave height is based upon speckle correlation techniques. Before discussing the theory developed in Jain's paper for the SAR case, it is desirable to first discuss his general technique as it applies to other applications which are well founded and experimentally verified by numerous authors.

### 7.2.1 SPECKLE CORRELATION TECHNIQUES FOR MEASUREMENT OF SURFACE ROUGHNESS

Our discussion will be qualitative and is meant only to provide the motivation behind the results of this theory. In Figure 31, we

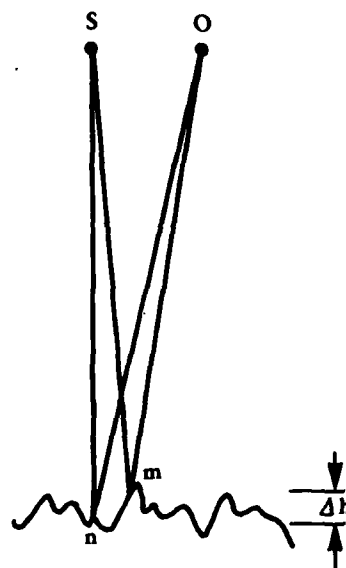


FIGURE 31. NORMAL GEOMETRY FOR SPECKLE CORRELATION.

illustrate coherent radiation from a source at  $S_{cr}$  falling on a small area of a rough scattering surface. We are interested in the far field at some observation point labeled 0 in the figure. Note in the figure that  $S_{cr}$  and 0 are near normal to the surface, although this is not an absolute requirement. The phase  $\phi_m$  at 0 of the wavelet scattered from point m on the surface is given by the total path length from the source to the observation point:

$$\begin{aligned}\phi_m &= \frac{2}{\lambda} [\overline{Sm} + \overline{m0}] \\ &= k [\overline{Sm} + \overline{m0}],\end{aligned}\tag{38}$$

where  $\lambda$  is the wavelength and  $k$  the wave number of the illumination. The net amplitude at the observation point is the coherent sum of the wavelets from all such scattering points within the illuminated area.

$$A = \sum_m a_m e^{j\phi_m}\tag{39}$$

and the intensity  $I$  at this point is  $AA^*$ , which is easily shown to be

$$I = \sum_{m,n} a_m a_n e^{j\Delta\phi_{mn}},\tag{40}$$

where  $\Delta\phi_{mn} = \phi_m - \phi_n$ .

For this geometry (in the far field), the phase difference between scattering points is determined mainly by the difference in the height of the scattering points. Thus,

$$\begin{aligned}\Delta\phi_{mn} &= 2k(h_m - h_n) \\ &= 2k\Delta h_{mn}\end{aligned}\tag{41}$$

A speckle pattern will exist in the region around the point 0. This is the result of random interference effects of the phases



$\Delta\phi_{mn}$ . The sum in Eq. (40) will destructively interfere in some places and the interference will be constructive in other places.

We now consider what will happen if we make a small change in the illumination wavelength  $\lambda$ , or equivalently the wave number  $k$ . We let  $k' = k + \Delta k$ . The phases  $\Delta\phi_{mn}$  in Eq. (41) becomes

$$\Delta\phi'_{mn} = \Delta\phi_{mn} + 2\Delta k \Delta h_{mn} \quad (42)$$

If  $\Delta k$  is small so that  $2\Delta k \Delta h \ll 2\pi$ , then the sum in Eq. (41) will be unaffected. If the sum in Eq. (41) represented a bright or dark region in the speckle pattern, then it will continue to do so, and the new speckle pattern will therefore have a high degree of correlation with the old one. Clearly, for the two speckle patterns to become uncorrelated, the product  $2\Delta k \Delta h$  must become some significant part of  $2\pi$ . The result of a detailed analysis which is given by many authors and confirmed by experiment (Parry, 1974; George and Jain, 1974) is that

$$\Delta k \sigma \sim 1 \text{ (radian)} \quad \text{or} \quad \Delta k \sim \frac{1}{\sigma}, \quad (43)$$

where  $\sigma$  is the rms value of  $\Delta h_{mn}$ . Thus, we can measure the surface roughness as defined by  $\sigma$ , by measuring the amount of change  $\Delta k$  in the illumination which is required to produce decorrelated speckle patterns. The results of detailed analysis further show that the degree of correlation  $R(\Delta k)$  between the speckle patterns is equal to the square of the characteristic function  $\eta_H$  of the surface height fluctuations (George and Jain, 1974; Goodman, 1963). This characteristic function is the Fourier transform of the probability density function of surface height:

$$R(\Delta k) = \eta_H^2 \quad (44)$$

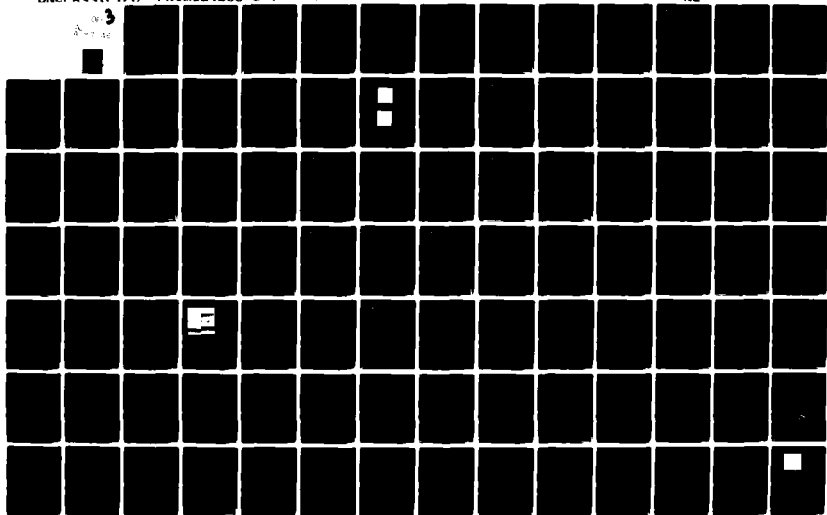
$$\eta_H = \text{F.T.}\{p(h)\} \quad (45)$$

AD-A097 946

ENVIRONMENTAL RESEARCH INST OF MICHIGAN ANN ARBOR RA--ETC F/6 17/9  
IMAGING OCEAN WAVES WITH SAR, A SAR OCEAN WAVE ALGORITHM DEVELO--ETC(U)  
DEC 79 R A SHUCHMAN, K H KNORR, J C DWYER N00014-76-C-1048  
FRIM124300-5-T NL

UNCI ASCTETFD

3  
A-7-10



### 7.2.2 JAIN'S THEORY

Jain's theory for the SAR case indicates that the correlation strength  $R(\Delta k)$ , is the square of the product of the radar range pupil function (defined below) and the characteristic function of the sea surface height distribution. This result has obvious similarity to the result just described in Section 7.2.1. Apparently, the SAR case only involves an additional dependence on the radar pupil function. The functional form of  $R(\Delta k)$  and the radar pupil function will be discussed more fully below. First, however, we will make a few general comments about the derivation of this result.

Apparently Jain's paper was not reviewed carefully before it was published. When one attempts to follow Jain's derivation, numerous errors and inconsistencies become obvious. These errors and inconsistencies are so serious as to prevent an unambiguous interpretation of the final results. Jain's derivation is, at best, very difficult to follow. We will look in detail at some of the errors and inconsistencies in Jain's paper. We will skip the errors which occur in the body of the derivation and concentrate on the final results. The significant results in Jain's paper are contained in Equations 9a, b and c (see page 377 of Jain's paper which is included as Appendix B of this report) and the discussion of the experimental results.

From careful examination of Jain's paper, there is apparently a factor of 2 missing from the last term in Eq. (9a) since Eq. (9b) cannot be obtained from (9a) by the operations indicated. The standard deviation of wave height,  $\sigma_H$ , in Eq. (9b) is misplaced. This term should be included in the argument of the characteristic function,  $\eta_H$ . Equation 9b of Jain's should thus read

$$R(\Delta f) = \eta_H^2\left(\frac{2\Delta f}{c\sigma_H}\right) \Gamma_r^2(\Delta f) \quad (46)$$

If one considers the processor range pupil function,  $\Gamma_r(\Delta f)$ , it is observed that this is a function which is proportional to the radar

chirp spectral intensity within the bandwidth  $W$  of the optical processor and zero outside this bandwidth. This function is thus approximately just the range aperture function used in the frequency plane of the processor. Jain defines this function on p. 375 as a rect function. The rect function is an appropriate approximation for this function, though Jain makes an error in the argument of this function as it occurs on p. 375.

The range pupil function  $\Gamma_r(\Delta f)$  makes no sense as a factor in Eq. (9b). To understand why, consider the case of  $\sigma_H \sim 0$ . Then  $\eta_H \cong 1$  and the correlation.  $R(\Delta f)$  is just the square of this pupil function. This leads to a correlation function which is essentially constant out to some  $\Delta f$ , at which point the correlation abruptly becomes 0. This behavior does not even remotely resemble the experimental data. On p. 381, while discussing experimental results, Jain describes quite a different behavior for  $\Gamma_r(\Delta f)$ ; for  $W = 2$  MHz and  $\Delta f = 1/2$  MHz, Jain indicates that  $\Gamma_r(\Delta f)$  should be about 0.65 and, for  $\Delta f = 1$  MHz,  $\Gamma_r(\Delta f)$  should be about 0.29. Since Jain states that these are close to the theoretical values, this leads one to speculate that perhaps Jain does not really intend the pupil function. Perhaps Jain intended the cross correlation squared of the pupil functions rather than the pupil function itself. This function would better fit the experimental results. Thus, in Eq. (46),  $\Gamma_r(\Delta f)$  should perhaps be replaced by

$$\left[ \int \Gamma_r(f) \Gamma_r(f + \Delta f) df \right]^2 \quad (47)$$

where

$$\Gamma_r(f) = \text{rect} \left( \frac{f - f_0}{W} \right)$$

Physically, this is just the area of overlap squared of the two frequency-plane apertures used to process the image pairs. For the rectangular functions used, this factor just becomes

$$\left(1 - \frac{\Delta f}{W}\right)^2$$

For the examples given by Jain, this function takes value of 0.56 and 0.25, which are closer to the values quoted to fit the experimental data. This ambiguity is summarized in Figure 32. We can only speculate as to whether Jain actually meant the pupil function or something else.

Additionally, on page 377, Jain indicates that the characteristic function  $\eta_H$  in Eq. (46) is given by

$$\eta_H = \exp \left\{ -\frac{1}{2} [4\pi(\Delta f/c)\sigma_H]^2 \right\}. \quad (48)$$

This is indeed the characteristic function for a Gaussian distribution of wave heights. Thus, Eq. (46) becomes

$$R(\Delta f) \propto \exp \left\{ -\frac{16\pi^2 \Delta f^2}{c^2} \sigma_H^2 \right\}. \quad (49)$$

Yet, on page 381 (for comparison with his experimental results), Jain evaluates instead

$$R(\Delta f) \propto \exp \left\{ -\frac{16\pi\Delta f}{c} \sigma_H \right\}. \quad (50)$$

As already mentioned, Eq. (49) above is the correct functional form. Evaluating this for  $\sigma_H = 4$  mrad and  $\Delta f = 0.5$  MHz yields 0.993. Thus, his theory, as given in Eq. (9b), predicts only a 0.7 drop in correlation strength for  $\sigma_H = 4$  m compared to  $\sigma_H \sim 0$  at  $\Delta f = 0.5$  MHz. At  $f = 1$  MHz, a 3% drop is predicted. Neither of these would be observable.

In summary, we can say that Jain does not fully document the derivation of the theory he presents. The derivation is difficult or possibly impossible to follow and contains many errors. The final result, as presented does not fit or even resemble the experimental data. Jain makes undocumented changes in his theory when comparing

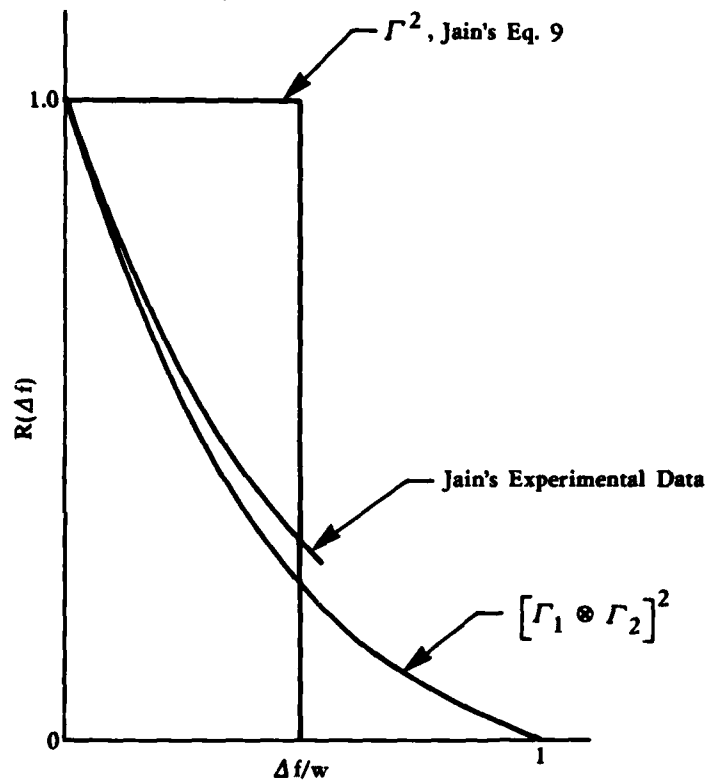


FIGURE 32. ILLUSTRATION OF AN INCONSISTENCY IN JAIN'S RESULT.

it with his experimental results. This leads, at best, to some ambiguity in the interpretation of his results.

### 7.2.3 AN ALTERNATE THEORY

An independent look at the speckle correlation technique as it should apply to SAR imagery was undertaken. A very simplified and idealized model was considered which is just sufficient to convey the essential physics involved.

Consider an array of ideal point scatterers located at distances  $r_m$  from a radar antenna, as shown in Figure 33. An idealized image of this array is indicated in Figure 34. Figure 34 represents a good approximation of actual imagery, if the resolution of the system is much finer than the separation between the points. The individual points are approximated by delta functions  $\delta(r - r_m)$ . The phase of each point in the image is proportional to the range  $r_m$  between the antenna and the scatterer.

More generally, the amplitude at the output of a SAR image processor is a convolution between the idealized output we have thus far described and the system impulse response. For simplicity, we will consider an impulse response which is described by a rect function whose width is equal to the resolution  $\rho$ . We have illustrated the mechanics of this convolution for a case where the individual scatterers are not resolved in Figure 35. Thus, the amplitude at  $r$  in the output of the processor is given by

$$\begin{aligned} A(r) &= \int \text{rect} \frac{r' - r}{\rho} \sum_m a_m \delta(r' - r_m) e^{j\phi_m} dr' \\ &= \sum_m a_m e^{j\phi_m}, \end{aligned} \quad (51)$$

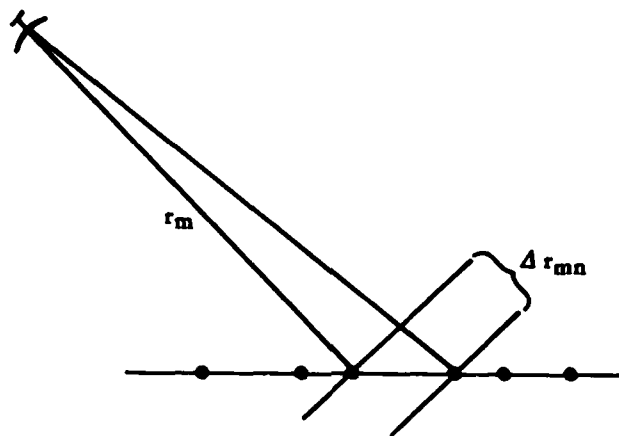


FIGURE 33. RADAR GEOMETRY.



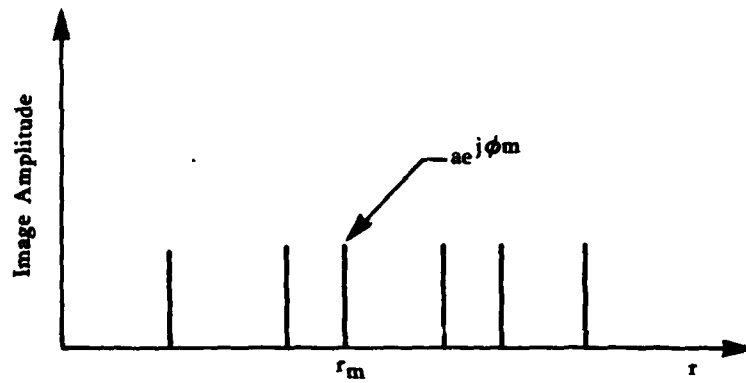


FIGURE 34. RADAR IMAGE APPROXIMATION FOR RESOLVED SCATTERERS.

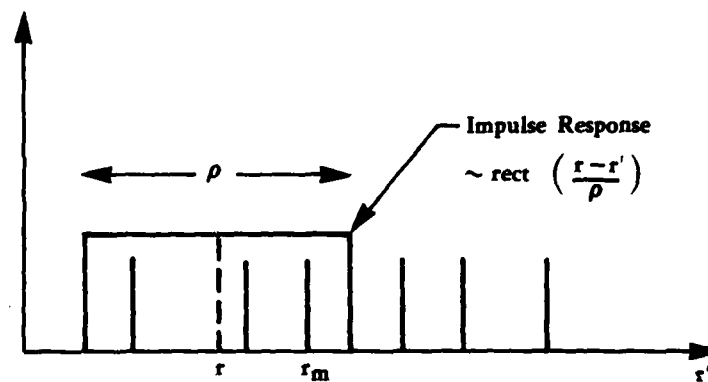


FIGURE 35. RADAR IMAGE APPROXIMATION FOR UNRESOLVED SCATTERERS.

where  $\sum_m^{\rho}$  is intended to mean a summation over  $m$  for which  $r - r_m = 2$ . The intensity is then given by

$$I(r) = \sum_{m,n}^{\rho} a_m a_n e^{j\Delta\phi_{mn}} \quad (52)$$

where

$$\begin{aligned} \Delta\phi_{mn} &= \phi_m - \phi_n \\ &= \frac{2\pi}{\lambda} 2(r_m - r_n) \\ &= 2k\Delta r_{mn} \end{aligned} \quad (53)$$

In Eq. (53),  $k$  or  $\lambda$  refers to the radar center frequency of the chirp spectrum which is processed. The similarity between Eqs. (52) and (40) is easily seen. The similarity between Eqs. (53) and (41) is likewise apparent; here  $\Delta h$ , which symbolized the surface roughness, has been replaced by  $\Delta r$ , the differential radar range between scatterers. The SAR image is analogous to a speckle pattern from a surface whose effective roughness is proportional to the resolution of the image itself and not the actual roughness of the surface. The results outlined in Section 7.2.1 can be used to determine the change in center frequency required to decorrelate two SAR image speckle patterns. Recall that

$$\Delta k \sim \frac{1}{\sigma} \quad (43)$$

is required. For the radar case,  $\sigma$  is the rms value of  $\Delta r$ , which is approximately  $\rho/2$ . Also recalling that for SAR

$$\rho = \frac{c}{2W}, \quad (54)$$

we obtain

$$\Delta k \sim \frac{4W}{c} \quad (55)$$

or, since  $\Delta k = 2\pi\Delta f/c$ ,

$$\Delta f \sim \frac{2}{3} W. \quad (56)$$

Thus, it is relatively easy to show that a change in the processed center frequency which is less than the processing bandwidth is sufficient to decorrelate the image speckle patterns; equivalently, there will be no correlation for  $\Delta f \geq W$ .

One can further consider the SAR case of a non-flat surface imaged at a fairly steep depression angle. This is reasonable since the SEASAT and other sea imaging radars use this condition.

A model is created in which the radar point scatterers are uniformly distributed along a surface which has gross height fluctuations. This model is consistent with experimental observations of wave imagery (Shuchman, et al., 1978). In particular, the scatterers are thought to be the small wind induced capillary waves riding on the larger gravity waves. Our model and the development of our argument are summarized in Figure 36. In this figure, we consider a comparison between a flat and a non-flat sea surface. Jain's primary results are for the case when the gross wave structure is not resolved. We therefore also consider this case; the resolution  $\rho$  has been made to correspond with the wave crest to crest distance. We have assumed a very special model for the shape of the sea surface as indicated in Figure 36. This model is used only to make a simplified geometric argument possible. It will become clear, however, that rigorous arguments for arbitrary surface shapes would yield the same conclusions.

It should be clear that the maximum phase difference  $\Delta\phi_{\max}$  is just equal to the range resolution interval  $2k\rho$ , and is entirely independent of the surface height fluctuations. Thus, we must look

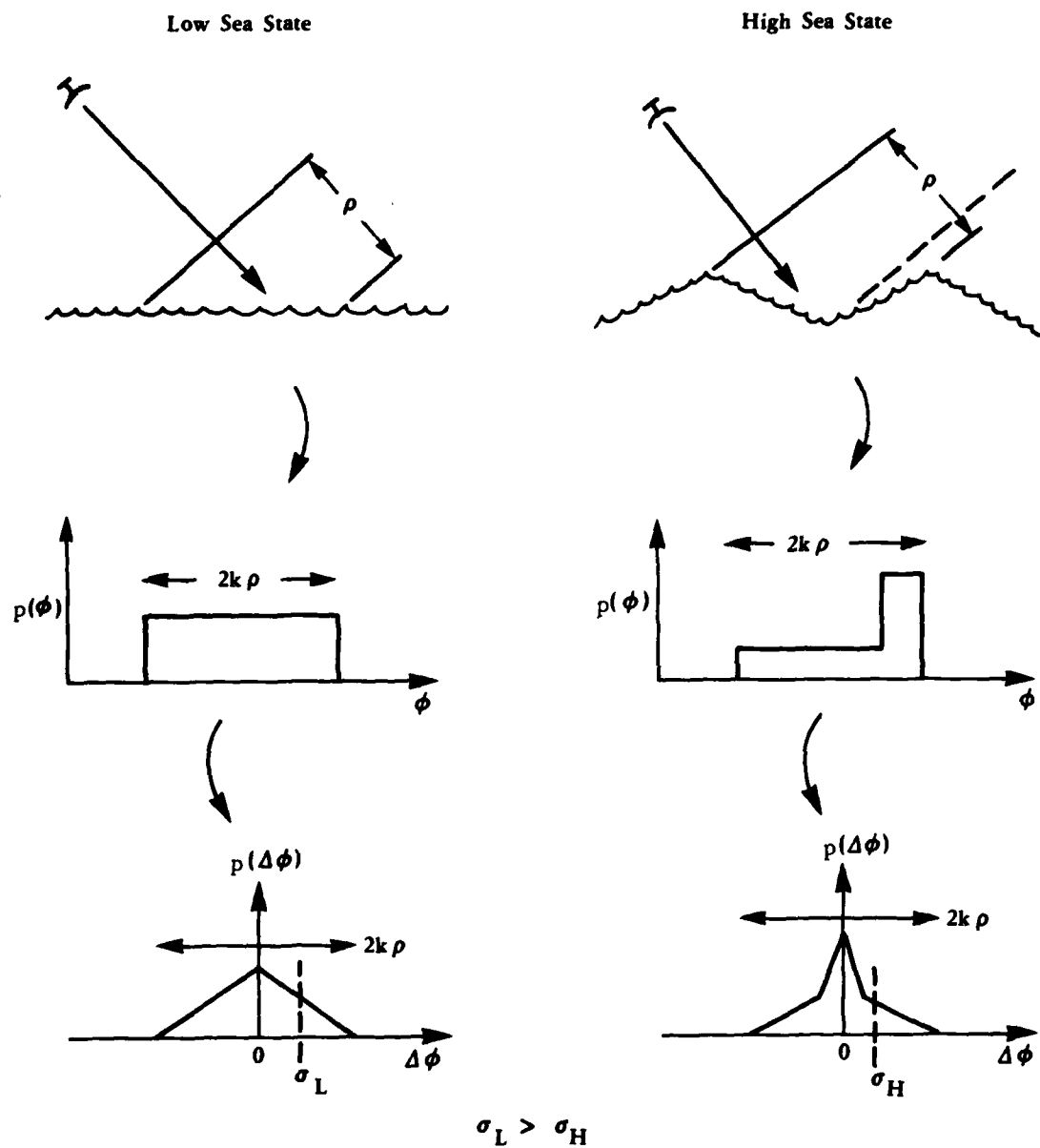


FIGURE 36. ILLUSTRATION OF HOW A HIGH SEA STATE PRODUCES A SMALLER rms  $\Delta\phi$ .

for the effects of the surface height fluctuations on the detailed statistical distribution of the phases  $\Delta\phi$  which occur in Eq. (52).

We first consider the probability density function  $p(\phi)$ , for the phase  $\phi$  to occur in the summation (51). For the flat surface, since the scatterers are uniformly distributed along the surface,  $p(\phi)$  will be a constant inside an interval of length  $2k\rho$  and zero outside this interval, as illustrated in Figure 36. For the non-flat surface, the interval  $2k\rho$  will be broken up into two subintervals of unequal length, as indicated. The distribution is uniform within each subinterval. Both subintervals have the same number of scatterers, but since their lengths are unequal, the density function will be unequal, as illustrated.

The probability density function for the phase differences  $\Delta\phi$  which occur in Eq. (52) is given by

$$p(\Delta\phi) = \int p(\phi + \Delta\phi)p(\phi) d\phi. \quad (57)$$

This is just the autocorrelation of  $p(\phi)$ . This function is indicated at the bottom of Figure 36 for the flat and non-flat sea surfaces. Note that  $p(\Delta\phi)$  is more concentrated at small values of  $\Delta\phi$  for the non-flat surface. The rms value of  $\Delta\phi$  is the square root of the second moment of these distributions. Due to the shape of these curves,  $\Delta\phi_{\text{rms}}$  will actually be smaller for the high sea state. We can let  $\sigma = \Delta\phi_{\text{rms}}/2k$ . The change  $\Delta k$  in wavenumber (or center frequency) required to decorrelate the image, as given by  $1/\sigma$ , is thus larger for the high sea state. This is the opposite of Jain's result.

Some further thought makes it clear that any surface departure from a flat condition will produce the same conclusion. In general, a disturbance of the sea surface from a flat condition produces a non-uniform clumping of scatterers which in turn produces a non-flat distribution of phases  $p(\phi)$ . This, in turn, causes the autocorrelation function,  $p(\Delta\phi)$ , to depart from its triangular form

and to be more sharply peaked near small values of  $\Delta\phi$ . This results in a smaller effective roughness  $\sigma$ . For a given change  $\Delta k$  in center frequency, we would therefore expect the higher sea state to produce a stronger correlation.

In addition, we would expect an amplitude disparity between the scatterers in the two subintervals of the resolution element. We normally expect the scattering coefficient  $\sigma_0$  to be larger for the subinterval which is more normal to the radar illumination. Thus, this effect will enhance the results which, we have thus far concluded, should occur.

What we have given is the outline of a theory which gives only qualitative predictions. Quantitative predictions are beyond the scope of such a simple theoretical outline. It should be emphasized however that we are talking about subtle effects which may not be measurable in a practical sense.

### 7.3 EXPERIMENTAL RESULTS

Three attempts were made to experimentally verify Jain's theory and results. However, there is no hint of a confirmation of Jain's theory in our results. Before discussing these results in further detail, we will discuss the experimental procedures involved.

#### 7.3.1 EXPERIMENTAL PROCEDURES

Our data source was ERIM's dual frequency (X-L) band radar. We chose the X-band parallel-polarized channel of this radar which has in excess of 50 MHz of useful bandwidth. Also, we chose data collected over three sea states (Table 8). Wave heights were estimated at 0.8 to 1.0 m, 2.5 to 2.7 m, and 2.0 to 2.5 m by various sea-truth measurements. Two of these flights occurred within 1 day of one another, while the third occurred a little less than a month later.

TABLE 8  
SUMMARY OF EXPERIMENTAL CONDITIONS

<u>Flight Date</u>	<u>Pass</u>	<u>Reported Wave Height</u>	<u>Polarization</u>	<u>Center Frequency</u>
18 Oct 78	4	0.8-1.0 m	HH	9.3 GHz
22 Sept 78	5	2.5-2.7 m	HH	9.3 GHz
23 Sept 78	4	2.0-2.5 m	HH	9.3 GHz

This Data Was Processed at

<u>Bandwidth</u>	<u>Frequency Difference between Pairs</u>
<u>W (MHz)</u>	<u><math>\Delta f</math> (MHz)</u>
2	0, 1/2, 1, 2
10	0, 5, 10
13	0, 6

Our goal was to measure the degree of correlation in the speckle intensity patterns of a pair of radar images, as defined by the equation

$$R(\Delta f) = \frac{\langle I_0 I_1 \rangle - \langle I_0 \rangle \langle I_1 \rangle}{\langle I_0^2 \rangle - \langle I_0 \rangle^2} \quad (58)$$

where  $I_0 = I_0(x, y)$  is the image intensity pattern obtained from the processor for some initial setting of the frequency plane aperture,

$I_1 = I_1(x, y)$  is the corresponding image obtained after moving the frequency plane aperture by  $\Delta f$ ,

and the brackets  $\langle \rangle$  denote a spatial average over the azimuth and range coordinates  $(x, y)$  of the image:

$$\langle I \rangle = \frac{1}{A} \int_A I(x, y) \, dx \, dy \quad (59)$$

The correlation  $R(\Delta f)$  is obtained experimentally by analog methods, in which the first step is a highly nonlinear recording of the image intensity patterns  $I(x, y)$  on photographic film. The intensity pattern is transformed into a transmittance pattern:

$$I(x, y) \rightarrow T(x, y),$$

Where  $T(x, y)$  is the intensity transmittance of the film. A duplicate positive may or may not then be made for use in the correlator. Both of these steps, because of their nonlinearity, could have significant impact on the final results. It is not known whether Jain used positive or negative transparencies. We used negatives, for which large values of  $I$  become small values of  $T$ .

Jain obtained his correlation in a relatively straightforward manner. He imaged the first transparency onto the second, thereby obtaining the product  $T_0 T_1$ . He then integrated the transmitted



light over the spatial dimensions  $x$  and  $y$  to obtain  $\langle T_0 T_1 \rangle$ . He measured  $\langle T_0 T_1 \rangle$  by misaligning the two patterns by a large enough distance to decorrelate them, i.e., he used the approximate result

$$\langle T_0(x, y) T_1(x + \Delta x, y + \Delta y) \rangle = \langle T_0 \rangle \langle T_1 \rangle \quad (60)$$

for  $\Delta x, \Delta y \gg$  speckle size

Although Jain's method for measuring  $R(\Delta f)$  is straightforward, it nevertheless requires an extremely high degree of precision. For example, the correlation coefficient,  $\langle T_0 T_1 \rangle$ , is a very sharply peaked function for small  $\Delta x$  and  $\Delta y$ . This coefficient goes from its initial high level to an essentially uncorrelated level within the span of  $\Delta x$  or  $\Delta y$  equal to the speckle size. Thus, to obtain  $\langle T_0 T_1 \rangle$  requires a mechanical micropositioner to align the two transmittance functions rotationally as well as in range and azimuth within tolerances of a small fraction of the speckle size. This also requires that the optical system which images  $T_0$  onto  $T_1$  be of unity magnification and have low distortion within these same tolerances. It should be remembered that we are trying to measure very subtle differences in correlation strength.

In order to mitigate some of these requirements and also save time, we used another (perhaps more elegant) method for obtaining the correlations. Our method is summarized in Figure 37. We first arrange the pair of frames into a composite frame as indicated in the figure. The composite frame has a transmittance function which is the sum of the two individual frames:

$$T_c(x, y) = T_0(x, y) + T_1(x, y - d_0) \quad (61)$$

One of the advantages of our technique is that, as will become clear, the  $x$  and  $y$  positioning of the frames in the composite is not critical. Thus, the precise value of  $d_0$  is not critical, nor is it critical that there is no displacement of the frames in the  $x$

dimension, as indicated in Eq. (61). Parallel alignment of the frames is critical however. The composite frame is inserted in the liquid gate of an optical Fourier-transform processor, as indicated in Figure 37. The power spectrum of the composite frame is recorded on film at the transform plane of the processor.

Another advantage of our method for obtaining the correlation is that the d.c., which represents the bias term of the transmittance is easily removed at this time by placing a mechanical stop in the transform plane. We thus record the power spectrum of the transmittance function  $t_c(x, y)$ , where

$$t_c(x, y) = T_c(x, y) - t_b \quad (62)$$

and where

$$t_b = \langle T_c \rangle. \quad (63)$$

One of the disadvantages of our method is the introduction of another nonlinear recording step. We performed some experiments to maximize the linearity of this step. We also maintained constant exposure levels and recorded all of the power spectra on a single roll of film. Thus, the effect of this nonlinearity should be very nearly a constant, which can be ignored in this feasibility test.

The power spectrum of the composite frame is inserted in the optical processor (the original composite frame having been removed) and its Fourier transform taken. The Fourier transform of a power spectrum is known to be equal to the autocorrelation function. We thus readily obtain the autocorrelation function of the original composite frame. We actually measure the intensity or the square of the Fourier transform. Thus, the intensity as a function of the transform plane coordinates,  $u$  and  $v$ , is represented by

$$I(u, v) = \langle t_c(x, y) t_c(x + u, y + v) \rangle^2. \quad (64)$$

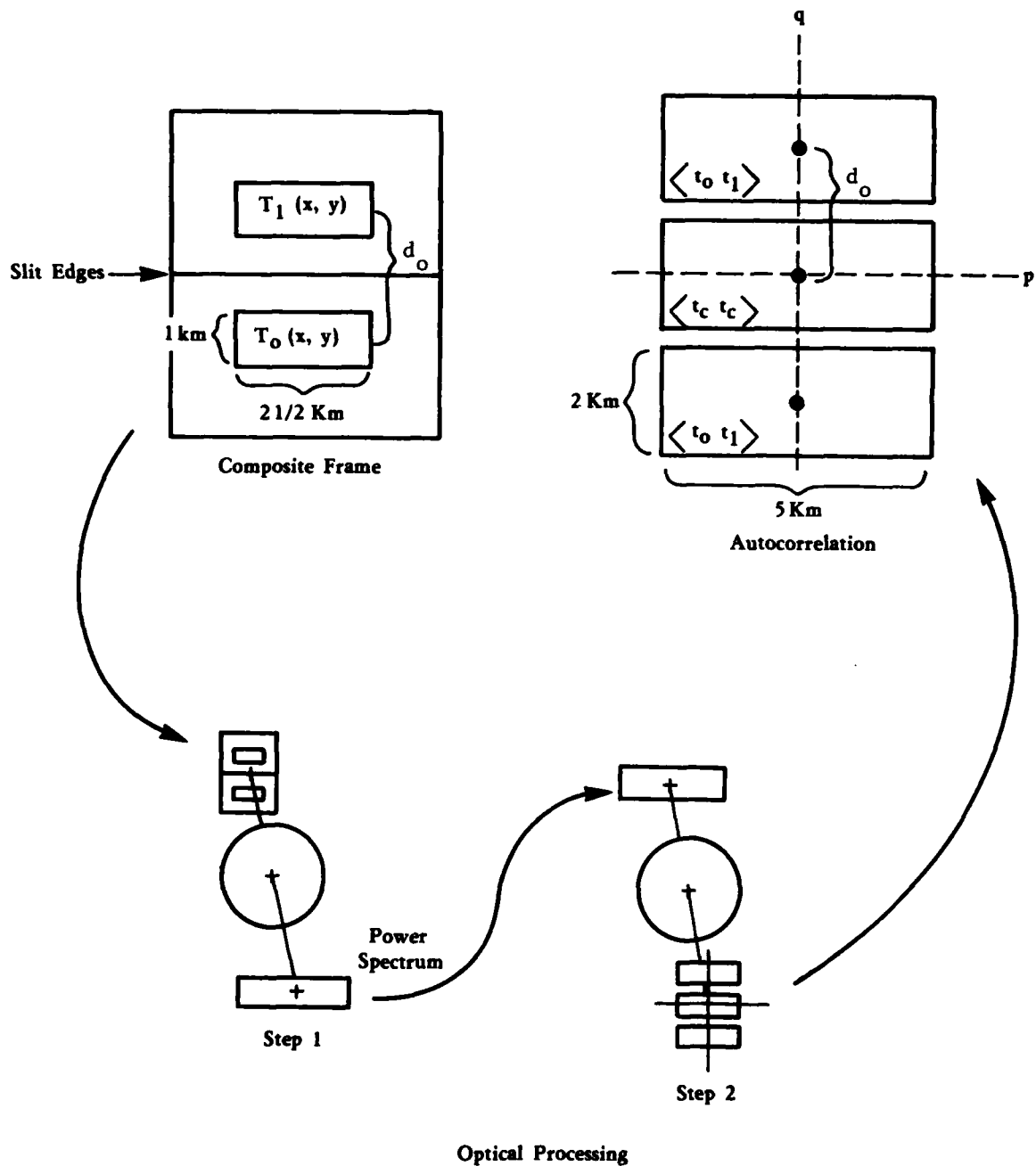


FIGURE 37. METHOD FOR OBTAINING THE CROSS CORRELATION OF A PAIR OF FRAMES.

The desired cross correlation of the pair of frames occurs as a part of this autocorrelation:

$$\sqrt{I(0, d_0)} = \langle t_0(x, y) t_1(x, y) \rangle. \quad (65)$$

In this process, we have made  $d_0$  large enough so that there is no overlap between the various parts of the autocorrelation function.

Figure 38 is a photograph of  $I(u, v)$  obtained from this process. Near d.c., which is blocked, we have the autocorrelation of the entire composite frame against itself (corresponding to small values of  $u$  and  $v$ ). At the distance  $d_0$  from d.c., corresponding to the displacement between the pair of frames, the desired cross correlation peak of the pair of frames is visible. For values of  $u$  near zero and  $v$  near  $v_0$ , we see the low level (uncorrelated) cross correlation between the pair of frames. Figure 38b is an enlargement of a circular region of  $I(u, v)$  centered at  $(0, v_0)$ . Note the very sharp rise and fall of the intensity of the cross correlation peak.

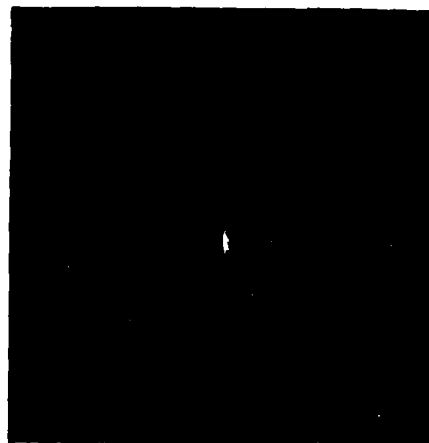
We measured the energy in the mainlobe of the correlation peak and also the energy in the circular region surrounding this peak as indicated in Figure 38b. We divided the energy in this correlation peak by the energy in the surrounding low level cross correlation. This served to remove any laser power fluctuations or photographic variations in the recording of the power spectra. For example, one of the power spectra was apparently blurred by some motion during its exposure. Both the correlation peak and the surrounding cross correlation were reduced by 10 dB. Yet, their ratio remained a constant as verified by measurements of this ratio from a second exposure. Typically, the absolute values of these power levels were quite constant.

The value thus obtained represents an unnormalized correlation coefficient between the two frames:



← Cross Correlation  
Peak  
d<sub>o</sub>  
← D.C.

(a) Entire Correlation Function



(b) Enlargement of the Region  
Near the Cross Correlation  
Peak

FIGURE 38. PHOTOGRAPHS OF COMPOSITE FRAME CORRELATION FUNCTION.

$$\begin{aligned}\langle t_0 t_1 \rangle &= \langle (T_0 - t_b)(t_1 - t_b) \rangle \\ &= \langle T_0 T_1 \rangle - \langle T_0 \rangle \langle T_1 \rangle\end{aligned}\quad (66)$$

To normalize this and obtain  $R(\Delta f)$  as defined in Eq. (58), it was necessary to form a composite frame of two identical recordings of  $T_0$ . Then, we carried out the remaining operations to obtain  $t_0 t_0$  and divided to obtain  $R(\Delta f)$ :

$$R(\Delta f) = \frac{\langle t_0 t_1 \rangle}{\langle t_0^2 \rangle} \quad (67)$$

However, we can also use the unnormalized correlation given by Eq. (66) above. The advantage of this is that it does not allow additional possible experimental errors due to measurements from a second pair of frames. This corresponds to a normalization with respect to the lowest level of correlation possible instead of the highest level of correlation possible.

### 7.3.2 FIRST SET OF EXPERIMENTAL DATA

For the first two experiments, we processed the pairs of frames in a normal tracking processor. We restricted the frames to about 1 km from the center of the slant-range swath in order to avoid any effects of slant-range distortion. In the azimuth direction, we used 2 1/2 km. After processing all of the required frames, we put the film through a precision slit. This slitting operation allowed us to arrange the pairs of frames into a composite frame, as shown in Figure 37. We were able to choose an approximate value of  $q_0$  which was large enough to prevent overlap of the various parts of the composite frame autocorrelation function, while at the same time not so large as to impose undue burdens on the liquid gate and transform-lens aperture. The slit edges of the film, being parallel with the frame edges, were used as guides to obtain precise parallel alignment of the frames.

The first set of experimental data duplicated Jain's parameters as much as possible. Thus, we processed only a 2 MHz bandwidth.

We show the shape of  $k(\Delta f)$  for  $W = 2$  MHz in Figure 39. As can be seen, the correlation essentially disappears by the time  $\Delta f/W = 1/2$ . This presentation is too compressed to observe whether a difference in correlation strength occurs with sea state. We have therefore replotted the points for  $\Delta f = 1/2$  MHz ( $\Delta f/W = 1/4$ ) in Figure 40a for the 3 sea states. Clearly, there is no resolvable difference in the degree of correlation between the different sea states. Figure 40b shows a similar presentation of the unnormalized correlations. If anything, there is a trend which is the reverse of that which Jain predicts. The average experimental error is 0.7 dB or 17%. This is larger than the 5% accuracy which Jain claimed. The unnormalized data has an error of 0.3 dB or 7%. These errors represent a completely independent set of measurements, but from the same pairs of image frames originally processed.

### 7.3.3 SECOND SET OF EXPERIMENTAL DATA

We thought that a larger  $\Delta f$  might have a better chance at producing an observable difference in correlation strength. We therefore ran a set of data in an identical fashion for a bandwidth  $W$  of 10 MHz and  $\Delta f = 5$  MHz. These data begin to violate the condition that the waves themselves not be resolved. However, Jain's theory also treats this case and predicts a decreasing correlation strength with an increasing wave height.

This data is plotted in Figure 41. Again we have plotted both the normalized and unnormalized values in this figure. There appears to be a strong reverse trend in this data. However, the discrepancy between the normalized and unnormalized data is somewhat troubling.

Two (and possibly three) experimental problems were noted after these data were plotted.

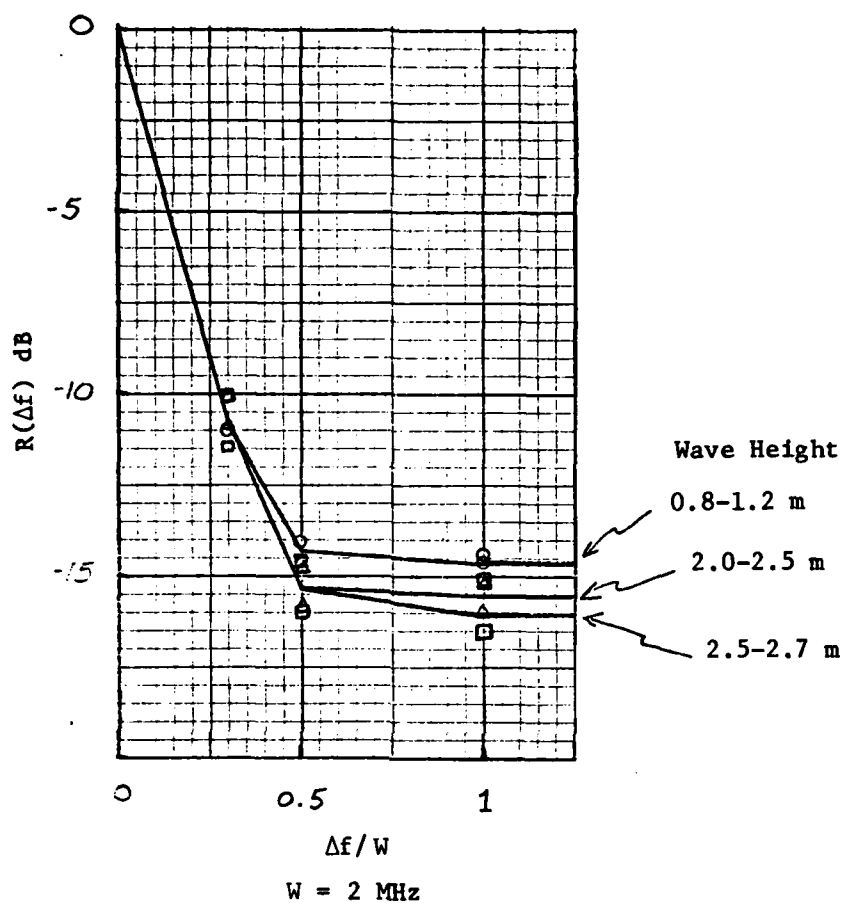


FIGURE 39. SPECKLE PATTERN DECORRELATION VS. CHANGE IN PROCESSED CENTER FREQUENCY FOR A PROCESSED BANDWIDTH OF 2 MHz.



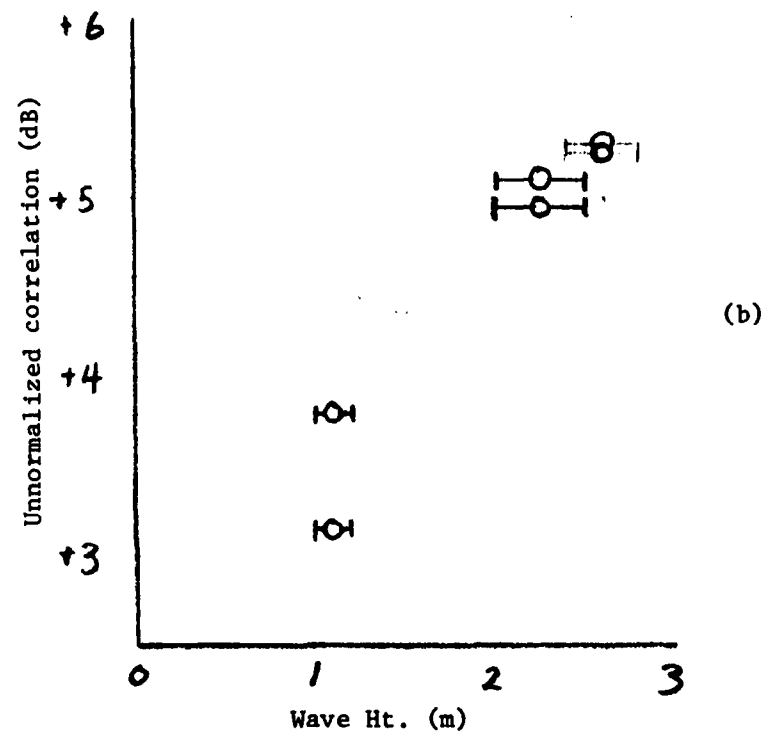
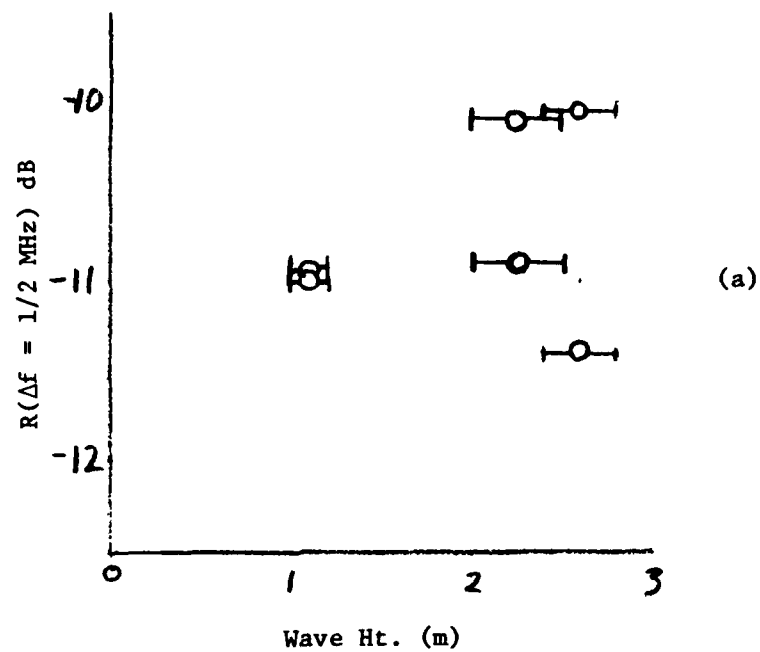


FIGURE 40. SPECKLE CORRELATION VS. WAVE HEIGHT  
FOR  $W = 2 \text{ MHz}$ ,  $\Delta f = 1/2 \text{ MHz}$ .

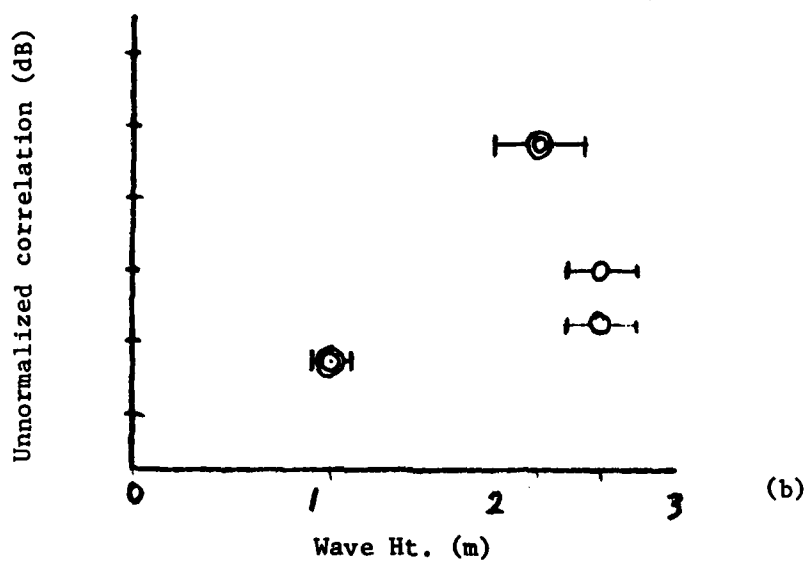
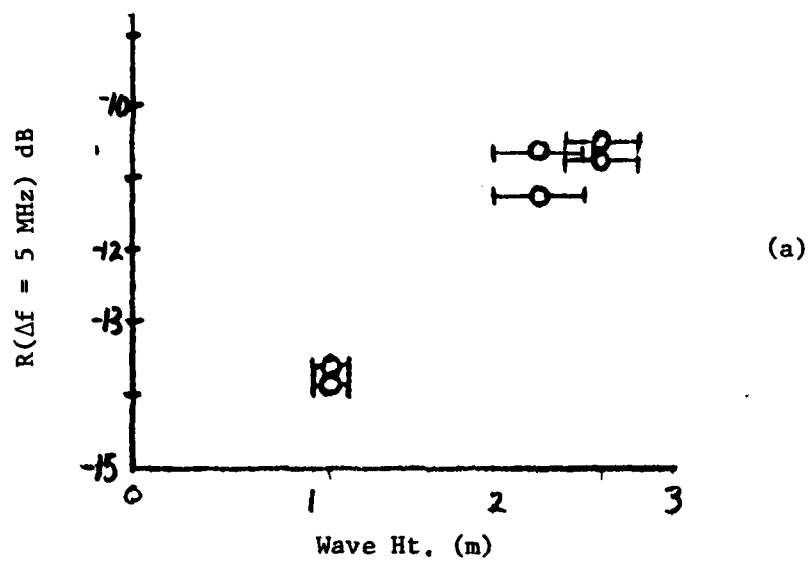


FIGURE 41. SPECKLE CORRELATION VS. WAVE HEIGHT  
FOR  $W = 10 \text{ MHz}$ ,  $\Delta f = 5 \text{ MHz}$

1. Due to an oversight during the measurements, the frequency change  $\Delta f = 5$  MHz was made with an unknown degree of precision, certainly less precision than was maintained for the first set of data.
2. Another intermittent problem was noted on one of the pairs of frames with  $\Delta f = 0$ . It appeared that the signal film tended to wander a small amount in the range direction as it tracked through the processor. (The film guides allow a small amount of this wandering.) This caused the pair of frames to be slightly distorted and non-overlapping. The amount of this distortion and lack of overlap was only a fraction of the range resolution or speckle size, but produced quite a noticeable drop in the correlation. As we pointed out earlier, the correlation function is extremely sensitive to displacements or distortions smaller than a resolution element.
3. We noted that one of the  $W = 2$  MHz pairs did not appear to be properly indexed when the slit edges were butted one against the other. It is possible that the slit did not track accurately in this case or that problem 2 occurred again. In general, the slit edges produced quite good rotational alignment of the frames.

#### 7.3.4 THIRD SET OF DATA

As a result of the difficulties encountered in the first two sets of data, a third set of data was taken. This third set of data used a bandwidth of 13 MHz and a  $\Delta f$  of 6 MHz.

To eliminate signal-film tracking errors, we let the signal film sit motionless in the liquid gate and just made still pictures. The maximum azimuth aperture which could be processed in this way was a little less than 1 km.

The pairs of frames were recorded on a single piece of film by mounting the camera on a machine slide. Our experimental procedure then consisted of merely making the exposure of the nominal frame  $T_0$ , moving the frequency plane aperture by  $\Delta f$ , moving the output camera up by the distance  $d_0$  and exposing the second frame  $T_1$ . The machine slide guaranteed parallelism of the frames.

In order to get a better idea of the true experimental errors and other fluctuations involved in these measurements of correlation strength, we recorded two sets of data for each sea state involved. The two sets of data corresponded to two different patches of sea which were, however, in the same general vicinity.

The different correlation strength vs. sea state data from these measurements is summarized in Figure 42. In this case, there is very good agreement between the normalized and unnormalized data. In one case (for the middle sea state), we duplicated all parameters of these measurements and experimental error involved here is 0.1 dB or 2%, which is very low. Different nearby patches of sea produce somewhat bigger fluctuations of 0.3 dB or 7%. Note that no consistent trend of either increasing or decreasing correlation strength with wave height is observed. The correlation strength is essentially a constant within experimental error.

We noted during the course of generating the composite frames for this third test that a significant percentage of the energy, both in the image and in the frequency plane of the processor, was processor noise. This (by itself) is not surprising, since sea return is generally quite small, especially for the low sea states. Two things are particularly bad about this case, however. First, due to a conflict regarding equipment needs, a substandard quality mirror was used in the processor. This mirror caused an abnormally high amount of processor noise. Secondly, this processor noise normally averages out to a uniform background level in a tracking processor. This happens because the noise, being stationary with respect to the

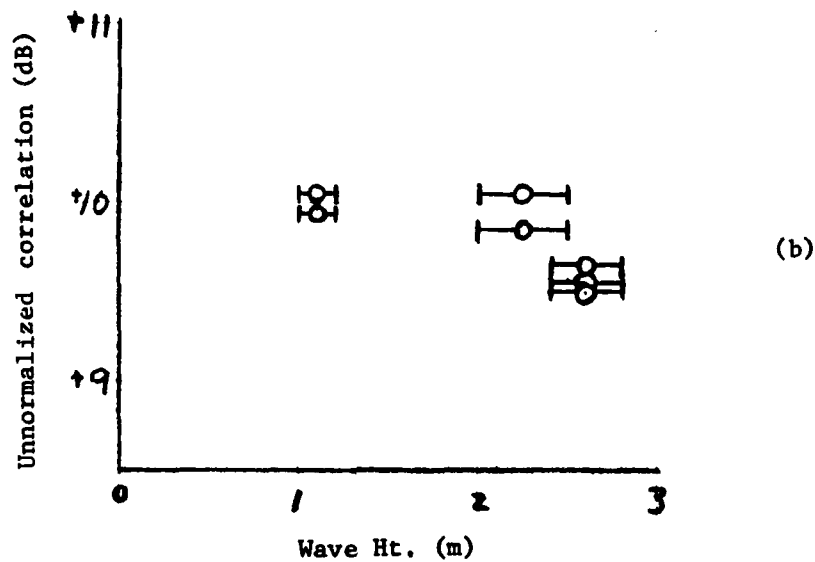
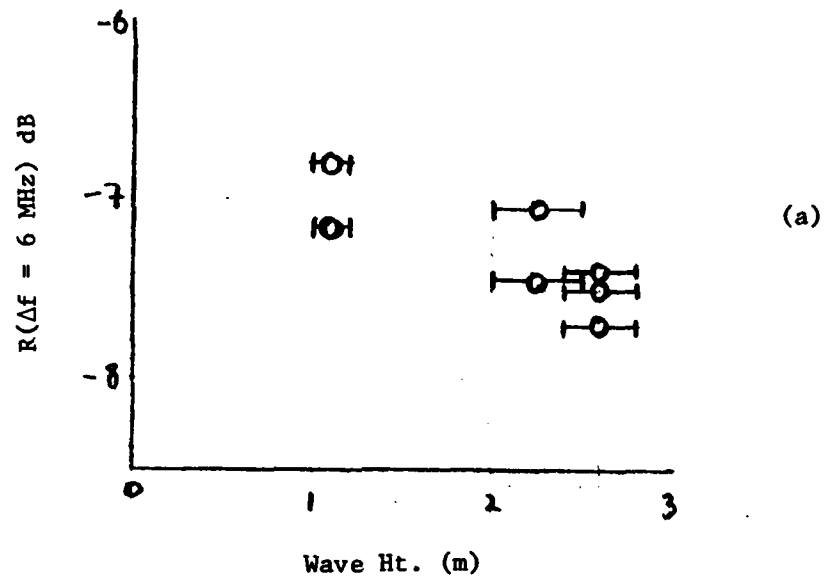


FIGURE 42. SPECKLE CORRELATION VS. WAVE HEIGHT  
FOR  $W = 13 \text{ MHz}$ ,  $\Delta f = 6 \text{ MHz}$

processor, becomes smeared and averaged over many resolution elements as the signal and output films are tracked through the processor. Since we were not tracking in this case, however, this processor noise becomes a part of the image speckle pattern, which is correlated.

As we were generating the composite frames, we noted the laser power required to maintain a fixed intensity in the image plane. Since the processor noise is just proportional to this laser power (multiplied by the average transmittance of the signal film), it is reasonable to presume that the percentage of noise would rise and fall with this laser power. There is thus a strong suggestion that the small differences in correlation strength between the three sea states is a consequence of processor noise.

To demonstrate the effects of this noise, we generated a composite image consisting of two entirely different (and therefore uncorrelated) patches of sea. The correlation strength of this pair of images was 8 dB above that of truly uncorrelated speckle patterns.

#### 7.3.5 SUMMARY DISCUSSION

For Jain's technique to be of value, substantial differences in correlation strength are required. The use of these analog techniques to obtain the correlation function is adequate to confirm the existence of differences in correlation strength. But the absolute level of correlation, which is required for the utility of this algorithm, is significantly altered by the nonlinearities involved. A relatively simple analysis is sufficient to demonstrate this.

Another fundamental problem associated with this technique is noise. The radar itself is an analog device subject to variability. Although processor noise could be alleviated by using a tracking processor, receiver, recorder, and film-grain noise would still be present. The average signal-to-noise ratio of sea imagery is

typically low (3-6 dB) due to the low radar cross section of the sea. This cross section is subject to large variability with sea state, so we can expect the average signal-to-noise ratio to vary with sea state also. This will influence the results. The effects of this noise in either increasing or decreasing the correlation strength is likely to depend on whether positives or negatives are used in the analog correlation process.

It is unfortunate that experimental problems have precluded our obtaining the most consistent results possible. Nevertheless, the sensitivity and consistency of our results appear good enough to rule out the practicality of this method, at least for the bandwidths and changes in frequency tried. On the positive side, our experimental problems serve to emphasize the non-triviality of measuring the correlation function with the degree of accuracy claimed by Jain, and they demonstrate how easily extraneous factors can influence the results.

8  
SYNTHETIC APERTURE RADAR MODELING OF SURFACE  
OCEAN WAVES

Results of the ONR-sponsored SAR modeling of ocean surfaces is best summarized by two papers found in Appendix C of this report. The first paper entitled "Synthetic Aperture Radar Modeling of Surface Ocean Waves" was presented by invitation at the Thirteen International Symposium on Remote Sensing of the Environment (held April 1979 in Ann Arbor, Michigan).

This paper summarizes a study that examines a number of existing models which attempt to explain wave imagery obtained with a synthetic aperture radar (SAR). These models are of two types: static models that depend on instantaneous surface features and dynamic models that employ surface velocities. SAR imagery has been discussed in the literature using both types, though as yet there exists no widely-accepted understanding of the imaging mechanism for SARs. This study attempts to draw together analytical and experimental results based on a combination of these two types in order to approach a more satisfactory model for SAR ocean-wave imaging.

Radar backscatter values ( $\sigma_0$ ) were calculated from 1.3 and 9.4 GHz SAR data collected off Marineland, Florida. The  $\sigma_0$  data (averaged over many wave trains) collected at Marineland can best be modeled by the Bragg-Rice-Phillips model which is based on the roughness variation and complex dielectric constant of oceans. This result suggests that capillaries on the surface of oceanic waves are the primary cause for the surface return observed by a synthetic aperture radar (SAR).

An examination of salinity and sea temperature at small and medium incidence angles indicated that their effects upon sea surface reflection coefficients seem to be insignificant, for either of the linear polarizations. At large incidence angles, i.e., near-grazing,



there is a more pronounced change in the behavior of the vertical-polarization reflection coefficient.

The authors' observations of moving ocean, imaged by the SAR and studied in the SAR optical correlator, support a theory that the ocean surface appears relatively stationary in the absence of currents. The reflecting surface is most likely moving slowly (i.e., with capillary-wave phase velocity and orbital-wave velocity) relative to the phase velocity of the large gravity waves. The stationary theory still applies, since the phase velocity of the capillaries and the orbital velocity of the gravity waves are more nearly stationary when compared to the phase velocity of the gravity waves.

The second paper was also presented by invitation at the Fifth Canadian Symposium on Remote Sensing (held August 1978 in Victoria, British Columbia). This paper discusses a scattering model which appears to explain for the first time almost all features observed in the Doppler and image domains of SAR imagery of oceanic waves. The model, which is suitable for airborne and orbital radars, accounts for the coherence time of capillary-centered scattering cells, and their coherently-observable wave motions, including their vertical displacements. SAR wave imagery, together with the results of detailed observations on the ERIM optical processor, are presented to illustrate the pertinent effects. These results lead to the generic description of an optimum processor for wave contrast enhancement.

The work in this paper further outlines the culmination of theoretical and experimental investigation of a SAR's response to a typical sea surface. The requirement of scene as well as sensor coherence is proposed (for the first time, apparently) as the foundation for a coherent SAR wave-reflectivity theory. Three restraints on image resolution quality follow which in increasing order of

severity are pixel dwell time, scattering-cell coherence, and differential azimuth shift. A partially-coherent processing concept is suggested as the optimal method of coping with these fundamental constraints.

## REFERENCES

Ausherman, D.A., W.D. Hall, J.N. Latta, and J.S. Zelenka, Radar Data Processing and Exploitation Facility, Proceedings IEEE International Radar Conference, Washington, D.C., 1975.

Beal, R.C., The Seasat SAR Wind and Ocean Wave Monitoring Capabilities, Johns Hopkins University Applied Physics Laboratory Report No. SIR 79U-019, Columbia, Maryland, 1979.

Brigham, E.O., The Fast Fourier Transform, Prentice Hall, Englewood Cliffs, N.J. (1974).

Burg, J.P., Maximum Entropy Spectral Analysis, Paper presented to 37th Annual Meeting of the Society of Exploration Geophysicists, Oklahoma City, OK, 1967.

Feldkamp, G.B., Correction of SAR-Induced Distortion in Seasat Imagery, Paper for SPIE Conference on Applications of Digital Image Processing, San Diego, CA, August 1978.

George, N. and A. Jain, Space and Wavelength Dependence of Speckle Intensity, Appl. Phys., Vol. 4, p. 201, 1974.

Gonzalez, F.I., R.C. Beal, W.E. Brown, P.S. DeLeonibus, J.W. Sherman III, J.F. Gower, D.B. Ross, C.L. Rufenach, and R.A. Shuchman, Seasat Synthetic Aperture Radar: Ocean Wave Detection Capabilities, Science, Vol. 204, No. 4400, 29 June 1979.

Goodman, J.W., Stanford Elec. Lab. Tech. Report SEL-63-140 (TR 2203-1), 1963.

Gower, J.F.R. and B.A. Hughes, Radar and Ship Observations of Coastal Sea Surface Roughness Patterns in the Gulf of Georgia, Proceedings of the Thirteenth International Symposium on Remote Sensing of Environment, Ann Arbor, MI, pp. 103-115, April 1979.

Jackson, P.L., Study of Two-Dimensional High Resolution Frequency Analysis for Application to Synthetic Aperture Radar, University of Michigan Radiation Laboratory, Report to Rome Air Development Command, October 1978.

Jain, A.K. and S. Ranganath, Two-Dimensional Spectral Estimation, Proceedings of the RADC Spectrum Estimation Workshop, Rome, N.Y., May 1978.

Jain, A., Determination of Ocean Wave Heights from Synthetic Aperture Radar Imagery, Appl. Phys., Vol. 13, p. 371, 1977.

Kasischke, E.S., R.A. Shuchman and J.D. Lyden, Detection of Bathymetric Features Using Seasat Synthetic Aperture Radar - A Feasibility Study, ERIM Final Report No. 135900-2-F2, 77 pp., 1980.

Lacoss, R.T., Data Adaptive Spectral Analysis Methods, Geophysics, Vol. 36, No. 4, 1971, pp. 661-675.

Longuet-Higgins, M.S., D.E. Cartwright, and N.D. Smith, Observations of the Directional Spectrum of Sea Waves Using the Motions of a Floating Buoy, Ocean Wave Spectra, pp. 111-136, Prentice-Hall, Englewood, N.J., 1963.

Mitsuyasu, H., F. Tasai, T. Suhara, S. Mizuno, M. Ohkusu, T. Honda, and K. Rikiishi, Observations of the Directional Spectrum of Ocean Waves Using a Cloverleaf Buoy, J. Phys. Oceanogr., 5, pp. 750-760, 1975.

Parry, G., Some Effects of Surface Roughness on the Appearance of Speckle in Polychromatic Light, Optics Comm., Vol. 12, p. 75, 1974.

Raney, R.K. and R.T. Lowry, Oceanic Wave Imagery and Wave Spectra Distortions by Synthetic Aperture Radar, Proceedings of the Twelfth International Symposium on Remote Sensing of Environment, Manila, Philippines, pp. 683-702, 1978.

Schwab, D.J., R.A. Shuchman, and P.C. Liu, Wind Wave Directions Determined from Synthetic Aperture Radar Imagery and from a Tower in Lake Michigan, J. Geophys. Res. (in Press), 1980.

Shemdin, O.H., W.E. Brown, Jr., F.G. Staudhammer, R. Shuchman, R. Rawson, J. Zelenka, D.B. Ross, W. McLeish, and R.A. Berles, Comparison of In-Situ and Remotely Sensed Ocean Waves Off Marineland, Florida, Boundary-Layer Meteorology, Vol. 13, pp. 225-234, 1978.

Shuchman, R.A., P.L. Jackson, and G.B. Feldkamp, Problems of Imaging Ocean Waves with Synthetic Aperture Radar, ERIM Report No. 124300-1-T, Ann Arbor, MI, 1977.

Shuchman, R., A. Klooster, and A. Maffett, SAR Mechanism for Imaging Ocean Waves, IEEE Electronics and Aerospace Convention Record, p. 128, 1978.

Shuchman, R.A. and G.A. Meadows, Airborne Synthetic Aperture Radar Observations of Surf Zone Condition, Geophys. Res. Letters, Vol. 7, pp. 857-860, 1980.

Shuchman, R.A. and J.S. Zelenka, Processing of Ocean Wave Data from a Synthetic Aperture Radar, Boundary-Layer Meteorology, 13, pp. 181-191, 1978.

Shuchman, R.A., E.S. Kasischke, and A. Klooster, Synthetic Aperture Radar Ocean Wave Studies, ERIM Final Report No. 131700-3-F, Ann Arbor, Michigan, 1978.

Shuchman, R.A., C.L. Rufenach, F.I. Gonzalez, The Feasibility of Measurement of Ocean Surface Currents Using Synthetic Aperture Radar, Proceedings of the Thirteenth International Symposium on Remote Sensing of Environment, Ann Arbor, MI, pp. 93-102, 1979.

Shuchman, R.A. and E.S. Kasischke, The Detection of Oceanic Bottom Topographic Features Using SEASAT Synthetic Aperture Radar Imagery, Proceedings of the Thirteenth International Symposium on Remote Sensing of the Environment, Ann Arbor, MI, pp. 1277-1292, 1979.

Shuchman, R.A., E.S. Kasischke, A. Klooster, and P.L. Jackson, Seasat SAR Coastal Ocean Wave Analysis - A Wave Refraction and Diffraction Study, ERIM Final Report 138600-2-F, 78 pp., 1979.

Thompson, T.W., D.E. Weissman, W.E. Brown, Jr., and F.I. Gonzalez, Comparison of SAR Relative Image Intensity with SASS Winds for Orbits 1126 and 1169, Paper Presented at the SEASAT Colloquium, Scripps Institute of Oceanography, 1979.

Ulrych, T.J., Maximum Entropy Power Spectrum of Truncated Sinusoids, J. Geophys. Res., 77, 1396, 1972.

Weissman, D.E., T.W. Thompson, and R. Legechis, Modulation of Sea Surface Radar Cross Section by Surface Stress: Wind Speed and Temperature Effects Across the Gulf Stream, J. Geophys. Res., 85, pp. 5032-5042, 1980.

APPENDIX A  
RADAR IMAGE DISTORTION OF OCEAN WAVES  
DUE TO MOTION EFFECTS

An ERIM Technical Memorandum  
by  
C. Liskow and R. Shuchman

27 October 1977

ELECTROMAGNETIC MEASUREMENTS  
DEPARTMENT

MEMORANDUM TO: ONR Program

FROM: C. Liskow and R. Shuchman

SUBJECT: Radar Image Distortion of Ocean Waves Due to Motion Effects.

Surface conditions of the world's oceans can be monitored expeditiously by radar. The all weather and day or night capabilities of radar along with its wide area coverage are particularly well suited to remote sensing of large areas of the earth's surface. However, radar imagery contains a number of distortions that must be considered in interpreting the imagery. Imagery of ocean waves is subject to distortion when produced by any system that utilizes scanning. This is because different sections of the image are produced at different times, and the waves are moving during the scan. This memorandum specifically addresses this distortion problem.

Scanned imagery of a moving wave will show the wave crests rotated and the crest to crest distance altered. Figure 1 illustrates the geometry of a scanning system and moving ocean waves. The solid lines indicate the position of the scanning beam and two moving wave crests at time  $T_1$ . The crests are indicated by lines CD and EF. A line along the scan direction is shown dotted. The distance between crests is the wavelength,  $L$ , and the direction of travel of the waves relative to the scan is shown as the angle  $\theta$ . At a later time,  $T_2$ , the waves have moved a distance  $V_W(T_2 - T_1)$ . At  $T_2$  the point G of the wave crest EF has moved to point H. As the scanning beam moved from  $T_1$  to  $T_2$  the wave crest EF moved and is imaged along the dashed line BH. The image appears to be rotated an amount  $\Delta\theta$ .

An expression for  $\Delta\theta$  has been derived:

$$\Delta\theta = \arctan \left( \frac{V_A}{V_W} \cos \theta - \cos^2 \theta \right) \left( \tan \theta + \frac{1}{\tan \theta} \right) \quad (1)$$

$V_A$  is the imaging system scan velocity and  $V_W$  is the wave velocity. The derivation of this expression is shown in Appendix A. It is interesting to note that this expression has no dependence upon radar range or frequency.

A plot of  $\Delta\theta$  as a function of  $\theta$  using the scan velocity of the ERIM radar (76 m/sec) and a number of wave velocities is shown in Figure 2. The image rotation under these conditions is enough to represent serious error in interpretation. The maximum image rotation occurs with  $\theta$  at  $80^\circ$ .

Figure 3 shows a similar plot using the Seasat scan velocity of 7,868 m/sec. The image rotation is much reduced and is maximum where  $\theta$  is  $90^\circ$ .

An expression was derived also from Figure 1 for the imaged water wave length:

$$L_i = L \left( \cos \Delta\theta - \tan \theta \sin \Delta\theta + \frac{\cos \Delta\theta}{\frac{V_A}{V_W} \cos \theta - \cos^2 \theta} \right) \quad (2)$$

The derivation of this expression is given in Appendix B. Figures 4 and 5 show plots of imaged wavelength as a function of  $\theta$  using the ERIM radar scan velocity and the Seasat scan velocity respectively.

In summary, the above discussed distortion of ocean waves will not have an adverse effect on Seasat-A SAR imagery. However, the distortion is clearly a problem for SAR ocean wave imagery collected by non-jet (low-velocity) aircraft. Shemdin et al (1977) reported a  $8-10^\circ$  discrepancy between wave direction as measured from pitch-and-roll bouy data, and wave direction as measured from SAR imagery collected by non-jet aircraft at Marineland. This discrepancy is accountable using the wave velocity and solving for  $\Delta\theta$  in equation (1). Dr. William McLeish of AOML/SAIL using equations (1) and (2) corrected for  $\Delta\theta$  and  $L_i$  in the Marineland data reported on by Shemdin and produced from SAR data wave spectra that corresponds within a couple of degrees to the NOAA pitch-and-roll bouy information.

CL:RS:krn

cc: R. Larson  
R. Rawson  
G. Feldkamp  
G. Mastin  
A. Klooster  
P. Jackson



APPENDIX A

DERIVATION OF ROTATION ANGLE OF IMAGED WAVES (EQUATION 1)

From Figure 1, the elapsed time, T is:

$$T = \frac{\frac{L}{\cos \theta} + V_W T \cos \theta}{V_A}$$

combining terms,  $T V_A - T V_W \cos \theta = \frac{L}{\cos \theta}$

$$T = \frac{L}{(V_A - V_W \cos \theta) \cos \theta} \quad \text{or} \quad \frac{L}{V_A \cos \theta - V_W \cos^2 \theta} .$$

From the triangle GHB the angle  $\Delta\theta$  can be expressed as:

$$\Delta\theta = \arctan \frac{V_W T}{L \tan \theta + \frac{L}{\tan \theta}} .$$

Inserting the expression for T:

$$\Delta\theta = \arctan \frac{V_W L}{L \cos \theta (V_A - V_W \cos \theta) \left( \tan \theta + \frac{1}{\tan \theta} \right)}$$

or

$$\Delta\theta = \arctan \frac{1}{\left( \frac{V_A}{V_W} \cos \theta - \cos^2 \theta \right) \left( \tan \theta + \frac{1}{\tan \theta} \right)} .$$

# APPENDIX B

## DERIVATION OF IMAGE WAVE LENGTH (EQUATION 2)

From Figure 1, the imaged wavelength AJ is seen from triangle AJK to be:

$$L_i = (AG + GK) \cos (\theta + \Delta\theta)$$

$$L_i = \left( \frac{L}{\cos \theta} + \frac{V_W T \cos \Delta\theta}{\cos(\theta + \Delta\theta)} \right) \cos (\theta + \Delta\theta) \cdot$$

Inserting the expression for T and rewriting the cos of the sum of two angles

$$L_i = \left( \frac{L}{\cos \theta} + \frac{V_W \cos \Delta\theta L}{V_A \cos \theta - V_W \cos^2 \theta \cos (\theta + \Delta\theta)} \right) \cdot (\cos \theta \cos \Delta\theta - \sin \theta \sin \Delta\theta)$$

$$L_i = L \left( \cos \Delta\theta - \tan \theta \sin \Delta\theta + \frac{\cos \Delta\theta}{\frac{V_A}{V_W} \cos \theta - \cos^2 \theta} \right) \cdot$$

ADDENDUM TO EM-77-1320

An alternative and perhaps easier derivation to understand for obtaining  $\Delta\theta$  and  $L_i$  are as follows:

From Figure 1:  $\sin \theta = \frac{L}{AB}$

and

$$\sin(\theta + \Delta\theta) = \frac{AJ}{AB} = \frac{L_i}{AB}$$

Solving for  $L_i$  we obtain,

$$L_i = AB \sin(\theta + \Delta\theta) = L \csc \theta \sin(\theta + \Delta\theta)$$

rewriting using a trigonometric identity

$$L_i = [ \csc \theta \sin \theta \cos \Delta\theta + \csc \theta \cos \theta \sin \Delta\theta ]$$

Again using trigonometric identities

$$\begin{aligned} L_i &= L \cos \Delta\theta \left[ 1 + \csc \theta \frac{\sin \Delta\theta}{\cos \Delta\theta} \right] \\ &= L \cos \Delta\theta [1 + \csc \theta \sin \Delta\theta] \end{aligned}$$

To obtain  $\Delta\theta$ , we again look at Figure 1 and observe

$$\tan \Delta\theta = \frac{V_w}{BG} = \frac{V_w}{BG' - GG'}$$

Also by inspection

$$\sin \theta = \frac{V_A}{BG'}$$

and

$$\tan \theta = \frac{V_w}{GG'}$$

Combining equations

$$\tan \Delta\theta = \frac{V_w}{V_A \csc \theta - V_w \cot \theta}$$

$$\Delta\theta = \arctan \left[ \frac{V_w/V_A}{\csc \theta - \frac{V_w}{V_A} \cot \theta} \right]$$

RAS:krm

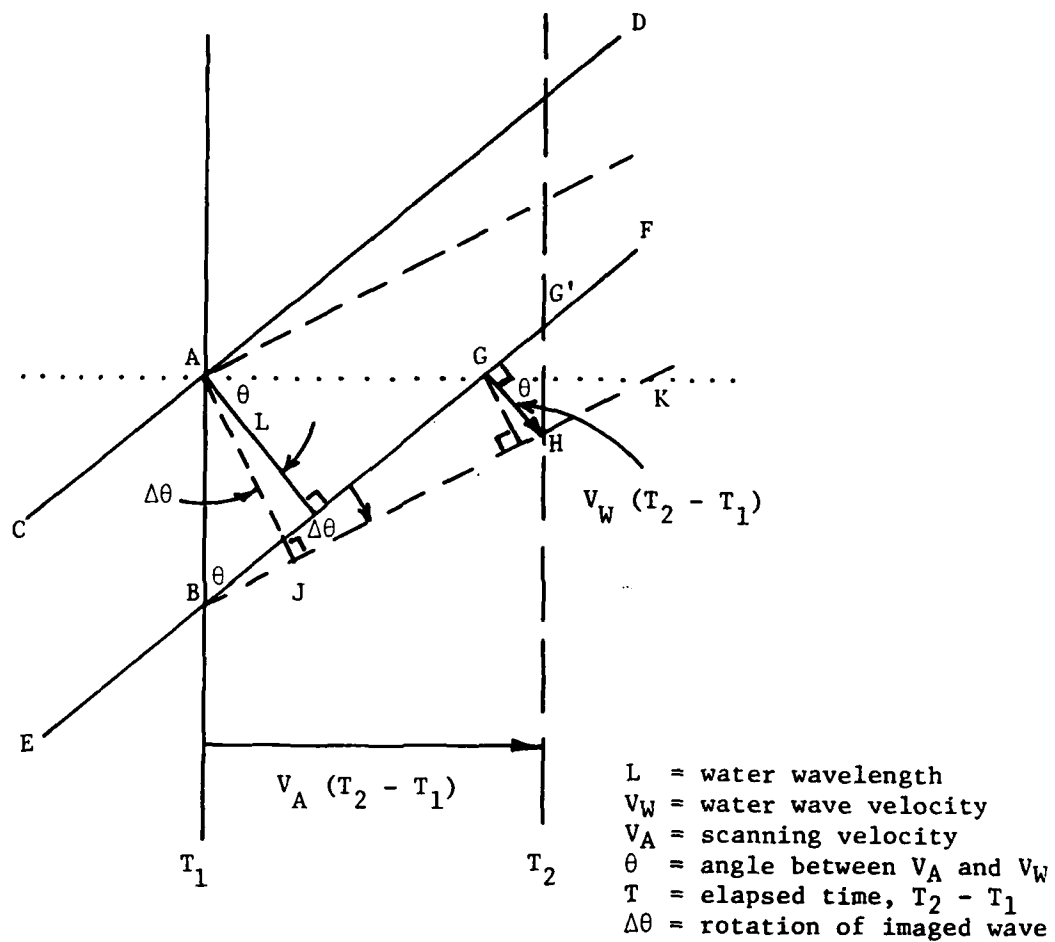


FIGURE 1. Geometry of a Scanning System and Moving Ocean Waves.

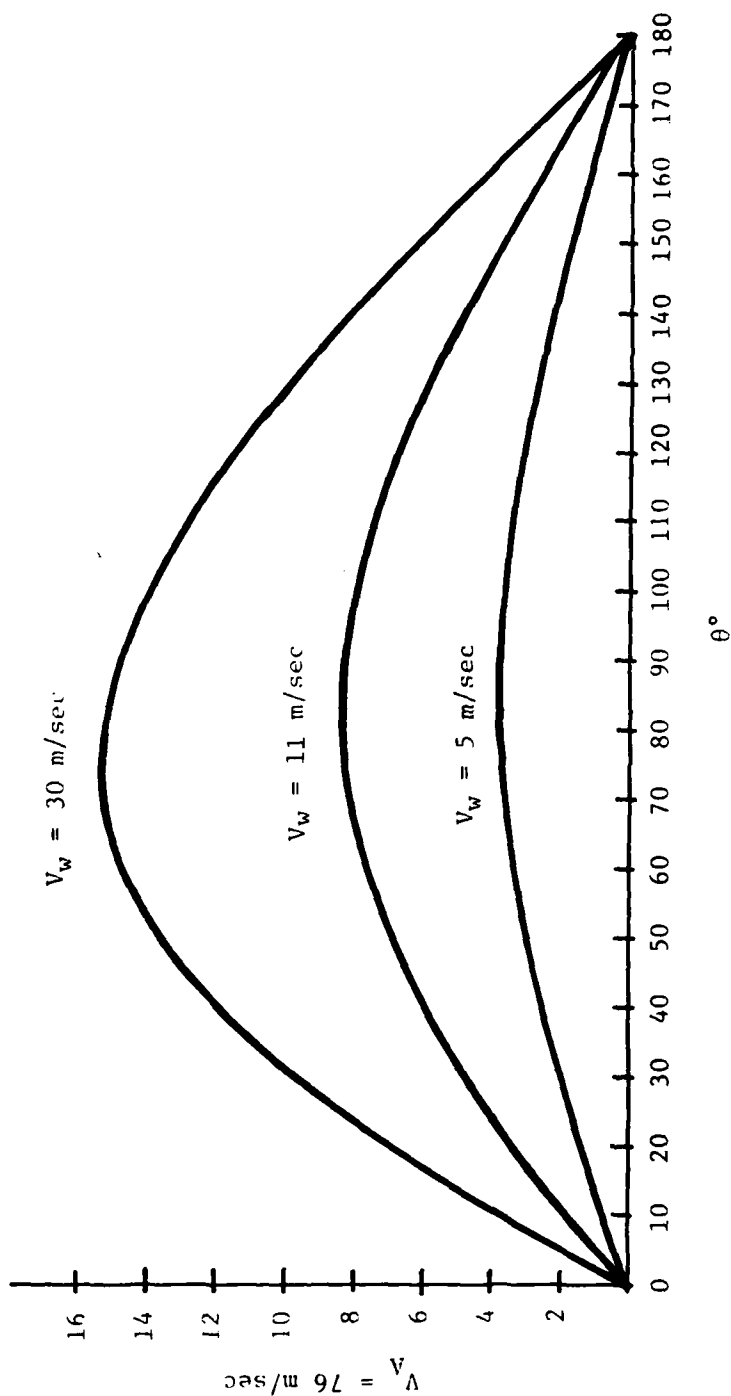


FIGURE 2. Plot of  $\Delta\theta$  as a Function of  $\theta$  Using the Scan Velocity of the ERIM Radar (76 m/sec)

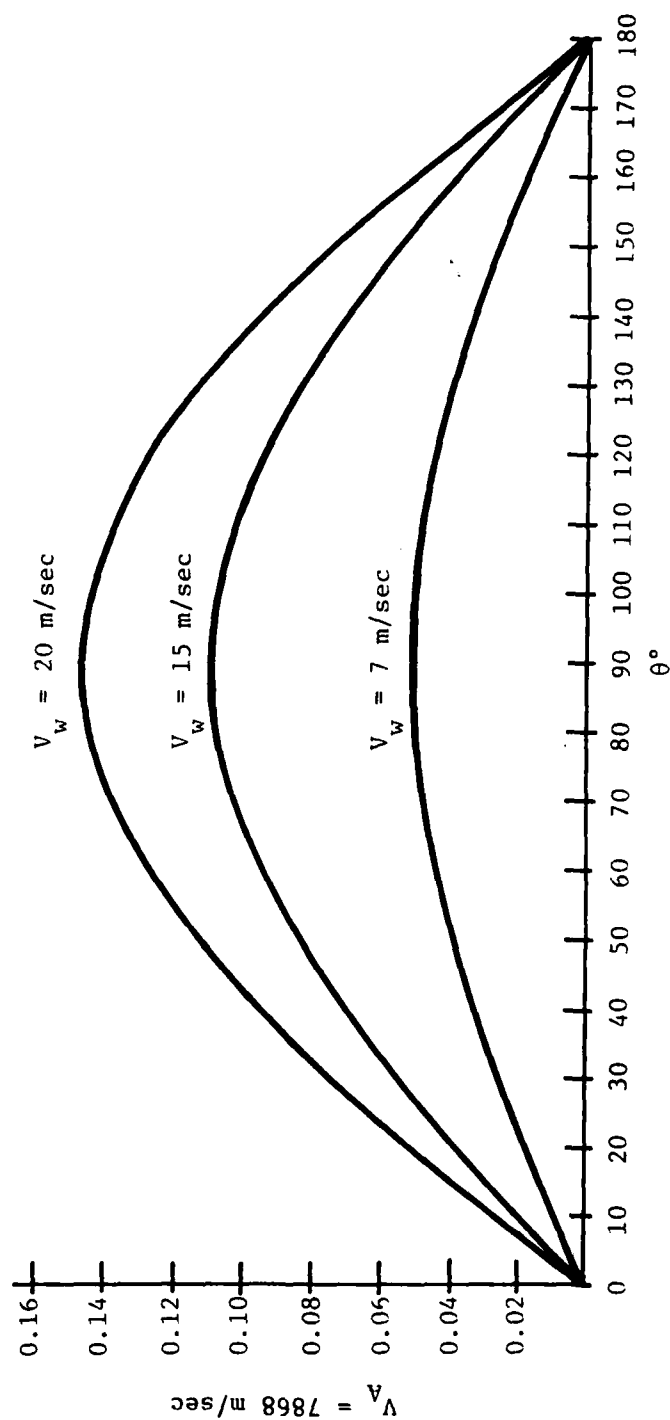


FIGURE 3. Plot of  $\Delta\theta$  as a Function of  $\theta$  Using the Scan Velocity of the SEASAT Radar (7,868 m/sec)

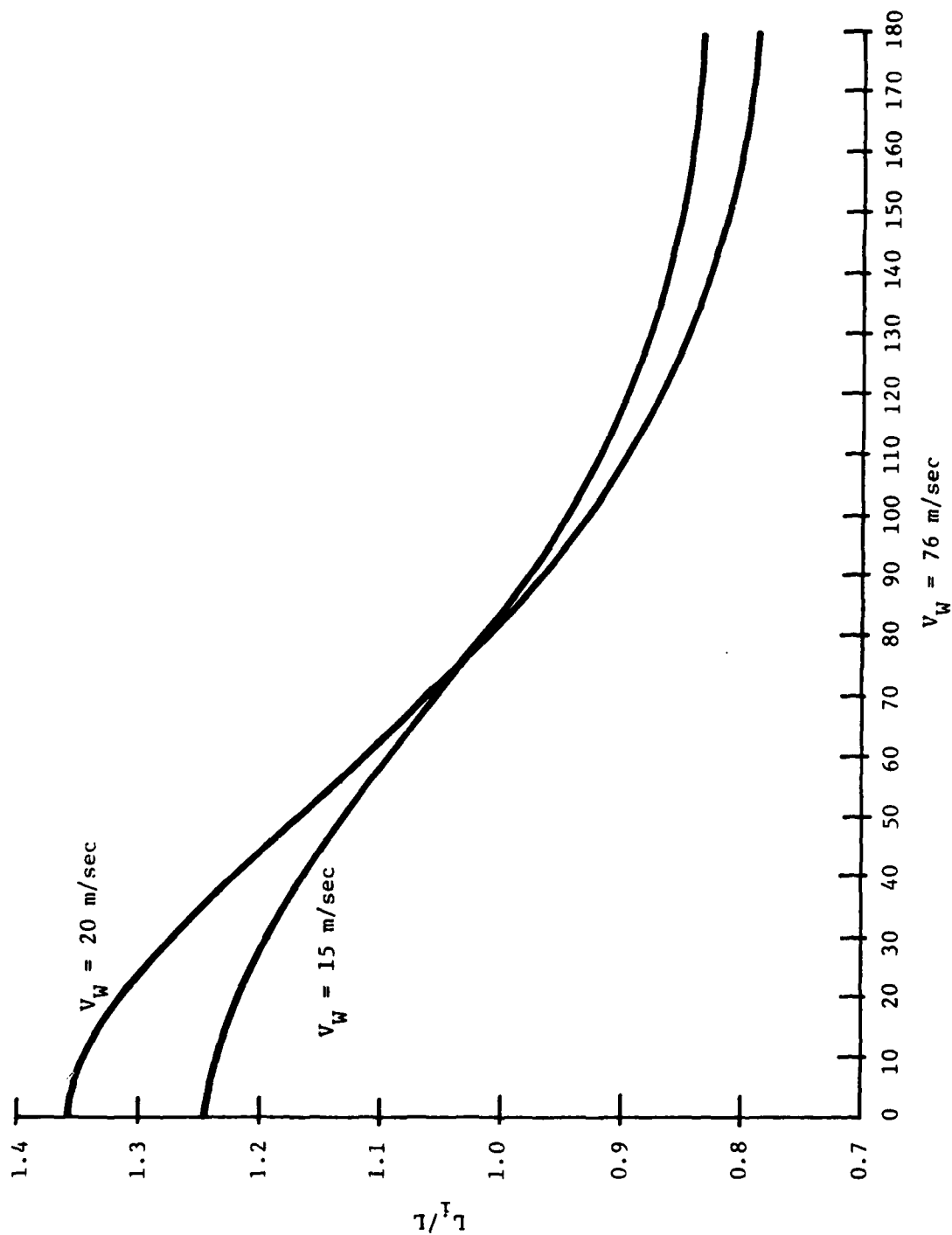


FIGURE 4. Plot of  $L_i/L$  as a Function of  $\theta$  for  $V_W = 15$  m/sec and  $V_W = 20$  m/sec Using Scan Velocity of the ERIM Radar (76 m/sec)



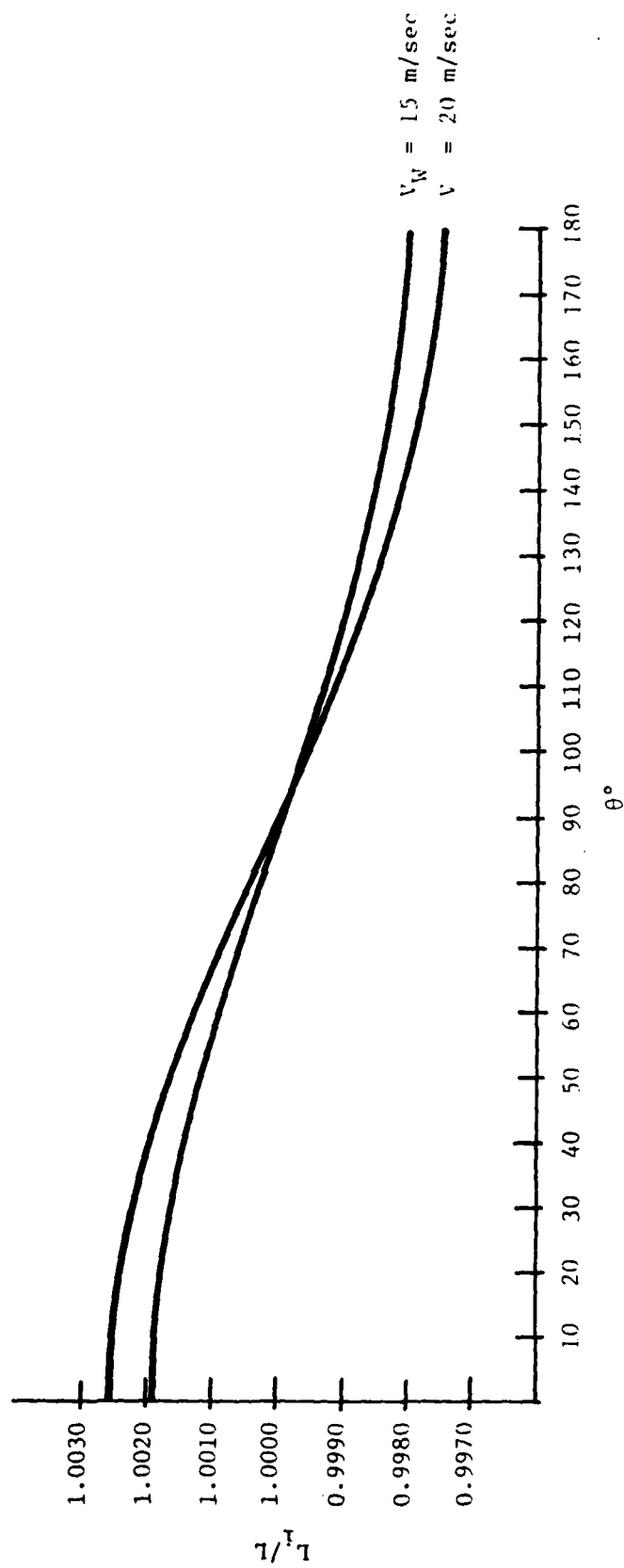


FIGURE 5. Plot of  $L_1/L$  as a Function of  $\theta$  for  $V_W = 15 \text{ m/sec}$  and  $V_W = 20 \text{ m/sec}$  Using Scan Velocity of SEASAT Radar (7,868 m/sec)

APPENDIX B  
"DETERMINATION OF OCEAN WAVE HEIGHTS FROM SYNTHETIC  
APERTURE RADAR IMAGERY"

An Article by Atul Jain  
Published in Applied Physics, Vol. 13, 1977.  
(with permission from publisher and author)

## Determination of Ocean Wave Heights from Synthetic Aperture Radar Imagery\*

Atul Jain

Space Sciences Division, Jet Propulsion Laboratory, California Institute of Technology, Pasadena, CA 91103, USA

Received 29 September 1976 Accepted 24 January 1977

**Abstract.** A calculation is presented for the cross-correlation of the radar images obtained by processing the same signal data over different portions of the chirp spectrum bandwidth as a function of the center frequency spacings for these portions. This is shown to be proportional to the square of the product of the characteristic function for ocean wave heights and the pupil function describing the chirp spectrum bandwidth used in the processing. Measurements of this function for ocean wave imagery over the coast of Alaska, the North Atlantic, and Monterey Bay, California, and correlation with the significant wave heights reported from ground truth data indicate that the synthetic aperture radar instrument can be used for providing wave height information in addition to the ocean wave imagery.

**PACS Codes:** 42.30, 84, 91

While the wavelengths of the ocean waves can be determined by inspection of the radar imagery or by obtaining its Fourier transform [1, 2], it is also of considerable interest to measure the heights of the ocean waves. A calculation, which outlines a method of processing the images obtained by the JPL L-band synthetic aperture radar to determine the heights of ocean waves at localized areas of interest in the images, and experimental results demonstrating this technique are presented.

Much work has been done on the remote measurement of ocean wave heights using nonimaging radar, and a review of such techniques was presented by Barrick [3]. Ruck et al. [4] have analyzed the possibility of using two-frequency radar interferometry for measuring wave slopes, and Weissman et al. [5, 6] have demonstrated the operation of a radar system utilizing this technique both in laboratory wave tank measurements

and flights over the Caribbean. The possibility of measuring ocean wave heights by studying the return from a short-pulse radar has also been demonstrated by Zamarayev and Kalmykov [7] and by Hammond et al. [8].

The principal concept involved in the wave height measurement, which is common to the interferometric techniques utilizing radar sensors, is that the resultant intensity for the electric field scattered from the ocean wave at some arbitrary point in space changes as the wavelength or angle of illumination for the electromagnetic radiation varies. This variation is dependent on the height difference between the crest and trough of the wave, and a measurement of the rate of this variation provides an indication of the ocean wave height. This principle has been used before in the design and operation of the tellurometer [9] for the precise determination of range differences. The various radar techniques for measuring ocean wave heights differ in the handling of the radar data, which is governed by the constraints set by the particular radar instrument being used, the accuracy and spatial resolu-

\* This paper presents the results of one phase of research carried out at the Jet Propulsion Laboratory, California Institute of Technology, under Contract NAS 7-100, sponsored by the National Aeronautics and Space Administration

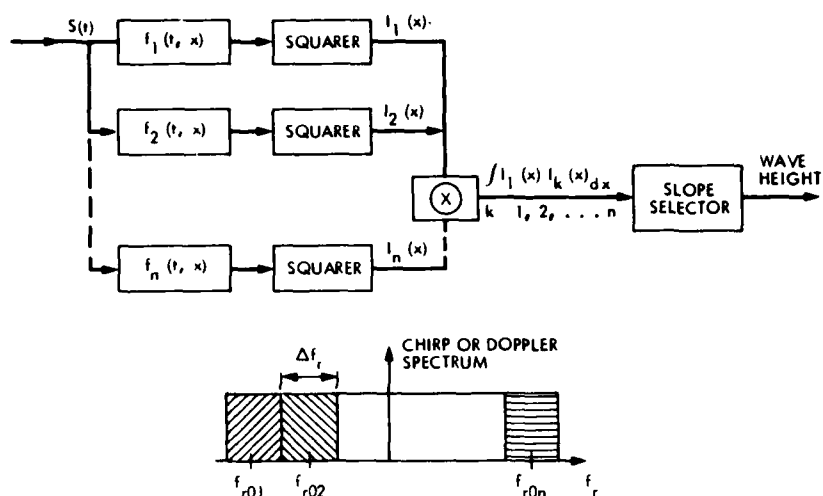


Fig. 1. System diagram for the wave height processor. The synthetic aperture radar signal  $S(t)$  is compressed by the matched filters  $f_1(t, x), f_2(t, x), \dots, f_n(t, x)$ , corresponding to a processing bandwidth of  $\Delta f$ , and at chirp or doppler processing frequencies  $f_{r01}, f_{r02}, \dots, f_{r0n}$  respectively, the square of these outputs cross-correlated by the operation  $\otimes$ , and the slope of the resulting curve measured to provide the wave height

tion of the measurement being related to the bandwidth and the resolution of the radar system involved.

An extensive theoretical and experimental treatment of the utilization of this concept to measure the height of surface features within a resolution cell in images obtained by a tunable dye laser has been performed by Jain [10], George and Jain [11], and George et al. [12]. The surface heights obtained by varying the wavelength can be determined quite accurately to the order of a wavelength, the accuracy improving with greater heights.

The essential elements in the processing of the synthetic aperture radar data for obtaining significant wave height information are shown in Fig. 1. They involve compressing the radar data for ocean images over different sections of the available chirp or Doppler bandwidths, cross-correlating these images and plotting the zero component of this cross-correlation value as a function of the spacings of the center frequencies for the bandwidths. A measure of the value of this curve for a given frequency spacing would provide a direct indication of the ocean wave heights.

In this article, we calculate this cross-correlation function, which is the output of the radar wave height processor in Fig. 1, and show that it is equal to the square of the product of the characteristic function of the ocean wave heights and the pupil function used in the chirp spectrum aperture for processing the radar signal. In the intermediate calculation of the image produced by the radar system, we have not taken into account the effect of the orbital velocity of the waves. While a detailed treatment of this effect will be discussed elsewhere, we briefly mention the consequences of

including the temporal motion of the waves in our formulation. Thus, a knowledge of the chirp spectrum pupil function of the radar and an experimental determination of the cross-correlation curve by the wave height processor would lead directly to a measurement of the ocean wave height distribution. We also present experimental curves of this cross-correlation function for ocean images taken off the coast of Alaska on March 31, 1975, North Atlantic on September 28, 1971, and in Monterey Bay, California, on October 6 and August 13, 1975. We find that the measured cross-correlation curve is equal to  $\Gamma_r(\Delta f_{r0}) \exp(-0.12 \Delta f_{r0} \sigma_H)$ , where  $\sigma_H$  is the significant wave height,  $\Delta f_{r0}$  the frequency separation for the cross-correlation value, and  $\Gamma_r(\Delta f_{r0})$  a number depending upon the chirp spectrum aperture function  $\Gamma_r$  for the radar processor.

### Theory for Wave Height Determination

The synthetic aperture radar is an imaging instrument, where the resolution is determined by the chirp and doppler bandwidths used for the radar system. Thus, any point on the image contains contributions from the field scattered by an area of the terrain determined by the resolution cell size of the radar. By narrowing the effective Doppler or chirp bandwidth utilized by the instrument, the area of the ocean surface contributing to the intensity at a given image point may be widened to any desired magnitude. The total path length that the radar wave has to travel to the image is different for the trough of the wave than for the crest, and the resultant phase difference for the contribution from these two regions of the wave is dependent on the

frequency or angle of illumination of the wave. As this frequency or angle of illumination is varied, the fluctuation of the intensity at the image point, which receives contributions from both wave regions, is related to the difference in heights between the crest and trough of the wave, modified by the effect due to the resolution cell size of the radar. By measuring the effective rate of this fluctuation, one can infer the heights of the ocean waves.

In the linear system idealization for the synthetic aperture radar performance [13, 14], the electric field  $e(x_0, y_0)$  in the image of the radar output is

$$e(x_0, y_0) = \int \int \psi(x_0, y_0; x, y) g(x, y) dx dy, \quad (1)$$

where  $(x_0, y_0; x, y)$  is the generalized ambiguity function, as defined by Cutrona [14] for the radar, and  $g(x, y)$  is the terrain reflectivity.

In the calculation for the ambiguity function, however, it is assumed that the terrain reflectivity does not depend upon the wavelength of illumination or the look angle of the radar. In the case of an uneven surface, this assumption is not applicable, and it is necessary to consider the effects of the wavelength and angular dependence of the radiation scattered by the surface. In order to take this phenomenon into account, we calculate the image field for each wavelength component of the chirp spectrum and position of the radar platform and integrate this electric field over the total synthetic antenna length and the chirp spectrum bandwidth available.

The impulse response function of the radar imaging system for a given value of the antenna position,  $x_A$ , and the chirp spectrum frequency  $f_r$  may be expressed as a convolution of the generalized ambiguity function with the Fourier transform of the pupil function for this range and Doppler aperture. This aperture is the Dirac delta function  $\delta(f_{da} - f_d)\delta(f_{rr} - f_r)$ , where the phase factor due to the time delay,  $f_d$ , is equal to  $x_A f_{r0}/Z$ ,  $f_{r0}$  being the frequency of operation of the radar and  $Z$  the height of the radar platform from the terrain. The Doppler shift of the scattered signal is  $f_d f_r/c$ , where  $v_r$  is the velocity of the radar platform; but this additional multiplicative factor disappears in the matched filtering operation to obtain imaging in azimuth. The Fourier transform of this delta function is defined by

$$U(x, y_0) = \int \int \delta(f_{da} - f_d)\delta(f_{rr} - f_r) \cdot \exp\left[\frac{i2\pi}{c}(f_{da}x + f_{rr}y_0)\right] df_{da} df_{rr} \quad (2)$$

the symbol  $y_0$  being used to specify the chirp processing operation, as shown by Rihaczek [15].

The resultant impulse response of the radar system for these particular frequencies ( $f_d, f_r$ ) is given by the convolution of the impulse response  $U(x, y_0)$  with the generalized ambiguity function  $\psi(x, y)$ . Thus, for the complex terrain reflectivity  $g(x, y)$ , the electric field recorded in the radar image is the convolution of  $g(x, y)$  with the convolution of  $\psi(x, y)$  with  $U(x, y_0)$ . Further, for the Doppler spectrum aperture function given by  $\Gamma_d(f_d - f_{d0})$ , which has an effective width of  $\Delta f_d$  and is centered at  $f_{d0}$ , and a chirp spectrum aperture function  $\Gamma_r(f_r - f_{r0})$  of width  $\Delta f_r$  centered at the radar frequency  $f_{r0}$ , the electric field in the radar image is the superposition of fields obtained for each Doppler and chirp frequency component weighted by the functions  $\Gamma_d(f_d - f_{d0})$ ,  $\Gamma_r(f_r - f_{r0})$ . We thus have the equation

$$e(x_0, y_0) = \int \int \left\{ g(x, y) * \psi(x, y) * \exp\left[\frac{i2\pi}{c}(f_d x + f_r y_0)\right] \right. \\ \left. \cdot \Gamma_d(f_d - f_{d0}) \Gamma_r(f_r - f_{r0}) \right\} df_d df_r, \quad (3)$$

where  $*$  denotes the convolution operation. Equation (3) describes the field in the image plane of the terrain reflectivity  $g(x, y)$  obtained by a synthetic aperture radar defined by the generalized ambiguity function  $\psi(x, y)$  and the processing Doppler and chirp spectrum apertures  $\Gamma_d(f_d - f_{d0})$ ,  $\Gamma_r(f_r - f_{r0})$ . Since the azimuth aperture for the synthetic aperture radar processor is generally symmetric, it is safe to consider the value of  $f_{d0}$  to be zero in our further evaluation of (3).

From the geometry of Fig. 2, the terrain reflectivity function  $g_P(x, y)$  for a particular area surrounding the point  $P$ , located at  $(0, y_P)$ , can be shown to be, using similar arguments as in [16],

$$g_P(x, y) = R(x, y) \exp\left[\frac{i4\pi}{c} f_r \cos \theta_{Px} h(x, y)\right] \\ \cdot \exp\left\{\frac{i2\pi}{c} f_r [x \sin(\theta_{Px} - 2\theta_{Py}) + y \sin(\theta_{Py} - 2\theta_{Px})]\right\}. \quad (4)$$

$R(x, y)$  is the amplitude reflectivity of the terrain due to absorption and dielectric constant variations;  $h(x, y)$  is the profile of the terrain resting on the local slopes of angles  $(\theta_{Px}, \theta_{Py})$ , which vary slowly compared to the variation of  $h(x, y)$ . The distance of point  $P$  from the radar,  $\sqrt{Z^2 + y_P^2}$ , is considered to be large, so that the radar wave incident on the area surrounding  $P$  is essentially plane and is at angles  $(\theta_{Px}, \theta_{Py})$  with respect to the normal to the horizontal plane. The function  $\exp[(i4\pi/c) f_r \cos \theta_{Px} h(x, y)]$  is the phase mod-

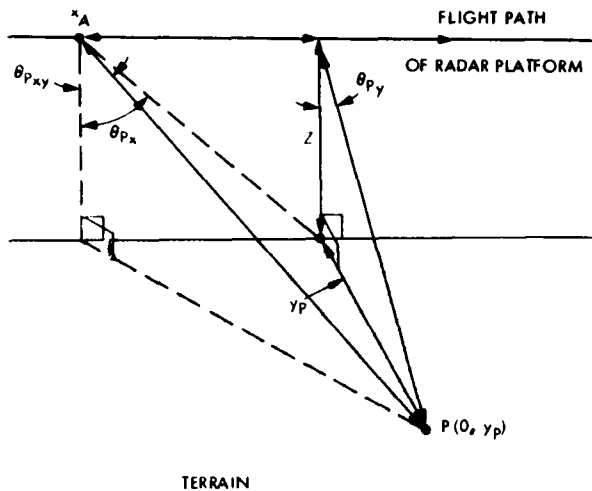


Fig. 2 Radar imaging geometry. The point  $P$  is located at  $(0, y_p)$ , the terrain is at distance  $Z$  from the radar platform, and the angles  $\theta_{px}$ ,  $\theta_{py}$ , and  $\theta_{pxy}$  describe the instantaneous radar position from  $P$ .

ulation in the reflected wave due to the small-scale roughness  $h(x, y)$  causing backscattering of the radar radiation. The factor

$$\exp \left\{ \frac{i2\pi}{c} f_r [x \sin (\theta_{px} - 2\theta_{pix}) + y \sin (\theta_{py} - 2\theta_{piy})] \right\}$$

is the phase modulation in the reflected wave from the tilt variations of the ocean wave and the angles of incidence  $\theta_{px}$  and  $\theta_{py}$  of the radar wave and is determined from equating the angle of incidence to the angle of reflection from the surface. The angle  $\theta_{px}$  is generally small, and for a typical spacecraft radar it is less than 0.1 radian.  $(\theta_{pix}, \theta_{piy})$  are the angles of tilt of an ocean wave when  $g_p(x, y)$  is an ocean surface and are generally limited to be less than 0.143 [17]. Thus, in our further computations involving  $g_p(x, y)$ , it is reasonable to consider  $\sin (\theta_{px} - 2\theta_{pix})$  as approximately equal to  $(\sin \theta_{px} - \sin 2\theta_{pix})$ . Since  $\sin \theta_{px}$  is equal to  $x_A/Z$ ,  $f_{r0} \sin \theta_{px}$  is the Doppler frequency  $f_d$ , and  $\theta_{py}$  is generally much larger than  $\theta_{piy}$  for side-looking radars.

To evaluate the radar performance for a given reflectivity, we substitute (4) into (3). For  $h(x, y) = \theta_{pix} = \theta_{piy} = 0$ , which corresponds to an even terrain of reflectivity  $R(x, y)$ , the image electric field is found to be

$$E \left( \frac{2x_0}{c}, \frac{y_0}{c} \sin \theta_{py} \right) = \psi \left( \frac{2x}{c}, \frac{y \sin \theta_{py}}{c} \right) \cdot \left[ R(x, y) \cdot \exp \left( \frac{-i2\pi}{c} f_{r0} y \sin \theta_{py} \right) \cdot \gamma_d \left( \frac{2x}{c} \right) \gamma_r \left( \frac{y \sin \theta_{py}}{c} \right) \right] \quad (5)$$

where

$$\gamma_d(x) = \int \Gamma_d(f_d) \exp(-i2\pi f_d x) df_d$$

and

$$\gamma_r(y) = \int \Gamma_r(f_r) \exp(-i2\pi f_r y) df_r$$

We have neglected the variation of  $x \sin \theta_{px}$  in comparison to  $y \sin \theta_{py}$ , which is a much larger term, in the function  $\gamma_d(y)$  in (5). For infinite processing bandwidths, given by the widths of  $\Gamma_d(f_d)$ ,  $\Gamma_r(f_r)$ , the functions  $\gamma_d(x)$ ,  $\gamma_r(y)$  reduce to delta functions, and (5) reduces to (1).

On the other hand, for a radar with an infinitely high resolution, when  $\psi(x, y)$  would be a delta function, the image electric field would be the convolution of the reflectivity with the impulse response functions  $\gamma_d$  and  $\gamma_r$ , and the image resolution would be determined primarily by the bandwidths utilized by the radar processor. In general, the resolution of the radar is indeed limited by the data handling capabilities of the processor, and so it is safe to assume, for our further analysis, that the generalized ambiguity function is the delta function.

We now consider the case of an uneven surface such as ocean waves and assume that the function  $R(x, y)$  is unity in (4). We describe  $h(x, y)$  as a series of steps whose perimeters are defined by the functions  $S_{ij}(x - x_i, y - y_j)$  centered at the various points  $(x_i, y_j)$ , and the profile of the surface within this  $(ij)^{\text{th}}$  step is defined by the function  $h_{ij}$ . The effective length of the  $S_{ij}$  function is given by  $l_i$  in the  $x$ -direction and  $l_j$  in the  $y$ -direction. Thus, the surface profile  $h(x, y)$  can be written as  $\sum_{ij} h_{ij} S_{ij}(x - x_i, y - y_j)$ . For nonoverlapping  $S_{ij}$ , the exponential  $\exp [(-i4\pi/c) \cos \theta_{px} h(x, y)]$  can be rewritten as [18]

$$g_p(x, y) = \exp \left\{ \frac{i4\pi}{c} f_r [x \sin (\theta_{px} - 2\theta_{pix}) + y \sin (\theta_{py} - 2\theta_{piy})] \right\} \cdot \left\{ 1 + \sum_{ij} S_{ij}(x - x_i, y - y_j) \cdot \left[ \exp \left[ \frac{i4\pi}{c} f_r \cos \theta_{px} h_{ij} \right] - 1 \right] \right\} \quad (6)$$

The first term in (6) represents the field reflected if the terrain had only tilt variations [i.e.,  $h(x, y) = 0$ ]. The

term identified by the summation consists of two terms, the first being the component of the reflected field due to the surface roughness, and the second being the component that must be subtracted from the field for the flat surface case to provide the reflected field for the smooth component of the terrain.

To obtain the electric field in the image of the field given by (6), we substitute (6) into (3). We neglect the effect of the variation of  $f_d^2$  compared to  $f_d$  in the term  $\cos \theta_{pxy}$ . We assume that the scattering cross-section of the terrain, determined by the Fourier transforms of  $S_{ij}(x-x_i, y-y_j)$  does not vary significantly with the Doppler chirp spectrum frequency variations over the bands used in the radar processor, as compared to the variations of the exponential phase terms containing this ( $f_d, f_r$ ) dependence. The resultant image electric field is

$$\begin{aligned} e_p \left[ \frac{2x}{c}, y \sin(\theta_{py} - 2\theta_{p_{iy}}) \right] \\ = \left\{ \exp \left[ \frac{i2\pi}{c} f_{r0} y \sin(\theta_{py} - 2\theta_{p_{iy}}) \right] \right. \\ \cdot \gamma_d \left( \frac{2x}{c} \right) \gamma_r [y \sin(\theta_{py} - 2\theta_{p_{iy}})] \Big\} \\ \cdot \left[ 1 + \sum_{ij} \beta_{ij} F_{ij}(x, y; x_i, y_i; h_{ij}) \right], \end{aligned} \quad (7)$$

where  $\beta_{ij}$  is the scattering cross-section factor and is equal to

$$s_{ij} \left[ \frac{-f_{r0}}{c} \sin 2\theta_{p_{ix}}, \frac{f_{r0}}{c} \sin(\theta_{py} - 2\theta_{p_{iy}}) \right]$$

for  $s_{ij}$  defined by

$$s_{ij}(l, m) = \int \int S_{ij}(x, y) \exp [i2\pi(xl + ym)] dx dy.$$

In the approximation, where  $S_{ij}(x, y)$  are given by the step functions  $[\text{rect}\{x/l_i\} \text{rect}\{y/l_j\}]$ , the cross-section factor  $s_{ij}$  is equal to

$$l_i l_j \text{sinc} \left[ \frac{f_{r0}}{c} l_i \sin 2\theta_{p_{ix}} \right] \text{sinc} \left[ \frac{f_{r0}}{c} l_j \sin(\theta_{py} - 2\theta_{p_{iy}}) \right].$$

The functions  $\gamma_d(2x/c)$ ,  $\gamma_r[y \sin(\theta_{py} - 2\theta_{p_{iy}})]$  are the same as those defined in (5) and, for the chirp and Doppler spectrum pupil functions, approximated by

$$\Gamma_d(f_d) = \text{rect} \left( \frac{f_d}{\Delta f_d} \right) \quad \text{and} \quad \Gamma_r(f_r) = \text{rect} \left( \frac{f_r}{\Delta f_r} \right)$$

these functions become

$$\Delta f_d \text{sinc} \left( \frac{2\Delta f_d x}{c} \right) \Delta f_r \text{sinc} \left[ \frac{\Delta f_r}{c} y \sin(\theta_{py} - 2\theta_{p_{iy}}) \right].$$

The product  $\gamma_d \gamma_r$  on the left-hand side of the convolution sign in (7) corresponds to the impulse response of the radar, and the resolution cell size is determined to be  $2c/[A f_r \sin(\theta_{py} - 2\theta_{p_{iy}})]$  in the range dimension and  $c/\Delta f_d$  in the azimuth dimension, this being equal to the size of the radar antenna if the full Doppler aperture is used. The function  $F_{ij}(x, y; x_i, y_i; h_{ij})$  describes the effect on the image field due to the phase variations in the scattered field arising from the unevenness of the terrain and is given by

$$\begin{aligned} F_{ij}(x, y; x_i, y_i; h_{ij}) \\ = \delta(x - x_i) \left\{ \delta \left[ y - y_j + \frac{x_i \sin 2\theta_{p_{ix}} - h_{ij} \cos \theta_{p_{ix}}}{\sin(\theta_{py} - 2\theta_{p_{iy}})} \right] \right. \\ \left. - \delta \left[ y - y_j + \frac{x_i \sin 2\theta_{p_{ix}}}{\sin(\theta_{py} - 2\theta_{p_{iy}})} \right] \right\}, \end{aligned}$$

where  $\cos \theta_{p_{ix0}}$  is equal to the value of  $\cos \theta_{p_{ix}}$  at the Doppler frequency  $f_d$  equal to zero.

The scattering factor  $\beta$  is dependent on the tilts of the ocean waves ( $\theta_{p_{ix}}, \theta_{p_{iy}}$ ) and also the distance away from nadir as determined by  $\theta_{py}$  and the size of the small scale roughness ( $l_i, l_j$ ). A modulation in the wave tilt or roughness size would contribute to a modulation of the intensity in the image. A detailed analysis and experimental evaluation of the effect of tilt and roughness of the terrain on the image modulations for the radar system have been reported by Schaber et al. [19] for the case of desert images and by Elachi and Brown [20] for the case of ocean wave imaging.

While in principle, the synthetic antenna length is determined by the area illuminated by the radar, the actual length is modified by the finite angle over which the radiation is backscattered by the small-scale roughness. Since this angle is determined by the spatial lengths of these scatterers, a modulation in the size of the scatterers would also result in a modulation in the azimuth resolution of the radar if the scatterer sizes were larger than the size of the radar antenna.

We note that (7) does not include the effect of motions of the surface being imaged. Since  $f_d$  is the time variable in (3), the effect of surface motions can be included by making  $g(x, y)$  a function of  $f_d$  as well. A uniform motion of  $g(x, y)$  in the  $y$ -direction with a velocity  $v_d$  can be included by substituting the function  $g(x, y - \xi/f_d)$  for  $g(x, y)$  in (3).  $\xi$  is equal to  $Z v_d / f_{r0} v_r$ ,  $v_r$  being the velocity of the radar platform. A resulting evaluation provides no change in the image except for a uniform shift proportional to  $\xi$  in the azimuth direction. A uniform motion in the  $x$ -direction is equivalent to a change in the equivalent velocity of the aircraft and

thus a change in the focusing parameter for the radar imagery.

At any one point on the ocean surface, the height varies according to the orbital velocity, and the cross-section of this point according to the ocean wavelength. A patch of constant cross-section moves in the direction of the ocean wave propagation at the ocean wave velocity. Since the radar maps the time delay of the backscattered signal from a patch of constant cross-section, the ocean wave appears to it to be moving in a plane parallel to the radar platform motion and the orbital velocity effects are not important. However, an object of constant cross-section, such as a ship, resting at a particular point on the ocean, and moving vertically at the orbital velocity will have a modified image and its image will generally be degraded in the azimuth direction. It should be pointed out that the synthetic aperture radar is sensitive to the variation of time delays of the signal scattered by a target, and the actual effect of the instantaneous shift in the frequency of the backscattered signal due to the orbital motion is included in this time delay variation which depends on the variation of position of the scattering patch. In such a consideration, the variation of the velocity and radar cross-section of this patch must also be taken into account, and approximating these quantities by a constant number during the integration time of the radar processor has in the past led to considerable confusion in the interpretation of the synthetic aperture radar ocean wave imagery. A dependence of the ocean wave tilt angle  $\theta_{ptx}$  on time would lead to a change in the resolution cell size of the radar, the result being a smaller resolution cell size if the tilt angle is increasing and a larger cell size if it is decreasing. This effect, however, would be very small for the normally occurring rates of change of the tilt. The random motion of the small-scale roughness would have negligible overall effect on the radar image since its main contribution is in the backscatter modulation function  $\beta_{ij}$ , and a treatment of this effect has been considered by Elachi and Evans [21].

We examine (7) to consider the possibility of obtaining wave height information from the ocean image. For a particular point  $P_i$  in the area of interest, the image electric field may be rewritten as

$$e_{P_i}(x_{P_i}, y_{P_i}, f_{r0}) = \exp\left(\frac{i2\pi}{c} f_{r0} y_{P_i}\right) \cdot \left\{ \alpha + \sum_{ij} \beta_{ij} \exp\left[\frac{i2\pi}{c} f_{r0} (y_j \sin(\theta_{py} - 2\theta_{ptx}) - x_i \sin 2\theta_{ptx})\right] \right. \\ \left. \cdot \exp\left(\frac{i4\pi}{c} f_{r0} \cos \theta_{py} h_{ij}\right) - 1 \right\} \quad (8)$$

where we have used the fact that the finite size of  $\gamma_r(y)$ ,  $\gamma_d(x)$  limits the number of scatterers that contribute to the field at an image point. In this case, this number is given by the summation over the  $N$  scatterers;  $\alpha$  is the uniform background level term and is the first term on the right-hand side of (7);  $\beta$  is the scattering factor;  $(\theta_{py}, \theta_{ptx})$  are the tilt angles at points  $(x_i, y_j)$  and have been assumed to be slowly varying compared to the small-scale roughness  $h(x, y)$ . If we assume that the scatterers are densely packed [22],  $N$  is equal to the resolution cell area divided by the area occupied by a scatterer, and this quantity can be approximated by  $2c^2 (l_r l_p A f_r A f_d \sin \theta_{py})$  if we neglect the effect on the resolution cell size due to the small tilt angles, the scatterer size modulations, and the heights  $h_{ij}$ .

The small-scale roughness is usually less than the wavelength of the radar and the variation of  $\exp[(i4\pi/c) f_{r0} \cos \theta_{py} h_{ij}]$  with respect to  $f_{r0}$  is negligibly small over the chirp spectrum bandwidth available. Also, since  $\theta_{ptx}$  is a small number, we can approximate  $\sin(\theta_{py} - 2\theta_{ptx})$  by  $(\sin \theta_{py} - \cos \theta_{py} \sin 2\theta_{ptx})$ . The term  $\exp[(i2\pi/c) f_{r0} y_j \sin \theta_{py}]$  represents the variation of the phase of the radar wave incident at angle  $\theta_{py}$  across the resolution cell size of the radar, and with respect to change in radar frequency, occurs in an interval equal to the chirp bandwidth of the radar processor. The factor

$$\exp\left[\frac{-i2\pi}{c} f_{r0} (y_j \cos \theta_{py} \sin 2\theta_{ptx} + x_i \sin 2\theta_{ptx})\right]$$

corresponds to the phase variations due to the variations in the tilt angles of the terrain. If the resolution cell is small enough so that the tilt of the waves does not change appreciably across its length, the decorrelation length due to the tilt in the range and azimuth directions is determined by  $[\Delta f_r (2 \sin \theta_{ptx})] \times (\sin \theta_{py} \cos \theta_{py})$  and  $\Delta f_d (4 \sin \theta_{ptx})$ , respectively. The composite decorrelation length would depend upon the sum of the slopes of the individual decorrelation curves for the resolution cell size and the tilts approximated by

$$\Delta f_r + 1 + 2(\cos \theta_{py} \sin \theta_{py}) \sin \theta_{ptx} + (4 \sin \theta_{ptx}) \Delta f_d$$

The resolution cell size of the radar may be large enough to cover more than half an ocean wave, in which case the tilt angles  $(\theta_{ptx}, \theta_{py})$  cannot be assumed to be constant within a resolution cell of the radar. We can rewrite  $(y_j \cos \theta_{py} \sin 2\theta_{ptx} + x_i \sin 2\theta_{ptx})$  as  $2H_{ij}$ , corresponding to the height of the ocean wave. Due to the  $\cos \theta_{py}$  term, the dependence of the resolution cell size on  $\sin \theta_{py}$  and the tilt angle variations, the  $H_{ij}$  as defined is not strictly the ocean wave height parameter, but for the purpose of the statistical analysis, it may be considered to be equivalent. We calculate the cross-



correlation for the image intensities processed for the two frequencies  $f_{r0}$  and  $(f_{r0} + \Delta f_{r0})$  and obtain the following result

$$\begin{aligned} & \langle I_{P1}(f_{r0}) I_{P1}(f_{r0} + \Delta f_{r0}) \rangle \\ &= [x^4 + 4Nx^2\beta^2 + 2\beta^4 N(1 + 2N)] \\ &+ 2x^2\beta^2\eta_H \left( \frac{2\Delta f_{r0}}{c} \sigma_H \right) \left[ \eta_h \left( \frac{2\Delta f_{r0}}{c} \sigma_h \right) + 1 \right] \Gamma_r(\Delta f_{r0}) \\ &+ \beta^4(N^2 - N)\eta_H^2 \left( \frac{2\Delta f_{r0}}{c} \sigma_H \right) \\ &\cdot \left[ \eta_h \left( \frac{2\Delta f_{r0}}{c} \sigma_h \right) + 1 \right] \Gamma_r^2(\Delta f_{r0}). \end{aligned} \quad (9a)$$

The brackets  $\langle \rangle$  denote the mean value operation.  $\beta$  is the average value of  $\beta_{ij}$  within the resolution cell and is the backscattering cross-section of the area of interest.  $N$ , the number of scatterers in a resolution cell, is approximately equal to  $2c^2(\Delta f_r \Delta f_d \sin \theta_{py} l_i l_j)$ , where  $l_i l_j$  are the sizes of the small-scale scatterers.  $\sigma_H$  is the standard deviation of the ocean wave height function  $H_{ij}$ , and  $\sigma_h$  is the standard deviation of the heights of the scattering waves.  $\eta_H$  and  $\eta_h$  are the characteristic functions for the probability density of the wave height  $H_{ij}$  and the roughness  $h_{ij}$  and, for a Gaussian distribution, are equal to  $\exp\{-1/2[4\pi(\Delta f_{r0}/c)\sigma_H]^2\}$  and  $\exp\{-1/2[4\pi(\Delta f_{r0}/c)\sigma_h]^2\}$ , respectively. For the special case when the resolution cell size is smaller than an ocean wavelength, the characteristic function for the wave height  $\eta_H$  in (9) may be replaced by the characteristic function for the wave slopes equal to

$$\eta_{Hxy}(2\Delta f_{r0}\Delta y \cos \theta_{py} \sin \theta_{p_{ty}}) \eta_{Hxx}(2\Delta f_{r0}\Delta x \sin \theta_{p_{tx}}).$$

for  $\Delta x$ ,  $\Delta y$ , the resolution cell sizes. For a Gaussian density function for the slopes, this function is equal to

$$\begin{aligned} & \exp \left\{ -1/2 \left[ 4\pi \left( \frac{\Delta f_{r0}}{\Delta f_r} \right) \left( \frac{\cos \theta_{py}}{\sin \theta_{p_y}} \right) \sigma_{Hy} \right]^2 \right\} \\ & \cdot \exp \left\{ -1/2 \left[ 4\pi \left( \frac{\Delta f_{r0}}{4\Delta f_d} \right)^2 \sigma_{Hx} \right]^2 \right\}, \end{aligned}$$

where  $\sigma_{Hy}$ ,  $\sigma_{Hx}$  are the standard deviations of the wave slopes in the  $y$ - and  $x$ -directions, respectively.  $x$ , which corresponds to the specular reflection term, is negligibly small compared to  $\beta$  for the non-nadir angles and may be neglected in (9a). Further,  $N$  is a very large number, and the terms of order  $N$  can be neglected in comparison to the terms containing  $N^2$ .  $\sigma_h$  is a small number compared to  $\sigma_H$ , and  $\eta_h[2\Delta f_{r0}/c\sigma_h]$  may be approximated by unity for the values of  $\Delta f_{r0}$  involved with the radar chirp. We define the quantity

$$\langle I_{P1}(f_{r0}) I_{P1}(f_{r0} + \Delta f_{r0}) \rangle \frac{1}{4N^2\beta^4} = 1$$

by  $R(\Delta f_{r0})$  as the normalized cross-correlation function for the radar image. This quantity is simply a product of the square of the radar processor pupil function,  $\Gamma_r^2(\Delta f_{r0})$ , and the square of the characteristic function of the wave heights or the characteristic function for the wave slopes. This may be written as

$$R(\Delta f_{r0}) \approx \eta_H^2 \left( \frac{2\Delta f_{r0}}{c} \right) \sigma_H^2 \Gamma_r^2(\Delta f_{r0}) \quad (9b)$$

for the radar resolution cell much larger than an ocean wavelength, and

$$\begin{aligned} R(\Delta f_{r0}) \approx & \eta_{Hy}^2 \left( \frac{2\Delta f_{r0}}{c} \Delta y \cos \theta_{py} \sigma_{Hy} \right) \\ & \cdot \eta_{Hx}^2 \left( \frac{2\Delta f_{r0}}{c} \Delta x \sin \theta_{p_{tx}} \right) \Gamma_r^2(\Delta f_{r0}) \end{aligned} \quad (9c)$$

for the radar resolution cell smaller than an ocean wavelength. Thus, an experimental determination of the cross-correlation function along with a prior knowledge of the pupil function in range for the radar processor would lead to a determination of the characteristic function for the ocean wave heights from which the wave height spectra of the ocean waves may be determined. When the radar resolution cell is larger than the ocean wavelength, (9b) can be used to interpret the radar data to obtain information on the distribution of wave heights. When the radar resolution is smaller than an ocean wavelength, (9c) provides a distribution of wave slopes, and knowledge of the radar resolution cell size can be used to convert this information into wave height information. Also, by examining the rate of change of  $R(\Delta f_{r0})$  as a function of  $\sigma_H$ , we note that the sensitivity of the measurement of  $\sigma_H$  from  $R(\Delta f_{r0})$  increases with  $\sigma_H$ . The pupil function  $\Gamma_r(\Delta f_{r0})$  in (9) has the effective width  $(\Delta f_r/\Delta f_{r0})$ . For  $\Delta f_{r0}$  larger than  $\Delta f_r/2$ , the cross-correlation function becomes very small, and for a measurement of the characteristic function  $\eta_H$ , it is necessary to measure  $R(\Delta f_{r0})$  for  $\Delta f_{r0} < \Delta f_r/2$ . While the theoretical form of the pupil function  $\Gamma_r(f_r)$  is a step function of bandwidth  $\Delta f_r$ , practical radar systems do not realize this functional form because of the antenna pattern and nonlinearities in the data recording and processing operations.

The result in (9) could have been obtained directly from simple physical considerations by adding up the phases of the electric field reflected by the terrain within a resolution cell area of the terrain. The pupil function factor  $\Gamma_r(\Delta f_{r0})$  is a direct consequence of the non-vertical angle of incidence of the radar radiation, and the characteristic function factor  $\eta_H$  is a consequence of the phase variations for reflection from a rough surface.

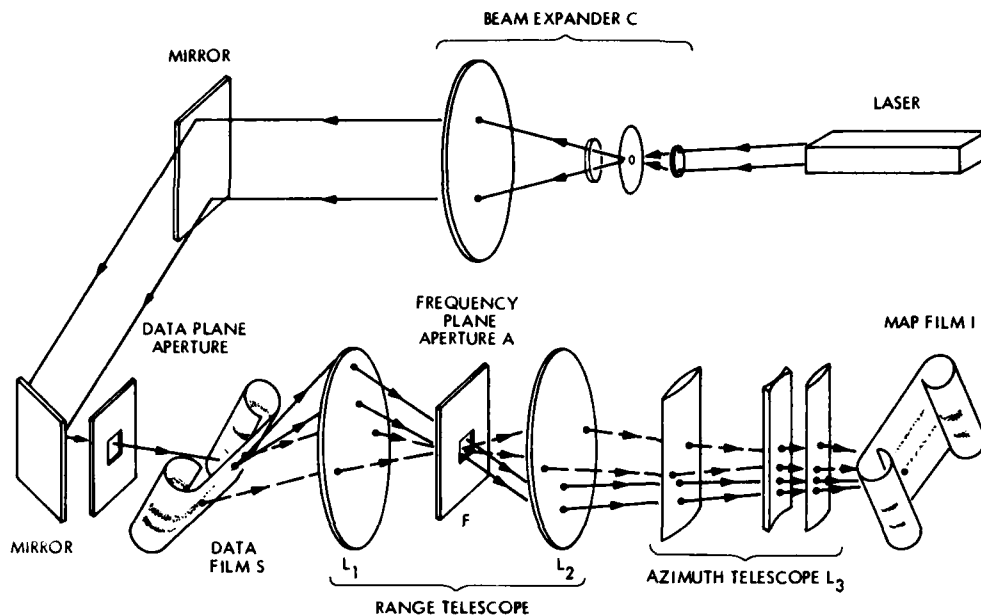


Fig. 3. Configuration of the tilted plane processor for compressing the radar signal data. The bandwidth of the chirp or Doppler spectrum is controlled by the size of aperture A of the frequency plane filter F, and the center frequency by the position of A.

### Experimental Procedure

The radar system used for obtaining the ocean wave images is the JPL L-band synthetic aperture radar; its performance has been described in detail by Brown et al. [1]. It operates at 25-cm wavelength, with a phased array antenna 75 cm long, 25 cm wide, and 5 cm thick to obtain a range beamwidth of 90 deg, centered 45 deg off vertical and an azimuth beamwidth of 18 deg, centered on zero doppler. The transmitted peak power is 7 kW, the pulse repetition frequency 1 kHz, the radar platform velocity 250 m/s, the pulse-width 1.25  $\mu$ s, and the total chirp spectrum bandwidth 10 MHz. The data are recorded optically by the Good-year 102, dual-channel recorder and processed optically to convert the signal film into imagery with a resolution of 20 m range (45 deg) and 10 m along track.

The configuration of the optical processor used to convert the synthetic aperture signal data into images is shown in Fig. 3, and a detailed analysis of this type of system is given by Kozma et al. [23]. The signal film S is illuminated by the output of a HeNe laser after it has passed through the spatial filter-collimating lens system C. The Fourier transform lens  $L_1$ , the frequency plane filter F, and the imaging lens  $L_2$  convert the range data into the range image at plane I. The cylindrical azimuth telescope  $L_3$  has the function

of additionally bringing the azimuth data to an along-track image focus at plane I. By controlling the slit aperture and the spatial position of the frequency plane filter F, the chirp frequency and the center bandwidth can be controlled. By setting the value of aperture A at a given range bandwidth, the same strip of signal film can be processed for different center frequencies to provide the required images by positioning the location of A at the corresponding spatial coordinate in the range dimension.

The optical setup used to cross-correlate pairs of images of the same area but obtained for different chirp spectrum center frequencies is shown in Fig. 4. An argon-ion laser L, combined with a spatial filter collimator system C, is used to illuminate the image film  $I_1(x, y, f_{r0})$  processed for the particular chirp spectrum frequency  $f_{r0}$  and the bandwidth  $f_r$ . The two Fourier transform lenses  $L_1$  and  $L_2$ , each of focal length  $f$ , are used to provide a unity magnification image onto plane II, where the transparency of transmissivity  $I_2(x + \Delta x, y + \Delta y, f_{r0} + \Delta f_{r0})$  is situated, which is the image of the same area as  $I_1(x, y, f_{r0})$  but processed at the chirp spectrum frequency  $f_{r0} + \Delta f_{r0}$  and shifted by  $(\Delta x, \Delta y)$  in the  $x$ - and  $y$ -directions for the optical system. The distance between  $L_1$  and  $L_2$  is  $2f$ , and between  $I_1$  and  $L_1$  and  $I_2$  and  $L_2$ ,  $f$ , so that no

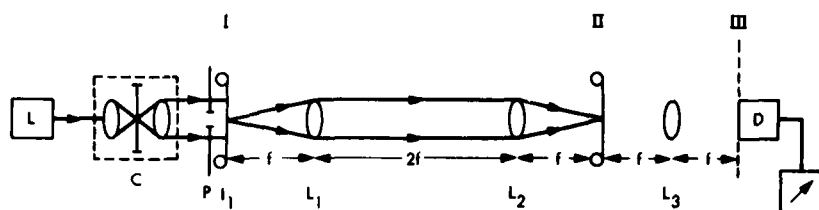


Fig. 4. Configuration of the optical cross-correlator. The pupil P limits the area of I, at plane I illuminated by laser L and collimator C. The lenses  $L_1$  and  $L_2$  of focal lengths  $f$  (30.5 cm each) image  $I_1$ , onto plane II. The lens  $L_3$  of focal length  $f$ , Fourier transforms the product  $I_1 I_2$  onto plane III, where the total power is detected by detector D

phase effects are introduced by the imaging process. The spatial distribution of the electric field at the exit plane of II is proportional to  $I_1(x, y, f_{r0})I_2(x + \Delta x, y + \Delta y, f_{r0} + \Delta f_{r0})$ , and this is Fourier transformed by the lens  $L_3$  of focal length  $f$  onto plane III. The power incident on plane III is measured by a photodetector whose aperture is large enough to collect all the Fourier components involved. Using Parseval's theorem, and assuming a unit amplitude illumination at  $I_1$ , the power measured by the detector is

$$W_{\Delta f_r}(\Delta f_{r0}, \Delta x, \Delta y) = \int \int_{-\infty}^{\infty} |I_1(x, y, f_{r0})I_2(x + \Delta x, y + \Delta y, f_{r0} + \Delta f_{r0})|^2 dx dy,$$

where  $\Delta f_r$  is the bandwidth at which  $I_1$  and  $I_2$  were processed.  $(\Delta x, \Delta y)$  are relative shifts of  $I_1$  with respect to  $I_2$ , and  $f_{r0}, f_{r0} + \Delta f_{r0}$  are the two processing frequencies involved. For the purposes of the wave height measurement,  $\Delta x$  and  $\Delta y$  would be equated to zero and the function  $W_{\Delta f_r}(\Delta f_{r0}, 0, 0)$  plotted as a function of  $\Delta f_{r0}$ . In considering  $I_1$  and  $I_2$  to be the two images of the ocean wave, we have assumed that the film nonlinearities of the image film can be ignored and have factored out the gamma of the film.

In order to obtain an experimental evaluation of  $\langle I_{P_1}(f_{r0})I_{P_1}(f_{r0} + \Delta f_{r0}) \rangle$  in (9) for a given ocean area, we use the optical processor to obtain the successive images  $I(x, y, f_{r0}), I(x, y, f_{r0} + \Delta f_{r01}), \dots, I(x, y, f_{r0} + \Delta f_{r0n})$  at the frequencies  $f_{r0}, f_{r0} + \Delta f_{r01}, \dots, f_{r0} + \Delta f_{r0n}$  but for the fixed processing bandwidth of  $\Delta f_r$ . The transparency  $I(x, y, f_{r0})$  is placed in plane I of the optical cross-correlator in Fig. 4, and using the time codes in these images as a reference for accurate superposition of the image of  $I(x, y, f_{r0})$  on  $I(x, y, f_{r0} + \Delta f_{r0k})$  at plane II, the quantity  $W_{\Delta f_r}(\Delta f_{r0k}, 0, 0)$  is measured for each successive  $I(x, y, f_{r0} + \Delta f_{r0k})$ . In order to account for the effects of laser power fluctuations and background exposures on the film, a measurement of  $W_{\Delta f_r}(\Delta f_{r0k})$  is also made for large  $\Delta x, \Delta y$ , and this is subtracted from  $W_{\Delta f_r}(\Delta f_{r0k}, 0, 0)$ . To normalize the effects of average intensity variations for different

$I(x, y, f_{r0} + \Delta f_{r0k})$  further, the difference

$$[W_{\Delta f_r}(\Delta f_{r0k}, 0, 0) - W_{\Delta f_r}(\Delta f_{r0k}, \Delta x, \Delta y)]$$

is divided by the correlation number when there is no frequency shift, i.e., by  $W_{\Delta f_r}(0, 0, 0) - W_{\Delta f_r}(0, \Delta x, \Delta y)$ . The resulting curve  $R^E(\Delta f_{r0})$ , which is defined by

$$\frac{W_{\Delta f_r}(\Delta f_{r0k}, 0, 0) - W_{\Delta f_r}(\Delta f_{r0k}, \Delta x, \Delta y)}{W_{\Delta f_r}(0, 0, 0) - W_{\Delta f_r}(0, \Delta x, \Delta y)}$$

is plotted as a function of  $\Delta f_{r0}$  and corresponds to the normalized value of  $|\langle I_{P_1}(f_{r0})I_{P_1}(f_{r0} + \Delta f_{r0}) \rangle|^2$ , the area on the image correlated being controlled by the pupil P. The quantity  $R^E(\Delta f_{r0})$  measured by the cross-correlator is equivalent to  $R(\Delta f_{r0})$  defined in (9), the superscript E being used to differentiate between the experimental and the theoretical functions involved.

## Results

An effective visual demonstration of the decorrelation of the radar images, processed for different sections of the chirp bandwidth, as a function of the center frequency separations for these bandwidths, can be observed by superimposing pairs of the images, rotating them slightly with respect to each other and observing the resulting moiré fringes [24]. The higher the correlation between two transparencies superimposed and rotated slightly with respect to each other, the higher the contrast of the moiré fringes observed. Figure 5a is an image of the ocean, where the full chirp and Doppler bandwidths available to the radar processor are used. The ocean waves can be seen quite clearly. Figure 5b is an image of the same area, processed for a 2-MHz chirp bandwidth. The elongation in the range dimension of the image speckles, whose average size is equal to the resolution of the radar system, can be readily seen, and the ocean waves are not visible. Figure 5c is the result obtained when two images processed at 2-MHz bandwidth but separated in their chirp spectrum center frequencies by an interval of 1 MHz are superposed on each other and rotated slightly. The moiré fringes are easily visible, indicating

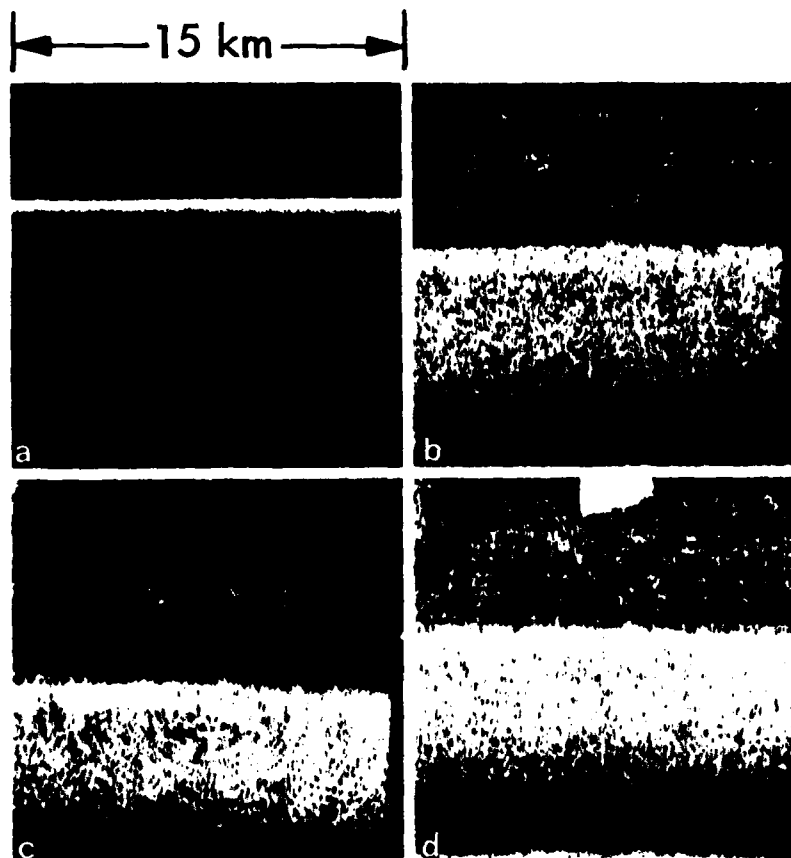


Fig. 5.(a) Radar image of an ocean wave pattern. The image was generated using the total 10 MHz chirp bandwidth in the radar signal. (b) Image of the same area as (a), generated from the same signal film after a chirp bandpass optical filter (from 1200 to 1202 MHz) has been used during processing. (c) Two superimposed and slightly rotated images of the same area, processed with 1200- to 1202-MHz and 1201- to 1203-MHz bandpass filters, respectively. The high contrast of the moiré fringes implies good correlation. (d) Same as (c) except that the two images were obtained with 1200- to 1202-MHz and 1203- to 1205-MHz chirp bandpass filters, respectively. The moiré fringes have extremely low contrast.

reasonably high correlation between the two images. Figure 5d is the result of two superimposed and rotated images of the same area, each processed again for the chirp bandwidth of 2 MHz but with a center frequency separation of 3 MHz. The low contrast of the moiré fringes indicates that considerable decorrelation has taken place for the frequency separation of 3 MHz.

In order to evaluate the function  $R(\Delta f_r)$  experimentally and determine the feasibility of measuring ocean wave heights from a measurement of this cross-correlation function, images taken by the synthetic aperture radar for the following four areas were processed: 1) in the vicinity of the ship Papa in the Gulf of Alaska on March 31, 1975, where the significant wave height reported was 4 m; 2) the North Atlantic near Shannon, Ireland, on September 28, 1974, where the significant wave height reported was 1.8 m; 3) the California coast of Monterey Bay on October 6, 1975, where the significant wave height reported was 1.1 m; and Monterey

Bay on August 13, 1975, where the significant wave height reported was 0.9 m.

Figure 6 is a plot of the function  $R^2(\Delta f_r)$ , where the bandwidth used in processing the successive images was 2 MHz, the processing chirp frequency interval for each successive pair being 0.5 MHz. Since the curves are a product of the characteristic function for the ocean wave heights and the radar pupil function, and since the radar pupil function falls quite drastically for the frequency separations greater than half the chirp bandwidth for the radar processor, it is necessary to confine the examination of the experimental curves for  $\Delta f_r < 1$  MHz to obtain the wave height information. For a given ocean area, the curves were obtained by performing cross-correlations over different portions of that area, and the deviation of the values of  $R^2(\Delta f_r)$  for a given  $\Delta f_r$  was approximately  $\pm 0.05$ . As expected, no effect was noticed for the variation of  $R^2(\Delta f_r)$  for different positions along the y-axis since the radar aperture function is independent of the look angle.

An examination of  $R^E$  (0.5 MHz) shows a variation in the wavelength decorrelation with respect to the ocean wave heights involved, and the points appear to fit the curve  $0.65 \exp(-0.066\sigma_H)$ , where  $\sigma_H$  is the significant wave height. The coefficient 0.066 in the exponential is due to the decorrelation factor from phase from crest to trough of a wave, and is close to the theoretical value of  $[16\pi(1/f_{r0} c)]$ . The factor of 0.65 is the value of the radar chirp spectrum function at 0.5 MHz.

The dependence of the decorrelation function  $R^E(\Delta f_{r0})$  on the chirp spectrum bandwidth used was verified by obtaining the curves  $R^E(\Delta f_{r0})$  for 6-, 4-, 2-, 1-, and 0.5-MHz bandwidths, and extensive decorrelation was noted for the frequency separations  $\Delta f_{r0}$  equal to half the bandwidth employed in the processing. For an infinite-bandwidth radar, the effect on the decorrelation should be nonexistent. By extrapolating the  $R^E$  (0.5 MHz) for an infinite bandwidth and comparing this result for  $R^E$  (0.5 MHz) at 2 MHz, the value of 0.65 for the chirp aperture effect was verified.

When the cross-correlation function  $R^E(\Delta f_{r0})$  is evaluated for the frequency separation of  $\Delta f_{r0} = 1$  MHz for the different wave heights, the functional value obtained is  $0.29 \exp(0.12\sigma_H)$ . The doubling of the factor in the exponent is due to the doubling of  $\Delta f_{r0}$ . The effect of the chirp spectrum aperture function is given by the factor 0.29 for this case.

The chirp aperture function is the Fourier transform of the radar resolution in range. This resolution can be readily measured by plotting  $R^E(0)$  for different position separations of the two transparencies being correlated, and an experimental examination of this resolution function shows that the width of the resolution cell is inversely proportional to the chirp bandwidth used.

In our results, we have focused our attention on measuring the effect on the radar images due to different effective frequencies of the radar operation. A similar calculation and experimental procedure can be employed to exploit the effect on the radar images of different look angles for the radar, and this can be done by processing the radar data for different Doppler bandwidths and cross-correlating these images as a function of the center Doppler frequency separations for these bandwidths.

### Conclusions

In (7), we calculate the electric field at the image of a synthetic aperture radar for an uneven surface, such

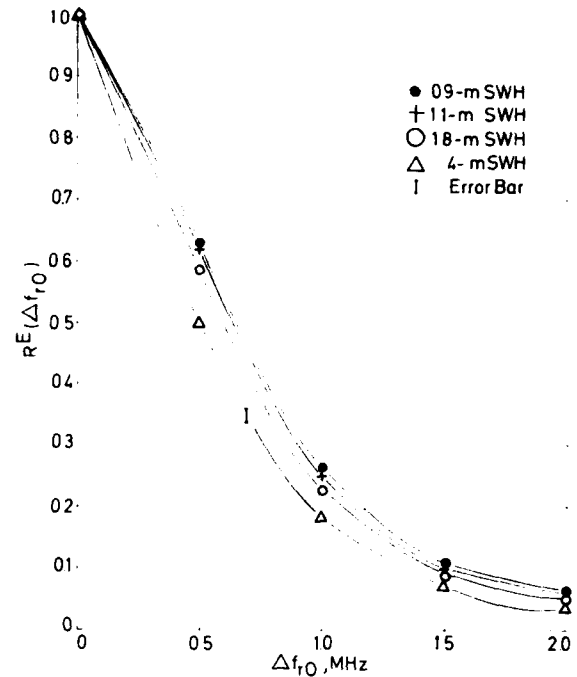


Fig. 6. Cross-correlation data curves,  $R^E(\Delta f_{r0})$ , for the ocean wave heights of 0.9, 1.1, 1.8, and 4 m as a function of frequency separation for the chirp center frequencies used in the processing. The chirp bandwidth used in the processing was equal to 2 MHz.

as ocean waves, and evaluate the cross-correlation for pairs of those images, as a function of their frequency spacing of the radar processing, in (9). We show that this cross-correlation is the square of the product of the ocean wave heights and the radar range pupil function used in the processing. An optical technique is outlined to determine this cross-correlation function, and Figure 6 presents a set of measurements of this curve for ocean wave heights of 4, 1.8, 1.1, and 0.9 m, respectively. The value of this cross-correlation for a frequency spacing of 0.5 MHz is measured to be  $0.65 \exp(-0.066\sigma_H)$ , where  $\sigma_H$  is the significant wave height and the chirp bandwidth used is 2 MHz, and the corresponding value for a frequency spacing of 1 MHz is determined to be  $0.29 \exp(-0.12\sigma_H)$ .

**Acknowledgements.** We express our special thanks to Dr. Charles Elachi for his invaluable support and encouragement during the course of this work. We also acknowledge helpful discussions with W. E. Brown Jr. and Prof. David E. Weissman. We thank Tom Bicknell and Tom Anderson for providing the necessary optical processor image data, Prof. Nicholas George and David E. Drake for their support during the preliminary stages of building the optical cross-correlator, and Jean-Michelle Caillat for the collection of the surface truth data on the ocean wave heights from ship reports and buoy measurements.

## References

1. W.E. Brown Jr., C. Elachi, T.W. Thompson: *J. Geophys. Res.* **81**, 2657 (1976)
2. C. Elachi: *J. Geophys. Res.* (in press)
3. D.E. Barrick: In *Remote Sensing of the Troposphere*, ed. by V.L. Derr (U.S. Government Printing Office, Washington, D.C., 1972) Ch. 12
4. G.T. Ruck, D.E. Barrick, T. Kaliszewski: *Bistatic Radar Sea State Monitoring* (Battelle Columbus Laboratories, Columbus, Ohio, 1971) Rep. 1388-19
5. D.E. Weissman: *IEEE Trans. AP-21*, 649 (1973)
6. D.E. Weissman, C.T. Swift, W.L. Jones Jr., J.W. Johnson, W.L. Grantham, J.A. Howell, J.C. Fedors, J.J. Davis: *URSI Fall Meeting*, Boulder, Colorado (1974)
7. B.D. Zamarayev, A.I. Kalmykov: *Izvestia, USSR Academy of Sciences Atmospheric and Ocean Physics* **5**, 64 (1969)
8. D.L. Hammond, R.A. Manella, E.J. Walsh: *URSI Fall Meeting*, Boulder, Colorado (1975)
9. T.L. Wadley: *Trans. South African Inst. Electr. Engrs.* **49**, 143 (1958)
10. A. Jain: *A Wavelength Diversity Technique for Smoothing of Speckle*, Ph. D. Thesis, California Institute of Technology, Pasadena, California (1973)
11. N. George, A. Jain: *Appl. Phys.* **4**, 201 (1974)
12. N. George, A. Jain, R.D.S. Melville: *Appl. Phys.* **1**, 157 (1975)
13. R.O. Harger: *Synthetic Aperture Radar Systems* (Academic Press, New York 1970)
14. L.J. Cutrona: *Synthetic Aperture Radar, Radar Handbook*, ed. by Merrill I. Skolnik (McGraw Hill, New York 1970) Ch. 23
15. A.W. Rihaczek: *Principles of High Resolution Radar* (McGraw Hill, New York 1969) Ch. 4
16. P. Beckmann, A. Spizzichino: *The Scattering of Electromagnetic Waves from Rough Surfaces* (The Macmillan Co., New York 1963) Ch. 3
17. B. Kinsmann: *Wind Waves - Their Generation and Propagation on the Ocean Surface* (Prentice Hall, Englewood Cliffs N.J. 1965)
18. N. George, A. Jain: *Appl. Opt.* **12**, 1202 (1973)
19. G.G. Schaber, G.L. Berlin, W.E. Brown, Jr.: *Geol. Soc. Amer. Bull.*, March 1975
20. C. Elachi, W.E. Brown Jr.: *IEEE Trans. on Ant. and Prop.* (in press)
21. C. Elachi, D.D. Evans: *IEEE Trans. on Ant. and Prop.* (in press)
22. L.I. Goldfischer: *J. Opt. Soc. Am.* **55**, 247 (1965)
23. A. Kozma, E.N. Leith, N.G. Massey: *Appl. Opt.* **11**, 1766 (1972)
24. G. Oster: *Symposium on Quasi-Optics* (Polytechnic Institute of Brooklyn, June (1964))

## APPENDIX C

## TWO PAPERS ON SAR MODELING OF OCEAN WAVES

- \*Paper 1: "Synthetic Aperture Radar Modeling of Surface Ocean Waves," by R.A. Shuchman, A. Klooster and A.M. Maffett
- \*Paper 2. "A SAR Mechanism for Imaging Ocean Waves," by R.K. Raney and R.A. Shuchman

- \*1. Published in the Proceedings of the 13th International Symposium on Remote Sensing of Environment, Ann Arbor, Michigan, 1979.
- \*2. Published in the Proceedings of the 5th Canadian Symposium on Remote Sensing, Victoria, British Columbia, August, 1978.

SYNTHETIC APERTURE RADAR MODELING OF  
SURFACE OCEAN WAVES\*

R.A. Shuchman  
A. Klooster

Environmental Research Institute of Michigan (ERIM)  
Ann Arbor, Michigan

A.L. Maffett  
ERIM Consultant  
Adjunct Professor  
University of Michigan, Dearborn

ABSTRACT

A number of models exist that attempt to explain wave imagery obtained with a synthetic aperture radar (SAR). These models are of two types, static models that depend on instantaneous surface features and dynamic models that employ surface velocities. SAR imagery has been discussed in the literature using both types, though as yet there exists no widely accepted understanding of the imaging mechanism for SARs. This study attempts to draw together analytical and experimental results based on a combination of these two types in order to approach a more satisfactory model for SAR ocean wave imaging.

Radar backscatter values ( $\sigma_0$ ) were calculated from 1.3 and 9.4 GHz SAR data collected off Marineland, Florida. The  $\sigma_0$  (averaged over many wave trains) data collected at Marineland can best be modeled by the Bragg-Rice-Phillips model which is based on roughness variation and complex dielectric constant of oceans. This result suggests that capillaries on the surface of oceanic waves are the primary cause for the surface return observed by a synthetic aperture radar (SAR).

An examination of the effect of salinity and sea temperature at small and medium incidence angles, indicated that their effects upon sea surface reflection coefficients seem to be insignificant, for either of the linear polarizations. At large incidence angles, i.e., near-grazing, there is a more pronounced change in the behavior of the vertical polarization reflection coefficient.

The authors' observation of moving ocean, imaged by the SAR and studied in the SAR optical correlator, support a theory that the ocean surface appears relatively stationary in the absence of currents. The reflecting surface is most likely moving slowly (i.e., capillaries, wave, phase velocity and orbital wave velocities) relative to the phase velocity of the large gravity waves. The stationary theory still applies since the phase velocity of the capillaries and orbital velocity of the gravity waves is more nearly stationary when compared to the phase velocity of the waves.

---

\*This work was supported by ONR Contract N00014-76-C-1048.  
The technical monitor is Mr. Hans Dolezalek.



## 1. INTRODUCTION

Imaging radars are active devices that sense the environment with short wavelength electromagnetic waves. As active sensors, radars provide their own illumination in the microwave region of the electro-magnetic spectrum and thus are not affected by diurnal changes in emitted or reflected energy from the earth's surface. Additionally, radars have the recognized ability to image the earth's surface independently of weather conditions or solar illumination. Most radars operate in the frequency region of 300 Mz (1 m) to 30 GHz (1 cm), and bandwidths are commonly designated by letters. The radar discussed in this paper is designated as L-band (23.5 cm) and X-band (3.2 cm).

Side-looking airborne radar (SLAR), as will be discussed in this paper, uses pulse ranging, whereby the radar antenna attached to a moving aircraft illuminates a section of the ground and the amplitude, phase and polarization of the returned echoes are processed to determine the distance to the scene and to obtain the measure or relative strength of the return ( $\sigma_0$ ).

This paper discusses a specialized form of SLAR called a Synthetic Aperture Radar (SAR). SAR utilizes the Doppler history (change of phase) associated with the motion of the aircraft, recording both the phase and the amplitude of the backscattered energy, thus improving the along track or azimuth resolution. The longer the radar data length, the greater the improvement in the along track resolution of the system.

The principle in imaging any surface with a radar is that the backscatter of microwave energy (echo) received by the radar receiver contains information on the roughness characteristics (shapes, dimensions, and orientations) of the reflecting area. These parameters that influence the echo received from ocean waves include the motion of the scattering surfaces, the so-called speckle effect, system resolution and non-coherent integration as well as contributions attributable to wind, waves, surface currents and surface tension. Also, the orientation of ocean waves to the radar look direction must be considered. When attempting to understand the SAR ocean-wave imaging mechanism, one must also consider factors pertaining to wave orbital velocity, Bragg scatter velocity, and long (or resolvable) wave phase velocity (Teleki, et al., 1978).

A number of models exist that attempt to explain wave imagery obtained with a synthetic aperture radar (SAR). These models are of two types, static models that depend on instantaneous surface features and dynamic models that employ surface velocities. SAR imagery has been discussed in the literature using both types; though as yet there exists no widely accepted understanding of the imaging mechanism for SARs. This paper attempts to draw together analytical and experimental results based on a combination of these two types in order to approach a more satisfactory model for SAR ocean wave imaging.

## 2. RADAR SYSTEM AND FLIGHT PATTERNS

The experimental observations presented in this paper were obtained from analysis of the ERIM dual frequency and dual polarized SAR system. The ERIM X-L system described by Rawson, et al. (1975) consists of a dual-wavelength and dual-polarization SAR that simultaneously images at X-band (3.2 cm) and L-band (23.5 cm). Alternate X- and L-band pulses (chosen to be either horizontally or vertically polarized) are transmitted, and reflections of both polarizations are received; thus four channels of radar imagery are simultaneously obtained. Both polarizations of X-band are recorded on one film, both polarizations of L-band on the other. The Marineland data presented in this paper were obtained from the horizontal-transmit horizontal-receive channel (HH) of both the X- and L-band receivers. The polarization of the electromagnetic radiation is defined by the direction of the electric field intensity, E, vector. For example, a horizontally polarized wave will have its E vector parallel to the local horizon.

The along-track or azimuth resolution on the ERIM system is obtained from the Synthetic-Aperture techniques given by Brown and Porcello (1969) and the cross-track or range resolution from the frequency modulated pulse compression.

During flight, the radar signals are recorded in their frequency-dispersed form and are later optically compressed in a ground based processor. The latter has been extensively described by Kozma, et al. (1972). The ERIM precision optical processor was utilized to obtain the raw  $\sigma_0$  backscatter data as well as to observe ocean wave motion effects (Cindrich, et al., 1977).

The SAR ocean data set presented was collected by the ERIM SAR system at Marineland, Florida during mid-December 1975. The Marineland experiment was conducted to obtain SAR ocean wave data in support of SEASAT-A with its L-band SAR (launched June 1978). The specific objectives of the Marineland experiment are outlined by Shemdin, et al. (1978). Wave heights and directions of long waves and slope intensities of capillary and short gravity waves were measured by an array of in-situ instruments, including a capillary sensor mounted on a wave follower, pitch-and-roll buoy, and paired orthogonal current meters.

The ERIM radar was flown over the Marineland test area using a flight pattern shown in Fig. 1. This enabled the authors to study the sensitivity of wave orientation to radar look direction.

The data discussed in this paper were collected on December 10 and 15, 1975. Figure 2 summarizes the flight lines, wind and wave conditions on December 10, 1975. Note from the figure that an offshore wind existed which was blowing from  $310^\circ$  (true) towards the incoming waves which were propagating towards  $340^\circ$  (true). The wind was blowing at 14-20 knots while the significant wave height was 0.8-1.25 meters with a period of 5-6 seconds. On December 15, a wave train identified as swell (8 sec period) was traveling in the approximate direction of  $275^\circ$  with respect to true north. The significant wave height ( $H_{1/3}$ ) was 1.5-1.8 m. The wind speed at the site on December 15 was  $5-7 \text{ ms}^{-1}$  from the east, a direction of  $90^\circ$  with respect to true north.

As mentioned previously, synthetic-aperture radar (SAR) is a coherent airborne radar that uses the motion of a moderately broad physical antenna beam to synthesize a very narrow beam, thus providing fine azimuthal (along-track) resolution (Brown and Porcello, 1969; Harger, 1970). Fine range (cross-track) resolution is achieved by transmitting either very short pulses or longer coded pulses which are compressed by matched-filtering techniques into equivalent short pulses. Usually, the coded pulse is a waveform linearly modulated in frequency.

Typically, the phase history of a scattering point in the scene is recorded on photographic film as an anamorphic (astigmatic) Fresnel zone plate. The parameters of the zone plate are set in the azimuth direction by the Doppler frequencies produced by the relative motion between the sensor and the point scatterer, and in the range direction by the structure of the transmitted pulses. The film image is a collection of superimposed zone plates representing the collection of point scatterers in the scene. This film is used by a coherent optical processor which focuses the anamorphic zone plates into the points which produced the individual microwave scatterers of the scene.

Propagating ocean wave data collection by a SAR is not suited to conventional processing techniques which assume stationary objects. Because moving ocean waves perturb the Doppler frequencies, and hence the phase histories recorded on the anamorphic zone plate, the conventional processing of these zone plates produces images of the waves that are defocused in the azimuth direction relative to stationary terrain. This defocusing by the along-track velocity of the moving ocean waves can be refocused in the processor. This is done by readjusting the azimuth focus (cylindrical focus) an amount proportional to the relative velocity of the wave trains.

The radial motion of a moving ocean wave imaged by a SAR will also perturb the signal history of a scatterer. Radial wave velocity produces an apparent tilt to the phase history as recorded on the signal film. In addition, the scatterer history will also shift across the signal film. The rotation effect described above is referred to as "range walk" and can be compensated by rotation of the cylindrical optics in the processor. These along-track and radial

velocity effects will be discussed in greater detail in the section dealing with a dynamic model of SAR wave imagery.

### 3. STATIC MODELS

The three principal static models for the backscatter ( $\sigma_0$ ) from the ocean are the facet, Bragg-Rice, and the Rayleigh scattering models. The tangent plane or facet model is based on reflections from areas whose slopes are oriented normal to the line of sight. It is assumed that the surface radius of curvature exceeds the radar's wavelength and that one can neglect random scattering and shadowing effects (Brown, et al., 1976). The radar cross section of the facet model, according to Beckman and Spizzichino (1963) is

$$\sigma_0(\theta) = \cot^2 \beta_0 \exp(-\tan \theta / \tan \beta_0)^2 \quad (1)$$

where  $\theta$  is the radar incidence angle, and  $\tan \beta_0 = 2\sigma/T$ ,  $T$  being the autocorrelation distance for a rough surface whose heights are distributed with standard deviations  $\sigma$ .

The Bragg-Rice model uses the concept that the ocean surface can be represented by a combination of periodic surfaces, so that the dominant backscatter will match some portion of the ocean wave spectrum. The model assumes that the number of favorable additions satisfy the criterion of adequate sample size, that the height and slopes of the backscattering elements are small relative to the incident wavelength, and that their distribution is isotropic. The maximum return, as measured by Wright (1966), is obtained when

$$k_w = 2k \sin \theta \quad (2)$$

where  $k_w = 2\pi/L$  and  $k = 2\pi/\lambda$  are the wave numbers and  $L$  and  $\lambda$  the wavelengths, respectively, of the capillary waves and the radar. For this model, the radar cross section

$$\sigma_0(\theta) = 4\pi k^4 \cos^4 \theta R(\theta, \psi) W(k) \quad (3)$$

where  $R(\theta, \psi)$  is the reflectivity as a function of the surface electromagnetic properties, the incidence angle measured from nadir,  $\theta$ , and the polarization angle,  $\psi$ , and where  $W(k)$  is the energy density spectrum of surface height variation evaluated at the Bragg resonant condition in Eq. (2). The energy density spectrum,  $W(k)$  can be defined for the high frequency region of the spectrum as  $Bk^{-4}$ , where reasonable values of  $B$  are approximately  $6 \times 10^{-3}$  for gravity waves and  $1.5 \times 10^{-2}$  for capillary waves (see Phillips, 1966).

Backscatter from the sea is composed of contributions from many fluctuating individual scatterers, which in the Rayleigh scattering model are represented by segments of spheres or complex shapes that are small relative to the radar wavelength. The resultant echo varies in time, reflecting relative phase differences among the echoes received from each of the scattering elements (Skolnik, 1970). The resultant radar cross section, which is relatively insensitive to look-direction because the scattering elements are moving randomly and are distributed nearly isotropically, is described by a probability density function. According to Trunk (1976), the Rayleigh scattering is more sensitive to vertical polarization and more applicable to wide pulse widths, wherein the received echo contains returns from several breaking waves, added non-coherently.

Two of the static models, the facet and Bragg-Rice scattering models were evaluated with data from the Marineland experiment as previously mentioned. Analysis indicates the facet model agrees only marginally with the data obtained with the synthetic aperture radars operated by the Environmental Research Institute of Michigan (ERIM). Results shown in Fig. 3 include the range of data reported by Beckman and Spizzichino (1963), and X-band ( $\lambda = 3.2$  cm) and L band ( $\lambda = 23.5$  cm) measurements normalized to the 12 knot wind speed measured at Marineland (equivalent to  $\beta_0 = 10^\circ$ ).

Alternatively, the Bragg-Rice model discussed by Brown, et al. (1976) and by Trunk (1976) offers more promise. For the HH polarization case, Trunk (p. 3) describes this model as

$$\sigma_{\text{HH}} = 4\pi k \sin^4 \gamma \alpha_{\text{HH}} W(2k \cos \gamma) \quad (4)$$

where  $W(K)$  is the energy density spectrum of surface height variation evaluated at the Bragg resonant condition,  $K = 2k \cos \gamma$ , and  $\gamma = \pi/2 - \theta$  is the grazing angle.  $\alpha$  is a function of the complex dielectric constant  $\epsilon$  of the ocean and is given by

$$\alpha_{\text{HH}} = \left| \frac{\epsilon - 1}{[\sin \gamma + (\epsilon - \cos^2 \gamma)^{1/2}]^2} \right|^2 \quad (5)$$

Recall that Phillips (1966) has given a bound for  $W(k)$  as  $BK^{-4}$ , where, although there is some uncertainty about its value,  $B$  can be approximated by  $6 \times 10^{-3}$  for gravity waves and by  $1.5 \times 10^{-2}$  for capillary waves. Thus, a bound for the Bragg-Rice model is given for horizontal polarization by Guinard and Daly (1970)

$$\sigma_{\text{HH}} = 1.5\pi \times 10^{-3} \alpha_{\text{HH}} \tan^4 \gamma, \quad (6)$$

Data summarized by Guinard and Daley (1970), together with data obtained by ERIM on December 15, are shown in Fig. 4 for X-band (using  $\epsilon = 48.3 - 34.9i$ ) and in Fig. 5 for L-band (using  $\epsilon = 73 - 85i$ ). The Bragg-Rice-Phillips upper bound is shown as a solid line. For the limited range of incidence angles, agreement between theory and data is good.

In summary, the reflectivity of a large area of sea surface observed by a SAR which, when averaged to yield a coarse resolution reflectivity estimate, provides an apparent brightness that approaches the Bragg-Rice-Phillips upper bound, suggests that capillaries on the surface of the oceanic waves are the primary basis for the surface properties observed by both real and synthetic aperture radar (Raney and Shuchman, 1978).

#### 4. BACKSCATTER DISTRIBUTION STUDIES

The radar backscatter distributions of Marineland data were examined to ascertain wind and wave propagation sensitivity in respect to the radar look direction. It was hoped that a study of the statistical distributions would reveal characteristic behavior which could be used to distinguish up-, down-, and cross-wave returns.

Distributions of data sets corresponding to incidence angles of 20, 30, 40, and 50° for Passes 3, 4, 5, 6, 7, and 8 of the Marineland flight of 12/10/75 for X-band-HH were examined. The directions of the 6 passes with respect to (ocean) wavefront direction and wind direction were shown in Fig. 2. Pass 8 is down-wave; Passes 3 and 6 are up-wave, with Pass 6 being cross-wind; Pass 3 is with, Pass 8 against, the wind. Pass 5 is both cross-wave and cross-wind. Passes 4 and 7 are down-wave and against the wind.

The X-band HH data discussed here are normalized to  $\sigma_0$ -values. The digitized data are, in fact, proportional to square root of power received and are normalized to an arbitrary level convenient to the processing. Samples consisting of 12,500 points were chosen for statistical analysis. These points are obtained from an azimuth swath extending over 100 pixels and a range swath extending over 125 pixels. Each pixel (or sample in a resolution cell) is approximately equivalent to a square 1.5 m on a side. A statistical program obtains the mean  $\mu$  and standard deviation  $\sigma$  of the digital data as well as its density (or frequency) distribution. Using the calculated mean and standard deviation of the sample, the program also obtains lognormal, gamma, and normal distributions having these properties, since each of these distributions can

be completely determined by these properties alone. A discussion of these distributions and their properties is given by Maffett, et al. (1978). The goodness of fit of each of the three standard distributions to the data distribution is tested with the chi square test. Figure 6 gives a sample of the results. Under the heading CHI2 MAX is printed the test statistic to which the numbers printed under the headings NORMAL, LOGNOR, and GAMMA must be compared. If any of the latter is larger than the test statistics, then that particular distribution does not provide a satisfactory fit, according to the chi square criterion. (Note that the column headed DOF gives the number of degrees of freedom.) Although such is the case in Fig. 6 for all the standard distributions, the lognormal distribution appears to furnish an entirely satisfactory fit under the "eyeball test." Indeed, the lognormal distribution fails the chi square test for goodness-of-fit because it does not provide a good fit at the "tails" of the data. If the tails of the data are not important, then the lognormal distribution can be accepted as a reasonably good fit.

All data to be presented have been adjusted for resolution, range (power loss) and antenna effects. A complete description of the corrections made can be found in Maffett, et al. (1978).

The results of the statistic analysis of the December 10 Marineland data for incidence angles of 20, 30, 40 and 50° is summarized in Tables 1 and 2. The statistics recorded are the mean  $\mu$  and standard deviation  $\sigma$  of the original data as digitized, the degrees of freedom DOF for the chi square test statistic CHI2, the lognormal chi square statistic LOGNOR, and the minimum and maximum data values. Table 1 represents statistics for Passes 3 (up-wave), 5 (cross wave), and 7 (down-wave) while Table 2 summarizes Passes 8 (down wave), 6 (up-wave), and 4 (down wave). Note on each table that an adjusted mean  $\mu_a$  and standard deviation  $\sigma_a$  are recorded in the final two columns. These are the corrected values of the mean and standard deviation respectively when resolution, range and antenna effects are taken into account.

It has not been possible to apply the radar parameter corrections to the individual members of each data sample as should have been done. But the following theorem can be verified: the mean and standard deviation of an adjusted sample are equal, respectively, to the adjusted mean  $\mu_a$  and standard deviation  $\sigma_a$  of the original sample. So we can at least take the means and standard deviations of the data and apply to them the adjustments of resolution, range and antenna pattern.

Figures 7 and 8 show comparisons of up-, down-, and cross-wave distributions for  $\theta_i = 20^\circ$  (Fig. 7) and  $\theta_i = 40^\circ$  (Fig. 8). The most pronounced trend appears in Fig. 7 where both the adjusted mean and the adjusted standard deviation decrease as the incidence direction goes from the up- to the cross- to the down-wave condition. The trend in Fig. 8 is less distinct with, in fact, the distributions for the cross- and the down-wave cases being very much alike.

It is useful to illustrate the nature of the distributions of data as a function of incidence angle for fixed incidence direction (i.e., either up-, cross-, or down-wave). Figures 9, 10, and 11 show, respectively, Pass 3 (up-wave), Pass 5 (cross-wave), and Pass 7 (down-wave). The distributions are not exactly corrected since the data points from which they were determined were not adjusted for resolution, range and antennae. The means, however, have been adjusted by a simple translation of the distributions. Thus, the distributions as shown have the corrected means  $\mu_a$  but uncorrected standard deviations  $\sigma$  (see Tables 1 and 2). Consider, for example, the Pass 3 data shown in Fig. 9. The 20°-distribution has an unadjusted standard deviation  $\sigma$  of 8.56 but has an adjusted standard deviation  $\sigma_a$  of 24.41. Thus, the distribution curve should be stretched out to roughly three times the spread shown. Since the curve should continue to be normalized to some fixed amount of area underneath it, the horizontal stretching of the distribution width must be accomplished by a corresponding vertical squashing of the peak value. A similar adjustment should be imagined for the 30°-distribution; but it need not be so severe as the previous one since the adjustment causes the fairly small change from  $\sigma = 8.79$  to  $\sigma_a = 11.76$ . The 40°- and 50°-distributions require essentially no

modification. Finally, a similar set of remarks is appropriate for Passes 5 (Fig. 10) and 7 (Fig. 11).

Figures 12, 13, and 14 show the same kind of distribution variation with incidence angle for Passes 8, 6, and 4, respectively. These passes correspond essentially to down-, up-, and down-wave direction, respectively. Once again, the distributions for incidence angles of 20° and 30° should be thought of as stretched out and squashed down. For 40° and 50°, the distributions are essentially as they should be for adjusted data.

Distributions of data for the medium incidence angles, 40° and 50°, appear to be very similar in type and shape. As the incidence angle decreases to 30° and 20°, both the adjusted mean  $\mu_a$  and adjusted standard deviation  $\sigma_a$  increase in size. Figure 15 summarizes the behavior of the adjusted standard deviation.

To summarize, distributions have been determined for moderate-sized samples of X-band ocean data measured at Marineland for incidence angles of 20, 30, 40, and 50° and for up-, cross-, and down-wave conditions. Note that the Marineland conditions were such that the wind was blowing against the direction of wave travel. The lognormal distribution appears to fit the data histograms better than either the gamma or the normal distributions.

The X-band data distributions do not provide any special features that can be associated with up-, cross-, or down-wave conditions. For example, the trends of the adjusted mean  $\mu_a$  and standard deviation  $\sigma_a$  for Passes 3 and 7 are exactly reversed for Passes 6 and 4 (the order in both cases being essentially up- and down-wave). This result is in contrast to some preliminary L-band findings for tundra, ice, and mountains. There, the type of distribution appears to change from lognormal for tundra and ice to gamma for mountains for depression angles of 30°. Of course, this same behavior might not be in evidence at X-band; so perhaps we should not expect any special distributional behavior of the up-, cross-, and down-wave data.

The X-band data distributions for a fixed wave condition do, however, change their mean locations and their shapes (standard deviations) with changes of incidence angle. The trend of the means with incidence angle is similar to the trend of the Bragg-Rice-Phillips theory as presented previously.

##### 5. SEA REFLECTION COEFFICIENT VARIATION WITH TEMPERATURE AND SALINITY

An examination was also undertaken to ascertain the effects of salinity and sea temperature upon sea surface reflection coefficients. This analysis was undertaken to aid in explaining the large  $\sigma_0$  differences observed on the SAR data collected near the Gulf Stream during the Marineland experiment. The analysis is also germane to the examination of SAR data collected by the SEASAT satellite. At small and medium incidence angles, the effects of temperature and salinity variations upon sea surface reflection coefficients, for either of the linear polarizations, seem to be of insignificant proportions. At large incidence angles, i.e., near-grazing, there is a more pronounced change in the behavior of the vertical polarization reflection coefficient. In fact, in the vicinity of 80° incidence, the ratio of the reflection coefficient for high temperature, high salinity to the reflection coefficient for low temperature, low salinity can take an excursion of as much as 20 dB.

The reflection coefficients used are for reflections from a smooth surface. They are taken from Beckmann and Spizzichino (1963) and are:

$$R_o^- = \frac{\sin \gamma - \sqrt{\epsilon_r - \cos^2 \gamma}}{\sin \gamma + \sqrt{\epsilon_r - \cos^2 \gamma}} \quad (7)$$

for horizontal polarization; and

$$R_O^+ = \frac{\epsilon_r \sin \gamma - \sqrt{\epsilon_r - \cos^2 \gamma}}{\epsilon_r \sin \gamma + \sqrt{\epsilon_r - \cos^2 \gamma}} \quad (8)$$

for vertical polarization.  $\epsilon_r$  is the relative dielectric constant  $\epsilon/\epsilon_0$  where  $\epsilon_0$  is the dielectric constant of a vacuum.  $\gamma$ , the depression angle, is the complement of the incidence angle  $\theta$ . Beckmann and Spizzichino use the subscript o in  $R_O$  to designate the reflection coefficient of a smooth surface. This is modified by the factor  $\zeta$ , which depends only on the shape of the irregularities of the surface, to give the reflection coefficient for a rough surface as

$$R = \zeta R_O \quad (9)$$

The superscripts - and + are then used to denote horizontal and vertical polarization cases, respectively. The roughness factor  $\zeta$  may have the effect of either increasing or decreasing the magnitude  $|R|$  of the reflection coefficient  $R$ . In fact, it is shown in Beckman and Spizzichino (1963) on the basis of experimental data, that the effect of roughness is to increase the vertical polarization reflection coefficient and to decrease the horizontal polarization reflection coefficient. Figure 16 shows the general level of change of the smooth surface reflection coefficient caused by the roughness effect  $\zeta$ .

Using values of  $\epsilon'$  and  $\epsilon''$  representative of the temperature ( $\sim 0^\circ$  C) fresh water and high temperature ( $\sim 30^\circ$  C) sea water (35 ppt salinity) as recorded in Hollinger (1973), expressions for  $|R_O^-|^2$  and  $|R_O^+|^2$  have been calculated as a function of depression angle  $\gamma$  and are shown in Fig. 17. The value  $\epsilon'' = 150$  may seem a bit high for higher temperature sea water; however, Hollinger (1973) shows the possibility of very high  $\epsilon''$ -values for frequencies of 1 GHz and lower. In any case, in going from low temperature fresh water to high temperature sea water, the difference in reflection coefficient values for either of the horizontal or vertical polarization cases is not startling, being at most some 25% for the vertical polarization reflection coefficient for medium to large depression angles. However, the ratio, particularly of the vertical polarization reflection coefficient values, does attain appreciable size for small depression angles, chiefly because both vertical polarization reflection coefficients take such low values at those angles. Figure 18 shows these ratios, plotted in dB. The horizontal polarization reflection coefficient ratio scarcely budges from 0 dB over the whole angular range. But the vertical polarization reflection coefficient ratio exceeds 20 dB in the vicinity of an  $8^\circ$  depression angle.

The foregoing discussion is pertinent for frequencies in the vicinity of 1 GHz. At 10 GHz, the value of  $\epsilon'$  should decrease somewhat to about the order of 50. However, the change of  $\epsilon'$  from 75 to 50 causes an almost imperceptible change in the reflection coefficient values. The value of  $\epsilon''$  also changes at 10 GHz to a value of approximately 40. Moreover, at 10 GHz, the value of  $\epsilon = 50 + 40i$  is essentially constant for the temperature range  $0^\circ$  to  $20^\circ$  C and for the salinity range 0 to 35 PPT. Figure 19 shows the reflection coefficients  $|R_O^+|^2$  and  $|R_O^-|^2$  as a function of depression angle at the average permittivity of  $\epsilon = 50 + 40i$  for 10 GHz. Note that, since the reflection coefficient varies monotonically with  $\epsilon''$ , the 10 GHz curve falls within the range of values shown in Fig. 19 for L-band.

In conclusion, it seems within the realm of possibility that changes in smooth sea reflectivity due to changes in temperature or salinity might be significant enough to be observable at L-band. But it is completely unlikely that such is the case at X-band, particularly if the incidence angles are not too large. It should be noted that this discussion has only considered the effect of salinity and temperature on the radar reflectivity. The authors, to date, have not considered the effect of temperature and salinity on the surface capillary wave field which could indeed be affected by these two parameters. Thus, SAR might be able to detect temperature and salinity differences by detecting subtle differences in the capillary wave field.

## 6. DYNAMIC MODELS

Application of static models to non-SAR radars has been reasonably satisfying. However, static models alone cannot be sufficient for SARs which, by definition, are very sensitive to Doppler velocity components in the scene to be imaged. The effects of motion of wave elements on SAR imagery, in order of importance, include azimuthal displacement, azimuthal image smearing, loss of azimuth focus, reduction of wave contrast and loss of range focus. The principles of wave motion must be incorporated into the static models to arrive at a more satisfying SAR imaging theory for waves.

Dynamic models, applied to SAR imaging, concentrate on either the phase velocity or on the orbital velocity of ocean waves. Early attempts to explain SAR wave imagery depended on phase velocity effects, and more recent work tends to develop orbital motion models.

The motion of ocean waves imaged by a SAR system may be blurred if the imaged waves move a substantial distance during the time they are in the radar antenna beamwidth. These blurring effects may, in some cases, be removed by compensatory adjustments of the optical correlator processor. Azimuthal velocity compensation is achieved by adjusting the correlator azimuth focus according to an algorithm utilizing radar and processor, and, in the case of azimuth traveling waves, the focus correction needed for producing the best azimuth focus can be explained on the basis of a radar scatterer moving at the phase velocity of the ocean wave (Shuchman and Zelenka, 1977). This is not the case, however, for range traveling waves where a point scatterer moving at the phase velocity of the wave would displace, but not defocus, the wave image. The observed defocusing can be accounted for if we assume the radar signals are reflected from a stationary scattering surface with variable reflectivity modulated by the passage of a moving ocean wave.

The appropriate model assumes that the energy returned to the radar receiver is reflected or scattered from an ocean surface that is stationary relative to its geographic location. The reflecting surface may, in fact, be moving slowly relative to the phase velocity of the wave. This would be the case where the reflecting surface was moving at the orbital velocity of the wave which generally is an order of magnitude lower than the waves' phase velocity. In this case, the stationary surface model would still apply, since the scattering surface is more nearly stationary compared to the phase velocity of the wave. This is consistent with the fact that the predominant echo in Bragg scattering is from waves either traveling toward or away from the radar.

This model is based on the following observations made on the ERIM-SAR optical correlator:

1. Measurement of the azimuth Doppler spectrum shift for a series of range traveling waves indicate a scattering surface velocity, at most, an order of magnitude lower in value than the phase velocity of the waves.
2. Radar image contrast for range traveling waves is maximized when the cylindrical optics used to focus the azimuth signal histories are rotated an amount proportional to the waves' phase velocity. No shifting of the azimuthal spectrum bandpass is required.
3. Wave images made from separated Doppler spectral bands show range displacements equal to the wave phase velocity times the equivalent time between the two Doppler spectra for a stationary target at the same radar range.
4. Azimuth traveling waves are defocused an amount equal in magnitude to that produced by radar reflectors moving at the phase velocity of the wave. Given the same wave velocity, defocusing is more pronounced at L-band than at X-band.

How the model is able to satisfy the above observations will be shown below.



### 6.1 Range History for a Fixed SAR Target

Consider the geometry of the SAR platform relative to the fixed reflecting point shown in Fig. 20. As the antenna beam moves across the reflecting point, the radar range vs. time changes as shown in Fig. 21. The slope of the curve is proportional to the relative velocity of the reflecting point and thus the Doppler frequency shift of the reflected radar signal. The reflector is illuminated over the time interval  $T$  and is at minimum range at time  $t_0$  when the reflector is directly abeam.

### 6.2 Range History for a Target Moving Toward the Flight Line

Suppose the reflector is not stationary, but is moving directly toward the flight line, as shown in Fig. 22. The radar range vs. time for this moving reflector is shown in Fig. 23. Here, the minimum range no longer occurs at  $t_0$  where the target is directly abeam, but is shifted to the right. The average slope of the curve is no longer zero, as in Fig. 21, but is equal to the instantaneous slope at  $t_0$ . Note that the slope of the curve and its corresponding Doppler frequency starts at a higher value and exits at a lower value than that for the fixed reflector. Note, also, that the range to the target changes a distance  $vT$  between target intercept and dropout; however, at equal but opposite slopes of the range curve (equal positive and negative Doppler frequencies) the range to the target is identical.

### 6.3 Theoretical Application to Range Traveling Waves

If we presume that a scattering point on the surface of a range traveling wave is moving at the phase velocity of the wave, we should observe a shift in the average Doppler frequency for that point relative to a stationary reflecting point. In addition, no shift in range should be apparent between images formed from equally displaced positive and negative Doppler frequency bands. However, by observations 1 and 3 listed earlier, no Doppler frequency shift is noted and image displacements are observed for symmetrically displaced Doppler bandpassed images of the ocean surface produced by ERIM's X-L Radar. Clearly, the range traveling waves do not behave like simple moving targets.

### 6.4 Range History for a Stationary Reflecting Surface Modulated by a Range Traveling Wave

We will now consider the range history of a series of stationary reflecting points modulated by the passage of a range traveling wave. Figure 24 shows reflecting points "a-e" at fixed positions on the ocean surface. As the traveling wave progresses toward the flight line, the energy reflected from points "a-e" is modulated to produce a composite range history, as shown in Fig. 25. This history has an overall displacement equal to that for the moving reflector shown in Fig. 23, but is discontinuous with each segment having the range vs. time slope of its corresponding stationary reflecting point. The Doppler spectrum of this composite will thus not be shifted with respect to a stationary reflecting field, and is therefore consistent with observation #1. If symmetric Doppler spectra are passed to form an image, such as those corresponding to segments "b" and "d," a displacement corresponding to the wave velocity " $v$ " times the difference in observation times would be observed. This is consistent with observation #3. We then have a model that is consistent with observations 1 and 3. It can also be shown that observation #2 cannot be explained on a basis of the moving reflector model if the processor bandpass is not adjusted to pass only the moving target spectrum. This was not the case for the ERIM data. The stationary surface model predicts a wave displacement over the stationary target spectrum that could be removed by rotation of the processor optics consistent with observation #2. It remains to be shown that the stationary surface model predicts the same degree of azimuth defocussing as a reflector model that correctly predicts the resulting focus shift.

### 6.5 Range History for a Reflector Moving Parallel to the Flight Line

If the reflecting point is moving parallel to the flight line with the velocity  $v$ , as shown in Fig. 26, the reflector's range history will have the

same variation as that for a stationary point; however, the time the reflector is in the antenna beam will be altered. If the reflector is moving in the same direction as the platform, the time will be increased. For the opposite direction, the time will decrease. For a stationary reflector, the aperture time

$$T = \frac{BR}{V} \quad (10)$$

where B = antenna beamwidth  
R = distance from reflector to flight line, and  
V = platform velocity.

For a reflector with velocity v, as shown in Fig. 26, the aperture time

$$T' = \frac{BR}{V + v} \quad (11)$$

Figure 27 shows the range histories for the two cases discussed above. Note that for the moving reflector case, the curvature of the range history is increased, the azimuth Doppler FM rate is raised, and the recorded azimuth focal length is reduced. This focal length variation will defocus the image of the moving reflector in the optical processor.

#### 6.6 Defocussing of Azimuth Traveling Waves

Observation #4 has shown that defocussing of azimuth traveling waves is equal to that of a reflector moving at the phase velocity of the wave. For the stationary surface model to be valid, it must predict an equal degree of defocussing. The discussion below demonstrates that this, indeed, is the case.

#### 6.7 Range History for a Stationary Reflecting Surface Modulated by an Azimuth Wave

Suppose we have a sequence of reflecting points "a-e" to be modulated by an azimuth traveling wave with velocity v, as shown in Fig. 28. If point "a" begins reflecting just as the antenna beam first illuminates it, the range history will proceed as shown in Fig. 29. Points "b, c, d and e" will reflect, in turn, to produce the segmented range history shown. Each segment will have the azimuth Doppler FM rate of its corresponding stationary reflecting point and will produce an in-focus image at the optical processor output. However, the image of the traveling wave will be blurred if the sequence of reflecting points extends over a substantial part of the ocean wavelength. This blurring may be removed if the processor is refocused to bring each segment to focus at a common point at the processor output. Then each segment will be slightly defocussed, but the moving wave will have the maximum contrast. The optimum focus setting of the processor would be that which best accommodates the range history shown in Fig. 28 as it might have been produced by a single point target. This range history is the same as that for the moving reflecting point shown in Fig. 26, except for some small perturbations. Consequently, the processor setting that properly focusses the image for the moving reflector of Fig. 26 also produces the best focus of the segmented range history of Fig. 29. This is the essential conclusion of observation #4. The stationary surface model is thus shown to be consistent with all of the cited observations.

### 7. SUMMARY

The reflectivity of large areas of the sea surface observed by a SAR appear to have a  $\sigma_0$  brightness that approaches the Bragg-Rice-Phillips upper bound, suggesting that capillaries on the surface of the oceanic waves are the primary basis for the surface return observed by the SAR. However, it should be noted that values presented here represent reflectivity of a large area of sea surface observed by the SAR, averaged to yield a very low resolution highly mixed integrated reflectivity estimate. However, further ERIM measurements indicate that the  $\sigma_0$  ratio of wave crest to wave trough is a function of orientation of wavetrains in respect to the radar look direction. This observation could be indicative of a facet model dependency for individual wavetrain detectability

or a further confirmation of the importance of wave motion in the SAR formation process as reported by Alpers and Rufenach (1977).

Future studies of the reflection from capillaries as observed from a SAR should include consideration of

1. The local wave slope effect taking into account windwave directions and the surface interactions that result, and
2. The impact of small scattering cell size

to converge on a fine resolution theory of reflectivity.

Distributions have been determined for moderate-sized samples of X-band ocean data measured at Marineland for incidence angles of  $20^\circ$ ,  $30^\circ$ ,  $40^\circ$ , and  $50^\circ$  and for up-cross-, and down-wave conditions. The lognormal distribution appears to fit the data histograms better than either the gamma or the normal distributions. Lognormal descriptions have been reported by Trunk (1976) for real aperture radar data of ocean surfaces.

The X-band data distributions do not provide any special features that can be associated with up-, cross-, down-wave conditions. This result is in contrast to some preliminary L-band findings for tundra, ice, and mountains. There the type of distribution appears to change from lognormal for tundra and ice to gamma for mountains for depression angles of  $30^\circ$ . Of course, this same behavior might not be in evidence at X-band; so perhaps we should not expect any special distributional behavior for the up-, cross-, and down-wave data.

The X-band data distributions for a fixed wave condition do, however, change their mean locations and their shapes (standard deviations) with change of incidence angle. The trend of the means with incidence angle is similar to the trend of the Bragg-Rice-Phillips theory.

An examination of the effect of salinity and sea temperature at small and medium incidence angles, indicated that their effects upon sea surface reflection coefficients seem to be insignificant, for either of the linear polarizations. At large incidence angles, i.e., near-grazing, there is a more pronounced change in the behavior of the vertical polarization reflection coefficient. In fact, in the vicinity of  $80^\circ$  incidence, the ratio of the reflection coefficient for high temperature, high salinity to the reflection coefficient for low temperature, low salinity can take an excursion of as much as 20 dB.

The authors' observation of moving ocean imaged by the SAR and studied in the SAR optical correlator support a theory that the ocean surface appears relatively stationary in the absence of currents. The reflecting surface is most likely moving slowly (i.e., capillaries, waves, phase velocity and orbital wave velocities) relative to the phase velocity of the large gravity waves. The stationary theory still applies since the phase velocity of the capillaries and orbital velocity of the gravity waves is more nearly stationary when compared to the phase velocity of the waves.

#### 8. REFERENCES

- Alpers, W.R. and C.L. Rufenach, The Effect of Orbital Motions on Synthetic Aperture Radar Imaging of Ocean Waves, IEEE Trans. Antennas Propagation, 1979 (in press).
- Beckman, P. and A. Spizzichino, The Scattering of Electromagnetic Waves from Rough Surfaces, McMillan Co., New York, 1963.
- Brown, W.E., Jr., C. Elachi, and T.W. Thompson, Radar Imaging of Ocean Surface Patterns, Journal of Geophysical Research, Vol. 81, No. 15, pp. 2657-2667, 1976.

- Brown, W.M. and L.J. Porcello, An Introduction to Synthetic Aperture Radar, IEEE Spectrum 6, pp. 57-62, 1969.
- Cindrich, I., J. Marks, and A. Klooster, Coherent Optical Processing of Synthetic Aperture Radar Data, 1977.
- Published in Proceedings of the Society of Photo-Optical Instrumentation Engineers, Vol. 128, Effective Utilization of Optics in Radar Systems, Huntsville, Alabama, 1977.
- Guinard, N.W. and J.C. Daley, An Experimental Study of a Sea Clutter Model, Proc. IEEE, Vol. 58, No. 4, pp. 543-55, 1970.
- Harger, R.O., Synthetic Aperture Radar Systems, Academic Press, New York, 1970.
- Hollinger, J.P., Microwave Properties of a Calm Sea, NRL Report No. 7110-2, 1973.
- Kozma, A., E.N. Leith, and N.G. Massey, Tilted Plane Optical Processor, Applied Optics 11, p. 1766, 1972.
- Maffett, A., H. Klimach, A. Liskow, R. Rawson, R. Heimiller, and P. Tomlinson, L-Band Radar Clutter Statistics for Terrain and Ice, ERIM Report No. 128900-9-F, Vol. 1 (Contract DAAK40-77-C-0012), 1978.
- Phillips, O.M., The Dynamics of the Upper Ocean, Cambridge Univ. Press, London, 1966.
- Raney, R.K. and R.A. Shuchman, SAR Mechanism for Imaging Waves, Proc. 5th Canadian Symposium on Remote Sensing, Victoria, B.C., 1978.
- Rawson, R., F. Smith, and R. Larson, The ERIM X- and L-Band Data Dual Polarized Radar, IEEE 1975 International Radar Conference, New York, p. 505, 1975.
- Shemdin, O.H., W.E. Brown, Jr., F.G. Staudhammer, R. Shuchman, R. Rawson, J. Zelenka, D.B. Ross, W. McLeish, and R.A. Berles, Comparison of In-Situ and Remotely Sensed Ocean Waves Off Marineland, Florida, Boundary Layer Meteorology, Vol. 13, pp. 225-234, 1978.
- Shuchman, R.A. and J.S. Zelenka, Processing of Ocean Wave Data from a Synthetic Aperture Radar, Boundary Layer Meteorology, Vol. 13, 1978.
- Skolnik, M.I., Sea Echo, Ch. 26 in M.I. Skolnik (ed.), Radar Handbook, McGraw-Hill, New York, 1970.
- Teleki, P.G., R.A. Shuchman, W.E. Brown, Jr., W. McLeigh, D. Ross, and M. Mattie, Ocean Wave Detection and Direction Measurements and Microwave Radars, Oceans, IEEE/MTS, Washington, D.C., 1978.
- Trunk, G.V., Non-Rayleigh Sea Clutter: Properties and Detection of Targets, NRL Rept. 7986, p. 81, 1976.
- Wright, J.W., Backscattering from Capillary Waves with Application to Sea Clutter, IEEE Trans. Antennas Propagation, Vol. AP-14, pp. 749-754, 1966.

#### ACKNOWLEDGEMENTS

Some aspects of the work reported herein were jointly supported by the Office of Naval Research as well as the National Oceanic and Atmospheric Administration (NOAA). The NOAA work was performed under Contract NO7-35328 under the direction of Mr. John W. Sherman, III of the National Environmental Satellite Service of NOAA.

TABLE 1. STATISTICS OF SEA RETURN VS INCIDENCE ANGLE AND WAVE DIRECTION  
(12500 pts, Marineland IPL 436 File 1 Flt 12/10/75)

X<sub>HH</sub> UP (3)0

$\theta_i$	$\mu$	$\sigma$	DOF	CHI2	LOGNOR	MIN	MAX	$\mu_a$	$\sigma_a$
20°	24.71	8.56	30	44	138	5	71	70.46	24.41
30°	21.72	8.79	32	44	107	4	76	29.05	11.76
40°	25.85	11.27	37	44	129	5	115	25.57	11.15
50°	21.33	9.31	37	44	261	4	83	21.33	9.31

X<sub>HH</sub> CROSS (5)X

$\theta_i$	$\mu$	$\sigma$	DOF	CHI2	LOGNOR	MIN	MAX	$\mu_a$	$\sigma_a$
20°	21.05	7.30	27	40	210	4	63	60.02	20.81
30°	20.50	8.75	31	44	159	2	70	27.42	11.70
40°	20.55	8.42	33	44	175	4	71	20.33	8.33
50°	19.3	8.17	29	43	271	2	67	19.33	8.17

X<sub>HH</sub> DOWN (7) V

$\theta_i$	$\mu$	$\sigma$	DOF	CHI2	LOGNOR	MIN	MAX	$\mu_a$	$\sigma_a$
20°	15.34	4.88	16	26	391	4	42	43.74	13.91
30°	20.52	10.13	32	44	319	4	77	27.45	13.55
40°	21.99	9.36	42	44	178	4	90	21.75	9.36
50°	21.68	8.90	35	44	219	4	82	21.68	8.90

TABLE 2. STATISTICS OF SEA RETURN VS INCIDENCE ANGLE AND WAVE DIRECTION  
(12500 pts, Marineland IPL 436 File 1 Flt 12/10/75)

$X_{HH}$  DOWN (4) V

$\theta_i$	$\mu$	$\sigma$	DOF	CHI2	LOGNOR	MIN	MAX	$\mu_a$	$\sigma_a$
20°	22.41	7.49	32	44	166	6	81	63.90	21.36
30°	23.53	9.44	32	44	152	5	88	31.47	12.63
40°	24.53	9.98	32	44	133	6	92	24.26	9.87
50°	21.59	8.73	32	44	259	5	81	21.59	8.73

$X_{HH}$  UP (CROSS-WIND) (6)X

$\theta_i$	$\mu$	$\sigma$	DOF	CHI2	LOGNOR	MIN	MAX	$\mu_a$	$\sigma_a$
20°	17.63	5.66	17	28	287	3	47	50.27	16.14
30°	21.18	8.69	32	44	191	4	79	28.33	11.62
40°	23.12	9.66	32	44	164	4	81	22.87	9.56
50°	16.78	7.21	22	34	291	2	55	16.78	7.21

$X_{HH}$  DOWN (8)O

$\theta_i$	$\mu$	$\sigma$	DOF	CHI2	LOGNOR	MIN	MAX	$\mu_a$	$\sigma_a$
20°	15.88	5.23	21	33	267	4	52	45.28	14.91
30°	23.91	10.03	32	44	155	5	101	31.98	13.42
40°	26.02	11.91	32	44	134	4	142	25.74	11.78
50°	23.54	9.55	32	44	259	6	91	23.54	9.55

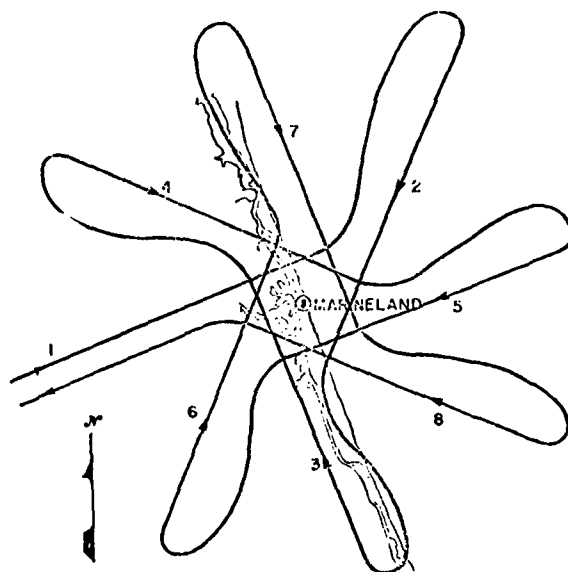


Figure 1. ERIM FLIGHT PATTERNS FLOWN OVER MARINELAND TEST SITE

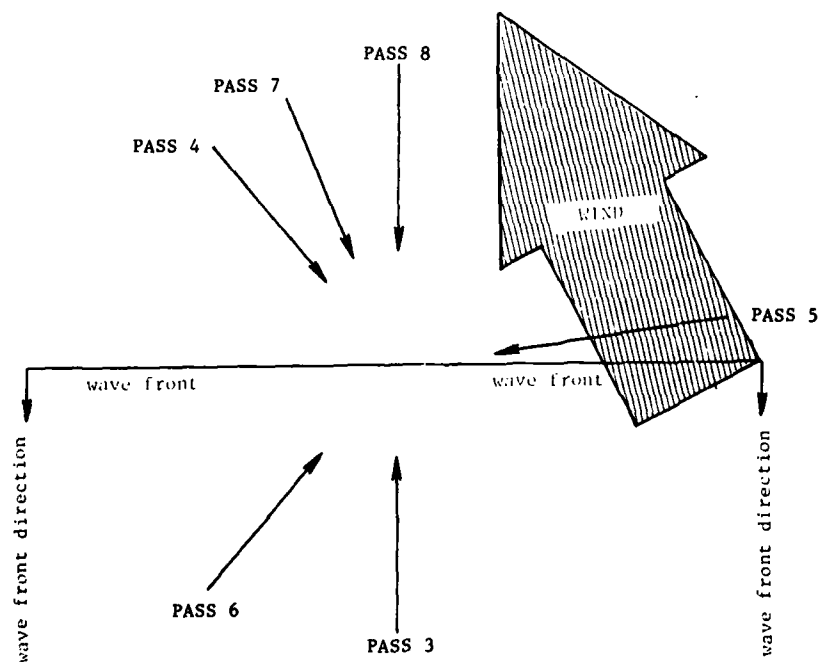


Figure 2. RADAR LOOK DIRECTION WITH RELATION TO WAVE FRONT AND WIND DIRECTIONS FOR 10 DECEMBER 1975

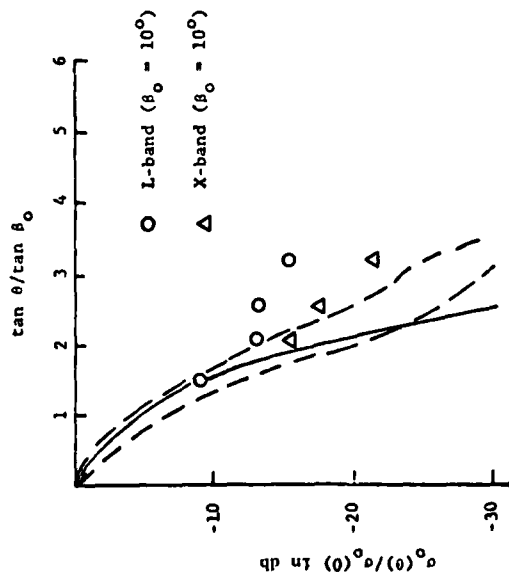


Figure 3. COMPARISON OF X-BAND AND L-BAND DATA OBTAINED AT MARINELAND ON DECEMBER 15, 1975 WITH THE FACET MODEL (SOLID LINE) AND WITH THE RANGE OF DATA REPORTED BY BECKMAN AND SPIZZICHINO (DASHED LINES)

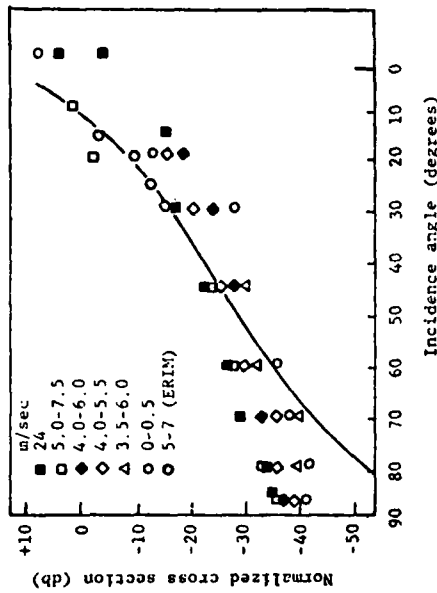


Figure 4. VARIATION OF THE NORMALIZED  $\sigma_0$  (HH) AT X-BAND WITH INCIDENCE ANGLE AND WIND SPEED. THE LINE REPRESENTS THE BRAGG SCATTERING RELATIONSHIP. DATA FROM GUINARD AND DALEY (1970) AND THE ERIM RADAR

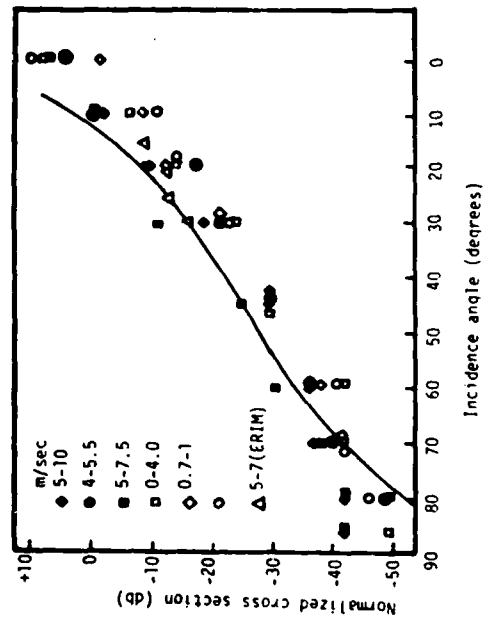


Figure 5. VARIATION OF THE NORMALIZED  $\sigma_0$  (HH) AT L-BAND WITH INCIDENCE ANGLE AND WIND SPEED. THE LINE REPRESENTS THE BRAGG SCATTERING RELATIONSHIP. DATA FROM GUINARD AND DALEY (1970) AND THE ERIM RADAR



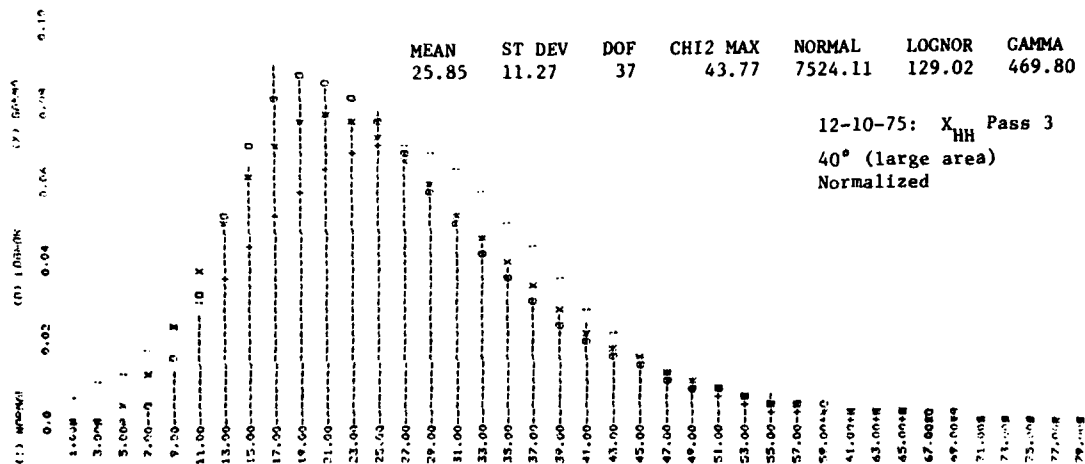


Figure 6. DISTRIBUTION OF OCEAN RETURN

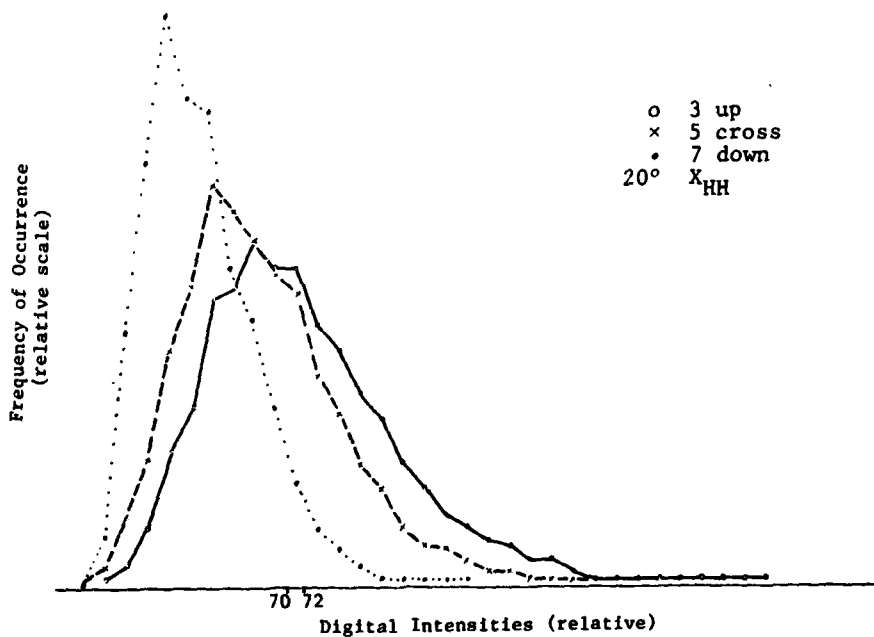


Figure 7. COMPARISON OF UP-, DOWN-, AND CROSS-WAVE DISTRIBUTIONS FOR  $\theta_i = 20^\circ$

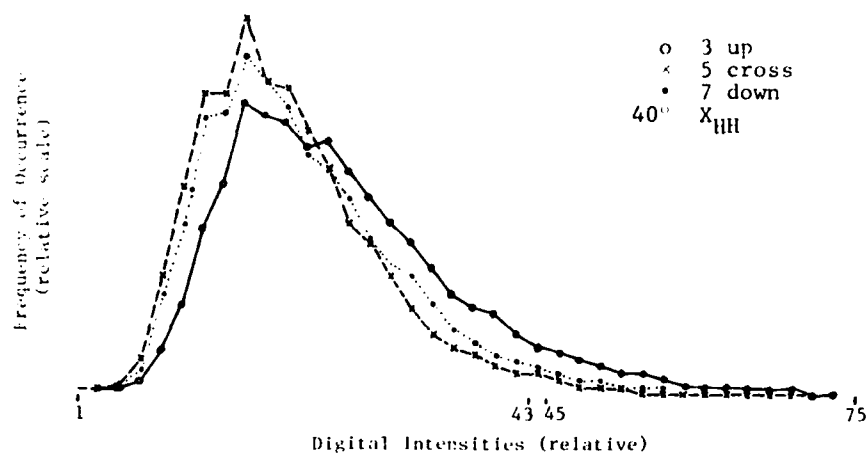


Figure 8. COMPARISON OF UP-, DOWN-, AND CROSS-WAVE DISTRIBUTIONS FOR  $\theta_i = 20^\circ$

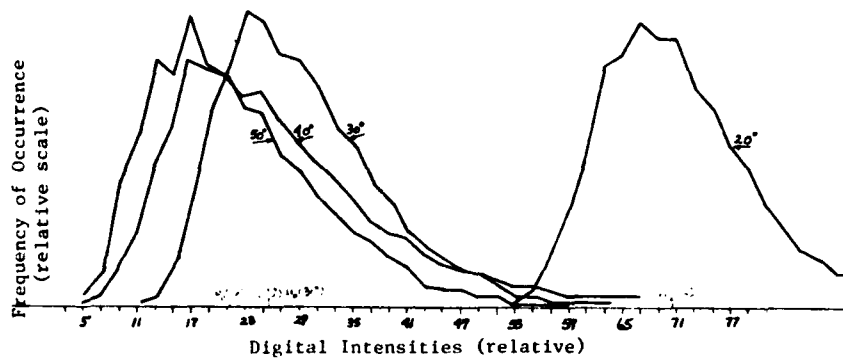


Figure 9. COMPARISON OF DISTRIBUTIONS OF MARINELAND  $X_{HH}$  PASS 3 DATA FOR  $\theta_i = 20^\circ, 30^\circ, 40^\circ, 50^\circ$

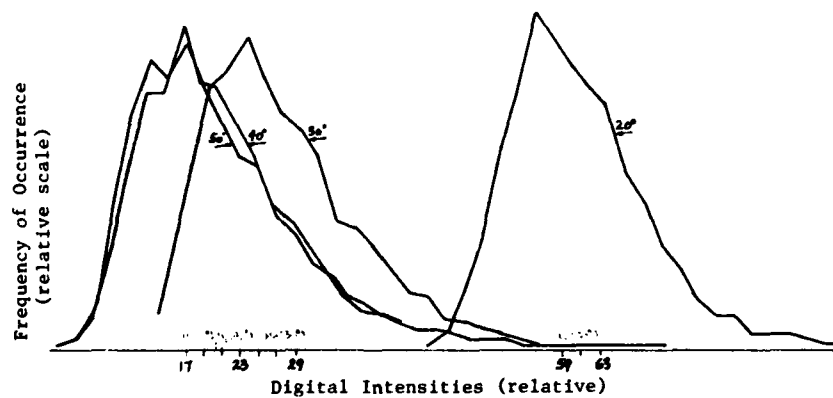


Figure 10. COMPARISON OF DISTRIBUTIONS OF MARINELAND  $X_{HH}$  PASS 5 DATA FOR  $\theta_i = 20^\circ, 30^\circ, 40^\circ, 50^\circ$

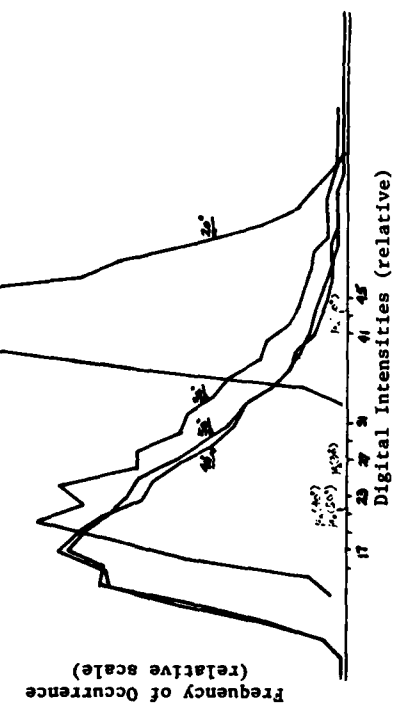


Figure 11. COMPARISON OF DISTRIBUTIONS OF MARINELAND  $X_{HH}$  PASS 7 DATA FOR  $\theta_i = 20^\circ, 30^\circ, 40^\circ, 50^\circ$

622

C-20

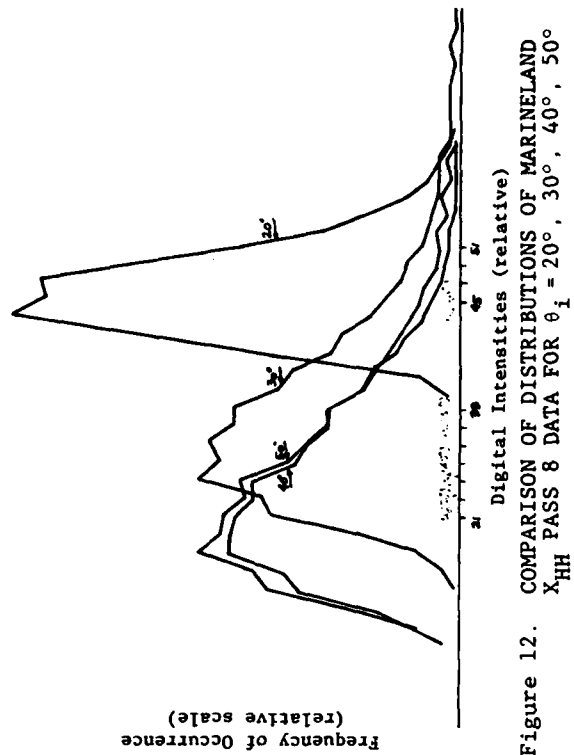


Figure 12. COMPARISON OF DISTRIBUTIONS OF MARINELAND  $X_{HH}$  PASS 8 DATA FOR  $\theta_i = 20^\circ, 30^\circ, 40^\circ, 50^\circ$

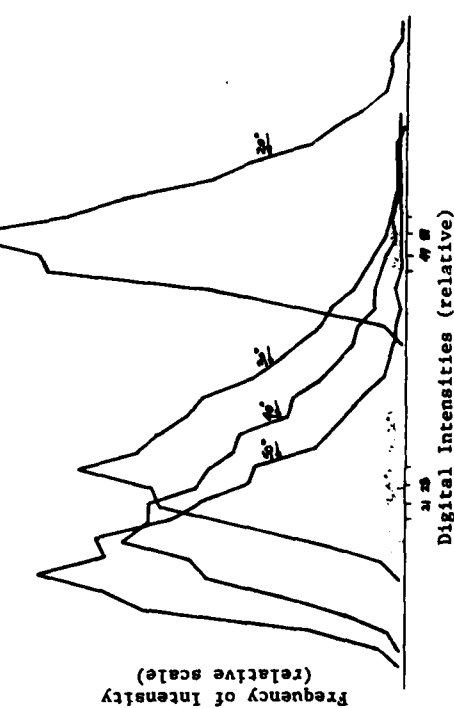


Figure 13. COMPARISON OF DISTRIBUTIONS OF MARINELAND  $X_{HH}$  PASS 6 DATA FOR  $\theta_i = 20^\circ, 30^\circ, 40^\circ, 50^\circ$

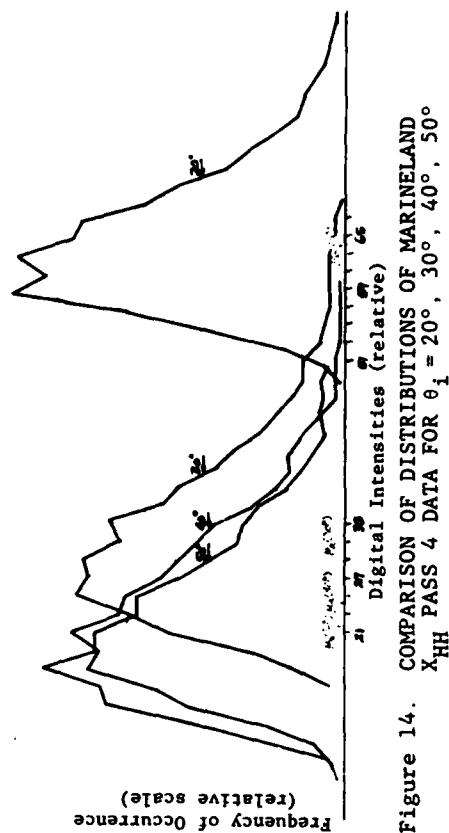


Figure 14. COMPARISON OF DISTRIBUTIONS OF MARINELAND  $X_{HH}$  PASS 4 DATA FOR  $\theta_i = 20^\circ, 30^\circ, 40^\circ, 50^\circ$

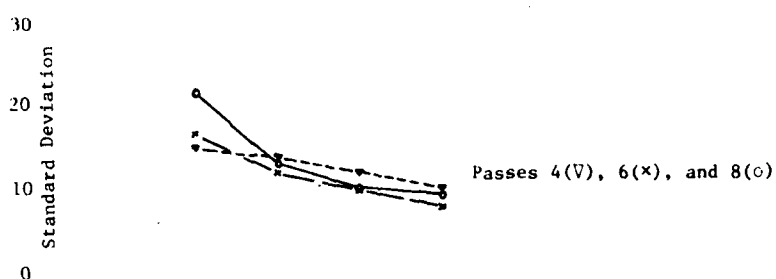
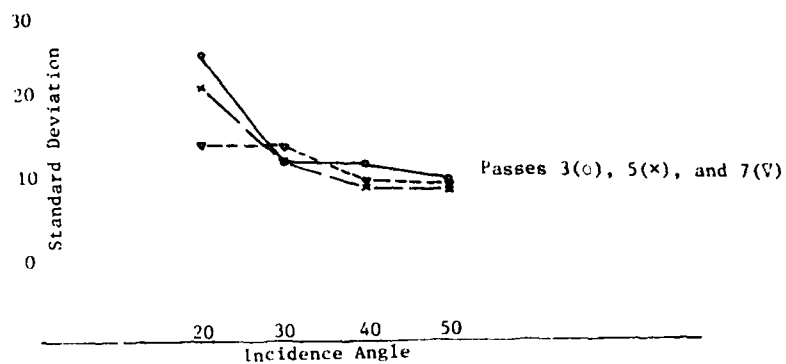


Figure 15. ADJUSTED STANDARD DEVIATION VERSUS INCIDENCE ANGLE

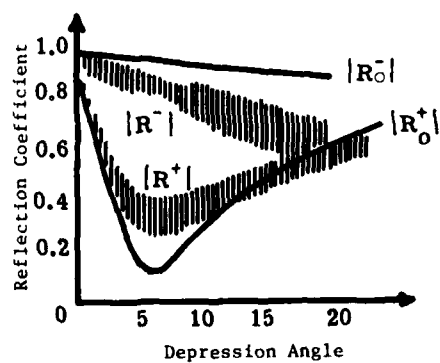


Figure 16. EFFECT OF SURFACE ROUGHNESS FACTOR  $\rho$  ( $R_0$  is theoretical,  $R$  is measured)

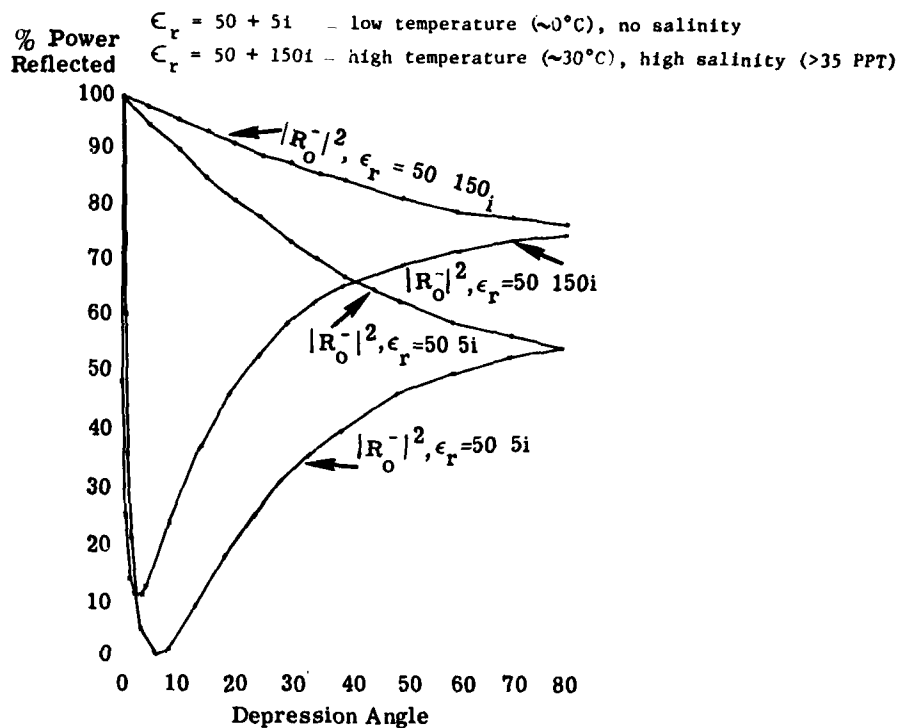


Figure 17. REFLECTION COEFFICIENT VS. DEPRESSION ANGLE FOR TEMPERATURE AND SALINITY RANGES AT L-BAND

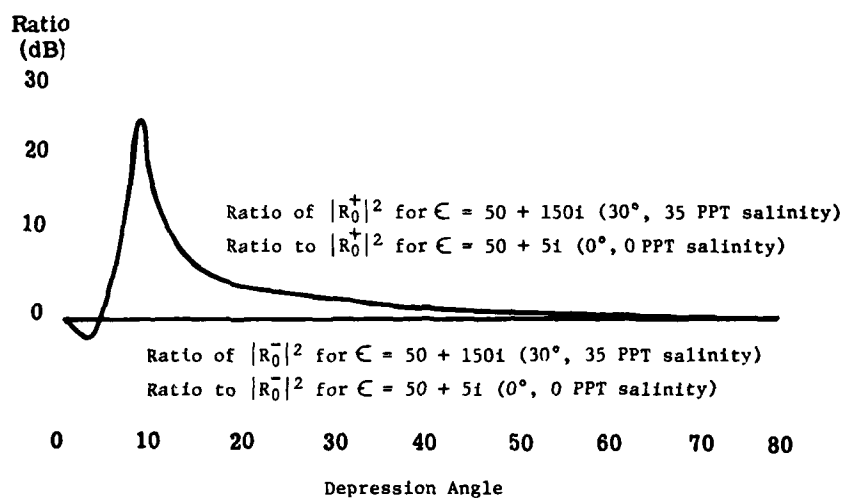


Figure 18. BEHAVIOR OF VERTICAL AND HORIZONTAL POLARIZATION REFLECTION COEFFICIENTS FOR LOW AND HIGH TEMPERATURE AND SALINITY CONDITIONS AT X-BAND

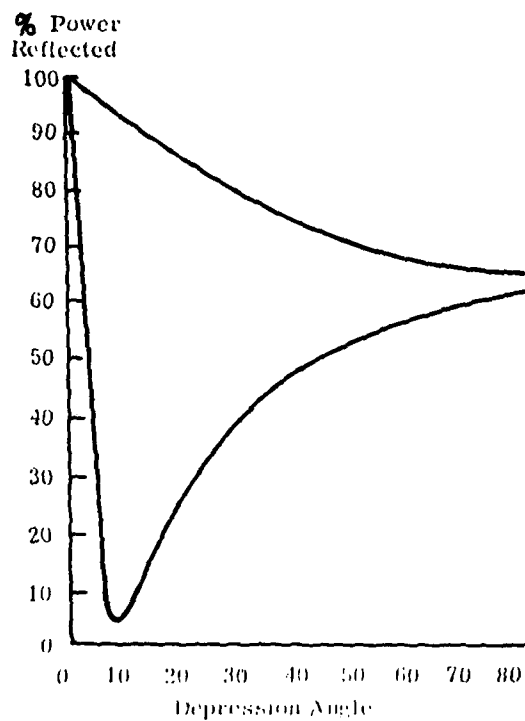


Figure 19. REFLECTION COEFFICIENT VS. DEPRESSION ANGLE FOR TEMPERATURE AND SALINITY RANGES AT X-BAND

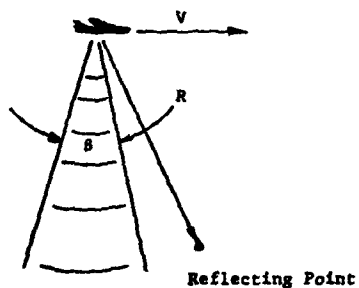


Figure 20. RADAR GEOMETRY FOR STATIONARY REFLECTING POINT

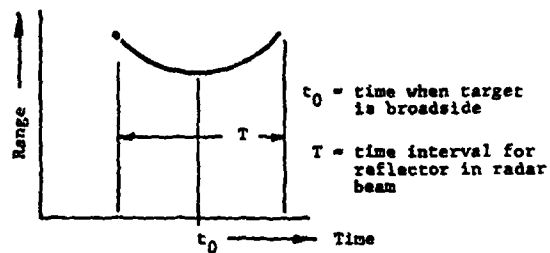


Figure 21. RANGE HISTORY FOR STATIONARY POINT

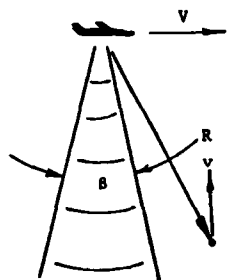


Figure 22. RADAR GEOMETRY FOR MOVING REFLECTOR

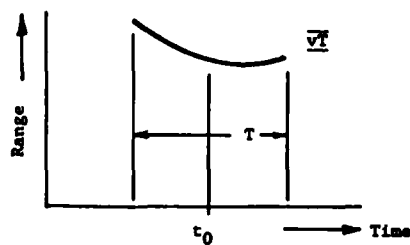


Figure 23. RANGE HISTORY FOR MOVING REFLECTOR

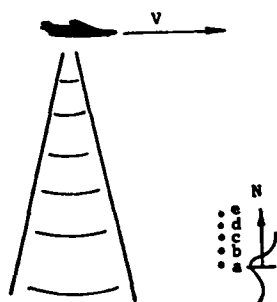


Figure 24. RADAR GEOMETRY FOR RANGE TRAVELING WAVE

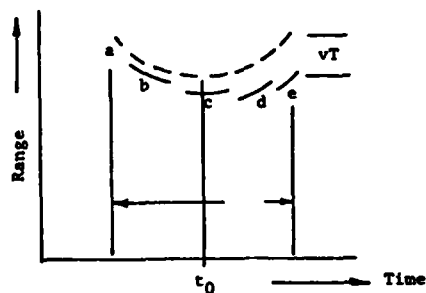


Figure 25. RANGE HISTORY FOR RANGE TRAVELING WAVE

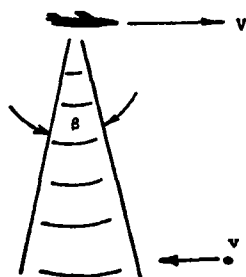


Figure 26. RADAR GEOMETRY FOR REFLECTOR WITH AZIMUTH VELOCITY

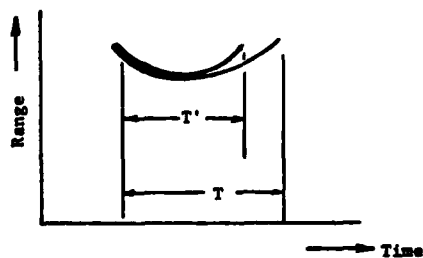


Figure 27. RANGE HISTORY FOR REFLECTOR MOVING IN AZIMUTH

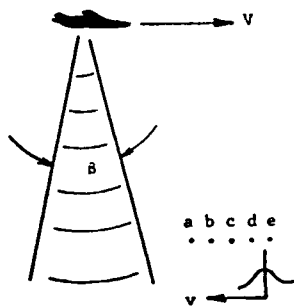


Figure 28. RADAR GEOMETRY FOR AZIMUTH TRAVELING WAVE

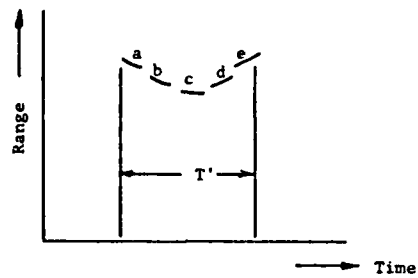


Figure 29. RANGE HISTORY FOR AZIMUTH TRAVELING WAVE



## SAR MECHANISMS FOR IMAGING WAVES

R. K. Raney  
SARSAT Project Office  
Canada Centre for Remote Sensing  
8th Floor, 580 Booth Street  
Ottawa, Ontario

R. A. Shuchman  
Environmental Research Institute of Michigan  
P.O. Box 8618  
Ann Arbor, Michigan, USA

### ABSTRACT

A scattering model is proposed which appears to explain for the first time almost all features observed in the Doppler domain and image domain of Synthetic Aperture Radar (SAR) imagery of oceanic waves. The model, which is suitable for airborne and orbital radars, accounts for the coherence time of capillary centered scattering cells, and their coherently observable wave motions, including their vertical displacements. SAR wave imagery together with the results of detailed observations on the ERIM optical processor are presented to illustrate the pertinent effects. These results lead to the generic description of an optimum processor for wave contrast enhancement.

### RESUME

Les auteurs proposent un modèle de diffusion qui semble expliquer, pour la première fois, la plupart des caractéristiques observées sur les clichés d'ondes marines obtenus par radar à ouverture synthétique (R.O.S.), tant dans le domaine Doppler que dans celui de l'image comme telle. Applicable à des radars aéroportés ou orbitaux, ce modèle tient compte du temps de cohérence des cellules de diffusion centrées sur des rides capillaires, ainsi que des mouvements des ondes observables de façon cohérente, y compris leurs déplacements verticaux. Pour illustrer les effets de cette dispersion, les auteurs montrent des clichés d'ondes obtenus par R.O.S., et présentent les résultats d'observations détaillées faites au moyen du processeur optique de l'ERIM. Ces études aboutissent à la description générale d'un processeur qui accentue le contraste des ondes de façon optimale.

### INTRODUCTION

Noncoherent radars that observe the sea

Presented to the 5th Canadian Symposium on Remote Sensing, Victoria, August 1978.

measure a "brightness" that is described almost exclusively by the average surface (power) reflectivity  $\sigma_0$ . Such a representation of surface reflectivity traditionally has been used for both land and sea return with comparable success for noncoherent radars.

We are concerned, however, with the response to ocean reflectivity of a synthetic aperture radar (SAR), a radar which by definition requires signal (and instrument) coherence in order to form a high resolution image. For such a radar, experience with reflectivity measures ( $\sigma_0$ ) derived over land is not directly transferable to the oceanic case for which the surface is in motion, thus reducing the coherence of the scene. The coherence requirement of SAR and its resulting consequences have not been systematically considered in literature concerned with SAR wave imagery, yet it is crucial to an understanding of the phenomena to be expected and that are in fact observed in imagery.

From the standpoint of a coherent radar, there are three different wave mechanisms that give rise to data that may be imaged (1). Most obvious, perhaps, are those elements of a wave field that move at 'phase velocities' of the gravity waves themselves. The radar observes these coherently only if the reflected energy has not been Doppler shifted outside of the radar pass band. In fact, this restraint is seldom satisfied. The second mechanism is that derived from oceanic turbulence, spray, and white caps. These wave elements are extremely dynamic, and result in signals having extremely short coherence time. They contribute more to the noise background than to discrete features in the image. The third mechanism is the reflectivity derived from the capillary structure on the water's surface. The apparent brightness in a SAR image of an oceanic surface is determined primarily by the roughness and coherence time of this capillary structure, and secondarily by effects concomitant to the first two mechanisms mentioned above, although the relative presence of each effect is a function of sea state.

This paper is concerned primarily with a theory for SAR imaging of an oceanic state composed of long non-breaking gravity waves with capillaries. Capillary reflectivity and coherence time are the focal point of the presentation; aspects of the previous two reflectivity mechanisms are discussed peripherally as required.

We base our discussion on two "axioms":

(1) The principal reflectivity mechanism is via the capillary wave structure.

The reflectivity of a large area of sea surface observed by a SAR which, when averaged to yield a coarse resolution reflectivity estimate, provides an apparent brightness that approaches the Bragg-Rice Phillips upper bound, suggesting that capillaries on the surface of the oceanic waves are the primary basis for the surface properties observed by a synthetic aperture radar as for other radars (2-4). Fine resolution models of reflectivity for an imaging radar include consideration of the local wave slope effect (2), surface fine structure and also the impact of small scattering cell size (5) which may cause scattering statistics to depart from the Rayleigh model (6). Evidence is consistent that radar backscatter at wavelengths of interest in SAR work derives from the surficial fine structure, predominantly the capillaries.

(2) Fine resolution image generation by a synthetic aperture radar requires that the sensor and scene are coherent.

SAR, a coherent sensor, imposes an inherent selectivity on the elements of the scene to be imaged. Only "coherent" scene elements are delivered to the image with synthetically improved resolution. SAR, in short, does not observe the conventional measure of radar surface scattering  $\sigma_0$ , a noncoherent averaged *ex post facto* artefact imposed by WW II engineers upon Nature.

A Synthetic Aperture Radar forms a high resolution image only on those elements of the scene which remain statistically coherent during the integration time that is exploited by the SAR to observe the scene. Elements of the scene having shorter coherence time will be transformed to the image with differing "resolution", even from the same nominal range/azimuth cell of the scene. Elements with loss of coherence combine randomly as noise, reducing contrast (7). Therefore, to describe the imaging properties of a SAR over an oceanic surface, the coherence time of the capillary scattering cells must be included in the model. Likewise, because these scattering cells are in motion with respect to the radar line of sight, the total velocity components  $v_r$  of this motion as projected onto the radar line of sight will impact the (coherent) Doppler response of the radar (8). The second order components ( $dv_r/dt$ ) of this velocity, when present, will impact the coherent focusing properties of the radar.

#### OCEANOGRAPHIC CONSIDERATIONS

From physical oceanography we know that the capillary structure of the surface is in effect locked to the local water surface (9). Capillaries do not move transversely at the phase velocity  $C_0$  of an underriding wave, itself only an aspect of energy being transported through the water. The capillaries do move at a net velocity  $V$  determined by the vector sum of the local current  $V_{cur}$ , the group velocity  $V_{cap}$  of the capillaries themselves caused by the local wind field, and finally the orbital velocity  $V_o(t)$  determined by the passage of the larger, faster wave (10). Figure 1 shows the principal contrast between the wave phase velocity, and the actual motion of capillary scattering cells.

The orbital motion imparted by the passage of the faster wave provides vertical motion as well as horizontal components of the velocity of each coherent scattering cell. The available SAR literature on reflectivity generally disregards the vertical component of motion although, in fact, it is this vertical component for orbital and most airborne oceanic observation SARs (operating at depression angles  $\theta$  steeper than  $45^\circ$ ) which is the most important source of coherent Doppler modulation of the return signal. With the vertical velocity component included, the net line of sight coherent velocity (11)  $v_r(t)$  shows only mild dependence on wave aspect angle  $\phi$  with respect to radar line of sight, as indeed it should based on detailed observations (1).

Waves, whether they be capillaries, larger gravity waves or swells, seldom are described by a single period or frequency. Waves in the real world have variety. Therefore, each scattering cell must be described by a distribution  $\delta v_r$  of line of sight velocities. This distribution of coherent velocities will cause a spreading in the Doppler shift of the reflected signal with which the synthetic aperture radar must contend. As noted below, this spread or "intrinsic spectrum" of a sea causes the most severe fundamental limit on resolution.

Based on the foregoing discussion, observations of an "average" sea by a SAR should result in a small shift and spread of the Doppler spectrum. Indeed, this has been verified by measurements at ERIM using the data set from Marineland. Figure 2 shows these phenomena for L-band, and Figure 3 for X-band. Note that the "sensitivity"

(Doppler shift to signal Doppler bandwidth ratio) is much more noticeable at X-band than at L-band, which is consistent with the theory in that this ratio is inversely proportioned to radar wavelength  $\lambda$ . Note also that the pair of X-band data illustrates the ability of this measurement to estimate the local current; the measured Doppler shift reverses sense, in this example, for the reciprocal radar aircraft heading, showing that a capillary wave field had a coherent velocity bias, or current.

As an important aside, note that these Doppler shifts, coherently observed, are much smaller than those predicted by a "phase velocity" model. Indeed, if the wave phase velocity were the cause of the Doppler shift, then the data would be shifted outside of the pass band of the radar, and a blank image would result (1).

#### PIXEL DWELL TIME

The point of brightest average reflectivity  $\sigma_0$  for an oceanic surface appears to be locally stable with respect to a given point on a swell or other large gravity wave; therefore, this noncoherent  $\sigma_0$  tends to move at the phase velocity of the larger wave. On the other hand, the synthetic aperture radar "images" (focuses coherently) only those statistically stable scattering cells which are locked to the capillaries, which do not move at the phase velocity. Thus, in general, a SAR does not form sea surface images in a manner analogous to incoherent radar or optical sensors. If the point of brightest reflectivity  $\sigma_0$  moves from resolution cell to resolution cell, it becomes by definition noncoherent and therefore becomes by definition impossible to coherently integrate (using a conventional SAR processor) in order to form a fully resolved image of the wave's brightest surface at the output of the radar (12). Therefore, a necessary condition for coherent observation of a given point of reflectivity moving (noncoherently) with a wave at phase velocity  $C_0$  is that the integration time  $T$  be less than the Pixel dwell time, or  $T < P/C_0$ . This restraint (which turns out to be the least severe of three discussed in this paper) is tabulated for typical conditions in Table 1. Note that whereas a SAR cannot sensibly track  $\sigma_0$  coherently for a moving wave, an optimum processor should attempt to track  $\sigma_0$  non-coherently (as discussed below).

#### COHERENCE CONSIDERATIONS

We noted above that the scattering cells on the surface of the ocean observed by a SAR

are statistically varying. They have as a consequence a coherence time  $\tau$  within which they may become coherently integrated by the SAR, and exceeding which coherent integration in general causes degradation of the resultant image. Capillary wave scattering cell coherence time has been measured experimentally (5). At X-band the average  $\tau$  is on the order of 100 ms, which is less than the nominal integration time  $T$  used in almost all SARs. For a given scene coherence time  $\tau$ , the resulting resolution cell  $\rho_n$  in azimuth is  $\rho_n > \lambda R / c \tau$ . This limitation on resolution, imposed by coherence, is a fundamental performance constraint.

It is instructive to calculate the impact of this restraint on resolution as a function of available integration time, as limited by scatterer coherence. Table II shows that as wavelength is increased, and as the ratio  $(R/V)$  is increased, more integration time is required in order to achieve a given nominal resolution. If this model is correct, then one may predict, for example, that Seasat should only infrequently image waves.

Most SAR imagery of oceanic surfaces reflects the presence of both surface roughness and scatterer coherence time as brightness variations. Note that an image built primarily of non-coherent contributions will have an average brightness governed by the local  $\sigma_0$  and an  $R^{-4}$  dependence, whereas coherent scatterers at the same range and with the same  $\sigma_0$  will appear brighter because of the  $R^{-3}$  dependence unique to SAR. Partially coherent scatterers will have an effective range dependence of  $R^{-n}$  ( $3 < n < 4$ ). (All of these cases will be modulated by coherent speckle noise at a spatial frequency determined by the bandwidth of the signal processor, so that from the speckle viewpoint, these signal-dependent coherence effects are not distinguishable.) It follows that coherence time variations in an oceanic scene will be mapped on an image as brightness variations, if the radar coherence time happens to fall in the transition zone of the surface scattering cell coherence time statistics. As a consequence, a radar may be very sensitive to physical oceanographic features of the water surface that directly affect capillary temporal stability (thus, "good") and simultaneously be unable to achieve sufficient resolution to image waves (thus, "bad"). Early results suggest that Seasat has just these properties.

### COHERENT DOPPLER SHIFT

It turns out that the small Doppler Shifts noted above cause a resolution restraint that is almost always more severe than that due to coherence time limitations. Coherent Doppler shifts provided by the net line of sight velocity  $v_r$  results in an azimuthal shift  $\Delta x = v_r R/V$  of the point being imaged (8). This is dramatically illustrated by the famous train-off-the track example (Figure 4). Any scatterer with a coherently sensible velocity will be shifted relative to its neighbours according to their respective radial velocity components.

When there is a spread in velocities  $\delta v_r$ , there will be a spread  $\delta(\Delta x)$  in the resulting azimuthal shifts (1). Of perhaps more importance is the fact that this spread as it appears in an image provides an effect that looks like defocusing although, in fact, it is not defocusing. (If there were a true defocusing  $\delta p$  present, then the spreading effect would be on the order of 10 to 100 times stronger than any defocusing (1), since  $\delta(\Delta x) \approx \frac{R}{\lambda} \delta p$ ).

Differential shift from the waves' intrinsic spectrum implies the most severe fundamental limit on SAR resolution of the sea surface. There is no way that a SAR processor can "unspread" an image which is built of differentially shifted data. In its most extreme form, it implies that to achieve "resolution", a real aperture radar is the better choice, since the upper (worst) bound is always the real beamwidth of the radar in question.

An example of this phenomenon is shown in Figure 5. These data (from Marineland) show breakers near shore that have large absolute and differential shifts. There is a spread in their image that is essentially equal to the width of the antenna patterns at that range for this X-band example (1). The L-band version shows less shift and spread compared to the antenna beamwidth, as it should, although the total image degradation is worse. Note also that the image of the offshore waves, although not demonstrably of the best resolution, evidences much less shift and focus degradation. The reflectivity mechanism for these offshore waves is the capillary structure, which (for the conditions of Marineland during the experiment) were much less exercised than the relatively specular, turbulent, and broad intrinsic spectral structure of the shorewise breakers.

Differential shift is frequently more severe than the coherence limit (above) as a restraint on azimuth resolution. Differential Doppler Shift  $\delta(\Delta x)$  may be explicitly compared to the coherence limited resolution  $p_n$  by the ratio

$$\frac{\delta(\Delta x)}{p_n} = \frac{2 \delta(v_r) \bar{t}}{\lambda}$$

which, if greater than unity, shifts the burden of resolution limitation to  $\delta(\Delta x)$ . For Seasat, this ratio is typically about 6.

### OPTIMUM PROCESSING

Essentially three restraints on image quality follow from the theory outlined above; Pixel dwell time, scattering cell coherence time, and differential shift due to the intrinsic wave spectrum. All three of these restraints are direct aspects of the coherent scattering model developed in this work. Given these restraints, how may one proceed to sensibly - even optimally - process oceanic SAR data to best image waves?

For signal sources that are partially coherent, it is well known that the optimum processor (SNR criteria) is also partially coherent (13, 14). In this case, the optimum processor is one which first coherently integrates up to a maximum time  $T \leq t_c$  determined by the coherence time  $t_c$  of the scattering cell itself, operating as if the scattering cell were entirely stationary in the radar scene being imaged (15). Second, it must at the output of the processor noncoherently combine the sequence of coherently generated sub-images  $\{\sigma_i\}$  along the locus of the apparent motion of the brightest reflectivity in the image plane during the available data time  $T$ . The optimum form of this adjacent cell averaging is directional, and adaptive to the directional spectrum of the wave structure being imaged. One may, in addition, non-coherently integrate along waves to increase SCR at no loss of wave spectral information (16, 17).

If a sea is observed that provides variety  $\delta v_r$  in the Doppler spectrum such that the spectral shift resulting from this wave pattern is many resolution cells  $\delta(\Delta x) \gg p_n$  in extent (18), then one might compromise again the specific processing properties of the radar to account for this fact and to achieve additional mixed integration to augment the image wave contrast. The coherent integration time of the radar

should be reduced from the coherence time  $T_c$  dictated by the statistics of the scattering cell coherence time  $\bar{t}$  to achieve a degraded resolution  $\rho = \lambda R / 2vT_c$ ,  $T_c < T_c$  approaching the spectral spread  $\delta(\Delta x)$  resulting from coherent line of sight Doppler velocities. The image spread is proportional to radar range. Excess bandwidth should be used for additional (frequency plane) mixed integration, to be followed by image plane directional adjacent cell averaging, as described above. Note that there is no processing possible to improve resolution (e.g., wave visibility) beyond the limits set by  $\delta(\Delta x)$  in any given situation.

#### ASIDE ON FOCUS

It is evident from the arguments above (and verified in available imagery) that the phase velocity  $C_0$  of larger, faster waves is never coherently sensible by SAR observation. Likewise, derivatives of this velocity are never coherently sensible by a SAR for capillary scattering.

It follows that "focus adjustment" in the formal sense is not necessary in SAR observation of the sea state (21). All of the references in the available literature to so called "focus adjustments" refer to adjustments of the processor that appear to make the wave structure have greater contrast in the output image. Efforts by various investigators to improve the appearance of wave imagery by processor adjustments have, in effect, been attempts to track the point of brightest reflectivity  $\hat{Q}$  as it moves with the waves. One may predict confidently that if this tracking were implemented noncoherently, there would be a noticeable improvement in the contrast of wave patterns. This, of course, is included in the generic processing outlined above.

#### COMMENTS AND A CAVEAT

From the theory, follow two additional observations of interest (18). First, surface currents  $V_{cur}$  should be observable by using a SAR, assuming that the SAR has adequate absolute reference of zero Doppler inherent in the system. Second, the principal variational Doppler source in each coherent scattering cell derives from the vertical orbital velocity component  $A\omega \sin \theta$  of that scattering cell (11). This vertical motion is in turn proportional to wave height  $A$ ; hence, under favourable circumstances, one should be able to estimate wave

heights of the surface by subjecting the data from a synthetic aperture radar to variational Doppler spectrum analysis.

In the event the opening assumptions of this report are not satisfied - in particular if one is observing breaking seas or cycloidal seas for which the scattering is dominated by the gross structure of the wave rather than the capillaries - then almost the entirety of the above discussion is no longer valid. Specifically, the point of noncoherent brightest reflectivity  $C_0$  will tend to be more coherent over time when the gross structure of the wave determines both the phase structure and the movement of that bright point. In the event that the bright point remains statistically coherent over an appreciable portion of the integration time  $T$  of the radar, then the radar becomes (coherently) sensitive to the phase velocity of that bright point. Consequently, the imagery will show markedly different features (1). There will, for example, be gross azimuthal shift  $\Delta x$  of images, which may easily become so large as to eliminate the wave image from the scene itself. Defocusing effects may become appreciable. These effects are observed in imagery of breaking seas (1, 19, 20).

#### SUMMARY

The work in this paper outlines the culmination of theoretical and experimental investigation of a SAR's response to a typical sea surface. The requirement of scene as well as sensor coherence is proposed (for the first time, apparently) as the foundation for a coherent SAR wave reflectivity theory. Three restraints on image resolution quality follow, which in increasing order of severity are pixel dwell time, scattering cell coherence, and differential azimuth shift. A partially coherent processing concept is suggested as the optimal method of coping with these fundamental constraints.

#### ACKNOWLEDGEMENT

The authors would like to acknowledge the support of the Office of Naval Research, CCRS, and the SURSAT Project for support of various portions of this work. Special thanks are due to Alex Klooster of ERIM for insightful observations based on examination of many miles of SAR imagery.

# REFERENCES AND NOTES

1. Raney, R.K. and R.T. Lowry, Oceanic Wave Imagery and Wave Spectra Distortions by Synthetic Aperture Radar. Twelfth International Symposium on Remote Sensing of Environment, Manila, Philippines, 20-29 April 1978.
2. Wright, J.W., Backscatter from Capillary Waves with Applications to Sea Clutter. IEEE Transactions on Antennas and Propagation, Vol. AP-14, pp 749-54, November 1966.
3. Long, M.W., Radar Reflectivity of Land and Sea. Lexington Books, D.C. Heath and Co., Lexington, MA, 1975.
4. Maffett, A., Private Communication (ERIM), 1978.
5. Trunk, G.V., Radar Properties of Non-Rayleigh Sea Clutter. IEEE Transactions on AES, AES 8 #2, March 1972.
6. Jakeman, E. and P.N. Pusey, A Model for Non-Rayleigh Sea Echo. IEEE Transactions on Aerospace and Electronic Systems, 1977.
7. The spatial bandwidth of the coherent speckle noise is determined by the radar integration time  $T$ , and is not a meaningful indicator of the effective resolution of scene elements if  $\bar{t} < T$ , where  $\bar{t}$  is scattering cell coherence time.
8. Raney, R.K., Synthetic Aperture Imaging Radar and Moving Targets. IEEE Transactions on Aerospace and Electronic Systems. Vol. AES-7, No. 3, May 1971.
9. Neumann, G. and W.J. Pierson Jr., Principles of Physical Oceanography. Prentice Hall, 1966.
10. The orbital rate is  $\omega = \frac{2\pi C_0}{L}$ , where  $L$  is the wavelength, for deep water waves. The radar observes coherently the projection of  $\vec{V}_c = \vec{V}_{cur} + \vec{V}_{cap} + \vec{V}(t)$  onto the slant range vector. The projection of  $\vec{V}$  is  $v_r$ , the coherently sensible range velocity which Doppler modulates the SAR signal.
11. 
$$v_r(t) = A\omega(\sin \omega t \sin \theta + \cos \omega t \cos \theta) + v_{cur} \cos \theta \cos \theta_{cur} + v_{cap} \cos \theta \cos \theta_{cap}$$
where  $\theta_{cur}$  and  $\theta_{cap}$  are the current and capillary velocity vector directions with respect to the radar line of sight.
12. For certain wave states the integration time  $T$  of the radar is sufficiently short with respect to the movement of the scattering centres on the waves that  $C T \ll \rho$  and thus the coherent scattering cell will contain the brightest (noncoherent) scattering point  $\alpha$  during the integration time of the radar. However, for radars that have finer resolution  $\rho$  or longer integration time  $T$  or for long swells that tend to move more rapidly,  $C T \gg \rho$  and thus the point of brightest reflectivity will move through many resolution cells of the radar during the observation time of the sensor.
13. Brown, W.M. and C.J. Palermo, Effects of Phase Errors on Resolution. IEEE Trans Mil Electronics. MIL-9, 4-9, 1965.
14. Raney, R.K., Quadratic Filter Theory and Partially Coherent Optical Systems, J. Opt. Society of America, 59, (9) September, 1969.
15. The resulting azimuth resolution of each cell is enlarged if  $T \ll T_n$ .
16. Raney, R.K., Alternative Statistics for Quantitative Radar Image Interpretation. Remote Sensing Science and Technology Symposium, Ottawa, Canada, 21-23 February 1977.
17. Note that there is a fundamental difference to be exploited here between noncoherent averaging implemented in the image plane of a processor versus that achieved in the frequency plane. Each method has its place.
18. This spread is observed in SAR imagery and it is of approximately the correct magnitude to fit the coherent descriptions given in this paper (1, 19, 20).
19. Shuchman, R., Series of Communications and Internal Memoranda, ERIM, 1977-78.
20. Lowry, R.T.; D.G. Goodenough; J.S. Zelenka and R.A. Shuchman, On the Analysis of Synthetic Aperture Radar Imagery of the Ocean, Proceedings of the 4th Canadian Symposium on Remote

Sensing, Quebec City, May 1977.

21. Focus is defined as providing a phase filter matched to the complex quadratic term in the exponential of the pertinent object function. One should keep in mind that the coherent scattering centres are not moving at phase velocities  $C_0$  of the waves. The component  $v_r$  of phase velocity parallel to the aircraft line of sight does not enter the radar coherently. If it did, then a focus adjustment of  $\delta\rho = \frac{1}{2} R \lambda / v_r$  would be needed in the formal coherent sense of the word. The component  $v_t$  does not enter and it does not need, therefore, to be compensated directly. The other element of focus perturbation that might enter has to do with accelerations  $a_r$  in the radial velocity component (8). In almost all cases, this term may be neglected. If it were present, however, the consequential differential shift  $\delta(\Delta x)$  caused by the spread velocity spectrum  $\delta v_r$  of the waves would overwhelm it and thus true defocus would not be observable in the wave image. Hence focus in the formal coherent sense normally should not be considered as a variable parameter in a radar to be optimized for sea surface observations.

TABLE SUMMARIZING THE  $T < P/c_0$  RESTRAINT FOR  
VARIOUS SAR SYSTEMS GIVEN THREE TYPICAL OCEAN WAVE CONDITIONS

OCEAN WAVELENGTH SAR SYSTEM	100 M ( $c_0 = 12 \text{ m/s}$ )	200 M ( $c_0 = 18 \text{ m/s}$ )	300 M ( $c_0 = 22 \text{ m/s}$ )
SEASAT (25 M)	NO	NO	NO
SAR 580 (6 M) X-BAND	YES	YES	YES
SAR 580 (6 M) L-BAND	NO	NO	NO
JPL 990 (6 M) L-BAND	NO	NO	NO

Table 1. Table summarizing the Dwell time restraint for several SAR systems and oceanic wave lengths.

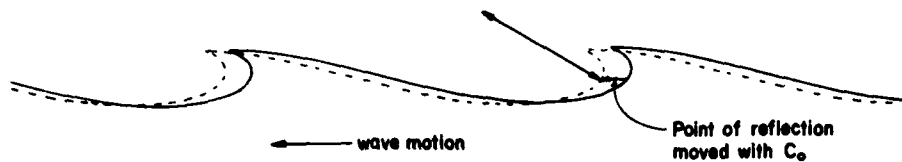
TABLE OF REQUIRED INTEGRATION TIME (SECONDS)

$P_{AZ}(M)$	25	6	2	R(KM)	V(M/SEC)
SAR 580 X	.03	.13	.4	7.45	150
SAR 580 L	.25	1.0	2.9	7.45	150
JPL 990 L	.18	.75	2.2 (N/A)*	9.4	250
SEASAT L	.5	2	N/A*	845	7868

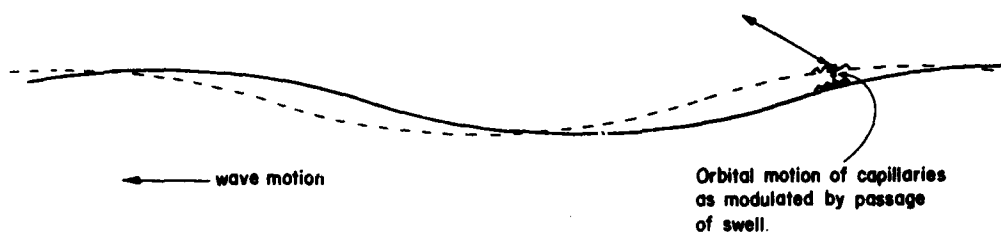
\*N/A = NOT APPLICABLE

Table 2. Table of required integration time (seconds).





(A) CRESTED OR BREAKING WAVE FOR WHICH SAR SCATTERING CENTER MOVES WITH THE WAVE PHASE VELOCITY  $C_0$



(E) LONG GRAVITY WAVE WITH CAPILLARIES FOR WHICH SAR SCATTERING CENTERS MOVE ACCORDING TO THE ORBITAL VELOCITY OF SURFACE ELEMENTS.

Figure 1. Contrast between dynamics of scattering cell for capillary and phase velocity cases.

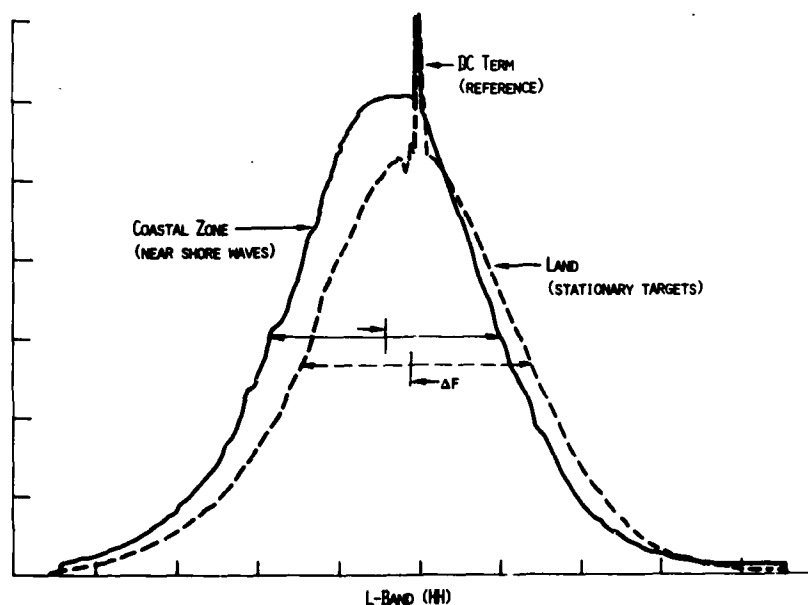


Figure 2. Shift and spread of L-band signal spectrum (Marineland).

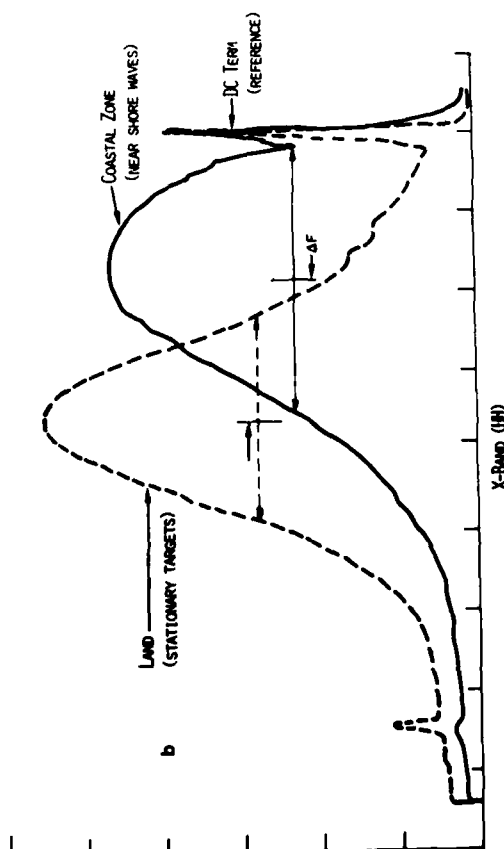
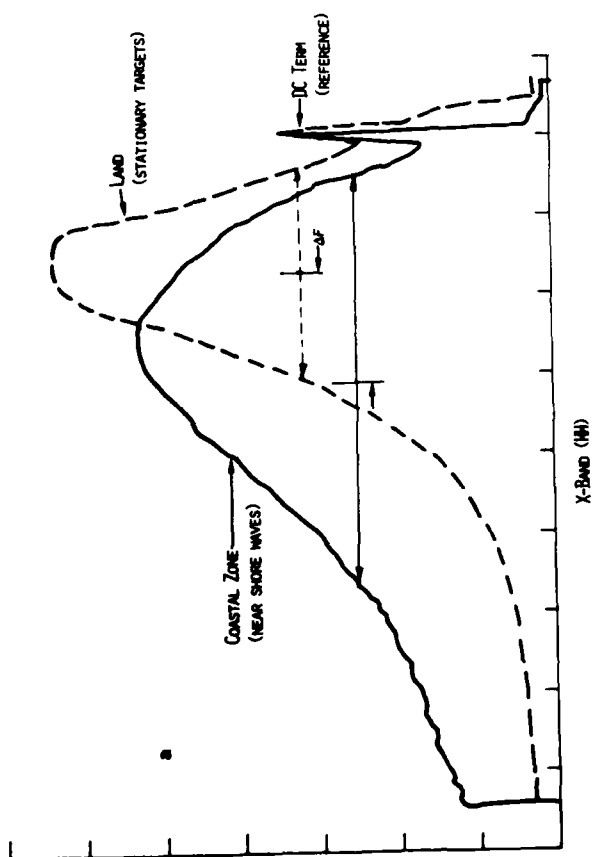


Figure 3. Shift and spread of X-band signal spectra (Marineland).  
 a. Easterly aircraft heading, shift due to Northerly current.  
 b. Westerly aircraft heading, shift due to the same current as in Figure 3a.

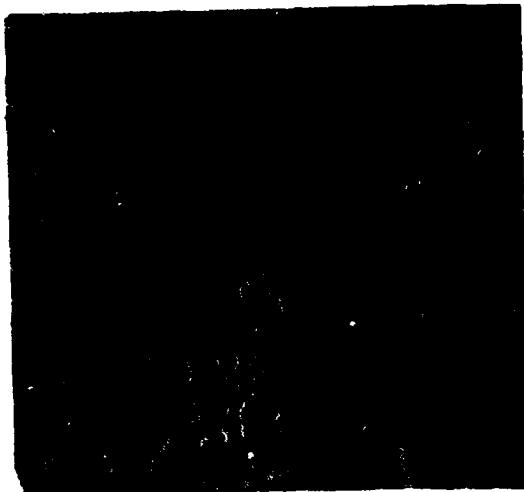


Figure 4. Image of train (moving at 3 mph toward switchyard) Doppler shifted in azimuth away from its own track.

AD-A097 946 ENVIRONMENTAL RESEARCH INST OF MICHIGAN ANN ARBOR RA--ETC F/G 17/9  
IMAGING OCEAN WAVES WITH SAR, A SAR OCEAN WAVE ALGORITHM DEVELO--ETC(U)  
DEC 79 R A SHUCHMAN, K H KNORR, J C DWYER N00014-76-C-1048  
UNCLASSIFIED FRIM124300-5-T NL

3-11  
2-1-82



END  
DATE  
FILMED  
9-81  
DTIC



Figure 5. Offshore and shorewise wave imagery from Marineland (X-band).

